UNIVERSITÉ DE STRASBOURG

ÉCOLE DOCTORALE Mathématiques, Science de l'Information et de l'Ingénieur
UMR 7357

THÈSE présentée par :

Karima BOURAS

soutenue le : **31 mars 2016**

pour obtenir le grade de : **Docteur de l'université de Strasbourg**

Discipline/ Spécialité : Sciences des Matériaux

RE-Doped SnO₂ Oxides for Efficient UV-Vis to Infrared Photon Conversion: Application to Solar Cells

THÈSE dirigée par :
  M. SLAOUI Abdelilah   Directeur de recherche, ICUBE, CNRS-Université de Strasbourg

RAPPORTEURS :
  M. PRELLIER Wilfrid   Directeur de recherche, CRISMAT, ENSICAEN, Caen
  M. MILLION Eric   Professeur, GREMI, CNRS-Université d'Orléans, Orléans

AUTRES MEMBRES DU JURY :
  M. LINCOT Daniel   Directeur de recherche, IRDEP/ IPVF, ENSCP, Paris
  M. RINNERT Hervé   Professeur, IJL, Université de Lorraine, Nancy

INVITES :
  M. POORTMANS Jef   Directeur de recherche, IMEC, Leuven, Belgium
  M. DINIA Aziz   Professeur, IPCMS, CNRS-Université de Strasbourg
  M. FERBLANTIER Gérald Maitre de conférences, ICUBE, CNRS-Université de Strasbourg

Titre en français :

Elaboration et caractérisation des oxydes transparents conducteurs dopés aux terres rares pour la conversion des photons pour le photovoltaïque

Remerciements

Faire une thèse est une expérience exceptionnelle, belle et complexe à la fois. Je tiens, en premier lieu, à remercier chaleureusement mon directeur de thèse Abdelilah SLAOUI de m'avoir accueillie au sein de son équipe de recherche et m'avoir permis de vivre cette belle et unique aventure. Il était à la fois mon directeur et mon encadrant. Merci pour tout le savoir-faire qu'il m'a transmis, la confiance qu'il m'a accordée tout au long de ce difficile parcours et l'atmosphère de travail pleine de bonne humeur et de sympathie qu'il a su propulser sans faille. C'est fût un réel plaisir de travailler avec lui.

Je remercie vivement tous les membres du jury, particulièrement les rapporteurs Wilfrid PRELLIER et Eric MILLON, malgré son épaule cassée, pour avoir examiné ce dense travail ainsi que les examinateurs Daniel LINCOT (Président du Jury), Hervé RINNERT, Jef POORTMANS, Aziz DINIA et Gérald FERBLANTIER. Le jeudi 31 mars 2016, jour de ma soutenance, était une journée noire en France dont on s'en souviendra tous. Malgré la grève de tous les services de transport, les membres du jury venant de différentes destinations, même lointaines, étaient tous présents ce jour-là. Merci encore une fois d'avoir su gérer cela pour ma soutenance.

Je tiens à remercier chaleureusement Aziz DINIA de m'avoir suivie depuis mon Master et avoir été toujours à l'écoute ; c'est grâce à lui que j'ai pu démarrer en quelque sorte cette thèse ! Merci de m'avoir accueillie aussi à l'IPCMS, d'avoir suivi et encadré de très près mes travaux de recherche. Merci pour les précieux conseils et orientations tout au long de ce long cheminement. J'ai eu de la chance de travailler avec lui.

Un grand merci, tout particulièrement à Guy SCHMERBER qui sans lui ce travail n'aurait jamais abouti. Merci pour son soutien, ses conseils et le temps qu'il m'a consacré ainsi que les « incomptables » mesures qu'il a faites dans des temps relativement courts. Parfois il lui arrivait de venir le week-end pour lancer une manip afin d'avoir le résultat en début de semaine. Merci pour son humour constante qui a rendu ce travail très agréable. Avec Guy, on a formé le super binôme jamais vu à l'ICube ou à l'IPCMS. Grâce à lui un travail de 3 thèses a été effectué en une, tout particulièrement en 1 an et demi.

Je remercie également Gérald FERBLANTIER pour sa formation pour la PVD, Thomas FIX pour m'avoir acheté les logiciels nécessaires pour faire avancer ce travail, Silviu COLIS pour les préparations des échantillons pour le TEM, et à tous pour les conseils et les riches discussions échangés lors des différentes réunions.

Je tiens à remercier chaleureusement Hervé RINNERT de l'IJL Nancy, de m'avoir accueillie dans son laboratoire et m'avoir laissé la liberté d'utiliser les manips de PL, PLE et QY qui représentent une partie très importante de mes travaux de recherche. Grâce à lui j'ai pu présenter de très beaux spectres de PL dans des conférences, des articles et également dans ce manuscrit. Merci pour les discussions fructueuses, les conseils qui m'ont été d'un grand bénéfice et la grande disponibilité pour répondre aux moindres questions avec toute sympathie. J'en suis fort reconnaissante.

Table of content

Introduction

Transparent conducting oxides (TCOs) are widely used in optoelectronic devices, among others, in all types of solar cells, from silicon-based to organic. These materials in addition to their high optical transparency in the visible range and good electrical properties can be functionalized by doping with rare earth elements which exhibit additional new functionality known as photon conversion denoted also 'photon management'. This new class of materials has recently stirred exceptional interest for their particular optical properties. The combinations of RE-TCOs, by choosing the right couple, are used as spectral converters to adapt the incident solar spectrum to the solar cell absorption. Transparency and thermalization losses can be significantly reduced through Up-conversion (UC) and Down-conversion (DC)/Down-shifting (DS), respectively.

The work of this thesis emphasizes on the conversion of high-energy photons into lower-energy photons through DC or DS processes for application to solar cells. For this purpose, we have chosen SnO_2 as host matrix for incorporation of RE elements such as Pr, Nd, Tb and Yb. The first goal of this Phd work is (i) investigating photon conversion using $RE-SnO_x$ systems by varying several experimental parameters and (ii) gain in-depth understanding of the photon-conversion mechanisms involved.

This thesis is organized in 5 chapters. Chapters 1 and 2 are introductory chapters that constitute literature reviews. Chapter one reports the state of the art on basic properties of TCOs in general and SnO_2 in particular. A detailed review from crystal and electronic structures, chemistry to physics of tin oxide is provided. Chapter 2 is dictated to lanthanides and their spectroscopy: lanthanide electronic structure and energy levels, excitation and de-excitation including radiative and non-radiative transitions, selection rules for intra 4f-transitions and energy transfer processes. The chapter ends with an overview on RE-doped SnO_2 materials reported in the literature.

Subsequently chapters 3, 4 and 5 present our experimental results on RE-doped SnO_2 materials. Chapter 3 treats RE-doped SnO_2 powders synthesized with two chemical routes: co-precipitation and sol-gel. The purpose is to investigate the possibility of incorporating RE elements in such host matrix and search whether an energy transfer is occurring between the components and determine the photon-conversion process of this system. Chapter 4 deals with RE-doped SnO_2 thin films by sputtering. These studies are of great importance from the application point of view since converting layers are applied to solar cells as thin films. Nd^{3+} and Yb^{3+} for their interesting infrared emission have been selected for investigations. Several

key parameters for the rare activation and energy transfer have been studied, as among them oxygen gas flow during deposition, growth temperature, post annealing treatment and RE content. Chapter 5 summarizes the electrical properties of the functionalized TCO films and Quantum Yield (QY). The chapter ends with application of some selected layers on solar cells, mainly on Si and CIGS.

This PhD work has been carried at ICUBE laboratory, CNRS/University of Strasbourg. It has been conducted with strong collaboration with Institut de Physique et Chimie des Matériaux (IPCMS), CNRS/University of Strasbourg, Institut Lavoisier (ILV), CNRS/University of Versailles, Institut Jean Lamour (IJL), CNRS/ University of Lorraine and School of Chemical Engineering, Yeungnam University, South Korea.

Chapter 1: Transparent Conducting Oxides (TCOs): Materials and Properties

1.1. Introduction

The family of transparent conducting oxides materials is the particular and unique class of materials able to exhibit simultaneously both transparency and electronic conductivity. That has opened the door to widespread applications with continued sweeping strides progress, especially in larger flat screen high-definition televisions (HDTVs including LCD, Plasma and OLED based displays), higher-resolution and larger flat screens for computers, photovoltaics, flexible and transparent electronics, electrochromic and low-e windows. In spite of the great success of these materials in the industry market, increasingly, the demands now require higher performance TCOs and extend beyond transparency and conductivity. Additional properties such as work function, morphology, long term stability and obviously low cost are needed to attract again more and more researcher and industrials.

Historically, TCO materials were limited to tin and zinc oxides with fluorine and aluminium doping, respectively, and Indium tin oxide. Over the past 10 years, the field of TCOs materials has been extended to numerous and variety of n-type materials as well as the synthesis of p-type materials and novel TCOs composites. This does not stop here, the emergence of new amorphous TCOs with properties as good as -or even better- than the crystalline TCOs has raised new challenges to improve the counterparts properties, particularly the low temperature processing and application in flexible electronics including deposition on polymer substrates. It is quite amazing to notice how dramatically this field progressed recently in both basic and applied science. Nowadays, the dominant markets for TCOs are flat panel displays, architectural windows and the growing PV industry.

The most often used TCO materials for energy efficient windows are Fluorine-doped tin oxide (FTO) with less used metal-oxide/Ag/metal oxide stacks such as ZnO/Zg/ZnO. The use of tin oxide coating for such applications (low-e windows in moderate climates as well) allows preventing radiative heat losses, thanks to the low thermal emissivity, such property makes it a potential candidate for use in heated glass freezer doors (particularly in commercial uses), in which defrosting freezer doors can be done by connecting to small current through the TCO coating. Tin oxide is also used in plasma displays and PV modules, but less developed than In_2SnO_3 and ITO; more recently amorphous In-Zn-O have been also used for these applications.

ZnO, In_2O_3 and SnO_2 are the most used and important semiconductors developed For TCO application. Combination of these three main materials results in multi-compound TCO materials, including ternary compounds such as Zn_2SnO_4, $ZnSnO_3$, $Zn_3In_2O_6$, $In_4Sn_3O_{12}$. Multi-component oxides have been investigated as well. However, due to the complexity in their composition it has been reported that is quite difficult to elaborate them with desirable compromise between optical and electrical properties. Figure 1 summarizes the widely used n-type TCO materials and best candidates for practical application encompassing the In_2O_3-SnO_2-ZnO system.
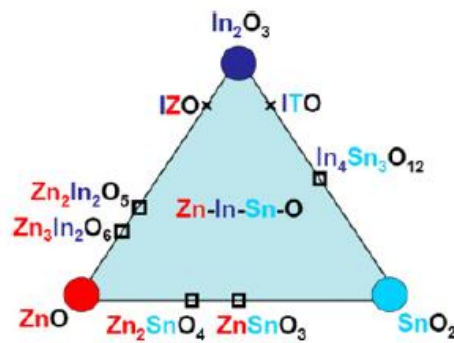
Figure 1. TCO semiconductors for thin film transparent electrodes, from reference [[1]]

The key spectral features of a typical commercial ZnO as a conventional TCO material are shown in figure 2. As mentioned above, among the relevant opto-electronic properties of a typical TCO material are optical reflection, transmission and absorption whose the spectra are shown in the left panel of figure 1 as useful baseline for discussion. In the case of ZnO and many other TCO materials, the transparency in the visible range (400-700 nm) should be quite high, in the order of 80 to 90 %. As the figure 2 displays, it is possible to observe some interference effects translating by oscillations in the transmission and reflection spectra. The fundamental band gap of the material can be deduced by fitting the short wavelength cut of in the UV region, here is at $\approx$ 300 nm. The latter indicates the excitation energy from the valence band to the conduction band (depicted in the right side of figure1).
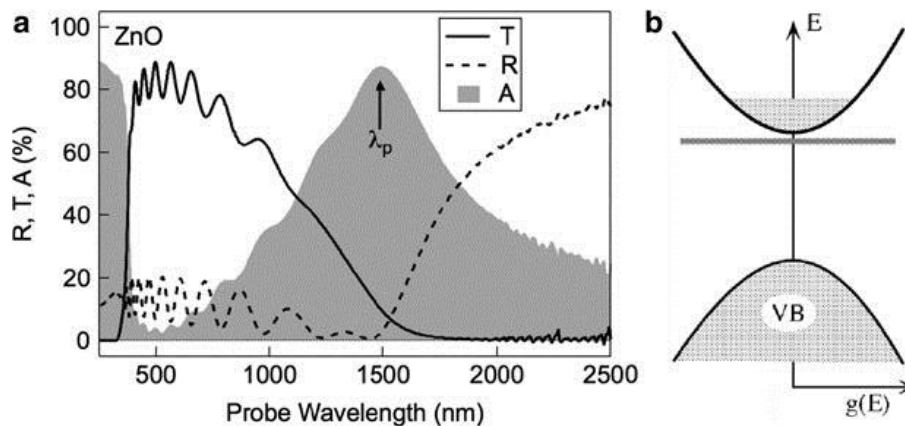
Figure 2. Optical spectra of typical (ZnO) transparent conductor (left side) and schematic electronic structure of conventional TCO materials (right side) from reference [[2]] (handbook of transparent conductors)

The gradual decrease of transmission in long wavelength starting from 1000 nm and simultaneous increase of the reflection from 1500 nm can be explained by the plasma oscillations or Plasmons for short, in other words, collective oscillations of the conduction band electrons. Due to these plasma oscillations, a substantial absorption can occur at the characteristic plasma wavelength λ_p, as is the case of this sample. It turns out that the increase of the number of the conduction band electrons N (free carrier concentration), by substitution doping for example, leads to a shift of the plasma wavelength to shorter wavelengths as $\lambda_p \propto 1/\sqrt{N}$, leading to a tradeoff between conductivity and long wavelength transparency limit. Figure 3 shows the evolution of the transmittance of Ga doped ZnO (GZO) films as a function of the carrier concentration as an example of this phenomenon. From the spectra, it can be clearly seen that the shift in the NIR region is more pronounced than that in the UV region. It appears that the increase of the carrier concentration (high doping level) results in narrowing the transmission window of the film. At this stage, it is very important to find a compromise between the material conductivity and the optical window, especially when the material is used for a specific application. For example, LED devices require only a narrow transparent window near the emission wavelengths, while solar cell devices need high transparency covering the whole solar spectrum. Therefore, the challenge for the use of TCOs in PV is the material quality. In one hand, the carrier concentration should be as low as possible in order to reduce or even get ride of the unwanted free carrier absorption in the IR, and in the other hand, the carrier mobility should be as high as possible to ensure the right electrons transport.
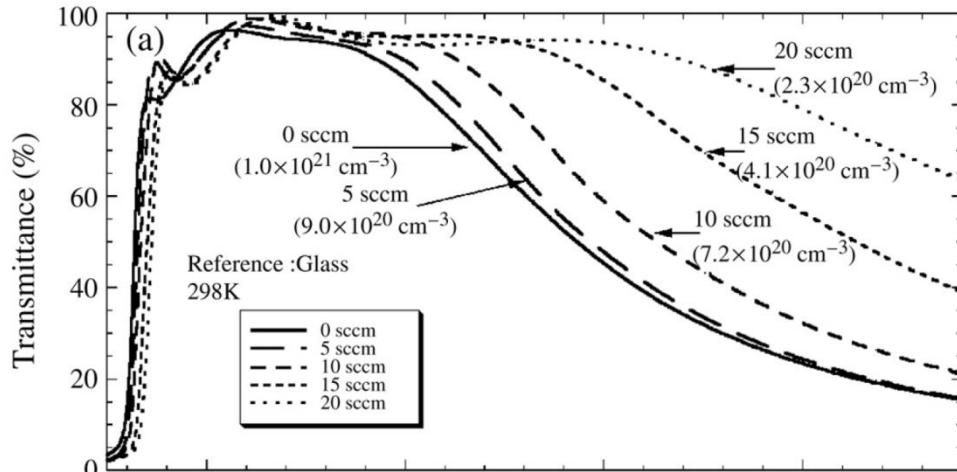
Figure 3. Transmittance spectra for GZO films with various carrier concentrations (2.3×10^{20} cm^{-3}–10×10^{20} cm^{-3}). The two boundaries (in the near-UV and IR regions) shift to shorter wavelength with the increase of carrier concentration, making the transmittance window narrower. Taken from reference [[3]]

We have mentioned above, that among nowadays required properties of TCOs is the work function, particularly for use in organic and hybrid devices. Figure 4 plots the work function of some TCO materials[4, 5]. It turns out that the n-type TCOs have very high work functions. Moreover, their conduction band minima (CBM) are lying below the vacuum level. Often, the oxygen-rich outer surface of the oxide films leads to increase the work function. It is particularly interesting to notice from the figure 4 that CBM of the SnO_2 and In_2O_3 oxides lie deeper the Fermi level of the parent metal. This behaviour typically indicates the best n-type TCO materials from the normal oxides.
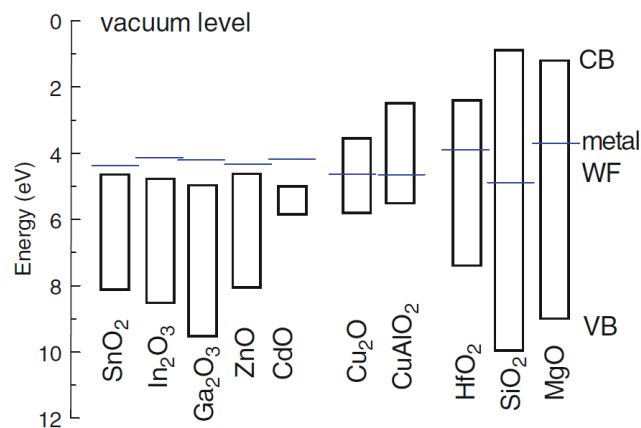
Figure 4. Work functions and electron affinities of selected oxides, compared to the work functions of their parent metals. Note how the metal WF of the n-type materials is situated above the CB of its oxide[5].

To get better quality thin film TCOs, oxide materials have been often doped by a variety of elements. Table 1 summarizes the important TCO materials as well as the potential dopants and compounds.

Table.1 Oxide materials potentially used as TCOs, particularly as transparent electrodes [[6]]

Material	Dopant or compound
SnO_2	Sb, F, As, Nb, Ta
In_2O_3	Sn, Ge, Mo, F, Ti, Zr, Mo, Hf, Nb, Ta, W, Te
ZnO	Al, Ga, B, In, Y, Sc, F, V, S, Ge, Ti, Zr, Hf
CdO	In, Sn
Ga_2O_3	
$ZnO-SnO_2$	Compounds Zn_2SnO_4, $ZnSnO_3$
$ZnO-In_2O_3$	$Zn_2In_2O_5$, $Zn_3In_2O_6$
$In_2O_3-SnO_2$	$In_4Sn_3O_{12}$
$CdO-SnO_2$	Cd_2SnO_4, $CdSnO_3$
$CdO-In_2O_3$	$CdIn_2O_4$
$MgIn_2O_4$	
$GaInO_3$, $(Ga, In)_2O_3$	Sn, Ge
$CdSb_2O_6$	Y
$Zn-In_2O_3-SnO_2$	$Zn_2In_2O_5$-$In_4Sn_3O_{12}$
$CdO-In_2O_3-SnO_2$	$CdIn_2O_4$-Cd_2SnO_4
$ZnO-CdO-In_2O_3-SnO_2$	

1.2. Basic properties of the most used TCO materials

Some physical properties of the most used TCOs are summarized in table 2. We will discuss some of their features.

In_2O_3 is classically doped with Sn resulting in the famous ITO material that exhibits both excellent optical and electrical properties making it the predominantly TCO used in optoelectronic devices; in reality this material is an In_2O_3-rich compound of In_2O_3 and SnO_2. Doping the latter compounds with Fluorine results in FTO, the most dominant SnO_2-based binary TCOs. Compared to ITO, FTO is less expensive and exhibits better chemical stability in dye sensitized solar cells as well as better thermal stability of its charge transport properties (ref 35). Moreover, it turns out that FTO is the second most used TCO in solar cells due to its stability at high temperatures (while device fabrication) and hydrogen environment. In spite of the average transmittance of FTO that turns around 80%, its electrical conductivity is relatively low [7].On the other hand, ZnO-based compounds as alternative materials to replace ITO are since a decade also subject of extensive studies. The most popular dopants of ZnO are Ga and Al, dubbed GZO and AZO, respectively. The two last materials have shown performances even better than ITO and FTO. Thus, dopant concentration as high as 10^{20}-10^{21} cm^{-3} and motilities near 95 cm^2/V has been reported in literature. Table 3 compares the basic electrical properties of ITO, FTO, GZO and AZO.

Table.2 Summary of some physical properties of the most used TCOs materials, In_2O_3, ZnO and SnO_2 (token from reference [8, 9])

Property	In_2O_3	ZnO	SnO_2
Mineral name		Zincite	Cassiterite
Abundance of the metal in the earth's crust (ppm)	0.1	132	40
Crystal structure	Cubic, bixbyite	Hexagonal, wurtzite	Tetragonal, rutile
Space group	$I2_13$	$P6_3mc$	$P4_2mnm$
Lattice constants [nm]	$a = 1.012$	$a = 0.325$	$a = 0.474$
		$b = 0.5207$	$b = 0.319$
Density ρ [g cm^{-3}]	7.12	5.67	6.99
Thermal expansion coefficient (300 K) [10^{-6} K^{-1}]	6.7	$\parallel c$: 2.92	$\parallel c$: 3.7
		$\perp c$: 4.75	$\perp c$: 4.0
Melting point [°C]	2190	2240	>1900[a]
Heat of formation [eV]	9.7	3.6	6.0
Band gap [eV]	3.75	3.4	3.6
Static dielectric constant ε_r (the complex dielectric functions are calculated	~9	$\parallel c$: 8.75	$\parallel c$: 9.6
		$\perp c$: 7.8	$\perp c$: 13.5
Effective electron mass of conduction electrons m^*/m_0 (experimental)	0.3	–	$\parallel c$: 0.23
			$\perp c$: 0.3
Effective electron mass of conduction electrons m^*/m_0 (computational)	0.34	$\parallel c$: 0.58, 0.59	$\parallel c$: 0.20
		$\perp c$: 0.6, 0.59	$\perp c$: 0.26
Common extrinsic n-type dopants	Sn, Ti, Zr, F, Cl, Sb, Ge, Zn, Pb, Si	B, Al, Ga, In, Si, Ge, Sn, Y, Sc, Ti, Zr, Hf, F, Cl	Sb, F, Cl

[a]Decomposition into SnO and O_2 at 1500 °C.

Table 3. Basic electrical properties of ITO, FTO, AZO and GZO elaborated by different techniques[1]

TCO	Deposition technique	Band gap (eV)	Carrier concentration (10^{20} cm^{-3})	Mobility (cm^2/Vs)	Resistivity (10^{-4} Ωcm)	T (%)
ITO	Commerical	--	--	--	1-1.9	--
	PLD	--	13.8	53.5	0.845	≥ 80
	Sputtering	3.8	14.6-18.9	25.7-32.7	1.28-1.29	≥ 80
FTO	Spray pyrolysis	3.15-3.57	4.5-7	12-24	3.85-7.51	~ 80
	CVD	3.51-3.86	3.05	19	10.9	~ 80
AZO	PLD	3.51-3.86	20.2	16.2	1.91	75-90
	Sputtering	--	9	25	2.7	> 85
GZO	PLD	3.51	146	30.96	0.812	> 90
	Sputtering	3.37-3.43	1-6	5-35	5.3	~ 90

The average resistivity of the different ITO films elaborated by different techniques is about $\sim 1 \times 10^{-4}$ Ω.cm, that is still lower than that of FTO yet strongly dependent in the elaboration technique. For instance, resistivity as low as 3.8×10^{-4} Ω cm can be obtained by the spray pyrolysis deposition method (the typically employed tool for FTO elaboration). For the listed AZO and GZO films, the electrical properties seems to be better than the reported FTO films but remains lower than the values recorded with ITO. However, from transparency point of view these films exhibit a very good transparent degree, which make them potential candidates to replace ITO as transparent electrodes.

Synthesis

Metallic oxides can be obtained in powders, thin or thick films, grains, nanoparticles and can be synthesized using three basic families of deposition techniques:

-Slurry deposition

- Screen-printing

-Drop casting

-Spin coating

-Dip coating

-Spray deposition, sol-gel (solution-based processes)

-Chemical Vapor Deposition (CVD)

-Thermal CVD

-Plasma activated CVD

-Laser induced CVD

-Electrodes plating

-Physical Vapor Deposition (PVD)

-Sputtering

-Evaporation

-Pulsed laser deposition (PLD)

The choice of the elaboration technique will define the morphology of the material and its properties. The deposition technique used for thin films elaboration in this thesis is reactive magnetron sputtering

1.3. Case of Tin oxide

SnO_2 is an n-type large band gap semiconductor oxide that combines high transparency with good electrical properties, making it one of the potential candidates for TCO application. Tin oxide is a very particular material and quite difficult to analyze because of the dual valency of Sn. In fact, depending on the oxygen chemical potential of the system, stoichiometric surface with Sn^{4+} cations could be easily reduced into surface with Sn^{2+} cations[8]. This reversible surface modification induces the appearance of the Sn 5s derived levels lying deep within the oxide band gap that will then lower its work function (modification of the electronic structure of the oxide in the surface) whence the involvement of SnO_2 in gas sensing application and oxidation catalyst. This does not stop here, tin oxide (SnO_2) is also considered as a promising material for potential replacement of commercial graphite as anode for lithium-ion batteries[10].

For TCO application, the bulk properties of SnO_2 are at stake. Thanks to the low electrical resistivity and high optical transparency in the visible range, SnO_2 becomes an attractive material for use in different fields of optoelectronics, particularly in solar cells[11-13], LED, flat panel displays and other transparent field effect transistors[14, 15]. The idea is the possibility to establish an electric contact without prohibiting photons from entering or escaping the optical window. Moreover, TCO materials including SnO_2 are characterized by high reflectivity for infrared light, making them popular for energy conservation. Architectural windows based on SnO_2-coatings, nowadays, are able to transmitting light and keeping heat outside; more sophistically, the so-called 'smart windows' can tune the optical transparency as well as their colouring by simply applying a voltage across electrohomic films electrically connected to TCOs. Thanks to the high stability in different environments, SnO_2 is also applied in low-emission window coatings[16-18].

1.3.1. Crystallographic structure

Thanks to the dual valency of tin, two distinct oxides can be elaborated by monitoring the oxygen content in the structure. The Sn in its 4+ valency forms the tin dioxide (SnO$_2$) known as stannic oxide, while when it is in the 2+ valency, it forms the tin oxide SnO known as stannous oxide. Both compounds are stable; nevertheless, the latter is less known and less characterized than SnO$_2$.

SnO is a p-type semiconductor with a band gap of 2.5-3 eV. Increasing the oxygen content in the structure leads to the formation of n-type SnO$_2$ oxide with a larger band gap of 3.6 eV. Other tin oxides such as Sn$_2$O$_3$ and Sn$_3$O$_4$ also exist; however, the most abundant oxide of tin is stannic oxide (SnO$_2$), which is an asset for technological applications.

It is important to underline that the incorporation of O interstitials into SnO leads to the formation of SnO$_2$ and vice-versa since the introduction of O vacancies in SnO$_2$ results in SnO. The oxidation of tin from SnO to SnO$_2$ has been extensively studied in literature through a variety of preparation techniques[19-23]. Stannous tin oxide is crystallized into the tetragonal structure (litharge structure in the mineral form). In the unit cell of SnO, Sn^{2+} ions occupy the $(\frac{1}{2} 0 \frac{3}{4})$ and $(0 \frac{1}{2} \frac{1}{4})$ sites[21]. Each atom (Sn or O) is fourfold coordinated (tetrahedral coordination) with bonds length of 2.23 Å, all oxygen atoms are situated in the same side of the Sn atoms (like a pyramid that consists of one Sn and four O atoms)[19]. SnO oxide belongs to the symmetry space group P4/nmm with lattice constants: a=b= 3.8029 A and c= 4.8382 Å[24]. In contrast to the rutile structure of SnO$_2$, SnO have a layered structure (very similar to that of PbO) in the (001) direction with a Sn$_{1/2}$-O- Sn$_{1/2}$ sequence. The van-der-Waals distance between two neighbouring Sn layers is about 2.52 Å[8].

Deep analysis have shown that the Sn planes are screened by an electron charge clouds, due to the positive charge of the Sn^{2+} ions, resulting in reducing the coulombic repulsion between the Sn planes[25-27]. The electron charge clouds are also known as charge hats arising essentially from the Sn 5s electrons that do not participate to the bonding of Sn^{2+} ions. These electrons are described as lone pairs and have been identified in Galy's work[28] as intermediate state localized between an inert spherical orbital (s^2-type, centred on the nucleus) and a hybridized non-bonded and non-spherical orbital situated far from the nucleus. This spatial effect is very important to predict the local environment symmetries[29]. The latter can be very different for different Sn II based compounds. In the case of SnTe, which have a cubic structure, the electronic charge is spherically centred on the Sn atoms. While in the case of SnO, the electronic charge is strongly directional and forms chare hats[30].

As regards the stannic oxide, SnO$_2$ have a rutile structure. Its mineral form is known as Cassiterite. As many other oxides similar to SnO$_2$ such as TiO$_2$, RuO$_2$, MnO$_2$ and CrO$_2$, the rutile structure belongs to the

P4$_2$/mnm space group symmetry with a tetragonal unit cell of lattice constants of a=b=4.7374 Å and c= 3.1864 Å[31]. Each Sn atom is sixfold coordinated while the oxygen atoms are threefold coordinated. Thus we can imagine that Sn atoms are surrounded by distorted octahedrons of O atoms. (see figure5)
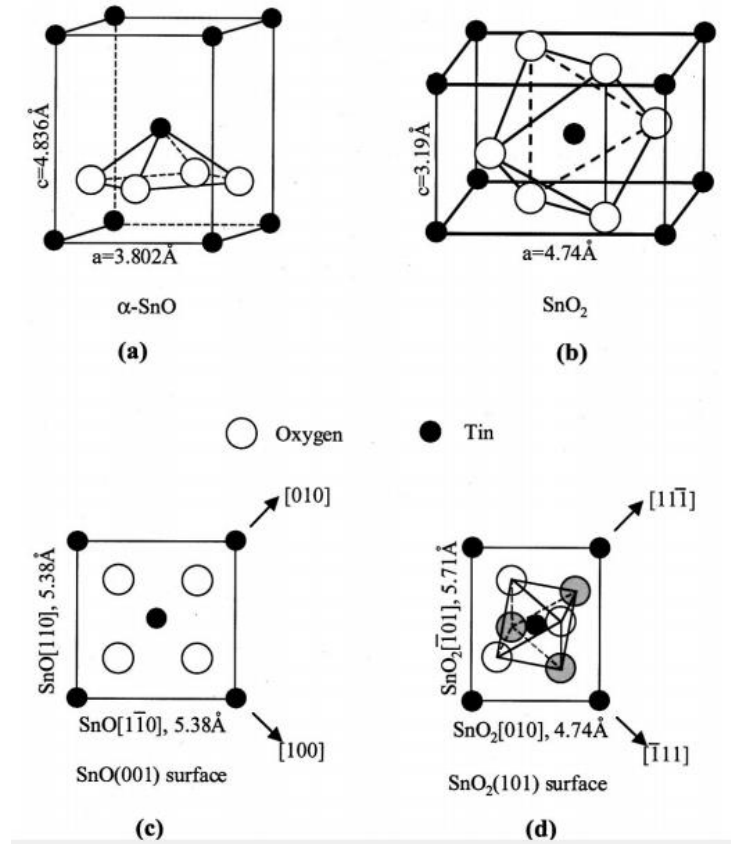
Figure 5 crystal structure of SnO (a) and SnO₂ (b), atomic configurations of the (001) and (101) surfaces of SnO and SnO₂ respectively [19].

1.3.2. Phonon modes of SnO and SnO₂

Raman or infrared spectroscopy is one of techniques that allow distinguishing between SnO and SnO₂. Thus, the vibrational modes of SnO group theory are as follow:

Γ= A$_{1g}$+B$_{1g}$+2E$_g$ +A$_{2u}$+2B$_{1u}$+E$_u$ + 3 acoustic modes[20],

while these of SnO₂ are:

Γ= A$_{1g}$+A$_{2g}$ +B$_{1g}$+B$_{2g}$+E$_g$+2A$_{2u}$+2B$_{1u}$+4E$_u$ [32-34] where 5 modes of A1g, B1g, B2g and Eg are Raman active and 7 modes of A2u and 3Eu are IR active and two modes of A2g and B1u are inactive[35-37].

Phonons modes that could be attributed to either to SnO nor SnO₂ were considered as a proof of presence of intermediate phases of tin oxide such as Sn₂O₃ and Sn₃O₄[20]. These Raman peaks have been observed at

$145cm^{-1}$ and $171cm^{-1}$ while those of SnO have been reported at 113 (115) cm^{-1} for B_{1g} and 211 cm^{-1} for A_{1g}[8].

The corresponding atomic replacement for the Raman active and IR modes for both SnO and SnO_2 are reported in figure 6.
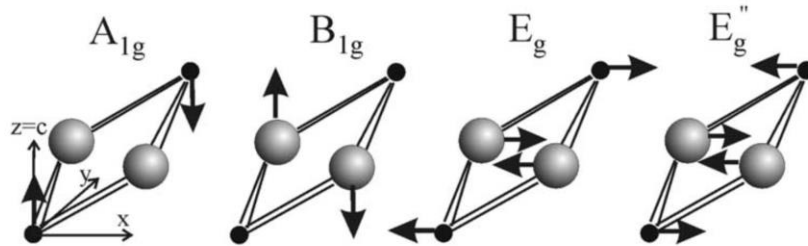
Figure 6.a Phonon normal coordinates in SnO : (a) Raman-active modes ; (b) IR-active modes[20].
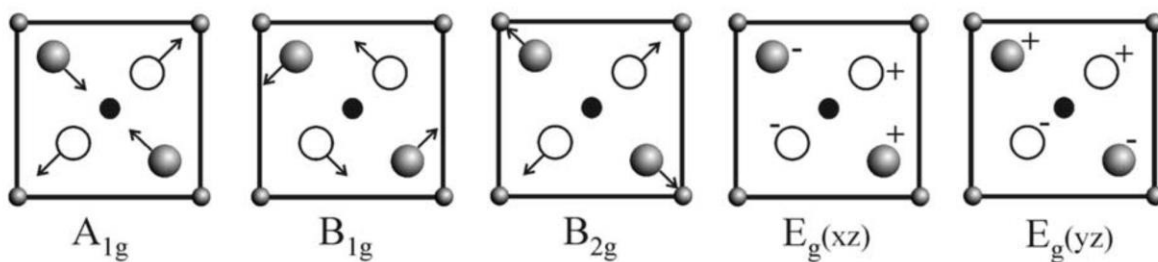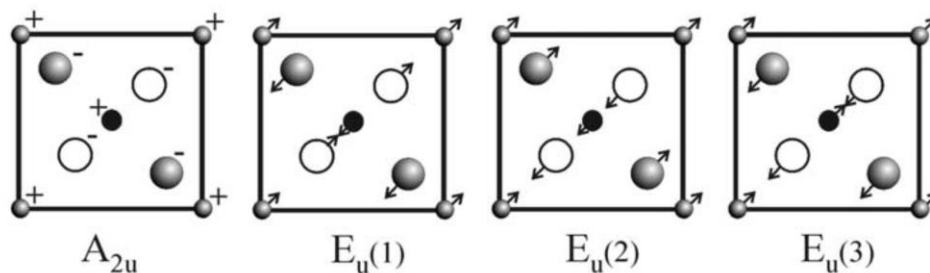
Figure 6.b Schematic representation of atomic displacements for the Raman and IR-active modes of SnO_2 (from Ref.[[34]]

In the IR modes of SnO, the Sn sublattice is placed with respect to the O sub-lattice which gives rise to a dipole moment. For the A_{2u} mode the polarization is parallel to the c axis and perpendicular for the E_u mode.

In the Raman active modes of SnO_2 the oxygen atoms vibrate while the Sn atoms are at rest. The nondegenerate modes, A_{1g}, B_{1g}, and B_{2g} vibrate in the plane perpendicular to the c-axis while the doubly degenerate E_g mode vibrates in the direction of the c-axis[20, 38]. The B_{1g} mode consists of rotation of the oxygen atoms around the c-axis, with all six oxygen atoms of the octahedral participating in the vibration. In the A_{2u} infrared active mode, Sn and oxygen atoms vibrate in the c-axis direction, and in the E_u mode both Sn and O atoms vibrate on the plane perpendicular to the c-axis[20]. The silent modes correspond to vibrations of the Sn and O atoms on the direction of the c-axis (B_{1u}) or in the plane perpendicular to this direction (A_{2g}).

1.3.3. Band structure of tin oxide

1.3.3.1. Band gap calculations

A variety of attempts to calculate the band gap of SnO_2 have been reported in the literature. The total energy as well as the electronic structure have been calculated through the Density-functional theory (DFT) employing the local-density approximation (LDA), generalized gradient approximation (GGA) and tight binding approximation (TBA) methods. The latter is usually employed to describe the oxides semiconductors by considering the entire valence and conduction bands. The theoretical predictions unfortunately did not much with the experimental values of the band gaps[39, 40]. These discrepancies have been ascribed to the discontinuity of the exchange correlation potentials[41-45]. Therefore, additional empirical correctional terms had to be added in order to get ride of these discrepancies. First-principles periodic Hartree-Fock linear combination of atomic orbitals (LCAO) approximation has been used to calculate the ground-state energy as a function of the unit-cell volume[46, 47]. Considering dominant self-interaction corrections (SIC) have been reported by Perdew et al as an alternative approach to improve the total energy values[48]. As for the correction of the electronic structure as well as the band gap of SnO_2, Schleife have recently reported a plane-wave GW method[49]. They have shown that adding SIC to LDA is very important to quantitatively describe systems with deeply localized states as is the case of SnO_2.

The structural parameters of SnO_2 have been obtained through the full potential-linearized augmented plane wave (FPLAPW) with the GGA and LDA schemes without considering the spin-orbit coupling effect[50-54]. In fact that was realised by calculating the total energy at different values of the lattice parameters, obviously around the experimental values.

It is reported that the conduction bands essentially arise from s and p orbitals of Sn atoms as states with a bottom located at the Γ point. The conduction band minimum (CBM) at the zone center Γ consists mainly of Sn 5s states[55], while in Tight-binding description it consists of 96 % of Sn s states. The lowest lying bands in the electronic structure of SnO$_2$ are originating from the oxygen s states. Just above these states, lie the upper valence bands, which are mainly formed by Sn and oxygen p states[50]. Robertson et al. reported that the upper valence band lying from 0 eV down to -8.1 eV is mainly O 2p states, with a mixture of some Sn s and p states[5]. The O 2s are lying at -16 eV and do not contribute to the bonding. A direct forbidden band gap of SnO$_2$ has been found at the symmetry point of the valence band maximum (VBM). The direct band gap of SnO$_2$ is found in the direction (Γ-X direction), or *Λ* direction (Γ-M direction) where the conduction band exhibits free-electron like character. The direct SnO$_2$ band gap was calculated at 3.7 eV by Mishra et al.[56], at 3.6 eV by Robertson Barbarat dans Calatayud et al.[55, 57, 58] The direct band gap has been supported by numerous authors. For instance, Gracia et al. have reported that the direct transitions corresponding to the direct band gap are occurring at the Γ-point of the Brillouin zone[59].

1.3.3.2. Band gap corrections

The ab-initio empirical methods mentioned above have in fact gave quite right information about the total energies, the structure as well as the bonds length. However, the estimation of the band gap values for semiconductors and dielectrics is very far to match with the experimental values[49, 50]. For example, the SnO$_2$ band gap calculated within LDA and GGA was found about 1.2 eV, which is much lower than the experimental values rather close to 3.6 eV[60]. Moreover, though the TB model gives a very good description of the dielectric properties, it suffers from inadequate knowledge of local wave function when it concerns small interactions between quasi-particles[61].

Robertson et al. reported that beyond the LDA approximation, there are a lot of methods that can predict better the band structure[5]. The most popular approximations among others are: self-consistent GW[41-43], SIC[62] and B3LYP[63-65]. The GW method is usually used to predict the fundamental band gap for a wide range of semiconductors[41, 44, 45]. Introducing some perturbation terms performs the band gap corrections. As for the Self-interaction correction (SIC), as reported by Perdew et al.[48], it considers the interactions between the orbitals whatever is the density functional of the energy. This method is known to accurately predict the electron densities and correct behaviours of potentials and densities. However, the only downside of this method is that most of reports dealing with it, involves accurate analysis of the electronic structure, particularly the intrinsic defects of SnO$_2$ or other semiconductors, which are very difficult to control[66-69]. Finally, the B3LYP exchange-correlation functional has been employed to extract accurate values of the band gap energies and density of states with excellent agreements with the experimental values[59, 70-73]. Trani et al have verified this approach for rutile SnO$_2$[71]. It was discussed in previous reports that the discrepancies in the energy gap calculations are due to the underestimation of the band gap O (p)-metal (d) repulsion, by using the DFT theory[74, 75]. In fact, the bottom of the

conduction band consists of the Sn (s) and O (p) states with an anti-bonding character while the top of the valence band arises from the O (p) states. The underestimation of the O (p) and metal (d) has been attributed to the lack of discontinuity in the exchange-correlation potential. In order to get accurate representation of the electronic structure, exchange-correlation self-energy can be replaced either by its linear expansion in the dynamically screened Coulomb interaction[76, 77] or by non-local potentials derivatives combining LDA and GGA with Hartree-Fock approximation (HFA)[50]. Adamo and barone[78] have reported the PBE0 functional while Heyd, Scuseria and Ernzerhof have showed the HSE03 as the hybrid functionals[46, 47]. In Figure 7 is shown the quasi-particule band structure of rutile SnO$_2$ using HSE03+G0W0 and LDA+U+ published by Schleife et al. The calculated band gap value is found to match very well with the experimental band gap.
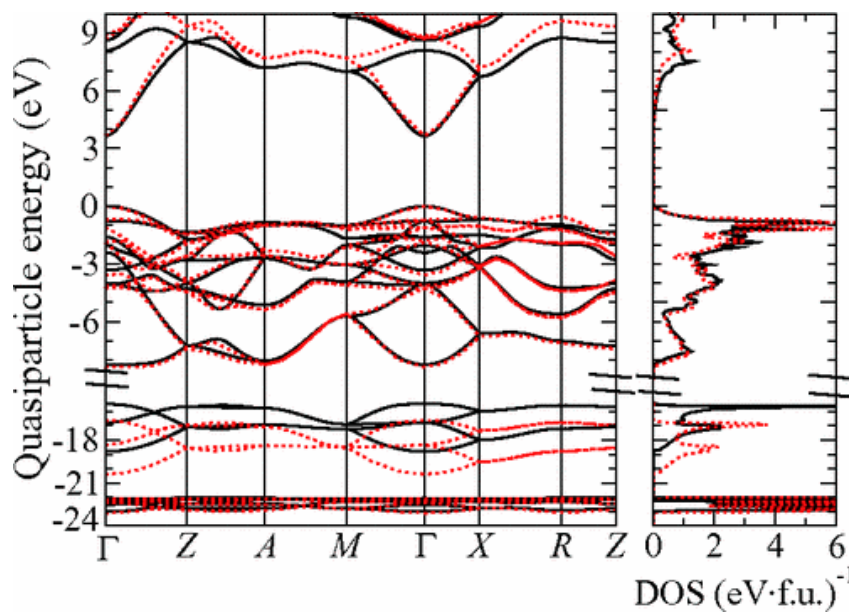
Figure7. Quasiparticle band structure of rutile SnO$_2$ in HSE03 + G$_\circ$W$_\circ$ (dotted red lines) and LDA + U + Δ (solid black lines). The VBM has been chosen as the common zero of energy. Taken with permission from A. Schleife, J.B. Varley, F. Fuchs, C. Rödl, F. Bechstedt, P. Rinke, A. Janotti and C.G. Van de Walle, Phys. Rev. B **83** (2011) 035116. © 2011 American Physical Society. Ref[[49]]

The atomic geometry of SnO$_2$ is shown in figure 8. It was found that the band gap of the rutile structure lies at the Γ point in the Brillouin zone; this band gap corresponds to direct transition. The width of the valence band is closer to 9 eV. The SnO$_2$ unit cell as well as the associated Brillouin zone are shown in figure 8.
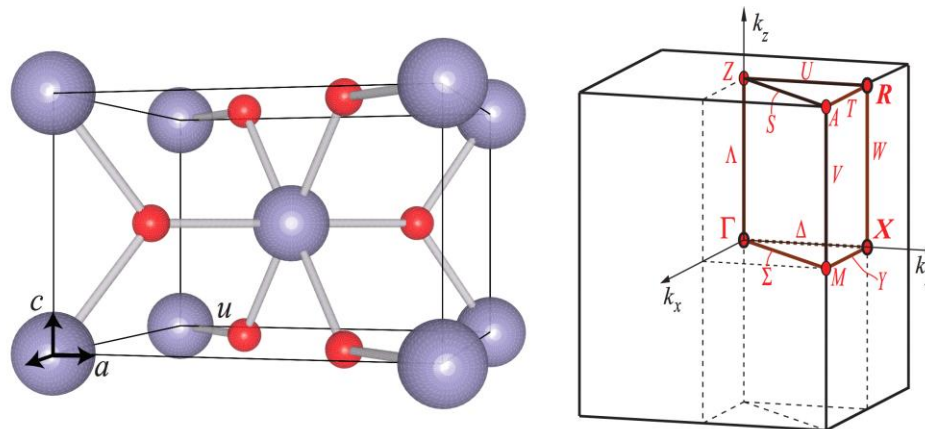
Figure 8. Bonding geometry of the tetragonal unit cell of SnO_2 in the rutile structure with the associated Bruillouin zone. The special points *R, X*, and the zine center Γ are highlighted from ref [49]

1.4. Doping of SnO₂ and transport properties

SnO_2 is an interesting material that has the unique feature of the simultaneous presence of transparency and conductivity among the IV-group elements of the periodic table. Madvedeva et al[79] reported the correlation between the electrical and optical properties with the structure. Therefore, they formulated essential criteria for good combination of transparency (in the visible) and high electrical conductivity[79]. They key property to understand the multi-aspects of SnO_2 is the dual valency of Sn by surface analysis.

Doped SnO_2 materials, usually incorporated in optoelectronic devices, possess carrier concentrations around~10^{20} cm^{-3}. At this level of doping, the optical constants are altered by free carriers light absorption in the NIR-to-visible range[80, 81]. Doping polycrystalline SnO_2 with In and Li give rises to excellent electrical conductivity with good optical transparency[82]. The reason of coexisting of these two properties is not clear yet. It was reported in reference [[83]] that the transparent conductivity is related to the presence of shallow donor levels near the conduction band, usually formed by the large amounts of oxygen vacancies. To understand this phenomenon, Kilic et al. have performed first-principles calculations in the framework of DFT within LDA using the Ceperley-Alder exchange correlation potential[84]. The calculations concerned essentially the donor, acceptor energy levels for different intrinsic defects such as oxygen vacancy (V_o), tin interstitial (Sn_i), tin antisite (SnO_o), tin vacancy (Vsn) and oxygen interstitial (Oi) in various charge states and under different chemical potential conditions in SnO_2. Kilic and their co-workers have shown that Sn_i and V_o are the most dominant defects in the SnO_2 structure due to the divalence of Sn, which therefore explains the natural non-stoichiometry of SnO_2. In fact, these structural defects are found to generate shallow donor levels within the band gap leading to n-type conductivity of intrinsic non-stoichiometric SnO_2. More particularly, the conductivity is determined by the oxygen vacancies whose the concentration is impossible to control. Numerous of earlier reports focussing on the conductivity in doped SnO_2 films[85-87]. The addition of the group III elements is found to decrease the

conductivity while doping with group V elements leads to conductivity increase[88]. In these films, the resistivity initially decreases as a function of the dopant concentration. However, at a certain point it increases back even at high doping level. Das et al reported that the optimum concentration ranges between 0.4 and 3 mol%[50].

To increase the n-type conductivity of SnO_2, the latter can be doped with antimony (Sb)[56, 89, 90], fluorine (F)[91] and molybdenum (Mo)[92]. Randhawa et al reported Sb-doped SnO_2 thin films with resistivity of $\rho \sim 5*10^{-4}$ Ωcm with transparency of 95%[93]. The same material have been studied by Kim et al and reported values of $9.8*10^{-4}$ Ωcm with T=88%[94]. Mishra et al have reported a calculated electronic structrure of antimony-doped tin oxide[56]. Using the self-consistent scattered wave molecular orbital cluster and augmented spherical wave supercell band structure approach, they reported that the conductivity of this material particularly arises from the Sn 5s-like band, and increases by thermal excitations of electrons to these 5s like bands[56]. Sb-doped SnO_2 material have been introduced into electronic devices as nanowires, and showed low turn-on/ threshold voltages[95, 96] (84, 85). Thangaraju et al[97] in the other hand reported an interesting study on Fluorine doped SnO_2 thin films with resistivity in the range of 10^{-4}- 10^{-3} Ω cm and mobility of 7-17.2 $cm^2V^{-1}s^{-1}$. Concerning the In doped SnO_2. Bhise et al[98] have reported carrier concentration of $1.3 \cdot 10^{20}$ cm^{-3}.

1.4.1. Carriers' generation and effect of doping on the electronic structure

The coexistence of good electrical conductivity with optical transparency can be understood in terms of the band structure, which combines several properties: (i) TCO materials possess usually wide optical band gap, which prohibit the interband band transitions in the visible; (ii) In the other hand, dopants, either intrinsic such as oxygen deficiency or impurities, donate electrons into the conduction band; (iii) The latter is found to be a single band with an s-type character, which is strongly dispersed with minimum at the Γ-point of the Brillouin zone resulting in a light conduction electrons effective mass. This allow a uniform distribution of the electron charge density and therefore relative low scattering. These properties contribute to high mobility of the conduction electrons. Moreover, the conduction band contains an internal large band gap, prohibiting inter-conduction-band adsorption of photons in the visible range.

The critical point of the TCOs properties is the creation of charge carriers. Charge carriers can be generated in three ways: (i) intrinsic/extrinsic dopants donate directly electrons to the conduction band and no need to an external energy such as light or heat to move the charge carriers; (ii) in the second scenario, the presence of impurities create localized bands below the conduction band and thus, an activation energy is needed to promote electrons to the conduction band; (iii) The last scenario consists in the hybridization of the donor states and the valence band levels where the donor band becomes part of the conduction band.

Kilic and Zunger[84] have reported that the oxygen vacancies defect levels in non-stoichiometric SnO$_2$ lie at just 114 meV below the conduction band minimum (CBM), and therefore can be easily thermally ionized. As concerns the tin interstitial atoms, a spontaneous donation of electron to the conduction band via a level situated at 203 eV above the CBM. Experimentally, the energy positions of the dopant levels in SnO$_2$ can be determined through a closer analysis of the activation energy. The latter was calculated by Marley and Dockerty and they found 150 meV for SnO$_2$ single crystals[99]. Other studies have reported values of 10-40 meV[100], 24±4 meV[101], 60 meV[102], 700 meV[103] (for minerals cassiterite) and 41-60 meV for Zn-doped SnO$_{2[104]}$.

Mizokawa and Nakamura have reported the presence of two donor levels with activation energy of 100 meV and 300 meV, respectively[105]. Detailed studies on the band structure modification induced by doping have been reported for Sb doped SnO$_{2[56]}$ and recently for Sn doped In$_2$O$_{3[106,\ 107]}$, where the impurity atoms donate one additional valence electron. This donation is expected upon substitutional replacement of host lattice cations. Calculations of the band structure of Sb doped suggested the formation of Sb 5s like band with the SnO$_2$ band gap with free electron-like character at the Γ point. This band was found to be half filled-metallic band, therefore, external thermal energy excite electrons into the Sn-like bands which can enhance the conductivity of the material. Similar results have been found for the Sn doped In$_2$O$_3$. In fact, doping with metallic Sn atoms induces hybridization of Sn and In 5s states separates states of the partially filled conduction band, as a consequence, the splitting of the conduction band reduces the optical adsorption by inter-conduction-band transitions. It was found that doping In$_2$O$_3$ with Sn leads to less dispersion of the conduction band, resulting in reducing the electrons mobility when increasing the Sn content. In the other hand, a strong dispersion of the s-type conduction band, leads to the increase of the optical band gap (shift of the absorption edge toward higher energies) with increasing the impurity concentration (increase of the carrier concentration). This behaviour is known as the Burstien-Moss effect and usual for most TCOs, particularly In$_2$O$_{3[108-114]}$, ZnO[115, 116], CdO[117, 118], Cd$_2$SnO$_{4[119,\ 120]}$ and SnO$_{2[90,\ 121-125]}$. In fact, the optical band gap value depend on the curvature of the conduction and valence band, which is proportional to the effective masse of electrons. This is schematically illustrated in figure 9.
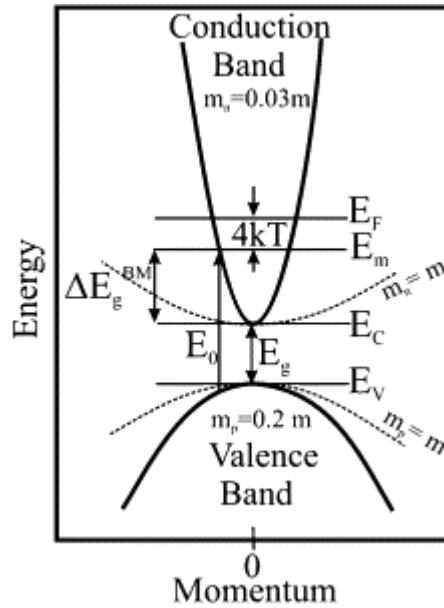
Fig. 9. Schematic of the broadening of the optical band gap due to the Burstein–Möss effect. E_G indicates the fundamental band gap and E_O, the optical band gap. The broadening of the optical band gap due to filling of the conduction band is the difference between E_O and E_G, and is indicated as ΔE_g^{BM} ΔEgBM. Such a broadening is observed for materials with strongly dispersing conduction bands. The effective masses for the valence band and conduction band are indicated as m_p and m_n, respectively (from Ref.[[126]], © (1954) by the American Physical Society).

The fact that the strongly dispersed conduction band is being filled, electrons in the valence band needs more energy to attain empty states in the conduction band. This extra needed energy is also measured with the real band gap of the material, and the sum of both represents the optical band gap.

1.4.2. Chemistry

As mentioned before, the lower symmetry of the tetragonal rutile structure of SnO₂ leads to anisotropy in its electronic and optical properties. For example, smaller atomic distance between the Sn atoms along the c axis promotes the overlap between the atomic orbitals and therefore more conductive pathways for electrons transport. Besides, it is well known that the carrier generation of conduction electrons are mostly created by the oxygen vacancies, this process can be described using the following equation (including the Kroger-vink notation):

$$O_O^X \rightarrow V_O^{\bullet\bullet} + 2e' + {}^1\!/_2\, O_2(g)$$
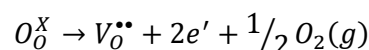
According to this equation, oxygen anions when escaping/leaving the crystal structure (migrate the occupied oxygen sites) create doubly ionized vacancy site ($V_O^{\bullet\bullet}$) and two free electron carriers. Moreover, the creation of multiple carriers from a single defect is highly desirable, and particularly important for TCO applications. This phenomenon is highly possible due to the minimization of carrier scattering on crystal

impurities. The presence of Vo in bulk SnO$_2$ have been studied by Kofstad et al using the X-ray diffraction technique[127]. The donor levels created by the oxygen vacancies have been found to lie about 3 and 140 meV below the conduction band for singly and doubly ionized states, respectively, according to the references [[128]] and [[129]]. It turns out that the oxygen deficiency of the structure can be easily controlled, in the case of thin films by sputtering, for instance by adjusting the oxygen partial pressure during deposition[86]. The authors reported that higher partial pressure leads to the carrier concentration decrease (lower electrical conductivity), indicating a decrease in the density of the oxygen vacancies defects in the SnO$_{2-x}$ thin films. In a very interesting work of Zunger et al[84] using first principle, they pointed out that the although oxygen vacancies contribute to the carriers generation, a large part of generated electrons (majority) comes from tin interstitial atoms (Sn$_i$). The Sn$_i$ related defects states are found to appear above the conduction band minimum (CBM) and therefore easily create the conduction electrons, whereas the oxygen vacancies related states (shallow donors) are located below the CBM.

Apart from oxygen deficiency, a variety of dopants have been used to improve the conductivity in SnO$_2$. For n-type doping, the most frequent method is substituting the Sn^{4+} and O^{2-} sites by the Sb^{5+} and F^{-1} elements, respectively[86, 90]. Other donors dopants also exist such as Mo, Ta, and Cl [86, 130, 131]. In these doping processes, the single electron generation is produced through substitution; the least ambiguous method is substituting the threefold coordinated O^{2-} by F^{-1} anions. Interestingly, due to the similarity of the ionic radius of oxygen and fluorine, the crystal lattice is the least affected upon substitution with minimum lattice distortion, which preserve the transport properties of the material. In the other hand, doping with larger anions such as Cl-, which also prefers a sixfold coordinated environment, however, it results in lowering the carrier concentration and their mobility[131]. The free electron generation can also be produced through incorporation of Ta as well, however, only small amounts of Ta and Mo can be incorporated in the SnO$_2$ lattice, in the order of few at.%[86, 130, 132], due to the concentration quenching effect. Beyond a certain concentration, the conductivity decreases because of the reduction of mobility.

As discussed before, from the substitution point of view, the difference in the ionic radius of the lattice ions and the dopants is very important. In the case of SnO$_2$ oxide, the size of Sn^{4+} cation is about 0.69 Å, which is appreciably larger than the ionic radius of most cation donor dopants with pentavalent or sixfold coordination[133]. In fact, these dopants may be incorporated into different oxidation states because of their multivalency. For example, Sb cation can be either Sb^{5+} with an ionic radius of 0.60 Å and therefore result in carrier's generation; or in the Sb3+ with ionic raddi of 0.7 Å which would create acceptor states. Saadeddin et al have reported on the presence of Sb^{3+} in bulk and thin film SnO$_2$:Sb using XPS measurements[134]. In addition, when SnO$_2$ is doped with elements of similar ionic radius such as Li (0.090 nm), Al (0.069 nm), Ga (0.076 nm), In (0.094 nm) and N (0.10), the insertion is done by substituting Sn in the crystal lattice. This will create a vacancy site in and above the VBM.

P-type doping can be also performed by introducing group II and III cations such as In, Ga, Al, Fe, Zn… etc [135-140], or by substituting anion sites by N3-, which results in creation of acceptor-like states in the SnO_2 structure. It was reported that the Zn doping leads to a decrease of the electron carriers concentration[133] It turns out that is very difficult to induce hole carriers in wide band-gap semiconductors, this lies in the generation of compensating donor-states in which the increase of the acceptor doping level leads to increase of the density of oxygen vacancies and tin interstitial[50]. Moreover, it has been shown that intrinsic SnO thin films exhibit p-type conductivity[141].

1.5. References

[1] H. Liu, V. Avrutin, N. Izyumskaya, Ü. Özgür, H. Morkoç, Transparent conducting oxides for electrode applications in light emitting and absorbing devices, Superlattices and Microstructures, 48 (2010) 458-484.

[2] D. Ginley, J. Perkins, Transparent Conductors, in: D.S. Ginley (Ed.) Handbook of Transparent Conductors, Springer US, 2011, pp. 1-25.

[3] S. Shirakata, T. Sakemi, K. Awai, T. Yamamoto, Electrical and optical properties of large area Ga-doped ZnO thin films prepared by reactive plasma deposition, Superlattices and Microstructures, 39 (2006) 218-228.

[4] T. Minami, T. Miyata, T. Yamamoto, Work function of transparent conducting multicomponent oxide thin films prepared by magnetron sputtering, Surface and Coatings Technology, 108–109 (1998) 583-587.

[5] J. Robertson, B. Falabretti, Electronic Structure of Transparent Conducting Oxides, in: D.S. Ginley (Ed.) Handbook of Transparent Conductors, Springer US, 2011, pp. 27-50.

[6] M. Tadatsugu, Transparent conducting oxide semiconductors for transparent electrodes, Semiconductor Science and Technology, 20 (2005) S35.

[7] J.W. Bae, S.W. Lee, G.Y. Yeom, Doped-Fluorine on Electrical and Optical Properties of Tin Oxide Films Grown by Ozone-Assisted Thermal CVD, Journal of The Electrochemical Society, 154 (2007) D34-D37.

[8] M. Batzill, U. Diebold, The surface and materials science of tin oxide, Progress in Surface Science, 79 (2005) 47-154.

[9] K. Ellmer, Resistivity of polycrystalline zinc oxide films: current status and physical limit, Journal of Physics D: Applied Physics, 34 (2001) 3097.

[10] J.S. Chen, X.W. Lou, SnO2 and TiO2 nanosheets for lithium-ion batteries, Materials Today, 15 (2012) 246-254.

[11] S.R. Vishwakarma, Rahmatullah, H.C. Prasad, Low cost SnO 2 :P/SiO 2 /n-Si (textured) heterojunction solar cells, Journal of Physics D: Applied Physics, 26 (1993) 959.

[12] K. Tennakone, G. R. R. A. Kumara, I. R. M. Kottegoda, V. P. S. Perera, An efficient dye-sensitized photoelectrochemical solar cell made from oxides of tin and zinc, Chemical Communications, (1999) 15-16.

[13] S. Ito, Y. Makari, T. Kitamura, Y. Wada, S. Yanagida, Fabrication and characterization of mesoporous SnO_2/ZnO-composite electrodes for efficient dye solar cells, Journal of Materials Chemistry, 14 (2004) 385-390.

[14] W. Lee, Y.-K. Fang, J.-J. Ho, C.-Y. Chen, R.-Y. Tsai, D. Huang, F. Ho, H.W. Chou, C.C. Chen, Pulsed-magnetron-sputtered low-temperature indium tin oxide films for flat-panel display applications, Journal of Elec Materi, 31 (2002) 129-135.

[15] R.E. Presley, C.L. Munsee, C.H. Park, D. Hong, J.F. Wager, D.A. Keszler, Tin oxide transparent thin-film transistors, Journal of Physics D: Applied Physics, 37 (2004) 2810.

[16] C.G. Granqvist, A. Hultåker, Transparent and conducting ITO films: new developments and applications, Thin Solid Films, 411 (2002) 1-5.

[17] B.G. Lewis, D.C. Paine, Applications and Processing of Transparent Conducting Oxides, MRS Bulletin, 25 (2000) 22-27.

[18] I. Hamberg, C.G. Granqvist, Evaporated Sn-doped In_2O_3 films: Basic optical properties and applications to energy-efficient windows, Journal of Applied Physics, 60 (1986) R123-R160.

[19] X.Q. Pan, L. Fu, Oxidation and phase transitions of epitaxial tin oxide thin films on ($\bar{1}012$) sapphire, Journal of Applied Physics, 89 (2001) 6048-6055.

[20] J. Geurts, S. Rau, W. Richter, F.J. Schmitte, SnO films and their oxidation to SnO_2: Raman scattering, IR reflectivity and X-ray diffraction studies, Thin Solid Films, 121 (1984) 217-225.

[21] W.K. Choi, H. Sung, K.H. Kim, J.S. Cho, S.C. Choi, H.J. Jung, S.K. Koh, C.M. Lee, K. Jeong, Oxidation process from SnO to SnO_2, Journal of Materials Science Letters, 16 (1997) 1551-1554.

[22] P. De Padova, M. Fanfoni, R. Larciprete, M. Mangiantini, S. Priori, P. Perfetti, A synchrotron radiation photoemission study of the oxidation of tin, Surface Science, 313 (1994) 379-391.

[23] K. Nose, A.Y. Suzuki, N. Oda, M. Kamiko, Y. Mitsuda, Oxidation of SnO to SnO_2 thin films in boiling water at atmospheric pressure, Applied Physics Letters, 104 (2014) -.

[24] J. Pannetier, G. Denes, Tin(II) oxide: structure refinement and thermal expansion, Acta Crystallographica Section B, 36 (1980) 2763-2765.

[25] G.W. Watson, The origin of the electron distribution in SnO, The Journal of Chemical Physics, 114 (2001) 758-763.

[26] J. Terra, D. Guenzburger, Electronic structure and electric-field gradients of crystalline Sn(II) and Sn(IV) compounds, Physical Review B, 44 (1991) 8584-8598.

[27] M. Meyer, G. Onida, M. Palummo, L. Reining, Ab initio pseudopotential calculation of the equilibrium structure of tin monoxide, Physical Review B, 64 (2001) 045119.

[28] J. Galy, G. Meunier, S. Andersson, A. Åström, Stéréochimie des eléments comportant des paires non liées: Ge (II), As (III), Se (IV), Br (V), Sn (II), Sb (III), Te (IV), I (V), Xe (VI), Tl (I), Pb (II), et Bi (III) (oxydes, fluorures et oxyfluorures), Journal of Solid State Chemistry, 13 (1975) 142-159.

[29] H. Bürger, Molecular Geometry. Von R. J. Gillespie. Van Nostrand Reinhold Comp., London 1972. 1. Aufl., IX, 228 S., zahlr. Abb. u. Tab., geb. ca. DM 38.—, Angewandte Chemie, 86 (1974) 565-565.

[30] I. Lefebvre, M.A. Szymanski, J. Olivier-Fourcade, J.C. Jumas, Electronic structure of tin monochalcogenides from SnO to SnTe, Physical Review B, 58 (1998) 1896-1906.

[31] A.A. Bolzan, C. Fong, B.J. Kennedy, C.J. Howard, Structural Studies of Rutile-Type Metal Dioxides, Acta Crystallographica Section B, 53 (1997) 373-380.

[32] R.S. Katiyar, P. Dawson, M.M. Hargreave, G.R. Wilkinson, Dynamics of the rutile structure. III. Lattice dynamics, infrared and Raman spectra of SnO2, Journal of Physics C: Solid State Physics, 4 (1971) 2421-2431.

[33] A. Diéguez, A. Romano-Rodríguez, A. Vilà, J.R. Morante, The complete Raman spectrum of nanometric SnO2 particles, Journal of Applied Physics, 90 (2001) 1550-1557.

[34] P. Merle, J. Pascual, J. Camassel, H. Mathieu, Uniaxial-stress dependence of the first-order Raman spectrum of rutile. I. Experiments, Physical Review B, 21 (1980) 1617-1626.

[35] J.F. Scott, Raman Spectrum of SnO2, The Journal of Chemical Physics, 53 (1970) 852-853.

[36] J.G. Traylor, H.G. Smith, R.M. Nicklow, M.K. Wilkinson, Lattice Dynamics of Rutile, Physical Review B, 3 (1971) 3457-3472.

[37] J.X. Zhou, M.S. Zhang, J.M. Hong, Z. Yin, Raman spectroscopic and photoluminescence study of single-crystalline SnO2 nanowires, Solid State Communications, 138 (2006) 242-246.

[38] J. Kaur, J. Shah, R.K. Kotnala, K.C. Verma, Raman spectra, photoluminescence and ferromagnetism of pure, Co and Fe doped SnO2 nanoparticles, Ceramics International, 38 (2012) 5563-5570.

[39] A.J. Williamson, L.W. Wang, A. Zunger, Theoretical interpretation of the experimental electronic structure of lens-shaped self-assembled InAs/GaAs quantum dots, Physical Review B, 62 (2000) 12963-12977.

[40] A. Kobayashi, O.F. Sankey, S.M. Volz, J.D. Dow, Semiempirical tight-binding band structures of wurtzite semiconductors: AlN, CdS, CdSe, ZnS, and ZnO, Physical Review B, 28 (1983) 935-945.

[41] M.S. Hybertsen, S.G. Louie, Electron correlation in semiconductors and insulators: Band gaps and quasiparticle energies, Physical Review B, 34 (1986) 5390-5413.

[42] J.A. Berger, L. Reining, F. Sottile, Efficient GW calculations for SnO2, ZnO, and rubrene: The effective-energy technique, Physical Review B, 85 (2012) 085126.

[43] M.J. van Setten, F. Weigend, F. Evers, The GW-Method for Quantum Chemistry Applications: Theory and Implementation, Journal of Chemical Theory and Computation, 9 (2013) 232-246.

[44] H. Lars, On correlation effects in electron spectroscopies and the GW approximation, Journal of Physics: Condensed Matter, 11 (1999) R489.

[45] F. Trani, J. Vidal, S. Botti, M.A.L. Marques, Band structures of delafossite transparent conductive oxides from a self-consistent GW approach, Physical Review B, 82 (2010) 085115.

[46] J. Heyd, G.E. Scuseria, M. Ernzerhof, Hybrid functionals based on a screened Coulomb potential, The Journal of Chemical Physics, 118 (2003) 8207-8215.

[47] J. Heyd, G.E. Scuseria, M. Ernzerhof, Erratum: "Hybrid functionals based on a screened Coulomb potential" [J. Chem. Phys.118, 8207 (2003)], The Journal of Chemical Physics, 124 (2006) 219906.

[48] J.P. Perdew, A. Zunger, Self-interaction correction to density-functional approximations for many-electron systems, Physical Review B, 23 (1981) 5048-5079.

[49] A. Schleife, J.B. Varley, F. Fuchs, C. Rödl, F. Bechstedt, P. Rinke, A. Janotti, C.G. Van de Walle, Tin dioxide from first principles: Quasiparticle electronic states and optical properties, Physical Review B, 83 (2011) 035116.

[50] S. Das, V. Jayaraman, SnO2: A comprehensive review on structures and gas sensors, Progress in Materials Science, 66 (2014) 112-255.

[51] L.S. Roman, R. Valaski, C.D. Canestraro, E.C.S. Magalhães, C. Persson, R. Ahuja, E.F. da Silva Jr, I. Pepe, A.F. da Silva, Optical band-edge absorption of oxide compound SnO2, Applied Surface Science, 252 (2006) 5361-5364.

[52] L.A. Errico, Ab initio FP-LAPW study of the semiconductors SnO and SnO2, Physica B: Condensed Matter, 389 (2007) 140-144.

[53] K. Parlinski, Y. Kawazoe, Ab initio study of phonons in the rutile structure of under pressure, Eur. Phys. J. B, 13 (2000) 679-683.

[54] J. Xu, S. Huang, Z. Wang, First principle study on the electronic structure of fluorine-doped SnO2, Solid State Communications, 149 (2009) 527-531.

[55] J. Robertson, Electronic structure of SnO 2 , GeO 2 , PbO 2 , TeO 2 and MgF 2, Journal of Physics C: Solid State Physics, 12 (1979) 4767.

[56] K.C. Mishra, K.H. Johnson, P.C. Schmidt, Electronic structure of antimony-doped tin oxide, Physical Review B, 51 (1995) 13972-13976.

[57] P. Barbarat, S.F. Matar, First-principles investigations of the electronic, optical and chemical bonding properties of SnO2, Computational Materials Science, 10 (1998) 368-372.

[58] M. Calatayud, J. Andrés, A. Beltrán, A theoretical analysis of adsorption and dissociation of CH3OH on the stoichiometric SnO2(110) surface, Surface Science, 430 (1999) 213-222.

[59] L. Gracia, A. Beltrán, J. Andrés, Characterization of the High-Pressure Structures and Phase Transformations in SnO2: A Density Functional Theory Study, The Journal of Physical Chemistry B, 111 (2007) 6479-6485.

[60] O. Hidefumi, I. Shuichi, T. Naoaki, O. Shuhei, K. Yasunori, S. Yuzo, Study on Electronic Structure and Optoelectronic Properties of Indium Oxide by First-Principles Calculations, Japanese Journal of Applied Physics, 36 (1997) 5551.

[61] R. Benchamekh, F. Raouafi, J. Even, F. Ben Cheikh Larbi, P. Voisin, J.M. Jancu, Microscopic electronic wave function and interactions between quasiparticles in empirical tight-binding theory, Physical Review B, 91 (2015) 045118.

[62] A. Filippetti, N.A. Spaldin, Self-interaction-corrected pseudopotential scheme for magnetic and strongly-correlated systems, Physical Review B, 67 (2003) 125109.

[63] A.D. Becke, Density-functional thermochemistry. III. The role of exact exchange, The Journal of Chemical Physics, 98 (1993) 5648-5652.

[64] J. Muscat, A. Wander, N.M. Harrison, On the prediction of band gaps from hybrid functional theory, Chemical Physics Letters, 342 (2001) 397-401.

[65] J. Robertson, P.W. Peacock, M.D. Towler, R. Needs, Electronic structure of p-type conducting transparent oxides, Thin Solid Films, 411 (2002) 96-100.

[66] K.G. Godinho, A. Walsh, G.W. Watson, Energetic and Electronic Structure Analysis of Intrinsic Defects in SnO2, The Journal of Physical Chemistry C, 113 (2009) 439-448.

[67] O. Fumiyasu, C. Minseok, T. Atsushi, S. Atsuto, T. Isao, Native defects in oxide semiconductors: a density functional approach, Journal of Physics: Condensed Matter, 22 (2010) 384211.

[68] A.K. Singh, A. Janotti, M. Scheffler, C.G. Van de Walle, Sources of Electrical Conductivity in SnO2, Physical Review Letters, 101 (2008) 055502.

[69] D.O. Scanlon, G.W. Watson, On the possibility of p-type SnO2, Journal of Materials Chemistry, 22 (2012) 25236-25245.

[70] F. El Haj Hassan, S. Moussawi, W. Noun, C. Salameh, A.V. Postnikov, Theoretical calculations of the high-pressure phases of SnO2, Computational Materials Science, 72 (2013) 86-92.

[71] F. Trani, M. Causà, D. Ninno, G. Cantele, V. Barone, Density functional study of oxygen vacancies at the SnO2 surface and subsurface sites, Physical Review B, 77 (2008) 245410.

[72] C.-M. Liu, X.-R. Chen, G.-F. Ji, First-principles investigations on structural, elastic and electronic properties of SnO2 under pressure, Computational Materials Science, 50 (2011) 1571-1577.

[73] F.c.R. Sensato, R. Custódio, M. Calatayud, A. Beltrán, J. Andrés, J.R. Sambrano, E. Longo, Periodic study on the structural and electronic properties of bulk, oxidized and reduced SnO2(1 1 0) surfaces and the interaction with O2, Surface Science, 511 (2002) 408-420.

[74] P. Borges, L.R. Scolfaro, H. Leite Alves, E. da Silva, Jr., DFT study of the electronic, vibrational, and optical properties of SnO2, Theoretical Chemistry Accounts, 126 (2010) 39-44.

[75] A. Schleife, F. Fuchs, J. Furthmüller, F. Bechstedt, First-principles study of ground- and excited-state properties of MgO, ZnO, and CdO polymorphs, Physical Review B, 73 (2006) 245212.

[76] F. Bechstedt, F. Fuchs, G. Kresse, Ab-initio theory of semiconductor band structures: New developments and progress, physica status solidi (b), 246 (2009) 1877-1892.

[77] M.N. Risto, Issues in first-principles calculations for defects in semiconductors and oxides, Modelling and Simulation in Materials Science and Engineering, 17 (2009) 084001.

[78] C. Adamo, V. Barone, Toward reliable density functional methods without adjustable parameters: The PBE0 model, The Journal of Chemical Physics, 110 (1999) 6158-6170.

[79] J.E. Medvedeva, A.J. Freeman, Combining high conductivity with complete optical transparency: A band structure approach, EPL (Europhysics Letters), 69 (2005) 583.

[80] H. Kawazoe, H. Yanagi, K. Ueda, H. Hosono, Transparent p-Type Conducting Oxides: Design and Fabrication of p-n Heterojunctions, MRS Bulletin, 25 (2000) 28-36.

[81] A.N. Banerjee, K.K. Chattopadhyay, Recent developments in the emerging field of crystalline p-type transparent conducting oxide thin films, Progress in Crystal Growth and Characterization of Materials, 50 (2005) 52-105.

[82] B.-M. Mohammad-Mehdi, S.-S. Mehrdad, Electrical, optical and structural properties of Li-doped SnO 2 transparent conducting films deposited by the spray pyrolysis technique: a carrier-type conversion study, Semiconductor Science and Technology, 19 (2004) 764.

[83] S. Samson, C.G. Fonstad, Defect structure and electronic donor levels in stannic oxide crystals, Journal of Applied Physics, 44 (1973) 4618-4621.

[84] Ç. Kılıç, A. Zunger, Origins of Coexistence of Conductivity and Transparency in SnO2, Physical Review Letters, 88 (2002) 095501.

[85] A. Rohatgi, T.R. Viverito, L.H. Slack, Electrical and Optical Properties of Tin Oxide Films, Journal of the American Ceramic Society, 57 (1974) 278-279.

[86] B. Stjerna, E. Olsson, C.G. Granqvist, Optical and electrical properties of radio frequency sputtered tin oxide films doped with oxygen vacancies, F, Sb, or Mo, Journal of Applied Physics, 76 (1994) 3797-3817.

[87] D.J. Goyal, C. Agashe, B.R. Marathe, M.G. Takwale, V.G. Bhide, Effect of dopant incorporation on structural and electrical properties of sprayed SnO2:Sb films, Journal of Applied Physics, 73 (1993) 7520-7523.

[88] A.F. Carroll, L.H. Slack, Effects of Additions to SnO2 Thin Films, Journal of The Electrochemical Society, 123 (1976) 1889-1893.

[89] C. Terrier, J.P. Chatelon, R. Berjoan, J.A. Roger, Sb-doped SnO2 transparent conducting oxide from the sol-gel dip-coating technique, Thin Solid Films, 263 (1995) 37-41.

[90] E. Shanthi, V. Dutta, A. Banerjee, K.L. Chopra, Electrical and optical properties of undoped and antimony-doped tin oxide films, Journal of Applied Physics, 51 (1980) 6243-6251.

[91] T. Ishida, O. Tabata, J.i. Park, S.H. Shin, H. Magara, S. Tamura, S. Mochizuki, T. Mihara, Highly conductive transparent F-doped tin oxide films were prepared by photo-CVD and thermal-CVD, Thin Solid Films, 281–282 (1996) 228-231.

[92] V. Casey, M.I. Stephenson, A study of undoped and molybdenum doped, polycrystalline, tin oxide thin films produced by a simple reactive evaporation technique, Journal of Physics D: Applied Physics, 23 (1990) 1212.

[93] H.S. Randhawa, M.D. Matthews, R.F. Bunshah, SnO2 films prepared by activated reactive evaporation, Thin Solid Films, 83 (1981) 267-271.

[94] H. Kim, A. Piqué, Transparent conducting Sb-doped SnO2 thin films grown by pulsed-laser deposition, Applied Physics Letters, 84 (2004) 218-220.

[95] Q. Wan, E.N. Dattoli, W. Lu, Transparent metallic Sb-doped SnO2 nanowires, Applied Physics Letters, 90 (2007) 222107.

[96] L. Huixuan, S. Jia, X. Ruijie, W. Qing, Transparent SnO2 Nanowire Electric-Double-Layer Transistors With Different Antimony Doping Levels, Electron Device Letters, IEEE, 32 (2011) 1358-1360.

[97] B. Thangaraju, Structural and electrical studies on highly conducting spray deposited fluorine and antimony doped SnO2 thin films from SnCl2 precursor, Thin Solid Films, 402 (2002) 71-78.

[98] A.B. Bhise, D.J. Late, B. Sathe, M.A. More, I.S. Mulla, V.K. Pillai, D.S. Joag, Fabrication of In-doped SnO2 nanowire arrays and its field emission investigations, Journal of Experimental Nanoscience, 5 (2010) 527-535.

[99] J.A. Marley, R.C. Dockerty, Electrical Properties of Stannic Oxide Single Crystals, Physical Review, 140 (1965) A304-A310.

[100] K. Ishiguro, T. Sasaki, T. Arai, I. Imai, Optical and Electrical Properties of Tin Oxide Films, Journal of the Physical Society of Japan, 13 (1958) 296-304.

[101] M. Nagasawa, S. Shionoya, S. Makishima, Electron Effective Mass of SnO2, Journal of the Physical Society of Japan, 20 (1965) 1093-1093.

[102] S.C. Chang, Oxygen chemisorption on tin oxide: Correlation between electrical conductivity and EPR measurements, Journal of Vacuum Science & Technology, 17 (1980) 366-369.

[103] E.E. Kohnke, Electrical and optical properties of natural stannic oxide crystals, Journal of Physics and Chemistry of Solids, 23 (1962) 1557-1562.

[104] H.E. Matthews, E.E. Kohnke, Effect of chemisorbed oxygen on the electrical conductivity of Zn-doped polycrystalline SnO2, Journal of Physics and Chemistry of Solids, 29 (1968) 653-661.

[105] M. Yusuke, N. Shogo, ESR and Electric Conductance Studies of the Fine-Powdered SnO 2, Japanese Journal of Applied Physics, 14 (1975) 779.

[106] O.N. Mryasov, A.J. Freeman, Electronic band structure of indium tin oxide and criteria for transparent conducting behavior, Physical Review B, 64 (2001) 233111.

[107] Hidefumi Odaka, Yuzo Shigesato, Takashi Murakami, Shuichi Iwata, Electronic Structure Analyses of Sn-doped In2O3, Japanese Journal of Applied Physics, 40 (2001) 3231.

[108] K. Chopra, S. Das, Why Thin Film Solar Cells?, in: Thin Film Solar Cells, Springer US, 1983, pp. 1-18.

[109] K.L. Chopra, S. Major, D.K. Pandya, Transparent conductors—A status review, Thin Solid Films, 102 (1983) 1-46.

[110] Z.M. Jarzebski, Preparation and physical properties of transparent conducting oxide films, physica status solidi (a), 71 (1982) 13-41.

[111] O. Lang, C. Pettenkofer, J.F. Sánchez-Royo, A. Segura, A. Klein, W. Jaegermann, Thin film growth and band lineup of In2O3 on the layered semiconductor InSe, Journal of Applied Physics, 86 (1999) 5687-5691.

[112] I. Hamberg, C.G. Granqvist, K.F. Berggren, B.E. Sernelius, L. Engström, Band-gap widening in heavily Sn-doped In2O3, Physical Review B, 30 (1984) 3240-3249.

[113] R.L. Weiher, R.P. Ley, Optical Properties of Indium Oxide, Journal of Applied Physics, 37 (1966) 299-302.

[114] W.G. Haines, R.H. Bube, Effects of heat treatment on the optical and electrical properties of indium–tin oxide films, Journal of Applied Physics, 49 (1978) 304-307.

[115] A.P. Roth, J.B. Webb, D.F. Williams, Band-gap narrowing in heavily defect-doped ZnO, Physical Review B, 25 (1982) 7836-7839.

[116] O. Caporaletti, Electrical and optical properties of bias sputtered ZnO thin films, Solar Energy Materials, 7 (1982) 65-73.

[117] Y. Dou, R.G. Egdell, T. Walker, D.S.L. Law, G. Beamson, N-type doping in CdO ceramics: a study by EELS and photoemission spectroscopy, Surface Science, 398 (1998) 241-258.

[118] Y. Dou, T. Fishlock, R.G. Egdell, D.S.L. Law, G. Beamson, Band-gap shrinkage in n-type-doped CdO probed by photoemission spectroscopy, Physical Review B, 55 (1997) R13381-R13384.

[119] Y. Dou, R.G. Egdell, Surface properties of indium-doped Cd2SnO4 ceramics studied by EELS and photoemission spectroscopy, Surface Science, 372 (1997) 289-299.

[120] A.J. Nozik, Optical and Electrical Properties of Cd2SnO4: A Defect Semiconductor, Physical Review B, 6 (1972) 453-459.

[121] T. Arai, The Study of the Optical Properties of Conducting Tin Oxide Films and their Interpretation in Terms of a Tentative Band Scheme, Journal of the Physical Society of Japan, 15 (1960) 916-927.

[122] E. Shanthi, A. Banerjee, K.L. Chopra, Dopant effects in sprayed tin oxide films, Thin Solid Films, 88 (1982) 93-100.

[123] K. Suzuki, M. Mizuhashi, Structural, electrical and optical properties of r.f.-magnetron-sputtered SnO2:Sb film, Thin Solid Films, 97 (1982) 119-127.

[124] G. Sanon, R. Rup, A. Mansingh, Band-gap narrowing and band structure in degenerate tin oxide SnO2 films, Physical Review B, 44 (1991) 5672-5680.

[125] K.B. Sundaram, G.K. Bhagavat, Optical absorption studies on tin oxide films, Journal of Physics D: Applied Physics, 14 (1981) 921.

[126] E. Burstein, Anomalous Optical Absorption Limit in InSb, Physical Review, 93 (1954) 632-633.

[127] P. Kofstad, Nonstoichiometry, diffusion, and electrical conductivity in binary metal oxides. (Wiley series on the science and technology of materials). P. Kofstad. 160 Abb. 11 Tab. XI, 382 S. Ca. 1060 Schrifttumshinweise. Format 15.5 × 23 cm. Wiley Interscience (J. Wiley & Sons, Inc.) New York-London-Sydney-Toronto,1972. Gebunden ca. DM 52, Materials and Corrosion, (1974) 335.

[128] C.G. Fonstad, R.H. Rediker, Electrical Properties of High-Quality Stannic Oxide Crystals, Journal of Applied Physics, 42 (1971) 2911-2918.

[129] R. Korotkov, A. Farran, T. Culp, D. Russo, C. Roger, Transport properties of undoped and NH3-doped polycrystalline SnO2 with low background electron concentrations, Journal of Applied Physics, 96 (2004) 6445-6453.

[130] S.w. Lee, Y.-W. Kim, H. Chen, Electrical properties of Ta-doped SnO2 thin films prepared by the metal–organic chemical-vapor deposition method, Applied Physics Letters, 78 (2001) 350-352.

[131] C. Agashe, S.S. Major, Effect of F, Cl and Br doping on electrical properties of sprayed SnO2 films, Journal of Materials Science Letters, 15 (1996) 497-499.

[132] Y.-W. Kim, S.W. Lee, H. Chen, Microstructural evolution and electrical property of Ta-doped SnO2 films grown on Al2O3(0001) by metalorganic chemical vapor deposition, Thin Solid Films, 405 (2002) 256-262.

[133] R. Shannon, Revised effective ionic radii and systematic studies of interatomic distances in halides and chalcogenides, Acta Crystallographica Section A, 32 (1976) 751-767.

[134] I. Saadeddin, B. Pecquenard, J.P. Manaud, R. Decourt, C. Labrugère, T. Buffeteau, G. Campet, Synthesis and characterization of single- and co-doped SnO2 thin films for optoelectronic applications, Applied Surface Science, 253 (2007) 5240-5249.

[135] K. Galatsis, L. Cukrov, W. Wlodarski, P. McCormick, K. Kalantar-zadeh, E. Comini, G. Sberveglieri, p- and n-type Fe-doped SnO2 gas sensors fabricated by the mechanochemical processing technique, Sensors and Actuators B: Chemical, 93 (2003) 562-565.

[136] Y. Huang, Z. Ji, C. Chen, Preparation and characterization of p-type transparent conducting tin-gallium oxide films, Applied Surface Science, 253 (2007) 4819-4822.

[137] B.-M. Mohammad-Mehdi, S.-S. Mehrdad, The influence of Al doping on the electrical, optical and structural properties of SnO 2 transparent conducting films deposited by the spray pyrolysis technique, Journal of Physics D: Applied Physics, 37 (2004) 1248.

[138] Z. Ji, Z. He, Y. Song, K. Liu, Z. Ye, Fabrication and characterization of indium-doped p-type SnO2 thin films, Journal of Crystal Growth, 259 (2003) 282-285.

[139] Z. Ji, Z. He, Y. Song, K. Liu, Y. Xiang, A novel transparent pn + junction based on indium tin oxides, Thin Solid Films, 460 (2004) 324-326.

[140] C. Chen, Z. Ji, C. Wang, L. Zhao, Q. Zhou, P-type tin–indium oxide films prepared by thermal oxidation of metallic InSn alloy films, Materials Letters, 60 (2006) 3096-3099.

[141] X.Q. Pan, L. Fu, Tin Oxide Thin Films Grown on the (1012) Sapphire Substrate, Journal of Electroceramics, 7 (2001) 35-46.

Chapter 2: Lanthanides and their optical properties

2.1. Introduction

Nowadays technologies and challenges heavily rely on lanthanides based materials due to their impressive magnetic and spectroscopic properties. In particular, they are able to generate sharp and intense emission lines covering the spectrum from the ultraviolet (UV)- visible to the near-infrared (NIR) region, which open the door to applications in many fields, including lasers, telecommunication and light emitting diodes, bio-medical imaging and sensing, and solar energy conversion[142, 143].

Lanthanides (denoted Ln in this thesis) are also named 'rare earths' (denoted RE in this thesis) are non-toxic[144]. This name originates from the discovery history of these elements. In fact, pure minerals of individual rare earths do not exist along all the earth's crust and they are never found as free metals but as oxides, which were particularly difficult to separate them from each other, especially to 18th and 19th century chemists. The 'rare' part of the name comes from the difficulty to obtain them as pure elements and no really to their relative abundance in the earth's crust, while the 'earths' part of the name refers to the definition of early Greeks, materials that could not be changed under source of heat. More details about their discovery can be found in references [145]. The unique properties of the RE ions originate from the fact that the spectral position of the emission lines is almost independent of the host lattice, in contrast to line emission generate by the emission metal ions.

In the following, we will highlight the energy levels of lanthanides. Then we will focus on the mechanisms of energy transition involving the rare-earth elements and possible energy transfer. Finally, we will present the structural and optical properties of selected lanthanides inserted into a SnO2 matrix, which is the subject of this thesis.

2.2. Energy levels of lanthanides

2.2.1. Electronic structure

The lanthanides consists in the group of fifteen metallic chemical elements in the f-block of period six in the periodic table, with atomic numbers from 57 to 71 (La to Lu). It is to underline that often, Scandium (Sc, Z= 21) and Yttrium (Y, Z= 39) are associated to the 15 Ln elements within the group of rare earth metals (by definition). Lanthanides are considered as a group separated from the rest of the periodic table. The neutral Ln atoms possess the ground state electronic configuration of a $[Xe]^1$ ($1s^2 2s^2 2p^6 3s^2 3p^6 4s^2 3d^{10} 4p^6 5s^2 4d^{10} 5p^6$) core with few outer electrons, mainly two or three ($6s^2$ or $6s^2 5d^1$). And a number of 4f electrons ranging from 0 to 14. Lanthanides may exist in two electronic configurations; the La, Ce, Gd element belong to the $[Xe]$-$4f^n 6s^2$ type while Pr, Nd, Pm, Sm, Eu, Tb, Dy, Ho, Er, Tm, Yb and Lu belong to the $[Xe]$-$4f^{n-1} 5d^1 6s^2$ configuration. The different electronic configurations of lanthanide elements are reported in table 1.1

The energetic order along the lanthanide group consists in the successive filling of the 4f electronic shell, from La ($4f^0$) to Lu ($4f^{14}$). Having lost their 5d and 6s electrons, lanthanides are chiefly in the trivalent ionised state, for which the ionic radius decreases steadily from La to Lu. They can also exist in the 2+ (Sm, Eu and Yb are often divalent) or 4+ oxidation states, though most of lanthanides are stable in the 3+ state. It turns out that the electrons of the partially filled 4f shell are well shielded from interactions with external fields by overlying the 5s and 5p electronic shells[146, 147] (with larger radial extension, see figure 2.1), since the 4f orbital has much smaller radius compared to the 3d shell. As a result, the chemical interactions between atoms are dominated by their outer electrons (5s and 5p), thus, the 4f energy levels are weakly perturbed by the surrounding charges of the lattice, and remain almost invariant, which explain the atomic nature of their absorption/emission spectra (RE ions in ionic crystals exhibit narrow optical lines as that of free atoms or ions because of the relatively weak interaction with crystalline environment). The photon conversion process studied in this thesis (down conversion or down shifting) is practically intra-4f transitions whose the absorption and emission cross section are very small with relatively long luminescence lifetime (up to few ms). We list in table 2.1 some basic information about RE, atomic number, elements, the outer electronic shells, free ion ground terms.

---

[1] Here [Xe] represents the electronic configuration of xenon, 54 electrons
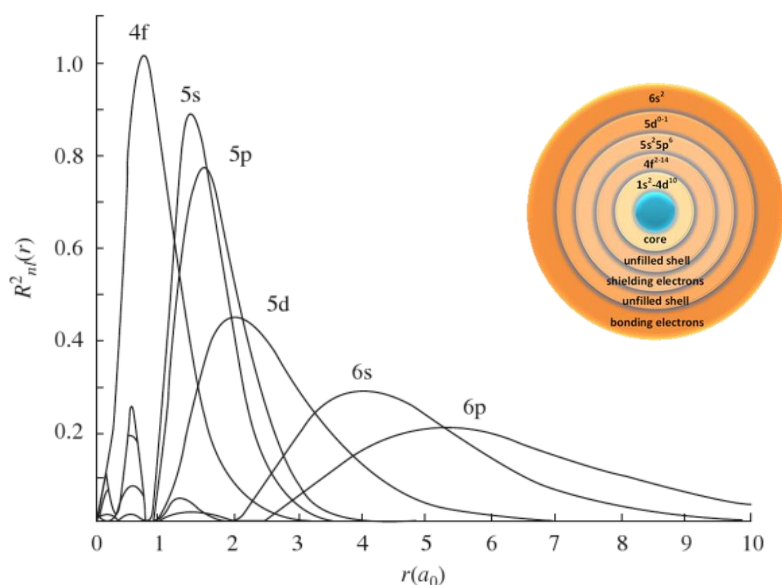
Figure 2.1. Radial distribution functions of cerium[148, 149]

Table 2.1. *The Rare Earth elements and some of their basic properties[146, 149, 150]*

Z	El.	Electronic configuration of neutral atoms					Electron configuration RE^{3+}	Ground term RE^{3+}	Ionic radius RE^{3+} (A)	Electron configuration RE^{2+}	Ground tem RE^{2+}
		4f	5s	5p	5d	6s					
57	La	0	2	6	1	2	$4f^05s^25p^6$	$^1S_0$	1.15		
58	Ce	1	2	6	1	2	$4f^15s^25p^6$	$^2F_{5/2}$	1.02		
59	Pr	2	2	6		2	$4f^25s^25p^6$	$^3H_4$	1.00		
60	Nd	3	2	6		2	$4f^35s^25p^6$	$^4I_{9/2}$	0.99		
61	Pm	4	2	6		2	$4f^45s^25p^6$	$^5I_4$	0.98		
62	Sm	5	2	6		2	$4f^55s^25p^6$	$^6H_{5/2}$	0.97	$4f^65s^25p^6$	$^7F_0$
63	Eu	6	2	6		2	$4f^65s^25p^6$	$^7F_0$	0.97	$4f^75s^25p^6$	$^8S_{7/2}$
64	Gd	7	2	6	1	2	$4f^75s^25p^6$	$^8S_{7/2}$	0.97		
65	Tb	8	2	6		2	$4f^85s^25p^6$	$^7F_6$	1.00		
66	Dy	9	2	6		2	$4f^95s^25p^6$	$^6H_{15/2}$	0.99		
67	Ho	10	2	6		2	$4f^{10}5s^25p^6$	$^5I_8$	0.97		
68	Er	11	2	6		2	$4f^{11}5s^25p^6$	$^4I_{15/2}$	0.96		
69	Tm	12	2	6		2	$4f^{12}5s^25p^6$	$^3H_6$	0.95		
70	Yb	13	2	6		2	$4f^{13}5s^25p^6$	$^2F_{7/2}$	0.94	$4f^{14}5s^25p^6$	$^1S_0$
71	Lu	14	2	6	1	2	$4f^{14}5s^25p^6$	$^1S_0$	0.93		

2.2.2. 4f energy levels

2.2.2.1. 4f energy level splitting [149, 151, 152]

It is common to use three spectral terms to describe the energy levels of the lanthanide ions:

- Total orbital quantum number L

- Total spin quantum number S

- Total angular momentum quantum number J, defined as $\vec{J} = \vec{L} + \vec{S}$

L and S are the sum of the *l* and *s* quantum numbers of each 4f electron of the ion under consideration, respectively. The spectral term L is a symbol that combines both azimuthal quantum number *l* and magnetic quantum number *m. l takes* values of 0, 1, 2, 3,… n-1 where n is the principal quantum number; while m takes the value of 0, ±1, ±2, ±3, … ±*l* . For example, in the 4f shell, seven orbital are present (*l*=3). Their magnetic quantum numbers are -3, -2, -1, 0, 1, 2, and 3, respectively. Table 2.2 shows the electronic distribution of the 4f electrons in the orbitals at the ground state of the lanthanide elements J is the sum of the orbital and spin momentum, its values are restricted to $\mid$ L-S $\mid \leq$ J $\leq \mid$ L+S $\mid$; J is equal to L-S for the seven first ions (La^{3+}-Eu^{3+}), and L+S for the last eight ions (Gd^{3+}-Lu^{3+}). Table 2.2 also lists the L, S, J values for the trivalent lanthanide ions in their ground state. These spectral terms can be expressed as $^{2S+1}L_J$. The top left represents the multiplicity of the spectral term, while the value of L (0, 1, 2, 3,4,5 and 6) and indicates the name of the level: S, P, D, F, G, H and I, respectively. Taking Nd^{3+} as an example, L=6 and its corresponding capital letter is I; S=3/2 (3 uncoupled electrons) so 2S+1=4; J=L-S=6-3/2=9/2. Thus, the spectral term for the ground state of Nd^{3+} is $^4I_{9/2}$.

Table 2.2. *Electronic configurations an spectral terms of trivalent lanthanides in their ground state[146, 149, 153]*

Ion	4f^n	Magnetic quantum number of 4f orbital							$L=\sum l$	$S=\sum s$	J
		3	2	1	0	-1	-2	-3			
											J=L-S
La^{3+}	0								0	0	0
Ce^{3+}	1	↑							3	1/2	5/2
Pr^{3+}	2	↑	↑						5	1	4
Nd^{3+}	3	↑	↑	↑					6	3/2	9/2
Pm^{3+}	4	↑	↑	↑	↑				6	2	4
Sm^{3+}	5	↑	↑	↑	↑	↑			5	5/2	5/2
Eu^{3+}	6	↑	↑	↑	↑	↑	↑		3	3	0
											J=L+S
Gd^{3+}	7	↑	↑	↑	↑	↑	↑	↑	0	7/2	7/2
Tb^{3+}	8	↓↑	↑	↑	↑	↑	↑	↑	3	3	6
Dy^{3+}	9	↓↑	↓↑	↑	↑	↑	↑	↑	5	5/2	15/2
Ho^{3+}	10	↓↑	↓	↓	↑	↑	↑	↑	6	2	8

	n								L	S	J
Er³⁺	11	↓↑	↓↑	↓↑	↓↑	↑	↑	↑	6	3/2	15/2
Tm³⁺	12	↓↑	↓↑	↓↑	↓↑	↓↑	↑	↑	5	1	6
Yb³⁺	13	↓↑	↓↑	↓↑	↓↑	↓↑	↓↑	↑	3	1/2	7/2
Lu³⁺	14	↓↑	↓↑	↓↑	↓↑	↓↑	↓↑	↓↑	0	0	0

When rare earth ions are placed into a solid, the degeneracy of the free-ion levels is lifted by coulombic, spin-orbit and the crystal field interactions leading to a large number of nondegenerate levels. The coulombic ones (electrostatic) arises from the mutual repulsion forces occurring between the 4f electrons, this kind of interactions results in a splitting of the free-ion levels into ^{2S+1}L, which are $(2L+1)(2S+1)$ fold degenerated. This electrostatic energy splitting is frequently around 10^4 cm⁻¹. The spin-orbit interactions arise from the electromagnetic interaction between the magnetic field (created by the electron's motion) and the electron spin. This interaction splits each ^{2S+1}L term into $(2J+1)$ states expressed $^{2S+1}L_J$ for which the typical splitting energy is about 10^3 cm⁻¹. While the interaction of the 4f electrons with the crystal filed produced by the surrounding charge distribution of the lattice results in the named Stark splitting of the $^{2S+1}L_J$ terms into $(2J+1)$ if the n number of the 4f electrons is even or into $(J+1/2)$ terms if the n is odd, denoted $^{2S+1}L_{J,\mu}$. the Stark splitting is namely a couple of 10^2 cm⁻¹ [[146]] (Figure 2.2).
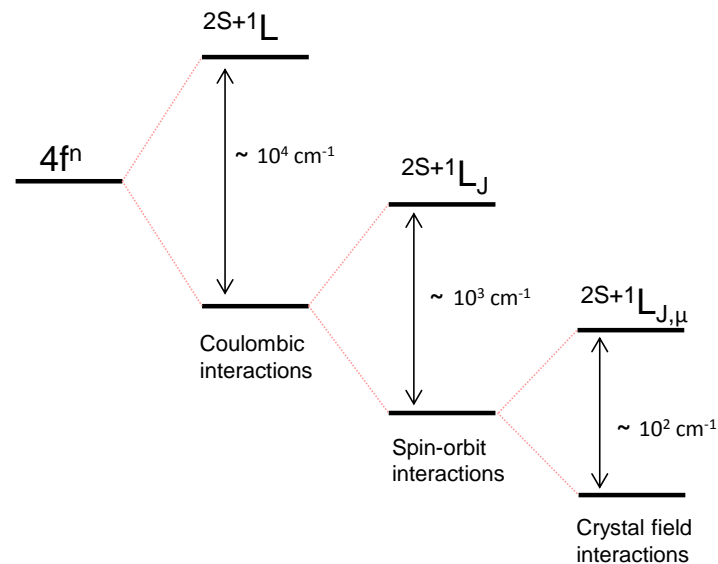
Figure 2.2. Coulombic, Spin-orbit and Crystal field interactions responsible on the 4f energy levels degeneracy. The states are described by the quantum numbers reported in the top.

It is to underline that for lanthanides, the 4f electrons interaction with the crystal field is much smaller than the coulombic and the spin-orbit interaction which are often roughly the same order of magnitude. This is due to the shielding character of the 4f shell. As shown in figure 1.1 from the radial distribution on the 4f, 5s, 5p and 6s electrons of Ce^{3+}. The graph shows that the 4f electrons are indeed inner electrons with relatively small $<r^n>$ values; therefore, they are shielded from external forces by the two electronic shells with larger radial extension, mainly the $5s^2$ and $5p^6$. In fact, the crystal field interaction is proportional to these $<r^n>$ values. Therefore the 4f electrons are somehow protected from interaction with external parities. This is not the case for the transitions metal ions, for which, luminescence arises from transitions along the partially filled 3d shell [146].

The properties of the f elements are strongly influenced by the core nature of the 4f electrons. In the metallic state, in addition to the 4f electrons, the valence configuration contains 6s and, in some cases, 5d electrons. As ions the oxidation state commonly seen is the 3+ state. The valence electron configuration then is composed only of 4f electrons. These f electrons display a large number of degenerate states in the absence of any interactions. However, perturbations such as electron-electron interactions, spin-orbit coupling, and external field or externa magnetic field lead to lifting the degeneracy and the appearance of numerous nondegenerate levels.

2.2.2.1. The Dieke diagram

Every rare earth ion is characterized by its own 4f energy levels whose the transitions in between (intra 4f transitions), for a given ion, are relatively invariant in different lattices. Since these energy levels are not the outermost ones, the nature of the lattice environment constitutes in fact a really weak perturbation on the atomic energy levels. Therefore, to study their spectroscopic properties (absorption/emission) is it essential to know their energy levels structure. In the 1960's, the $^{2S+1}L_J$ energy levels diagram of trivalent lanthanides in $LaCl_3$ have been constricted by Dieke[151, 154], the so-called *Dieke diagram*, which now represents the universal reference used to approximate the $^{2S+1}L_J$ multiplet of RE^{3+} ions whatever is the host matrix (lattice) (Figure 2.3). The thickness of each level represents the total crystal field splitting in $LaCl_3$ while the centre of each multiplet indicates the location of the free ion energy level ($^{2S+1}L_J$). The diagram has been later extended to higher energies by Ogasawara et al[155].
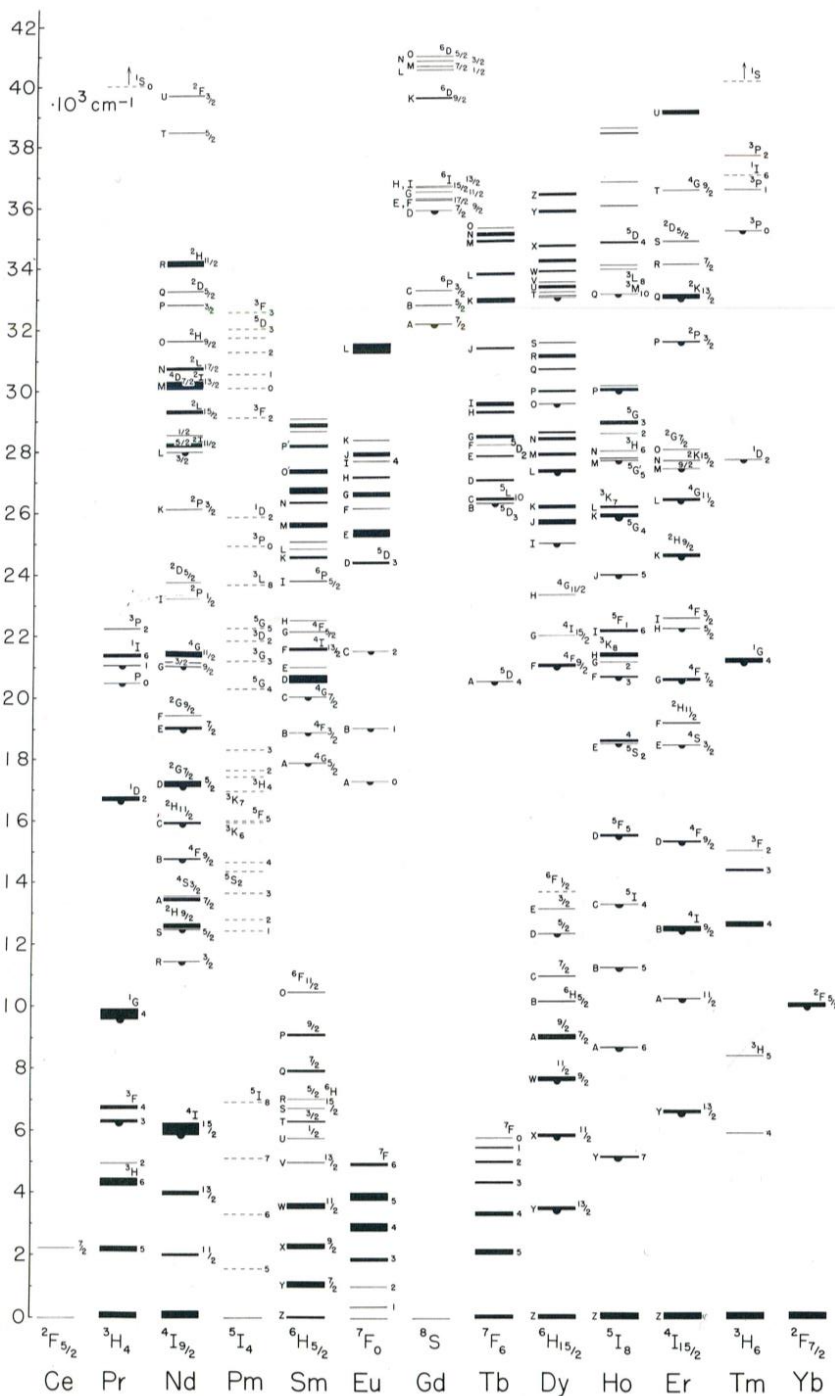
Figure 2.3. *Dieke diagram: Observed* energy levels of the 4f multiplet manifolds of trivalent rare earths. The pendant semicircles indicate that the selected levels give rise to fluorescence in LaCl$_3$ structure[151, 154]

2.3. Rare earths excitation processes [146, 153, 156]

Many of the absorption and emission lines in the optical spectra of RE solid compounds are as sharp as lines observed in free ions spectra. One intuitively guess that the RE energy levels still quite atomic like.

This can be explained by the shielding character of the 4f shell and the weak interaction with the crystal filed surrounding. This is not the case for the transitions metal elements (d-block compounds), for which the optical spectra arises from the 3d→3d transitions. Having their nd shell outside of the atoms remove the shielding effect, therefore the 3d electrons can easily interact with the crystal filed. In this part of the chapter, details about the different excitation processes of lanthanide ions by means of an electromagnetic radiation will be described.

It turns out that the lanthanides ions can be excited through three different ways, thereby three excitation transitions can be distinguished: intra 4f transitions (4f-4f), 4f-5d transitions, and charge transfer transitions. Illustration of these transitions are shown in figure 2.4.
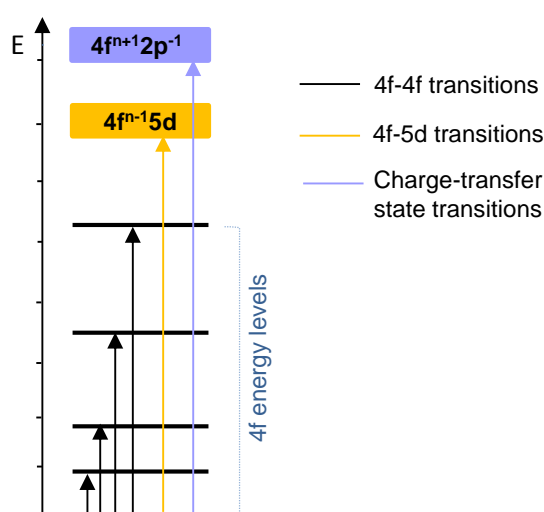
Figure 2.4. Schematic illustration of the electronic absorption transitions (excitation); 4f-4f, 4f-5d, and charge transfer transitions.

2.3.1. 4f-4f transitions

The intra-4f transitions represent the most important transitions known as the 4f-4f electric-dipole transitions. For this type transitions, we consider mainly the movement of the 4f electrons within the 4f manifold (between the different energy states of the 4f orbitals). Such transitions are forbidden by the parity selection rule (details are reported in section x). Nevertheless, these transitions become visible when embedding them into different host matrices, and exhibit emission bands usually weak and very narrow saving the atomic like character. In the 1937's, Van Vleck noted that in crystals the interaction with the lattice vibrations can mix states of the different parity wavefunctions into the 4f states, these admixture make the 4f-4f transitions possible.

2.3.2. 4f-5d transitions

In these transitions, a 4f electron can be excited to a higher energy orbital which is the 5d orbital. This

kind of transitions is commonly denoted as $4f^n \rightarrow 4f^{n-1}5d$ and typically observed for the Ce^{3+} which has an electronic configuration of $4f^1$. Moreover, as the most stable electron shells are the empty, half-filled or completely filled shells, the excess of the 4f electrons in Ce^{3+} can be easily transferred to the 5d orbital. Their broad absorption bands arise from configuration transitions, for example from $4f^n$ to $4f^{n-1}5d$. Unlike the intra-4f transitions, the 4f-5d ones are very intense (possess a broad absorption cross section) and allowed because they are no longer forbidden by the parity selection rule for electric dipole radiation. When they occur, they may therefore obscure the 4f-4f transitions (except the visible region for RE^{3+}).

2.3.3. Charge-transfer state (CTS) transitions

Here, the 2p electrons from the neighbouring anions (O^{2-} in oxides for example) can be transferred to the 4f orbital of the RE^{3+} ions. This type of transitions can be observed in Eu^{3+} which has an electronic configuration of $4f^6$ and needs one additional electron to be stable (to half-fill). Such transitions are allowed and exhibit an intense and broad absorption bands.

Assuming that the energy levels structure of a RE^{3+} is a simple 2-levels quantum system E_0 and E_1, see figure 2.4. Upon excitation (absorption of an incident photon with energy $h_1\nu_1$), the electrons jumps (are excited) from the ground energy state $|0\rangle$ with energy E_0 to higher energy state $|1\rangle$ of energy E_1, where $E_1 - E_0 = h_2\nu_2$; with $h_1\nu_1 > h_2\nu_2$. The time evolution of the population N_1 in the energy level $|1\rangle$ is given by the following equation:

$$\frac{dN_1}{dt} = \emptyset \sigma_{01} N_1(t) = -\frac{dN_1}{dt} \qquad \text{(Eq.1)}$$

$\emptyset$ is the incident pump rate

σ_{01} is the absorption cross-section per unit time between states ($|0\rangle$ and $|1\rangle$)
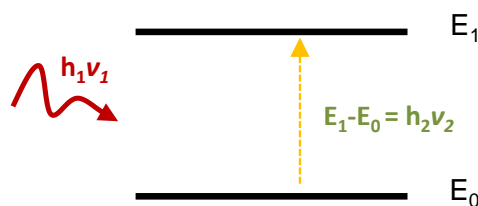
Figure2.5. Simple excitation process between two states in RE^{3+}

2.4. Rare earths de-excitation processes [146, 149, 157]

In this section we describe the intra-4f transitions, the selection rules for which these transitions can be allowed as well as an introduction to the Judd Ofelt theory for predicting the intensity of transitions of RE ions.

As mentioned in the previous section, after irradiation, the electrons are excited to upper energy states. However, this situation makes the electrons instable; therefore, they should then return to the lower energy state (ground state in case of a simple 2-levels quantum system). These transitions may be radiative or non-radiative. In the following, details about the nature of electrons transitions when returning to their ground states will be discussed.

2.4.1. Radiative transitions (emission)

In the case of radiative transitions, photons of energy hv equal to E_1-E_0 are emitted spontaneously through electrons de-excitation from a higher energy state $|1\rangle$ to the lower energy state $|0\rangle$. The time evolution of the population N_1 in the energy level $|1\rangle$ is given by the following equation:

$$\frac{dN_1}{dt} = -A_T N_1(t) = -(A_r + A_{nr})N_1(t) \qquad \text{(Eq.2)}$$

A_T is the total decay rate from the state $|1\rangle$ to the state $|0\rangle$, which is the sum of the radiative decay rate A_r (spontaneous emission, called Einstien coefficient) and the non-radiative decay rate A_{nr}. `

2.4.2. Selection rules for optical transitions

Since the light is considered as an electromagnetic wave, composed of an electric field E and an orthogonal magnetic field B, the interaction of electrons with the electromagnetic filed in RE ions-based systems can be distinguished into two distinct dipolar transitions. We can found: (i) the electric dipolar transitions (ED) which involves the interaction between the electron charge and the electric field, (ii) the magnetic dipolar transitions (MD) that involves interactions between the electron spin with magnetic field.

The optical transitions in lanthanides spectra are predominantly electric-dipole nature, though in some cases the magnetic dipole transitions are also observed. In free atoms, the latter are usually six orders of magnitude weaker than the electric dipole transitions.

The electric dipole transitions between states of the same configuration (optical transitions usually take place between levels of particularly 4f^N configuration) are strictly parity forbidden by the selection rules (Laportes selection rule). The reason why optical transitions are observed when embedding them into host

matrices is the mixing of the wavefunctions of states from the opposite parity (e.g. 5d states, CTs, etc) through interactions with the crystal field, resulting in breaking down/relaxing this selection rule[2].

The probability of electron transition between two states is given by the transition momentum $M = \langle\psi_i|\Gamma_D|\psi_f\rangle$, where Γ_D is the dipolar momentum operator[3], ψ_i and ψ_f are the wavefunctions associated with the initial and final states, respectively. The intensity of transition[4] indicates the coupling strength of the ions with the electromagnetic filed. The transitions intensity is found to be proportional to the square of the dipolar momentum M^2. According to the group theory, the transition can be allowed only if $M \neq 0$. The conditions so that the ED and MD will be allowed are listed below:

2.4.3. Electric dipole transitions

The electric dipole transitions, which have an odd parity, result as a consequence of perturbations induced by the crystal field. Van Vleck [158] pointed out that the electric dipole radiation can only occur if the transition is occurring from the $4f^N$ configurations to the $4F^{N-1}nl$ configurations that have opposite parities (*nl* will be mostly 5d). The admixture of the $4F^{N-1}nl$ wavefunctions into the $4f^N$ wavefunction is produced by odd parity interaction. Therefore two admixture mechanisms can be distinguished: (i) odd parity crystal field components and (ii) crystal vibrations of odd symmetry. It is important to underline that in crystals having an inversion centers, the crystal field cannot induce electric dipole radiation because the odd crystal field components are zero. However, this kind of transitions remains possible through the odd symmetry vibrations. As a consequence, the electric dipole transitions can be divided into two transitions, namely (i) forced electric-dipole radiation by odd crystal-field terms; (ii) forced electric-dipole radiation induced by lattice vibrations.

In the ED transitions, the selections rules concerning the L, S, J quantum numbers are essentially governed by the crystal field interaction. The parity rule or the Laporte rule for allowed electric dipole transitions are as follow:

$$\Delta S = 0, \Delta L = \pm 1 \ and \ \Delta J \leq 6 \ (\ for \ J = 0 \rightarrow J' = 0, the \ transitions \ are \ forbidden)$$

If, however, $J = 0 \ for \ \ the \ initial \ or \ final \ states, then \ \Delta L = \pm 1 \ and \ \Delta J = 2, 4, 6$

---

[2] The spectroscopic selection rules specify the transition's nature between the quantum levels due to the absorption of an electromagnetic radiation, thus we can distinguish allowed transition with high transition probability and forbidden transitions for which the dipolar momentum of the transition is zero.

[3] The dipolar momentum of the transition predicts the impulsion of a transition in an electromagnetic field.

[4] The intensity of transitions is predicted by the interaction of the ions with the electromagnetic field (E.g Intense transitions indicate strong coupling while weak transitions indicate weak coupling)

2.4.4. Magnetic dipole transitions

Unlike the ED transitions, the magnetic dipole operator is even parity. In this case the wavefunctions are not Russell-Saunders but intermediate coupling wavefunctions. Therefore, the MD transitions can occur only if the wavefunctions at the final and initial states have the same parities. Then we can conclude that the MD transitions can occur only if (It satisfies the relation)

$$\Delta S = \Delta L = 0, \ and \ \Delta J = 0, \ \pm 1 \ (\ except \ that \ J = 0 \rightarrow J' = 0, the \ transitions \ are \ forbidden)$$

$$If \ J = 0, \qquad \Delta L = 0 \ and \ \Delta J = \pm 1$$

Electric-quadrupole transitions are much less probable than the dipolar processes and have not been observed for rare earth ions

2.4.5. Judd-Ofelt theory [146, 159-162]

Judd (1962) and Ofelt (1962) through their rigorous work, they have shown that the calculation of the f-f transitions intensities in RE spectra can be possible once the excited configuration as completely degenerate is studied (also applicable to transitions between Stark levels). The feature that made the Judd-Ofelt approach very attractive is the calculation of the transition probability between any $4f^n$ levels once the intensity parameters are determined. This also concerns absorption and fluorescence intensities, excited states absorption, radiative lifetimes, and stimulated emission cross section. The treatment published by Judd and Ofelt have been successfully tested on most trivalent RE elements in crystals and solutions.   Additional works on the spectroscopic properties of REs have been published by Wybourne[163-165] (1962-1965). Few years after (1968), a very important and complete work with regard to the optical and spectroscopic properties of all rare earths in crystals have been published by Dieke[151], which becomes nowadays the 'universal reference' of the energy levels structure of lanthanides and a comparison to the theoretical results. Thorough review on the Judd-Ofelt theory can be found in reference [[166]]

2.4.5.1. Non-radiative transitions

Upon excitation, the electrons will relax from the higher excited energy state to the ground state without photon emission. In fact, there are two classes of non-radiative process: (i) electron-lattice relaxation by phonon process that arises from the interaction between the RE ion and the crystal field and in which, the electronic energy of the excited ion is transmitted to vibrational energy of the host lattice; (ii) Energy transfer process by ion-ion interaction that occurs by transmission of the electronic excitation from one RE ion to another. In (i), the relaxation process is similar to radiative process, with however, in this type

of transitions, the coupling between the final and initial states gives rise to emission of the lattice phonons. In (ii) the transfer of excitation energy may occur via resonance or non-resonance processes. Resonance energy transfer phenomena have been extensively discussed in a review of (Wright, 1976). Non-resonant energy transfer processes are made possible through the participation of lattice phonons in type (i) relaxation processes.

Non radiative relaxation can be distinguished into two categories: (a) the relaxation between crystalline Strack levels (separated by 10 to 100 cm^{-1}) that result in very fast one or two-phonon emission processes, mainly $\leq 10^{-12}$ s; and (b) non-radiative relaxation between J states (separated by several hundreds to thousands of cm^{-1}) which give rise to simultaneous emission of numerous phonons to conserve energy (multi-phonon relaxation). This last process usually proceeds with much lower rates. Orbach[167] (1975) has given a general discussion of non-radiative relaxation by one-phonon and multi-phonon processes and of energy transfer by ion-ion interactions.

2.4.5.2. Multiphonon relaxation

Multiphonon relaxation rates (MPR) among the $4f^n$ levels of RE have been studied in many crystals, including laser materials and found to increase exponentially with the decrease of the energy gap between the excited state and the next lower electronic state and also temperature dependent. This rate can be expressed as:

$$W_{NR} = Ce^{-\alpha\Delta E}\left[n(\omega_0 T) + 1\right]^p$$

Where W_{NR} is the non-radiative decay rate, C and α are constants characteristic of the host material, ΔE is the energy gap to the next lower ionic level, and p=$\Delta E/\hbar\omega$ is the number of phonon must be emitted to conserve energy in the transition. $n = (e^{h\nu/KT} - 1)^{-1}$ is the Bose-Einstein occupation number, which allows to determine experimentally the number of the phonons involved in the decays process as well as their energies.

It turns out that the phonons involved in the multiphonon relaxation process are those possessing the highest energies and largest densities of states. There is a rule of thumb stating that the intra-4f radiative transition can compete with the multiphonon relaxation only if the energy gap to be crossed is larger than 5 times the maximum phonon energy of the host. If it less than 5 times, non-radiative MPR process will be dominant. To minimise the MPR rates and therefore maximise the radiative emission probability, it is important to shoes hosts with low maximum phonon energy.

Typical low phonon hosts such as fluorides, bromides, iodides, and chlorides are not suitable for thin films for solar cells. However, high-phonon hosts, mainly oxides are the best candidates for this application. Moreover, the efficiency of the energy transfer from the host matrix to the rare earth might

depend on the ionization energy of excitons. In fact, hosts with large exciton binding energy ensure the carrier mobility in the semiconductor and only few excitons will be dissociated by thermal energy (25 meV at room temperature). From the optics point of view, free carrier recombination occurs in a wide energy range above the band gap, while excitonic recombination occurs resulting in a very intense emission and narrow range of the spectrum, which can be more efficiently coupled with other transitions in the REs.

Maximum phonon energy, optical band gap and the exciton binding energy of some potential materials (mostly oxides) potentially important for TCO application and can be doped with rare earth elements are summarized in table 2.3.

Table 2.3- Maximum optical phonon energy with relative mode, band gap and exciton binding energy of some important thin film hosts for REs.

Oxide	Phonon energy (meV)	Principal phonon mode	Band gap (eV)	Exciton binding energy (meV)
ZnO	72	E_1 LO	3.37	~60
GaN	~90	A_1 LO	3.4	~25
SnO$_2$ (rutile)	~80	$A_{1g},\ B_{2g}$	3.6	~130
TiO$_2$ (rutile)	~100	E_u^3 LO	3-4	
SrTiO$_3$ (cubic)	~50, ~100	t_{1u} LO3	3.2	
CeO$_2$	~58		3.6	
SiO$_2$ (amorph.)	~130-150		9 (indirect) 11(direct)	
CdS			2.4	28

2.4.5.3. Concentration quenching

The concentrations quenching phenomena is observed in highly doped systems where the energy transfer between the dopant is favoured. The Cross-relaxation is a particular type of energy transfer, in which a fraction of the excitation energy by one ion is transferred to another identical ion. In some cases the excitation energy can be trapped by a non-luminescent defect or impurity. By this way the excitation energy is lost non-radiatively which minimise the luminescence efficiency of the material.

2.5. Emission of Rare Earth activated compounds

The observed emission spectra in lanthanides based compounds correspond to the intra 4f optical transitions of predominantly electric-dipole character. Since the dipole strength of the 4f transition are naturally forbidden, their extinction coefficients are very small, typically of the order of 1 M^{-1}cm^{-1}. Therefore, an alternative way has to be found to relax these selection rules, <u>which </u>consists in the antenna effect, known as luminescence sensitization process. When embedding RE into organic ligand or a host matrix, the energy absorbed by matrix can be transferred through the surroundings to the ions which will emits a characteristic light. This process is so-called energy transfer and will be discussed further in the next section.

The emission efficiency can be quantitavely described by the quantum yield Q, defined as

$$Q = \frac{number\ of\ emitted\ photons}{number\ of\ absorbed\ photons}$$

2.5.1. Principal transitions in RE-doped compounds

The different kind of electronic transitions possible to occur in lanthanide-activated compounds are described in figure below: the most classical electronic transition is the band to band transition or inter-band that occurs in the host; the second type of transitions always in the host matrix is transitions involving intermediate states within its band gap. This type of transitions allows us extracting valuable information about the material absorption edge. In the other side, as discussed before, transitions in the rare earth ions also occur in several ways, we can distinguish mainly the intra 4f-transitions and inter-configurational 4f^n-4f^{n-1}5d transitions. Now electronic transitions can occur between the host and the incorporated rare earth: in one case, a electron can be transferred from the host to the RE or vice versa, resulting in the change of the RE oxidation state (its valency). The host material can also interact with the embedded rare earth without electrons migration but via energy transfer. In this case, transitions within the band gap of the host will excite electrons of the RE ions through photons with energy hv.

Among others, the last possible electronic mechanism is between two rare earth ions present in the host. This can occurs in two ways: (i) via charge transfer, in which one ion acts as a donor and the other one as acceptor, both ions change valence during the transition. Tb-Yb are a good example of efficient down-conversion via this process; (ii) via simply energy transfer process, mostly occurs when resonance between the energy levels of the ions exist.

It appears that the shielding of the 4f orbitals (responsible on rare earth emission) strongly affect the dynamic interaction of the 4f electrons with the host lattice phonons (vibrational modes). Therefore, the weak electron-phonon coupling in rare earth activated compounds results in sharp zero-phonon intra 4f-transitions lines with very weak phonon sidebands. By this way, non-radiative relaxation processes are considerably reduced and emission efficiencies can therefore reach their limits. Thanks to that, in some systems, the lifetime of the excited states can achieve the milliseconds for visible emitting ions, as is the case of Tb and the microseconds for infrared emitters such as for Eu. Nevertheless, the phonon-assisted transitions strongly depend on the maximum phonon energy of the host matrix and the energy gap between the excited level in the rare earth and the first lower lying level. This relationship will be more described in the following section.
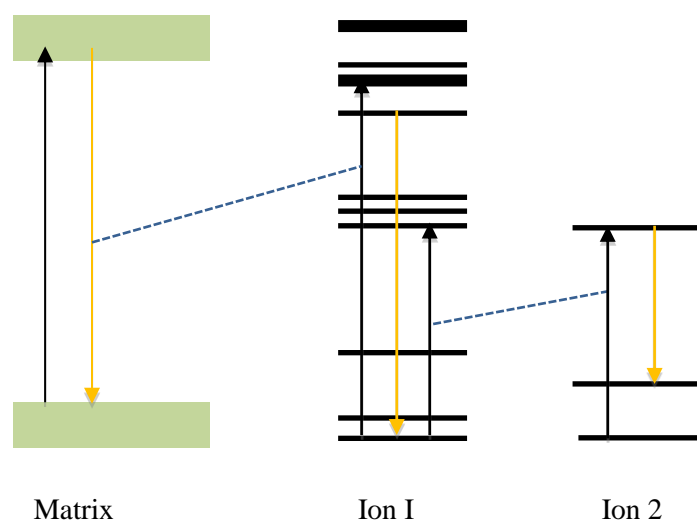
Figure 2.6. Different electronic transitions possible in RE-doped SnO_x systems

2.6. Radiative and non-radiative energy transfers

2.6.1. Introduction

Luminescence in oxide materials arises mainly from activated luminescent ions and/or intrinsic defects, the latter are found to introduce discrete levels in the electronic structure of the material. In some cases, the absorption cross-section of one of the luminescent centers mentioned above is too low, therefore the luminescence yield is too small. One solution to get ride of this phenomenon is the use of a second ion with a larger absorption cross-section as a sensitizer. Sensitization occurs via en energy transfer between two luminescent centers, that simply can be either (i) resonant, (ii) phonon assisted, or via (iii) cross-relaxation.
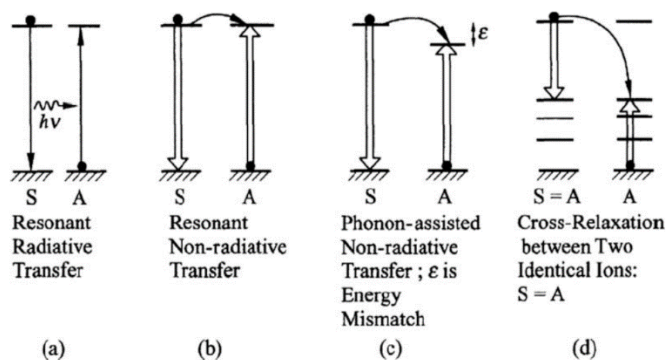
Figure 2.7. Schematic diagram of the different ET process between two ions

The resonant energy transfer (ET) may be radiative or non-radiative. Energy transfer processes will be described in details in the following paragraphs. In the resonant ET process, the radiative is the most complicated one. The efficiency of transfer depends strongly on how the sensitizer emission excites the activator. Numerous parameters are involved. A spectra overlap between the sensitizer's emission range and the activator's absorption is required to establish the transfer as well as a considerably intense sensitizer's emission whose the probability of reabsorption by the another neighboring sensitizer ion is not excluded, especially for higher concentrations. Given the complexity of such process, it is considered unlikely that this process would take place in the inorganic systems; in any case it is negligible ascompared to the non-radiative ET process. Besides, the non-resonant (phonon assisted) ET process can possibly occur under a very important condition: the energy mismatch between the two luminescent centers should be smaller than the highest phonon energy of the matrix. More details about the ion-ion interactions can be found in reference [168]Forster [169] and Dexter [170] [171]

2.6.2. Different energy transfer processes

In an energy transfer process, there is excited ion, usually called a donor (or sensitizer 'S') that will transfer its excitation energy to another ion, called acceptor (or activator 'A'). In the case of Radiative energy transfer, S through deexcitation will emit a real photon that will be reabsorbed by A, provided that the latter is located within the photon travel distance. This phenomenon is called 'emission-reabsorption mechanism'. In the other side, for the case of the non-radiative energy transfer, the excitation energy is transferred from the sensitizer S to the activator A without photon emission. All involved transfer mechanisms in this thesis are non-radiative type.

We can also understand the energy transfer from another side, namely from the resonance of the energy levels (between S and A) point of view. The different energy transfer mechanisms are schematically drawn in figure 2.7. They are noted from a to h.

(a) The first energy transfer process shown in figure 2.8.a corresponds to the classical resonant energy transfer in which an electron of the donor (ion A) goes from its excited state A* to its ground state A and thereby excites another electron from the ground state B to the excited state
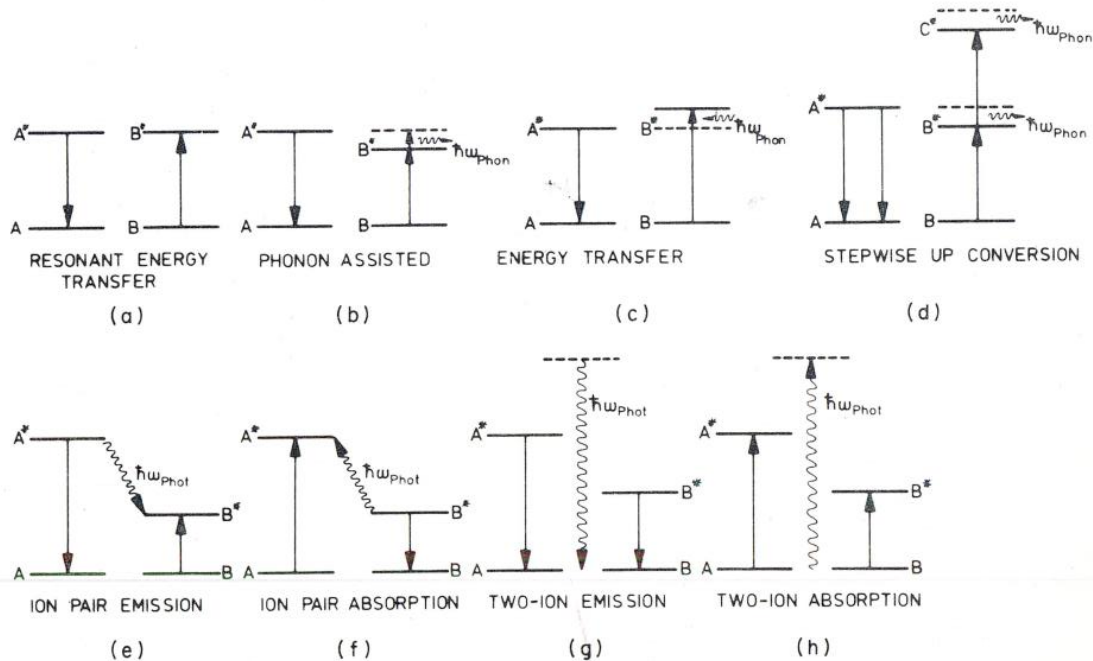
Figure 2.8. Diagrams of several energy transfer and two-ion processes. (a) Resonant energy transfer, (b) and (c) phonon assisted energy transfer with the emission (b) and absorption (c) of a phonon (d) stepwise up conversion by phonon assisted energy transfer. (e) Ion pair emission (f) ion pair absorption. (g) and (h) Two ion emission and absorption, respectively. [146]

a) B* of the second ion B (the acceptor). In this process, the energy is fully conserved, in other words, the A*→A transition have the same energy as the B→B*

b) The case b represents the phonon-assisted energy transfer in which there is an important mismatch in the energy levels positions between the donor and acceptor (as compared to linewidth). In this process, the electron of the ion B is excited to B* accompanied with a photon $\hbar\omega$ emission (the excess of energy) in order to conserve energy.

c) The case c is analogous to the one in (b), however here, the energy transition B→B* is larger than that of A*→A, so the missing energy is supplied through photon annihilation from the system. It is to underline that this process is not operative at low temperature.

d) The energy transfer process proposed in this case schematizes the stepwise up conversion. In this process, two successive transitions through the donor energy levels excite one electron in the acceptor ion system to an energy level with approximately twice of its energy. This phenomenon occurs via two steps. First, one photon is used to reach the B* state either by resonance or with phonon assisted energy transfer. After that, a second photon is used to make transition from B* to

C*(to reach the C* state) also resonantly or by phonon assisted if needed. Under this condition, a visible radiation can be produced from infrared radiations

e) The scheme e shows the ion pair emission. This latter and the next three processes have common point, is that the absorption or emission of one photon is performed by cooperation of both ions. Here, an electron in the ion A system decays from the excited state A* to the ground state A and simultaneously excites an electron in the ion B system from B to B*, therefore, a photon of energy A*→B* is emitted.

f) This is the reverse case of (e), we treat the ion-pair absorption. In fact, an electron in the system B decays from B* to B in addition to the absorbed photon, an electron in the system A is being excited from the ground state to the excited state A*. By this way, the energy of the absorbed photon is equal to the energy difference between A* and B*

g) In the case of two-ion emission, two electrons of the ions A and B decay simultaneously from the excited states A* and B* to the ground states giving rise to phonon emission with energy equal to the sum of the two transitions

h) The last case represents the two ions absorption, which is the reverse case of (g). Here absorption of a photon excites two electrons in the two ion systems from their ground states to the excited states

2.6.2.1. Non-Radiative energy transfer

In non-radiative energy transfer, the process can be dominated either by electrostatic multipolar or by exchange interactions. With the electrostatic interactions, the energy transfer between the two ions occurs without electrons exchange or physical contact. This type of interactions happens when the donor and acceptor systems are far from each other (e.g. 20 Å), it is enough if A exercises a dipole oscillation on B. As reported by Förster , the energy transfer probability can be expressed as

$$W_{NR}(R) = \frac{1}{\tau_s}\left(\frac{R_0}{R}\right)^6$$

Where τ_s is the sensitizer's excited state lifetime and R_0 is the Förster radius, which corresponds to the distance where 50% of the sensitizer's energy is transferred to the activator. In the case of the dipole-dipole interaction, the non-radiative energy transfer probability can be written as shown by Dexter:

$$W_{NR}(R) = \frac{1}{\tau_s}\left(\frac{R_0}{R}\right)^a$$

Where a is a positive integer that can take the values: 6 for dipole-dipole interactions, 8 for dipole-quadripole interactions and 10 for quadripole-quadripole interactions

When the energy transfer is occurring through exchange interaction, called Dexter transfer, an electron

exchange between the two systems takes place provided overlapping of the electronic charge distribution (electronic orbitals) of the donor and acceptor. Thus, A and B have to be very close to each other so that the (min distance around 6Å). The Dexter energy transfer probability strongly depends on the sensitizer to the activator distance R. It is found to decrease exponentially when R increases. One can conclude that this type of transition is a very short-range interaction and can be observed only at high doping concentration where the distance between the dopant ions is small.

2.6.2.2. Radiative energy transfer

The energy transfer can also occurs via radiative process, in which the electron decay from the excited state to the ground state of the ion A with photon emission, this latter will be reabsorbed by the second ion (acceptor/activator). This process is called photon emission-reabsorption mechanisms. The radiative energy transfer in contrast to the non-radiative one allows long-range energy diffusion in the material. The probability of the radiative energy transfer governed dipole-dipole interactions (PSA) varies as a function of R^{-2} vs R^{-6} for the non-radiative ET by dipole-dipole interactions.

The question is how to distinguish between radiative and non-radiative energy transfers ??

Radiative and non-radiative resonant energy transfers can be distinguished by means of three criteria. When the energy transfer deals with radiative transitions, the photons are initially emitted by the sensitizer and then reabsorbed by the acceptor (activator); the latter should be located within the photon travel distance. Therefore, the transfer rate depends strongly on the shape and size of the sample under consideration. Moreover, the excited level lifetime of the sensitizer is independent on the concentration of the acceptor ions and their distance to the sensitizer ions, however, the emission of the sensitizers is found to change with the acceptor's concentration.

2.6.2.3. Down-conversion and down-shifting

The most appropriate materials for photons down conversion are mainly oxides, ceramic glasses and polymers, thanks to their interesting luminescence properties, in the case of oxides and wide band gap semiconductors, the luminescent native structural defects are of potential interests for this application. In spite of the reach transitions within the discrete deep levels within the bang gap of these materials, it is necessary to incorporate other luminescent impurities, mainly REs, thanks to the intra 4f transitions, with which, efficient photons conversion can be achieved. In photons down conversion process, we can deal with either resonant non-radiative energy transfers from the host to the rare earth ions, which occurs mainly through the intermediate levels within the band gap, or via phonon-assisted energy transfer. For the latter, a little problem can be present. The phonon-assisted ET strongly depends on the maximum phonon energy of the host matrix. So if the latter is large, larger energy mismatch during the ET can be encompassed, in the other hand, as explained before, hosts with high phonon energies are threatened by

multi-phonon relaxation process.

The conversion type that will be treated in this thesis are mainly either down-conversion or down-shifting.

2.7. RE-doped SnO₂ materials-overview

In the past decades, rare earth (RE)-doped wide band gap semiconductors are considered as new class of materials if one considers their interesting properties and wide range of potential applications. While flat panel display technology stimulated research on visible light emitting RE such as Tb, Eu, Pr and Sm, those involving near-infrared (NIR) luminescence such as Nd, Yb, Er and Eu have stirred exceptional interest for electroluminescent devices, fiber amplifiers, fluorescent lamps and semiconductor lasers[172-175]. Beyond the optics, these materials have recognized a lot of success in telecommunication, imaging, biomedical and solar energy fields [142, 143, 176-179].

Most of the current research on lanthanide (Ln) doped semiconductor oxides are focused on ZnO and TiO₂ with few studies on tin oxides[180-182]. However, recently SnO₂ has also caught increasing attention due to its particularly interesting properties. Compared to other TCOs, SnO₂ has a wide band gap around 3.6 eV for the bulk material[183], and a considerable exciton binding energy of 130 meV, making it an attractive matrix for electrically activated emissions[184]. Due to the high concentration of native oxygen defects, which act as donors, in the undoped form, SnO₂ presents good electrical n-type conductivity along with a high carrier concentration. Moreover, this material has high transparency in the visible light range (above 90%) and strong reflectivity in the infrared region[185]. In the tin oxides family, there is SnO, which possesses also a wide band gap of 2.7-3.4 eV [186, 187] but exhibits p-type conductivity[186] which can be converted to n type by doping for instance with Sb[188].

A vast selection of nanostructured morphologies of tin oxides have been studied such as as nanorods[189, 190] [190] [191], nanosheets[192], nanowires[193], nanoflakes core-branched nanoarrays[194, 195], nanoribbons[196] and nanocrystals[197] [198], powders and nanoparticles[199, 200]. The final properties of tin dioxide nanoparticles are related to both the composition and the processing method. Tin dioxide powder in particular can be synthesized through different chemical methods, such as co-precipitation[199] [201], hydrothermal[202] and sol-gel[203] [204] methods among others.

On the other hand, efficient Ln³⁺ emissions are obtained via host sensitization. Nevertheless, critical points should be carefully considered such as the crystal symmetry (structure), the ligands, the coordination and interactions that Ln³⁺ ions experience around which can strongly affect their luminescence properties.

In the following we will review physical properties of tin dioxide doped with rare earth elements,[205] [206] [207] , namely Sm, Tb, Eu, Er, Pr and finally Nd and Yb.

2.7.1. Sm-doped SnO$_2$

To our best knowledge only few reports exist on Sm-doped SnO$_2$ and neither of them reports on the photoluminescence properties in spite of the potential PL in the visible that Sm can exhibit. Sm-doped SnO$_2$ thin films by pulsed laser deposition have been studied by Cao et al[208].(2013); they reported on the effect of Sm doping on the room-temperature magnetic properties of the SnO$_2$ films. XPS measurements showed that Sm possess the 2+ oxidation state at a deposition temperature of 400°C and switch to 3+ at 600°C. the authors reported that the substitution of the Sn4+ ions by the Sm^{3+} ones together with the oxygen vacancies, induce ferromagnetism in the Sm-doped SnO$_2$ thin films. The same material have been studied by Wang et al[209] (2000) for gas sensing application by the co-precipitation technique; they have found that the gas sensitivity of Sm-doped SnO$_2$ powder is dominated by the density of the oxygen vacancies. Tong Zhan et al[210]. (2008) have also studied Sm$_2$O$_3$-doped SnO$_2$ powders by the sol-gel method; they investigated the electrical and sensing properties of the material and found that the 6 wt% of Sm$_2$O$_3$ exhibits best sensing behavior to C$_2$H$_2$. SnO$_2$ powders by co-precipitation and doped with Sm together with Co and Nb with different concentrations have been reported by Bastami et al[211] (2010); They showed that Sm doping induces a decrease of the crystallites size of (Co, Nb)-doped SnO$_2$.

2.7.2. Tb-doped SnO$_2$

Similar to above, just few studies concerning Tb-doped SnO$_2$ are reported in literature. Hild et al [212] (2015) have reported on the Tb-doped SnO$_x$ films made by the evaporation technique. They showed that the rutile phase is necessary for the rare optical activation, obtained under annealing at 700°C in air.
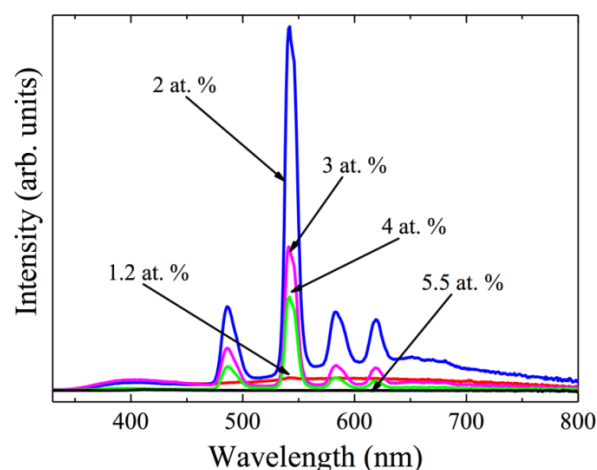
Figure 2.9. Room temperature PL spectra of Tb-doped SnO$_x$ alloys annealed at 700°c, for different concentrations.

As a matter of fact, Tb^{3+} ions in SnO_2 matrix exhibit spectacular emission in the visible region laying from 480 to 700 nm as displayed in figure 2.9. The authors showed that beyond 2 at% of Tb doping a quenching effect occurs.

On the other hand, Tb^{3+} and Eu^{3+} co-doped SnO_2 have been synthesized by Elhouichet et al[213].(2003) using the sol-gel method for electroluminescence electrodes or TCO applications. The Eu^{3+} ions seem to be excited through three channels: (i) direct excitation, (ii) SnO_2 nanocrystals, (iii) Tb^{3+} ions. The latter can be obviously noticed in figure2.10, in which the Tb do no emit under exciation of 465,8 nm. As the emission of Eu under excitation of 488 is better than that of 465,8, the authors speculate an energy transfer from Tb^{3+} to Eu^{3+} ions. The same group has reported few years after on the concentration quenching study of Tb^{3+}doped SnO_2 by sol-gel. The solubility limit in their process is found about 4 at.%.
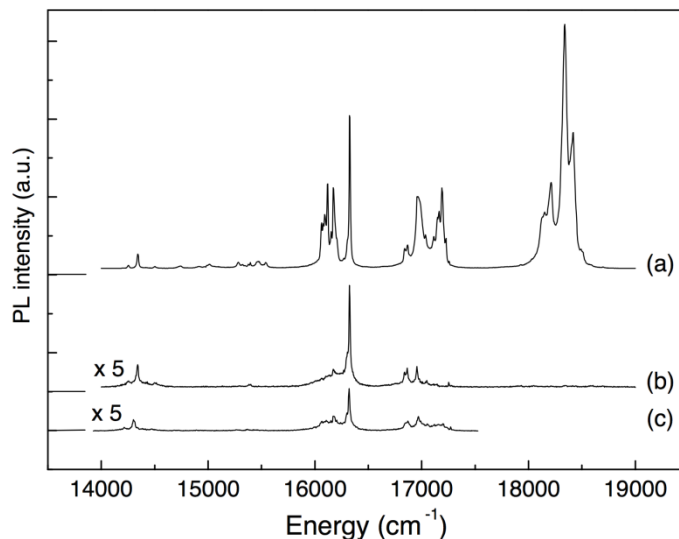
Figure 2.10. PL spectra of SnO_2:Tb^{3+}, Eu^{3+}/Si annealed in air at 700°C for excitation lines 488 nm (a) and 465,8 nm (b). The PL spectrum of SnO_2:Eu^{3+}/Si for the excitation line 488 nm is presented for comparison.

2.7.3. Eu-doped SnO₂

A very interesting study of the SnO :Eu powder by the sol gel method have been reported by Fu et al [214] (2005). The powders have been calcined at 400 and 1000°C. Using the excitation and absorption spectroscopies and they could identify a sharp absorption line at 395 nm assigned to the f-f transition of Eu3+ ions. The emission spectra under 300°C reported by the authors is shown in figure 2. 11.a. The emission band around 400 and 460 nm was assigned to the luminescence of SnO_2, more precisely, assigned to electron transitions along the defect levels in the band gap such as oxygen vacancies and tin interstitials. The band at 590 nm was attributed to the Eu3+ magnetic dipole transition. *

The increase of the emission of both SnO_2 and Eu with the increase of the sintering temperature (here at 1000°C) was attributed to the creation of more defects in the structure at higher temperature processing, mainly oxygen vacancies. In fact, the 1-charge resulting from the incorporation of the Eu^-_{Sn} has to be compensated from somewhere in the lattice, and obviously from oxygen vacancy, thus, high heat treament is know to accelerating the Eu^{3+} ions diffusion, which induces more oxygen vacancies. This can explain the SnO_2 emission originating from structural defects. Now concerning the Eu emission, since they are being excited indirectly via transitions along the intermediate defect states in the band gap of the host matrix (created by oxygen vacancies), the enhanced emission comes mainly from the large amount of trapped carriers excited from SnO_2. Figure 2.11.b shows the photoluminescence spectra of the same samples but under excitation of 395 nm (direct excitation of the $^7F_0$-$^5L_6$transition of Eu^{3+}). The band at 590 nm corresponds to the magnetic dipole transition $^5D_0$-$^5F_1$ and that at 614 nm is electrical dipole transition $^5D_0$-$^7F_2$. The latter is strongly dependent on the local symmetry of the Eu^{3+} ions. The intensity of the ED transition significantly increases by increasing the heat treatment indicating a change of the symmetry of the local environment of the rare earth ions (lower symmetry), mostly originating from the formation of oxygen vacancies.
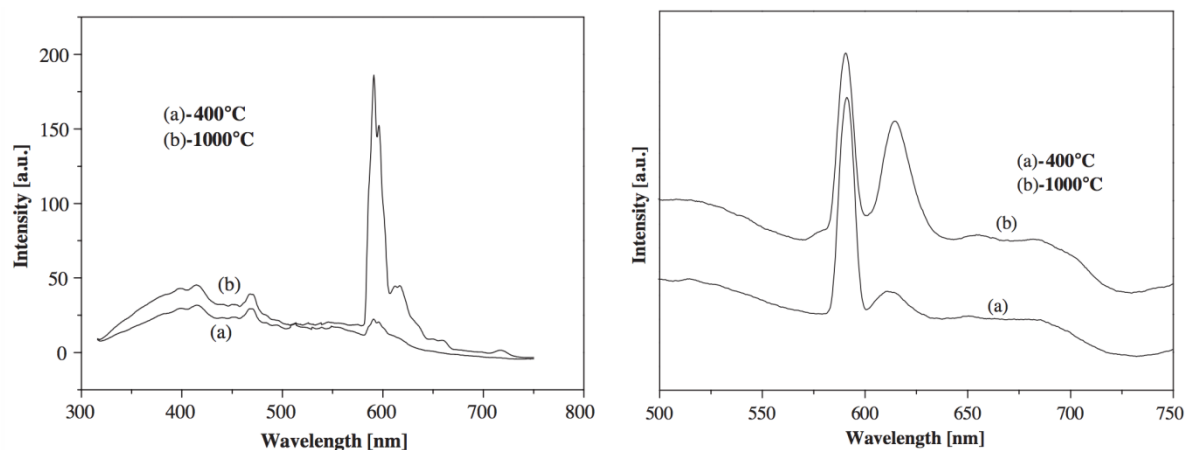
Figure. 2.11. (i) Emission spectra of SnO_2:Eu samples excited by 300nm: (a) calcined sample at 400 1C, (b) calcined sample at 1000 1C. (ii) excited by 395nm.

Few years later, Eu^{3+}:SnO_2 Crystallites with different dopant concentration fabricated by the sol gel method have been studied by Psuja et al [215](2012). They reported on the structural and photoluminescence properties of the powders. They found that the increase of Eu concentration results in a decrease of the crystallites size (figure 2.12.a). It can be seen that the luminescence intensity of Eu^{3+}:SnO_2 significantly increased with the Eu^{3+} concentration. In all spectra an orange emission ($^5D_0$→$^7F_1$) , corresponding to the magnetic dipole transition, strongly dominates over red emission ($^5D_0$→$^7F_2$) corresponding to the electric dipole transition.
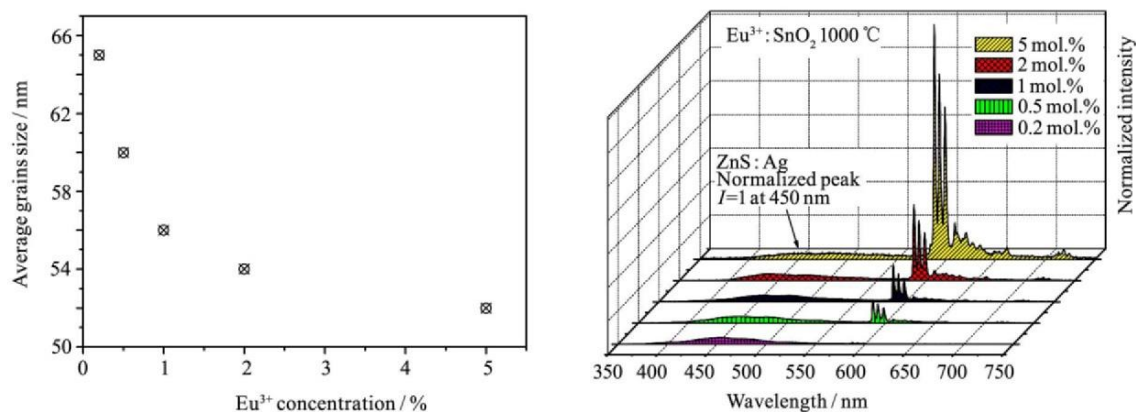
Figure 2.12.a. Influence of Eu³⁺concentration on average grain size of Eu: SnO₂ nanocrystallites sintered at 1000 °C, b. Comparison of photoluminescence spectra (λ_{ex}=266 nm) of ZnS:Ag/Eu³⁺:SnO₂ blends with Eu³⁺:SnO₂ crystallites with different Eu³⁺concentrations.

Zhang et al.[216] (2005) have reported an interesting work on doping SnO₂ :Eu powder by Li⁺ ions by the sol gel route. The idea of adding Li was to accelerate the crystallization of SnO₂ and also to enhance the PL properties. The authors reported PL spectra with Eu³⁺ emission at 580-630 nm, corresponding to $^5D_0 \rightarrow ^7F_{j(j=1,2,3)}$. The authors reported that because the substitution of Eu³⁺ to the Sn4+ ions results in a high symmetry of the local environment of Eu³⁺ ions (because Sn atoms occupy a slightly distorted sites in the rutile structure). Therefore, the electric-dipole transiton $^5D_0 \rightarrow ^7F_2$ is weak while the magnetic one $^5D_0 \rightarrow ^7F_1$ at 580 nm is strong. The luminescence of Eu³⁺ ions was found to increase with the increase of the Li content in the structure; this was explained by the lower symmetry of the local environment around Eu³⁺ induced by Li incorporation. In the other hand, the authors reported that since the ionic radius of Eu³⁺ ions is about 95 pm, much larger that of the Sn4+ ions which is about 76 pm, therefore the substitution of Sn⁴⁺ sites by Eu³⁺ ions may strongly deforms the octahedral sites; therefore, the more is the substitution, the lower the symmetry of the Eu surroundings is. We found this report quite contradictory, in one hand the authors states that the substitution of Eu results in a high symmetry, and in the other hand they say that the increase of the Eu amounts in the films reduces the symmetry of the crystal arounds, while the study was concerned the effect of the Li concentration of the luminescence of Eu³⁺. So the results shall be considered with a deep caution.

2.7.5. Er-doped SnO₂

Morais *et* al.(2009) studied Er and Eu doped SnO₂ thin films prepared by the sol-gel-dip coating method, which revealed that the luminescence properties of the RE are highly dependent on their location sites in the main matrix [217, 218] (substitutional to Sn⁴⁺ lattice sites and grain boundary interface). The temperature dependence of PL spectra measured at 50 K and 280 K for 2 at% Er-doped SnO₂ xerogel sample is shown in figure 2.13
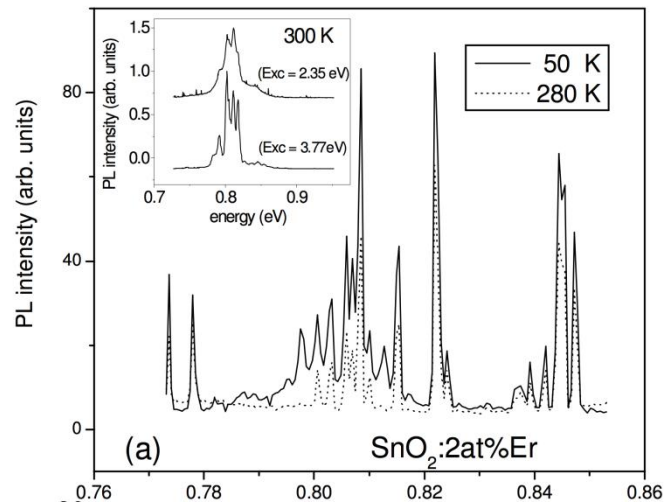
Figure 2.13 No legend of the figure have been reported in the paper

The authors reported that the Er^{3+} $^4I_{13/2} \rightarrow$ $^4I_{15/2}$ transition around 0.8 eV is evidenced by the appearance of several PL peaks after direct excitation of Eu^{3+} from the ground state to the $4f_{7/2}$ state (about 2.53 eV). The inset of the figure 2.13 shows the PL spectra of SnO_2 xerogel co-doped with Er and Yb (2 at%). The increase of the PL intensity when decreasing the temperature of the process was explained by the fact that cooling the samples decreases the lattice vibration of SnO_2 and therefore the phonon assisted non-radiative process, which enhances the PL efficiency of Er^{3+}. The figure shows that the sample at 50K exhibits additional peaks than at 280K. The presence of several peaks was attributed to the splitting of levels $^4I_{13/2}$ and $^4I_{15/2}$ by the crystal field effect of the matrix.

Concerning the co-doping with Yb and Er, the investigation of their PL spectra has yielded information about the Er localization in the matrix. When the excitation is performed indirectly via the band gap of SnO_2, the shape of the recorded spectra is typical of substitutional Er emission. While under direct excitation of the Er^{3+} ions, a typical emission of Er in vitrous matrix has been observed. Therefore, the authors identify two Er sites in the matrix: substitutional to Sn^{4+} and segregated at boundary layer. The latter is related to the solubility limit of the RE in the SnO_2, the doping excess become located at the boundary layer.

2.7.6. Pr-doped SnO₂

Unlike Eu and Er, doping SnO_2 oxide with Pr is much less investigate. Guo et al.[219] (2015) presented an experimental study and theoretical calculations on Pr-doped SnO_2 prepared by the electrodeposition method, The lattice parameters of Pr doped SnO_2 system have shown an approximate linear increased trend with increase of Pr doping concentration. They found that $Sn_{0.917}Pr_{0.083}O_2$ is a kind of indirect band gap material comparing to the pure SnO_2, which have a direct band gap. They reported that the

conductivity of the material would be improved by doping with Pr atoms and concluded that Pr-doped SnO$_2$ electrode is one promising acid proof anode. Ma et al [220](2014) have reported on the Pr-doped nanofibers using the electrospining method followed by calcination. The authors have investigated the sensing properties of the fabricated material. The found that comparing to the undoped fibers (pure SnO$_2$), the Pr-doped ones exhibit excellent ethanol sensing properties with maximum sensing response at a concentration of 0.6 wt% Pr. Low resolution and high resolution of the Pr-doped nanofibers are presented in figure below. The figure 2.14 (a) shown the uniformity diameter, figure2.14 (b) shows the 1D and mesoporous aspect of a single nanofiber, the figure2.14 (c) shows its polycrystalline structure. Figure2.14 (d) displays the HRTEM image and showing well the lattice distances of the different crystalline planes.
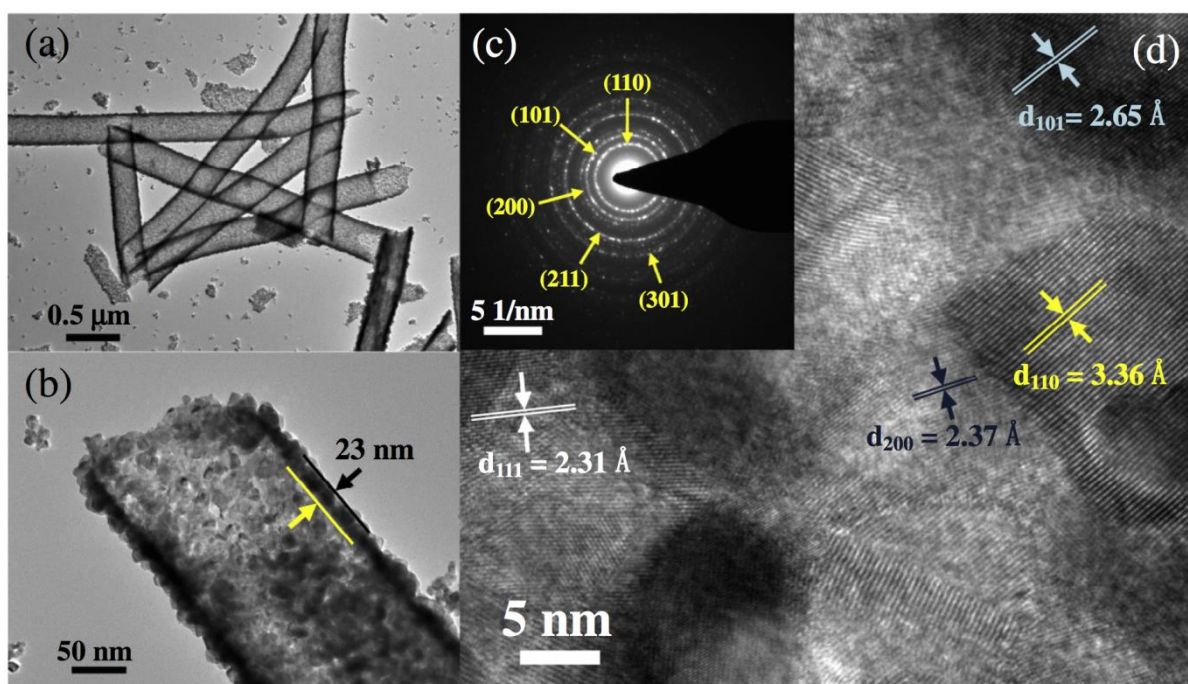
Figure2.14 (a) TEM and (b) high magnification TEM of 0.6 wt% Pr-doped SnO$_2$ hollow nanofibers; (c) SAED pattern of 0.6 wt% Pr-doped SnO$_2$ nanofibers; (d) HRTEM micrograph showing enlarged lattice images of SnO$_2$ nanofibers.

2.7.7.Ce-doped SnO$_2$

Chen at al[221]. (2012) have reported on Ce-doped SnO$_2$ thin films synthesized by the sol gel method, for which the host absorbs the incident energy and then transfers the energy to the Ce^{3+} ions via non-radiative transitions. The films were polycrystalline with a rutile structure. The authors have investigated the luminescence properties of the films as a function of the Ce concentration as well as the annealing temperature. Figure 2.15.a shows that Ce^{3+} ions exhibit photoluminescence around 470 nm corresponding to electron transition between the 5-d excited state and the 4f state. From the inset of figure 2.15.a, the intensity of Ce PL increases initially with the increase of Ce concentration and then decreases above 3%,

due to the concentration quenching effect. The 3 % doped sample has been annealed at different temperatures. The authors found that the Ce peak intensity slightly increases with the increase of the annealing temperature and rich the maximum at 550°C. They conclude a direct correlation between the PL of Ce-doped SnO_2 films and their crystalline quality.

Other studies on Ce-doped SnO_2 for gas sensing application have been reported by Mohanapriya et al.[222] (2013), and song et al[223] (2012).
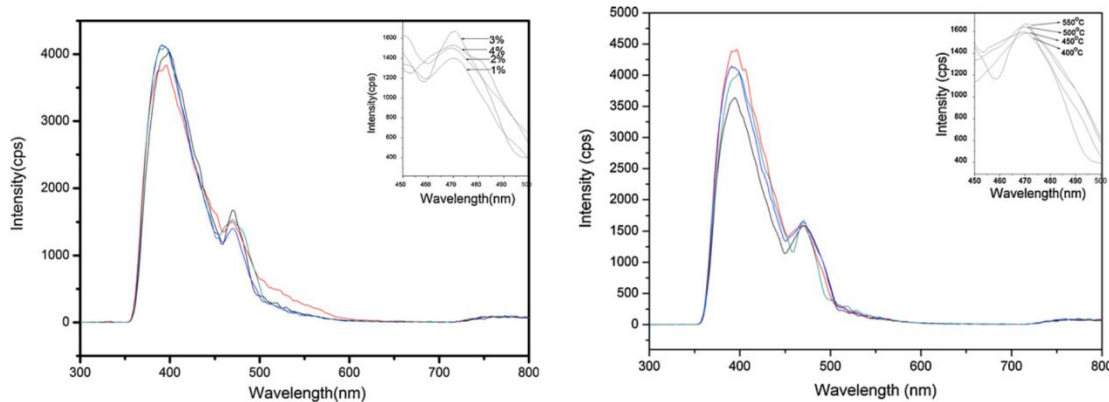
Figure 2.15 a). PL spectra for Ce-doped SnO_2 films with different concentrations. b) PL spectra for Ce-doped SnO_2 films annealed at different temperatures (Ce = 3%).

2.7.8. Nd-doped SnO₂

To our best knowledge, only two reports exist on Nd-doped SnO_2 material. The first one reported by Shide et al[224] (2010) on 2, 5 and 10% of Nd-doped SnO_2 powders which have been elaborated by the hydrothermal method. They found that the doped samples exhibit smaller grains size compared to the undoped ones. As for high Nd concentrations (5 and 10 at%), the films have shown best sensitivity and selectivity to ethanol.

The second report concerns the work of Rinnert *et* al.[225] (2012) who have investigated the photoluminescence properties of the Nd doped SnO_2 thin films elaborated by the electron beam evaporation technique. They started from tetragonal Nd-SnO films further annealed under air at 700°C in order to achieve the rutile SnO_2 phase, for which Nd ions were optically active and exhibit photoluminescence at 920, 1100 and 1300 nm, which corresponds to the optical transitions. They showed that the SnO_2 crystalline phase can be reached after an oxidation process at 700°C. Consequently, efficient Nd emission lines are obtained with a PL intensity decreasing while increasing the Nd content due to the quenching effect upon 3 at%[225]. The PL corresponds to transitions from $^4F_{3/2}$ excited state to the $^4I_{n/2}$ levels with n equal to 13, 11, and 9, respectively, as illustrated in figure 2.16. The authors also investigated the solubility limit of the Nd in the SnO_2 matrix, found at 2.9 at% for which, a

photoluminescence quenching effect has been observed. Resistivities as low as 0.018 Ω cm and mobilities as high as 0.8 cm^2/Vs have been measured.
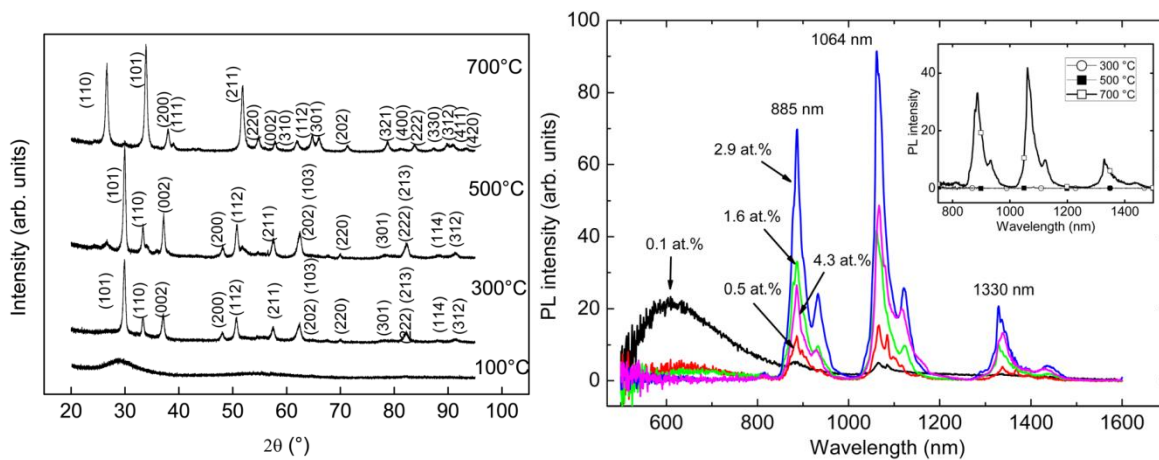
Figure 2.16.a. X-ray diffraction patterns of SnO$_X$ films versus annealing temperature. The peak assignment is for SnO$_2$ for the top spectrum and SnO for the other spectra. b) (Color online) Room-temperature PL spectra of Nd-doped SnO$_x$ alloys annealed at 700°C, for different Nd concentrations. The inset shows the influence of annealing temperature on the PL for Nd concentration equal to 1.6 at. %.

2.7.9. Yb-doped SnO$_2$

As is the case with the other RE-doped SnO$_2$ materials, Yb-doped SnO$_2$ nanofibers have been also reported in the literature for gas sensing application. Ma et al.[226](2015) have successfully doped the SnO$_2$ nanofibers with Yb^{3+} ions (the Yb^{3+} as well as the valency of tin have been identified through XPS) that exhibit perfect sensing performance toward ethanol with excellent selectivity, high response compared to pure SnO$_2$. Zhang et al.[227] (2014) have investigated the ferromagnetism properties of Yb-doped SnO$_2$ by first-principles calculations.

2.8 References

[142] J.-C.G. Bünzli, S. Comby, A.-S. Chauvin, C.D.B. Vandevyver, New Opportunities for Lanthanide Luminescence, Journal of Rare Earths, 25 (2007) 257-274.

[143] J.-C.G. Bünzli, S.V. Eliseeva, Lanthanide NIR luminescence for telecommunications, bioanalyses and solar energy conversion, Journal of Rare Earths, 28 (2010) 824-842.

[144] T.J. Haley, Chapter 40 Toxicity, in: Handbook on the Physics and Chemistry of Rare Earths, Elsevier, 1979, pp. 553-585.

[145] F. Szabadvary, Chapter 73 The history of the discovery and separation of the rare earths, in: Handbook on the Physics and Chemistry of Rare Earths, Elsevier, 1988, pp. 33-80.

[146] S. Hüfner, Optical Spectra of Transparent Rare Earth Compounds, Academic Press, New York, San Fransisco, London, 1978.

[147] S.H. Liu, Chapter 3 Electronic structure of rare earth metals, in: Handbook on the Physics and Chemistry of Rare Earths, Elsevier, 1978, pp. 233-335.

[148] Z.B. Goldschmidt, Chapter 1 Atomic properties (free atom), in: Handbook on the Physics and Chemistry of Rare Earths, Elsevier, 1978, pp. 1-171.

[149] C. Huang, Z. Bian, Introduction, in: Rare Earth Coordination Chemistry, John Wiley & Sons, Ltd, 2010, pp. 1-39.

[150] S.S.D. S D Barrett, INTRODUCTION TO THE RARE EARTHS, in: The Structure of Rare-Earth Metal Surfaces, PUBLISHED BY IMPERIAL COLLEGE PRESS AND DISTRIBUTED BY WORLD SCIENTIFIC PUBLISHING CO., 2011, pp. 1-19.

[151] G.H. Dieke, Spectra and Energy levels of Rare Earth Ions in Crystals, Interscience publishers, New York, 1968.

[152] V. Rivera, E. Marega Jr, F. Ferri, Localized Surface Plasmon Resonances: Noble Metal Nanoparticle Interaction with Rare-Earth Ions, INTECH Open Access Publisher, 2012.

[153] W.M. Yen, H. Yamamoto, Phosphor handbook, CRC press, 2006.

[154] G.H. Dieke, H.M. Crosswhite, The Spectra of the Doubly and Triply Ionized Rare Earths, Appl. Opt., 2 (1963) 675-686.

[155] O. Kazuyoshi, W. Shinta, S. Yuki, T. Hiroaki, I. Takugo, G.B. Mikhail, T. Isao, Calculations of Complete 4 f n and 4 f n -1 5 d 1 Energy Level Schemes of Free Trivalent Rare-Earth Ions, Japanese Journal of Applied Physics, 43 (2004) L611.

[156] M.F. Reid, Transition Intensities, in: R. Hull, J. Parisi, R.M. Osgood, Jr., H. Warlimont, G. Liu, B. Jacquier (Eds.) Spectroscopic Properties of Rare Earths in Optical Materials, Springer Berlin Heidelberg, 2005, pp. 95-129.

[157] J.H.V. Vleck, The Puzzle of Rare-earth Spectra in Solids, The Journal of Physical Chemistry, 41 (1937) 67-80.

[158] J.H. Van Vleck, The Dipolar Broadening of Magnetic Resonance Lines in Crystals, Physical Review, 74 (1948) 1168-1183.

[159] B.R. Judd, Optical Absorption Intensities of Rare-Earth Ions, Physical Review, 127 (1962) 750-761.

[160] G.S. Ofelt, Intensities of Crystal Spectra of Rare‐Earth Ions, The Journal of Chemical Physics, 37 (1962) 511-520.

[161] J.G. Solé, L.E. Bausá, D. Jaque, Applications: Rare Earth and Transition Metal Ions, and Color Centers, in: An Introduction to the Optical Spectroscopy of Inorganic Solids, John Wiley & Sons, Ltd, 2005, pp. 199-234.

[162] P. Goldner, F. Auzel, Application of standard and modified Judd‑Ofelt theories to a praseodymium‑doped fluorozirconate glass, Journal of Applied Physics, 79 (1996) 7972-7977.

[163] B.G. Wybourne, Structure of fn Configurations. I. Calculation of the Energy Levels, The Journal of Chemical Physics, 36 (1962) 2295-2300.

[164] B.G. Wybourne, Structure of fn Configurations. II. f5 and f9 Configurations, The Journal of Chemical Physics, 36 (1962) 2301-2311.

[165] B.G. Wybourne, Spectroscopic Properties of the Rare Earths, Interscience, New York, 1965.

[166] R. Peacock, The intensities of lanthanide f ↔ f transitions, in: Rare Earths, Springer Berlin Heidelberg, 1975, pp. 83-122.

[167] R. Orbach, Relaxation and Energy Transfer, in: B. Di Bartolo (Ed.) Optical Properties of Ions in Solids, Springer US, 1975, pp. 355-399.

[168] E. Desurvire, Erbium-Doped Fiber Amplifiers: Principles and Applications, Wiley, 1994.

[169] T. Förster, Zwischenmolekulare Energiewanderung und Fluoreszenz, Annalen der Physik, 437 (1948) 55-75.

[170] D.L. Dexter, A Theory of Sensitized Luminescence in Solids, The Journal of Chemical Physics, 21 (1953) 836-850.

[171] D.L. Dexter, Possibility of Luminescent Quantum Yields Greater than Unity, Phys. Rev., 108 (1957) 630--633.

[172] Y. Kotsar, E. Monroy, 18 - Infrared emitters made from III-nitride semiconductors, in: J. Huang, H.-C. Kuo, S.-C. Shen (Eds.) Nitride Semiconductor Light-Emitting Diodes (LEDs), Woodhead Publishing, 2014, pp. 533-565.

[173] K. Pavani, J.S. Kumar, L.R. Moorthy, Luminescence properties of single-phase SrMg 2 La 2 W 2 O 12 :Tb 3+ , Sm 3+ , Tm 3+ phosphor for multicolor- and white light-emitting LEDs, Materials Research Express, 1 (2014) 016201.

[174] G. Shao, C. Lou, D. Xiao, Enhancing the efficiency of solar cells by down shifting YAG: Ce3+ phosphors, Journal of Luminescence, 157 (2015) 344-348.

[175] O. Gusev, M. Bresler, A. Kuznetsov, V. Kudoyarova, P. Pak, E. Terukov, K. Tsendin, I. Yassievich, W. Fuhs, G. Weiser, Room-temperature electroluminescence of Er-doped hydrogenated amorphous silicon, Journal of Non-Crystalline Solids, 227–230, Part 2 (1998) 1164-1167.

[176] D. Chen, Y. Wang, M. Hong, Lanthanide nanomaterials with photon management characteristics for photovoltaic application, Nano Energy, 1 (2012) 73-90.

[177] Q.Y. Zhang, X.Y. Huang, Recent progress in quantum cutting phosphors, Progress in Materials Science, 55 (2010) 353-427.

[178] A. Shalav, B.S. Richards, M.A. Green, Luminescent layers for enhanced silicon solar cell performance: Up-conversion, Solar Energy Materials and Solar Cells, 91 (2007) 829-842.

[179] B.S. Richards, Luminescent layers for enhanced silicon solar cell performance: Down-conversion, Solar Energy Materials and Solar Cells, 90 (2006) 1189-1207.

[180] R. Pandiyan, R. Bartali, V. Micheli, G. Gottardi, I. Luciu, D. Ristic, G.A. Goget, M. Ferrari, N. Laidani, Influence of Nd3+ doping on the structural and near-IR photoluminescence properties of nanostructured TiO2 films, Energy Procedia, 10 (2011) 167-171.

[181] Y. Liu, W. Luo, H. Zhu, X. Chen, Optical spectroscopy of lanthanides doped in wide band-gap semiconductor nanocrystals, Journal of Luminescence, 131 (2011) 415-422.

[182] G. Gottardi, R. Pandiyan, V. Micheli, G. Pepponi, S. Gennaro, R. Bartali, N. Laidani, Effect of Nd3+ incorporation on the microstructure and chemical structure of RF sputtered ZnO thin films, Materials Science and Engineering: B, 178 (2013) 609-616.

[183] D. Fröhlich, R. Kenklies, R. Helbig, Band-Gap Assignment in SnO2 by Two-Photon Spectroscopy, Physical Review Letters, 41 (1978) 1750-1751.

[184] A.J. Kenyon, Recent developments in rare-earth doped materials for optoelectronics, Progress in Quantum Electronics, 26 (2002) 225-284.

[185] M. Batzill, U. Diebold, The surface and materials science of tin oxide, Prog. Surf. Sci., 79 (2005) 47-154.

[186] Y. Ogo, H. Hiramatsu, K. Nomura, H. Yanagi, T. Kamiya, M. Hirano, H. Hosono, p-channel thin-film transistor using p-type oxide semiconductor, SnO, Applied Physics Letters, 93 (2008) -.

[187] R. Sivaramasubramaniam, M.R. Muhamad, S. Radhakrishna, Optical Properties of Annealed Tin(II) Oxide in Different Ambients, physica status solidi (a), 136 (1993) 215-222.

[188] H. Hosono, Y. Ogo, H. Yanagi, T. Kamiya, Bipolar Conduction in SnO Thin Films, Electrochemical and Solid-State Letters, 14 (2011) H13-H16.

[189] L. Yu, D. Cai, H. Wang, M.M. Titirici, Hydrothermal synthesis of SnO2 and SnO2@C nanorods and their application as anode materials in lithium-ion batteries, RSC Advances, 3 (2013) 17281-17286.

[190] L.Z. Liu, X.X. Li, X.L. Wu, X.T. Chen, P.K. Chu, Growth of tin oxide nanorods induced by nanocube-oriented coalescence mechanism, Applied Physics Letters, 98 (2011).

[191] Y.J. Chen, L. Nie, X.Y. Xue, Y.G. Wang, T.H. Wang, Linear ethanol sensing of SnO 2 nanorods with extremely high sensitivity, Applied Physics Letters, 88 (2006).

[192] J.S. Chen, M.F. Ng, H.B. Wu, L. Zhang, X.W. Lou, Synthesis of phase-pure SnO 2 nanosheets with different organized structures and their lithium storage properties, CrystEngComm, 14 (2012) 5133-5136.

[193] D. Wei, Y. Shen, M. Li, W. Liu, S. Gao, L. Jia, C. Han, B. Cui, Synthesis and characterization of single-crystalline SnO2 Nanowires, Journal of Nanomaterials, 2013 (2013).

[194] TiO2 nanotube @ SnO2 nanoflake core–branch arrays for lithium-ion battery anode, 4 (2014) 105–112.

[195] C. Zhu, X. Xia, J. Liu, Z. Fan, D. Chao, H. Zhang, H.J. Fan, TiO2 nanotube @ SnO2 nanoflake core-branch arrays for lithium-ion battery anode, Nano Energy, 4 (2014) 105-112.

[196] J. Hu, Y. Bando, Q. Liu, D. Golberg, Laser-ablation growth and optical properties of wide and long single-crystal SnO2 ribbons, Advanced Functional Materials, 13 (2003) 493-496.

[197] E.J.H. Lee, C. Ribeiro, T.R. Giraldi, E. Longo, E.R. Leite, J.A. Varela, Photoluminescence in quantum-confined SnO2 nanocrystals: Evidence of free exciton decay, Applied Physics Letters, 84 (2004) 1745-1747.

[198] L. Jiang, G. Sun, Z. Zhou, S. Sun, Q. Wang, S. Yan, H. Li, J. Tian, J. Guo, B. Zhou, Q. Xin, Size-controllable synthesis of monodispersed SnO 2 nanoparticles and application in electrocatalysts, Journal of Physical Chemistry B, 109 (2005) 8774-8778.

[199] A. Bouaine, N. Brihi, G. Schmerber, C. Ulhaq-Bouillet, S. Colis, A. Dinia, Structural, optical, and magnetic properties of Co-doped SnO2 powders synthesized by the coprecipitation technique, Journal of Physical Chemistry C, 111 (2007) 2924-2928.

[200] F. Gu, S.F. Wang, M.K. Lü, G.J. Zhou, D. Xu, D.R. Yuan, Photoluminescence Properties of SnO2 Nanoparticles Synthesized by Sol−Gel Method, The Journal of Physical Chemistry B, 108 (2004) 8119-8123.

[201] H. Bastami, E. Taheri-Nassaj, Synthesis of nanosized (Co, Nb, Sm)-doped SnO2 powders using co-precipitation method, Journal of Alloys and Compounds, 495 (2010) 121-125.

[202] N.S. Baik, G. Sakai, N. Miura, N. Yamazoe, Preparation of stabilized nanosized tin oxide particles by hydrothermal treatment, Journal of the American Ceramic Society, 83 (2000) 2983-2987.

[203] A. Ayeshamariam, S. Ramalingam, M. Bououdina, M. Jayachandran, Preparation and characterizations of SnO2 nanopowder and spectroscopic (FT-IR, FT-Raman, UV-Visible and NMR) analysis using HF and DFT calculations, Spectrochimica Acta - Part A: Molecular and Biomolecular Spectroscopy, 118 (2014) 1135-1143.

[204] F. Gu, S.F. Wang, M.K. Lü, G.J. Zhou, D. Xu, D.R. Yuan, Photoluminescence properties of SnO2 nanoparticles synthesized by sol-gel method, Journal of Physical Chemistry B, 108 (2004) 8119-8123.

[205] E.A. Morais, L.V.A. Scalvi, L.P. Ravaro, S.M. Li, E.A. Floriano, Optical and transport properties of rare-earth trivalent ions located at different sites in sol-gel SnO2, Journal of Physics: Conference Series, 249 (2010).

[206] E.A.d. Morais, L.V.A. Scalvi, A.A. Cavalheiro, A. Tabata, J.B.B. Oliveira, Rare earth centers properties and electron trapping in SnO2 thin films produced by sol-gel route, Journal of Non-Crystalline Solids, 354 (2008) 4840-4845.

[207] L.P. Singh, M.N. Luwang, S.K. Srivastava, Luminescence and photocatalytic studies of Sm3+ ion doped SnO2 nanoparticles, New Journal of Chemistry, 38 (2014) 115-121.

[208] E. Cao, Y. Zhang, W. Hao, H. Peng, L. Sun, J. Hu, Room temperature ferromagnetism in Sm-doped SnO 2 PLD film, Applied Surface Science, 282 (2013) 376-383.

[209] D. Wang, J. Jin, D. Xia, Q. Ye, J. Long, The effect of oxygen vacancies concentration to the gas-sensing properties of tin dioxide-doped Sm, Sensors and Actuators B: Chemical, 66 (2000) 260-262.

[210] Q. Qi, T. Zhang, X. Zheng, H. Fan, L. Liu, R. Wang, Y. Zeng, Electrical response of Sm 2 O 3-doped SnO 2 to C 2 H 2 and effect of humidity interference, Sensors and Actuators B: Chemical, 134 (2008) 36-42.

[211] H. Bastami, E. Taheri-Nassaj, Synthesis of nanosized (Co, Nb, Sm)-doped SnO 2 powders using co-precipitation method, Journal of alloys and compounds, 495 (2010) 121-125.

[212] F. Hild, L. Eichenberger, A. Bouché, X. Devaux, M. Stoffel, H. Rinnert, M. Vergnat, Structural and Photoluminescence Properties of Evaporated SnO 2 Thin Films Doped with Rare Earths, Energy Procedia, 84 (2015) 141-148.

[213] H. Elhouichet, L. Othman, A. Moadhen, M. Oueslati, J. Roger, Enhanced photoluminescence of Tb 3+ and Eu 3+ induced by energy transfer from SnO 2 and Si nanocrystallites, Materials Science and Engineering: B, 105 (2003) 8-11.

[214] X. Fu, H. Zhang, S. Niu, Q. Xin, Synthesis and luminescent properties of SnO 2: Eu nanopowder via polyacrylamide gel method, Journal of Solid State Chemistry, 178 (2005) 603-607.

[215] P. Psuja, W. Strek, Influence of concentration and sintering temperature on luminescence properties of Eu 3+: SnO 2 nanocrystallites, Journal of Rare Earths, 30 (2012) 627-631.

[216] H. Zhang, X. Fu, S. Niu, G. Sun, Q. Xin, Luminescence properties of Li+ doped nanosized SnO 2: Eu, Journal of luminescence, 115 (2005) 7-12.

[217] E.A.d. Morais, L.V.A. Scalvi, A.A. Cavalheiro, A. Tabata, J.B.B. Oliveira, Rare earth centers properties and electron trapping in SnO2 thin films produced by sol–gel route, Journal of Non-Crystalline Solids, 354 (2008) 4840-4845.

[218] E.A. Morais, L.V.A. Scalvi, L.P. Ravaro, Optical emission and electron capture of rare-earth trivalent ions located at distinct sites in thin films, Physics Procedia, 2 (2009) 353-364.

[219] M. Guo, X. Xie, J. Jia, Z. Liang, C. Fan, P. Han, Experimental study and theoretical calculation on the conductivity and stability of praseodymium doped tin oxide electrode, Electrochimica Acta, 151 (2015) 177-185.

[220] W. Li, S. Ma, Y. Li, X. Li, C. Wang, X. Yang, L. Cheng, Y. Mao, J. Luo, D. Gengzang, Preparation of Pr-doped SnO 2 hollow nanofibers by electrospinning method and their gas sensing properties, Journal of Alloys and Compounds, 605 (2014) 80-88.

[221] S. Chen, X. Zhao, H. Xie, J. Liu, L. Duan, X. Ba, J. Zhao, Photoluminescence of undoped and Ce-doped SnO 2 thin films deposited by sol–gel-dip-coating method, Applied Surface Science, 258 (2012) 3255-3259.

[222] P. Mohanapriya, H. Segawa, K. Watanabe, K. Watanabe, S. Samitsu, T. Natarajan, N.V. Jaya, N. Ohashi, Enhanced ethanol-gas sensing performance of Ce-doped SnO 2 hollow nanofibers prepared by electrospinning, Sensors and Actuators B: Chemical, 188 (2013) 872-878.

[223] P. Song, Q. Wang, Z. Yang, Preparation, characterization and acetone sensing properties of Ce-doped SnO 2 hollow spheres, Sensors and Actuators B: Chemical, 173 (2012) 839-846.

[224] W. Shide, L. Chao, W. Wei, W. Huanxin, S. Yanliang, Z. Youqi, Nd-doped SnO 2: characterization and its gas sensing property, Journal of Rare Earths, 28 (2010) 171-173.

[225] H. Rinnert, P. Miska, M. Vergnat, G. Schmerber, S. Colis, A. Dinia, D. Muller, G. Ferblantier, A. Slaoui, Photoluminescence of Nd-doped SnO 2 thin films, Applied Physics Letters, 100 (2012).

[226] T. Wang, S. Ma, L. Cheng, J. Luo, X. Jiang, W. Jin, Preparation of Yb-doped SnO 2 hollow nanofibers with an enhanced ethanol–gas sensing performance by electrospinning, Sensors and Actuators B: Chemical, 216 (2015) 212-220.

[227] K.-C. Zhang, Y.-F. Li, Y. Liu, F. Chi, Density-functional study on the robust ferromagnetism in rare-earth element Yb-doped SnO 2, Journal of Magnetism and Magnetic Materials, 360 (2014) 165-168.

Chapter 3: RE doped SnO$_2$ powders

3.1. Introduction

As mentioned in Chapter 1, this work aims at producing oxide materials with high down conversion efficiencies serving as functional TCOs for optoelectronic and solar cell devices. From the fundamental point of view, it intends at gaining in-depth understanding of phenomena and processes involved in the photons conversion mechanisms. Emphasis is particularly on the investigation of functionalizing tin oxide SnO_x , as a host material, with lanthanides, as impurity dopants, for down shifting or down conversion properties.

This chapter addresses the structural, optical and photons conversion properties of SnO_x powders doped with different lanthanide elements. In fact, due to the large ionic radius of these elements, their insertion into the SnO_2 matrix is a quite difficult task. One way to explore the possibility of incorporating elements in host matrices is the study of their properties at the nanoscale. To do so, we proceed on the investigation of functional SnO_2 nanoparticles. Tin oxide nanomaterials have been widely studied in literature. Pioneering works have been reported on the synthesis of nanostructured SnO_2 covering a large selection of morphologies such as nanorods,[189, 190, 228] nanosheets[229] , nanowires[230] , nanoflakes , core-branched nanoarrays[195] , nanoribbons[196] and nanocrystals[197, 198]. From the fabrication point of view, SnO2 powder can be easily synthesized through different chemical methods, such as co- precipitation [199, 201] , hydrothermal [202, 231] and sol-gel [203, 204] . The resulting properties of the tin dioxide nanostructures can be strongly tuned through the initial precursors as well as the processing method.

In this chapter, we report on the properties of RE-doped SnO_2 powders synthesized by two different chemical routes. We will first investigate the insertion of various RE elements - namely 1 at.% of Prasodynium (Pr), Nyodinium (Nd), Terbium (Tb) and Ytterbium (Yb) - into the SnO_2 matrices using the *co-precipitation method*. This method is among the oldest wet chemical techniques widely used for commercial large area applications. Its main advantage is allowing a good control of composition in addition to easiness of processing. Morphological and structural properties of the synthesized materials have been studied by means of SEM, XRD and Raman techniques while their optical and luminescence properties were explored by the UV-Vis-NIR and photoluminescence spectroscopy methods. The aim of this study is to answer the question whether SnO_2 matrix allows incorporation of rare earth elements.

In a second part, we will investigate the doping of SnO_2 nanoparticles with Nd and Yb elements using the *sol-gel method*. The sol-gel process is an exciting R&D elaboration technique that offers the most outstanding advantages for mixed systems, in which the chemical homogeneity of the various elements can be controlled down to the atomic level. The solubility limit of Nd and Yb has been studied by varying the doping concentration. The insertion of the rare earths was checked by different analysis techniques, mainly SEM, TEM, XRD and Raman. The optical activity by means of UV-VIS-NIR absorption, PL and PLE of the incorporated REs confirmed the successful insertion of Nd and Yb into the SnO_2 structure. This study aims at monitoring the optical properties of the material by tuning the dopant concentration in the structure.

Regardless of the synthesis method, the goal is to find experimental conditions favouring strong optical activity of the rare earth elements and thus efficient photon conversion process from UV-Vis to infrared.

Furthermore, while individual rare earth element might lead to a down-shifting functionality, appropriate combination of two elements can be particularly promising for potential cooperative down-conversion properties. That will be the subject of the last part of this chapter, which deals with co-doping SnO_2 with Nd and Yb elements. The powders have been synthesised by the sol-gel method and analysed by numerous techniques.

In the following, we will give an experimental evidence of the rare earth sensitization via the SnO_2 host matrix, and demonstrate efficient energy transfer. In the case of co-doping, we report that in addition to an energy transfer from the host to each rare earth, an additional energy transfer process takes place between Nd^{3+} and Yb^{3+} ions. All these processes will be schematically illustrated by means of energy levels diagrams as well as the different involved mechanisms.

3.2 RE-doped SnO₂ powder prepared by the co-precipitation method

3.2.1 Synthesis

The initial ingredients consist mainly of Tin and rare earth salts. The exact weight ratio between the components has been calculated in order to obtain the desired nominal concentration (for this study we have chosen 1 at % of RE with respect to the Sn content).The slats were first dissolved in distilled water by means of a stirrer. The solutions were then heated gradually up to 80°C. Then, a 100 ml of ammonia was added to the solution in order to obtain a precipitate. The rotation speed and heating time were optimised for better results. Later, the precipitates were filtered and immediately washed by distilled water, then dried in the oven at 50°C during a whole night. The resulting crystals were placed into an agate mortar and grinded by means of pestle. One part is left for analysis and a second part was calcined at 700°C during 1h in order to achieve a crystallisation phase of SnO₂.

Figure 3.1 Different steps of synthesis of the RE doped SnO₂ powders by the co-precipitation method

3.2.2 Structural and morphological properties

3.2.2.1 SEM observations

The powders were first analysed by scanning electron microscopy (SEM) in order to get an insight on their morphologies and to check whether some impurities are present. Figure 3.2 shows the SEM micrographs in the SEI mode of the Pr, Nd and Yb-doped SnO₂ powders calcined at 700°C. It is found that all the SnO₂ powders prepared by the co-precipitation method consist of nano-aggregated round shaped grains with more or less regular size distribution. The analysis in the 'COMPO' mode did not reveal the presence of rare-earth oxide compounds nor other impurities within the detection limit of the SEM technique. Indeed, the aggregates that have a heavier atomic weight should appear with a darker contrast, which is not the case for our powders. This result suggests that the REs are correctly

inserted into the structure. This was expected for a low doping level. Moreover, the presence of the RE elements was confirmed by the EDS analysis, which showed RE contents in line with the nominal concentrations; the error bar was about 0.5 at. %. The SEM/EDS analysis were performed on different zones and showed similar results, namely homogeneity and uniformity of the REs distribution in the powder.
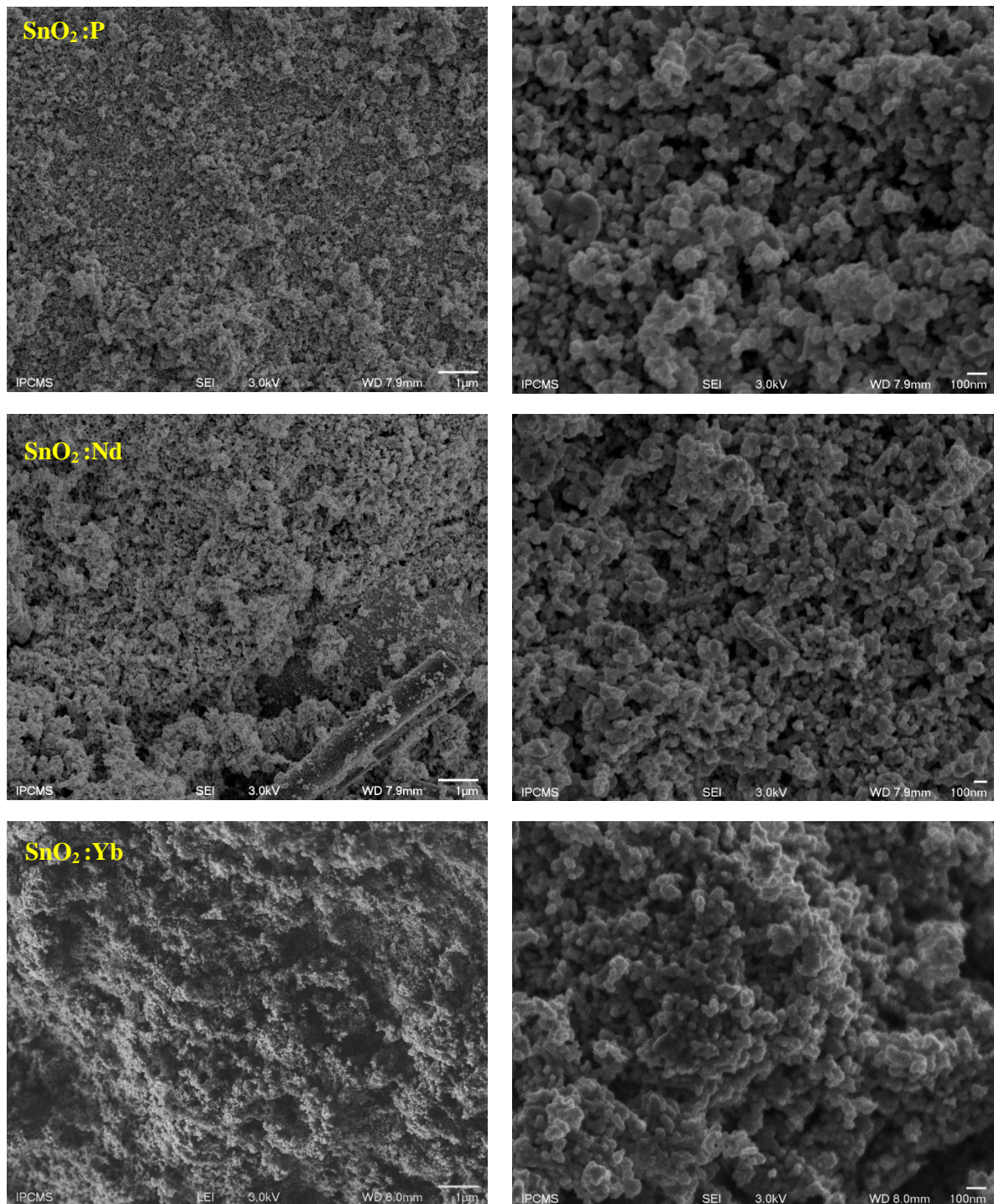
Figure 3.2 SEM micrographs of Pr, Nd and Yb doped SnO_2 powders sintered at 700°C. The left images are recorded at x10000, the right images are recorded at x50000.

It is important to underline that it was not possible to extract accurate values of the particles' size because of the small size of the particles.However, a clear idea on the grains size can be unambiguously noticed and found around 50 nm.

3.2.2.2 XRD analysis

Figure 3.3a shows typical θ-2θ XRD diffraction patterns of Nd-doped SnO_2 powder before and after annealing. We have found that the as prepared powder consists mainly of tin chloride ($SnCl_2$) and Neodymium sesquioxide (Nd_2O_3). After sintering at 700°C, no trace of chloride was detected. According to the JCPDS card n°= 00-41-1445 the powder is crystallised in the SnO_2 tetragonal rutile phase. No Nd oxides peaks have been recorded in the detection limit of the XRD technique. It can be stated that the annealing temperature at 700°C is necessary to achieve the SnO_2 phase. This is consistent with previous reports.Thus, Bouain et al have studied Co-doped SnO_2 powders by the co-precipitation method and reported the SnO_2 phase crystallization at 750 °C [199]; Rinnert et al. reported on the Nd-doped SnO_2 evaporated thin films and obtained the SnO_2 rutile phase only after annealing at 700°C [225].
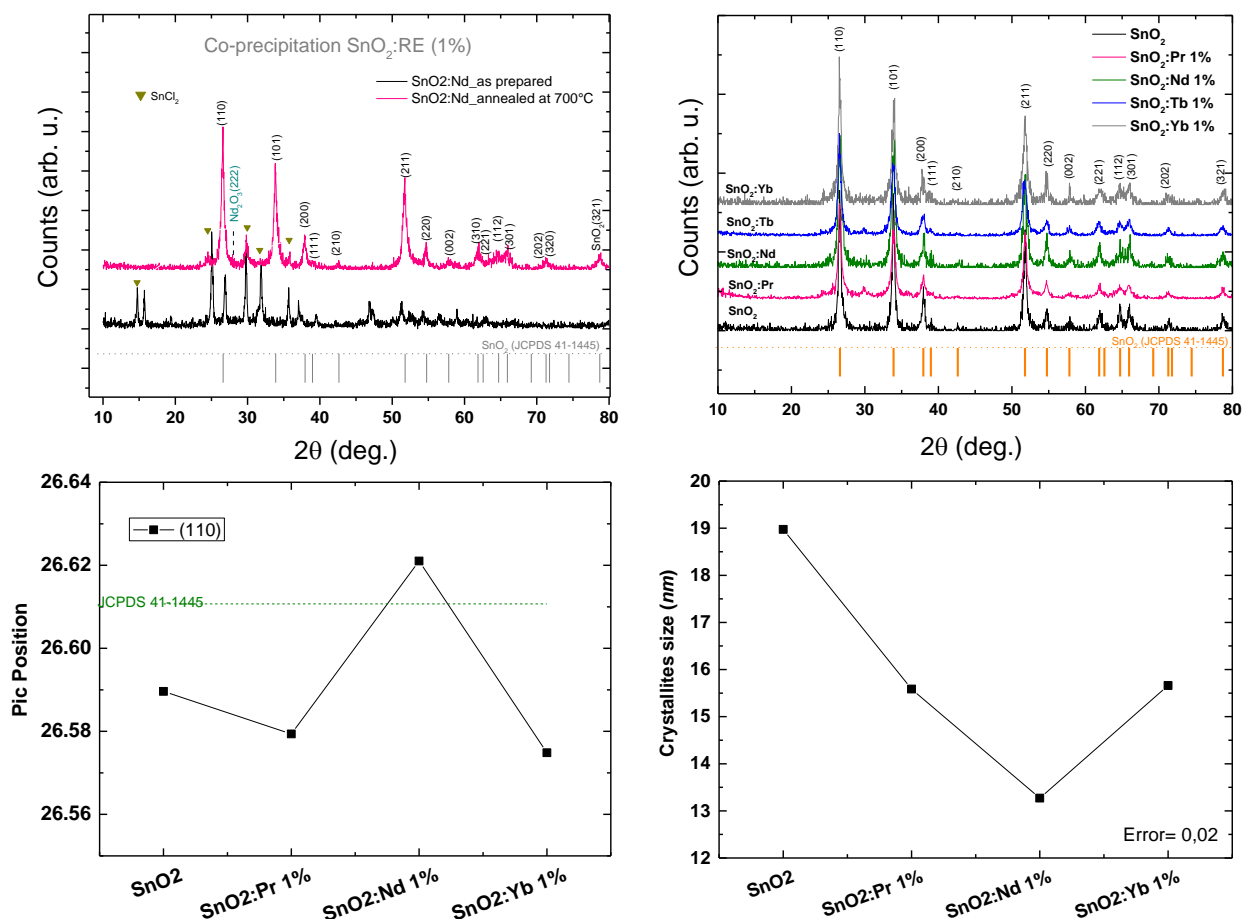
Figure 3.3 – a) typical θ-2θ XRD diffraction patterns of Nd-doped SnO_2 powder before and after annealing, **b)** diffraction patterns of different RE-doped SnO_2 powders calcined at 700°C,

c) and 110 peak position of the annealed powders with respect to the ionic radius of RE, respectively. **d)** crystallites size

For the following, all the fabricated doped powders were annealed at 700°C. Figure 3.3.b, plots the XRD spectra of undoped and doped samples; they all exhibit a polycrystalline SnO_2 rutile structure whatever is the incorporated rare earth element. As it can be clearly seen from Figure 3.3.c, the diffraction peaks position of the undoped powder are found slightly shifted to lower diffraction angles comparing to the JCPDS reference, most likely due to the stress in the lattice, resulting from the preparation technique.

All doped powders present a slight shift of the peaks position relative to the pure SnO_2 but the degree of shift clearly depends on the rare earth type and its ionic radius.. Usually, the shift to higher angles is due compressive stress on the lattice most likely due the presence of some defects in the structure, while the shift towards lower angles is due to tensile stress and indicates the insertion of impurity. In Some cases, the competition between the RE insertion and defects signatures induces some incoherencies in the diffraction peaks position. Therefore, one must be careful in interpreting quickly the XRD' peak positions data. Additional experiments are needed.

On the other hand, the Full Width at Half Maximum of the diffraction peaks is found to increase for the doped powders. This indicates a decrease in the crystallites size as shown in Figure 3.1.d., where values about 19 nm and 16nm are deduced for undoped and the doped powders, respectively. The smallest value is reached for Nd doping which has a medium ionic radius of 0.100 nm. Pr and Yb ions have ionic radius of about 0.101 and 0.086 nm, respectively. But in overall, all doped powders are composed of smaller crystallites compared to the undoped powders, which suggests an efficient RE insertion within the structure.

In reference to literature, our powders exhibit smaller crystallite size values to those reported by Bastami et al for the nanosized (Co, Nb, Sm) doped SnO_2 employing the same preparation technique [201]. Although Cobalt possess a smaller ionic radius (0.074 nm) as compared to lanthanides, the Co-doped SnO_2 powders reported by Bouain et al exhibited crystallite sizes raging between 85 nm for the undoped and 28 nm for the doped powders. This result reveals how efficient is the insertion of RE in SnO_2

3.2.2.3 Raman analysis

In the following, Raman spectroscopy analysis were carried out on the undoped and doped powders, but let's starts with some general considerations concerning SnO_2.

SnO_2 crystallizes in the rutile tetragonal structure which belongs to the point group D_{4h}^{14} and space group P4$_2$/mnm[232]. The unit cell consists of two metal atoms and four oxygen atoms[233]. Each cation is situated amidst to six oxygen atoms which approximately form the corners of a regular

octahedron. Oxygen atoms are surrounded by three tin atoms which approximate the corners of an equilateral

triangle. The lattice parameters are a = b = 4.737 Å, and c = 3.186 Å. The ionic radii for O^{2-} and Sn^{4+} are 1.40 and 0.71 Å, respectively[33].

The six unit atoms generate a total of 18 vibrational modes in the first Brillouin zone with an irreducible representation [8, 34, 232, 234, 235]:

$$\Gamma = A_{1g}(R) + A_{2g} + B_{1g}(R) + B_{2g}(R) + E_g(R) + 2A_{2u}(IR) + 2B_{1u} + 4E_u(IR)$$

Of these 18 modes, two are IR active (the single A_{2u} and the triply degenerated E_u mode), four modes are Raman active (three non-degenerate modes, A_{1g}, B_{1g}, B_{2g} and the doubly degenerate E_g) and two are silent (A_{2g} and B_{1u}). One A_{2u} and two E_u modes are acoustic. In the Raman active modes the oxygen atoms vibrate while the Sn atoms are at rest. The nondegenerate modes, A_{1g}, B_{1g}, and B_{2g} vibrate in the plane perpendicular to the c-axis while the doubly degenerate E_g mode vibrates in the direction of the c-axis[20, 38]. The B_{1g} mode consists of rotation of the oxygen atoms around the c-axis, with all six oxygen atoms of the octahedra participating in the vibration. In the A_{2u} infrared active mode, Sn and oxygen atoms vibrate in the c-axis direction, and in the E_u mode both Sn and O atoms vibrate on the plane perpendicular to the c-axis[20]. The silent modes correspond to vibrations of the Sn and O atoms on the direction of the c-axis (B_{1u}) or in the plane perpendicular to this direction (A_{2g}). To assess the crystallization of our powders into the rutile structure, one would expect the appearance of the four fundamental Raman modes (A_{1g}, B_{1g}, B_{2g} and E_g).

Fig. 2.4 shows the complete Raman spectra of the undoped and RE-doped SnO₂ powders in the 200 – 800 cm⁻¹ range. For purpose of clarity, an offset of the spectra have been made. All synthesized powders exhibit the three main vibration modes characteristic of a rutile structure, which supports the XRD results. In fact, the A_{1g}, B_{2g} and E_g Raman active modes can be distinguished at 632, 771, and 471 cm⁻¹, respectively [37, 236, 237]. Additional vibration modes appear at different frequencies: in the low-frequency region, the features at 251, 302 and 352 cm⁻¹ are usually attributed to the E_u (TO), E_u(TO) and E_u (LO) [228, 238, 239].; The weak peaks at 505, 553 and 694 cm⁻¹ are identified as B_{1u} (2TO), B_{1u} (3LO) and A_{2u} (LO) respectively [240-242]. Curiously, the intensity of the principal vibration mode A_{1g}, B_{2g} and E_g increases for the doped powders as compared to the pure SnO₂ suggesting better crystalline structure. Moreover, the E_u transversal optic mode at 302 cm⁻¹ becomes more pronounced resulting in a well resolved peak for the RE-doped powders except that of the Nd-doped one. This behaviour is most likely due to the insertion of the rare earth into the structure. Additionally, the B_{1u} features originating from the oxygen vacancies [243, 244] are better resolved for the doped powders, which suggests higher density of oxygen vacancies.
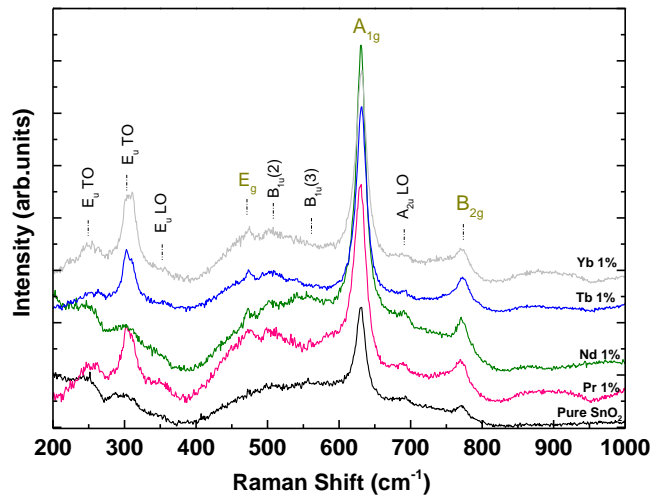
Figure 3.4 Raman spectra of undoped and RE doped SnO_2 powders calcined at 700°C. Raman actives modes are presented in green, the inactive ones are presented in black

3.2.3 Optical properties

Figure 3.5 plots the absorbance spectra of the different synthesized powders. All powders are found to absorb from 250 to 500 nm with an absorption threshold ranging between 450-500nm. When referenced to the pure SnO_2 case, the absorption edge of the doped powders are shifted towards higher or lower energies, meaning that the presence of the rare earth element within the SnO_2 structure affects the optical properties of the host matrix, particularly its absorption. Interestingly, the doped powders exhibit some absorption bands in the visible and NIR region, most likely linked to the absorption of the rare earth elements.
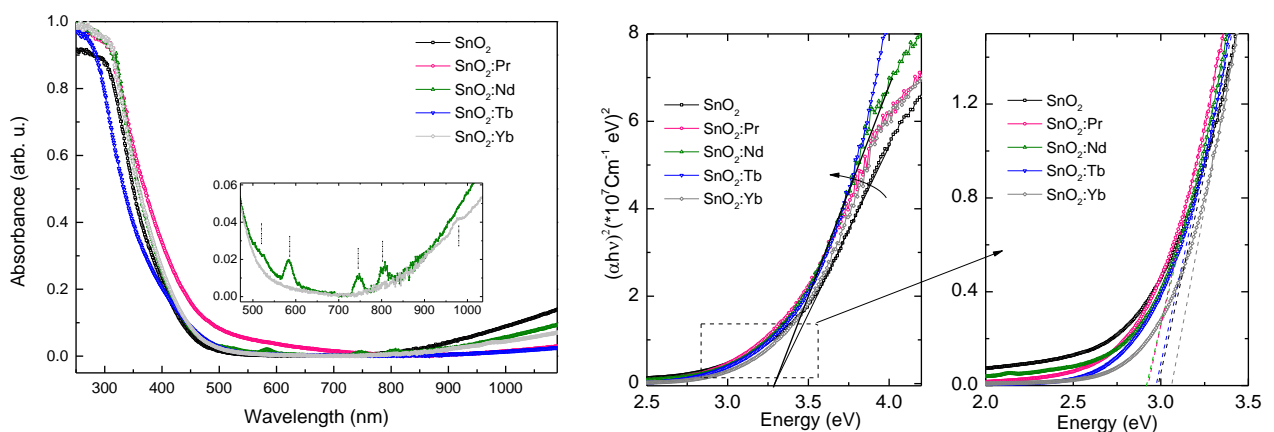
Figure 3.5 (a) Absorbance spectra, (b) Tauc plots of undoped and RE doped SnO_2 powders (c) Zoom of the TPs

The Nd-doped sample displays four absorption bands centred at 520, 583, 744 and 806 nm while the Yb doped one shows only one weak peak around 972 nm. When looking carefully to the Nd and Yb

energy level diagrams, the features in the absorption spectra correspond perfectly to the excitation of 4f electrons from the ground state to higher energy levels of Yb and Yb, suggesting their insertion in the lattice and their subsequent optical activation as we will see later. This is not the case for the Pr and Tb doped powders for which no additional absorption bands were detected. Although EDS analysis confirmed the presence of Pr and Tb in the powders without aggregates, the absence of their absorption peaks suggests that either Pr and Tb are not optically active (transitions are forbidden), or their absorption lines are too weak to be detected with such technique. Analysis at low temperature might reveal additional information on their spectroscopy.

In order to have a closer look to the SnO₂ band gap evolution when doping with rare earth elements, the absorption edges are presented as Tauc plots (Figure 3.5.b). Usually, the optical band gap E_g can be determined by plotting $(\alpha h\nu)^{1/n} \propto (h\nu)$ using the Eq. (1):

$$\alpha = B(h\nu - Eg)^n \quad (1)$$

B is constant that depends on the transition probability; n can have different values depending on the nature of the transition, namely 1/2, 2, 3/2, and 3 for allowed direct, allowed indirect, forbidden direct and forbidden indirect transitions, respectively. The band gap can be obtained by extrapolating the linear part of the curve $(\alpha h\nu) = 0$. The values of the optical absorption coefficient α of our powders were calculated from Equation (1) and using absorbance data: $\alpha = 2.303 \frac{10^3 \rho A}{lcM}$ (2), where ρ is the theoretical density of SnO₂, A is the absorbance, l is the optical path length of the quartz cell (1cm), c is the molar concentration and M is the molecular weight of the SnO₂ powder.

As mentioned in chapter 1, SnO₂ possess a direct band gap at the of the Brillouin zone, thus the transitions here are allowed direct nature with n=1/2.

Figure 3.5b allows rather visual information about the band gap of the material. Despite the possibility of calculations through equation 1, we will not report exact values of the band gap of our materials. In fact, the error in estimating the band gap by extrapolation is very high. For example, from fig 2.5.b one can say that all powders have more or less a comparable optical band gap value (around 3.26 eV±0.1) in spite of the shift of the absorption edge. Figure 3.5.c represents a zoom of the Tauc plots at lower intensities. One could easily notice a change in the band gap values to around ≈ 2.9-3.1 eV, whereas we deal with the same curves. A a consequence, we decided to be very careful when determining Eg with such method. Moreover, the Tauc law is not reliable in presence of excitonic features. If the last are very strong, the extracted values will correspond more to the excitonic absorptions than the band-to-band absorption.

 From the photons conversion point of view, both excitonic absorptions and band-to-band absorption are of interest.

In any case, from the absorption edges displayed in Figure 3.5.b and c, we can conclude that the variation of the band gap is less impressive compared to the shape and shift of the absorption edge. Comparing to the bulk SnO_2 (Eg=3.6 eV) our powders are exhibiting smaller values in the range 2.9-3.2 eV. This difference is most likely resulting from the preparation method as well as on the grains size. It is known that greater is the grains size, smaller is the band gap. In brief, the presence of the rare earth elements into the structure induces some changes in the electronic states at band edges of the host matrix. The most important information from these analyses is that all doped powders are found to absorb in the UV range.

3.2.4 Luminescence properties

One way to investigate the insertion of the incorporated rare earths and subsequently its optical activity is through the photoluminescence spectroscopy analysis. Figure 3.6a displays the UV-Vis-NIR emission spectra of pure SnO_2 and RE-doped powders recorded under a Nd YAG laser illumination at an excitation wavelength of 355 nm (3.49 eV). These spectra cover a large part of the spectral range useful for optoelectronic applications, particularly solar cells.

Since the gap energy of the pure SnO_2 powder is around 3.2 eV, the band to band emission should appear at about 387 nm. This emission is however not observed in the PL spectrum because of the detection limit of our PL setup. Yet, the pure SnO_2 powder exhibits a very strong luminescence band centred at 580 nm, and a much less intense one in the 400-450 nm region.

The large and intense band around 580 nm can be attributed to the presence of deep levels in the band gap of SnO_2 [196] whose the origin can be multiple. It is generally admitted that oxygen vacancies, which are present at a high concentration in oxide-based powders, can lead to the formation of important amount of trapped states within the band gap. In particular, oxygen vacancies are one of the dominant defects that form donor levels, which usually play an important role in the PL process [245-247]. Another source of luminescence centers in SnO_2 materials can be the presence of tin interstitial atoms resulting from the preparation technique. The large amounts of grains boundaries in the powder can also induce efficient recombining luminescent centers. Similar observations in quantum nanoparticles systems have been reported in literature [247-249].

The PL band in the 400-450 nm range has been often reported in literature. Earlier studies have shown a broad dominant peak near 396 nm (about 3.14 eV). Gu et al.[245] have also reported the presence of peaks centered at around 414 and 440 nm.

The peak at 414 nm is generally assigned to the electron transitions from the donor levels created by oxygen vacancies to the valence band [204], while the peak at 440 nm is quite often ascribed to the luminescent centers due to inter-grains defects [250].

Figure 3.6.a displays also the PL spectra of the Pr, Nd, Tb and Yb doped powders. The two bands in the UV region are also present and exhibit comparable PL intensities than that of the undoped SnO_2 sample. In contrast, the band in the visible region is almost 2 times weaker than that observed with pure SnO_2. Additional emission bands at different wavelengths have been detected. For the Nd-doped powder, a feature at 885 nm can be clearly seen. As for the Tb doped sample, a weak emission peak at 541 is distinguished. Markedly, the Yb doped SnO_2 powder exhibits very strong peaks at 973 and 1004 nm. This last PL emission is very close to the Si band gap, which could be of a potential benefit for Si based solar cells. Last but not least, no extra emissions was detected for the Pr-doped SnO_2 powders.
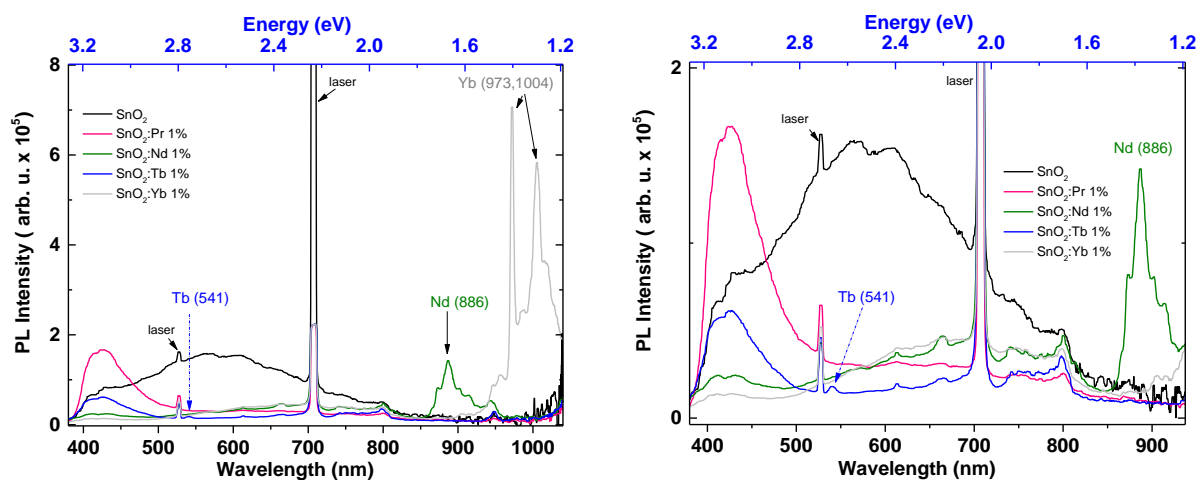
Figure 3.6 Photoluminescence spectra of undoped and RE doped SnO_2 powders excited with Nd-YAG laser wavelength of λ= 355 nm (a). Closer look to RE emission (b)

A careful look on the energy levels diagram of the different rare earth elements allowed us to identify the origin of the observed emission peaks. The peak of Nd at 885nm corresponds to a transition from the $^4F_{3/2}$ excited state to the $^4I_{9/2}$ ground state of Nd^{3+}. The peak of Tb at 541 nm can be assigned to the principal emission of Tb^{3+} originating from des-excitations from the ^4D to the $^7F_5$ excited levels. Finally, the two strong peaks at 971 and 1004 nm detected for Yb doped SnO_2 are related to Yb^{3+}, more precisely, they originate from transitions between $^2F_{5/2}$ to $^2F_{7/2}$.

3.2.5 Summary

1 at.% RE-doped SnO_2 powders have been successfully synthesised by means of the co-precipitation method. Annealing temperature of 700°C is found essential to avoid parasitic phases such as tin chloride or RE oxides. Analysis by SEM microscopy and EDX revealed the nano-aspect of the powders and gave evidence of the presence of RE elements without oxides agglomerates, which suggest an efficient RE incorporation into the SnO_2 structure. This result was confirmed by the XRD data. Furthermore, no RE based compounds were detected in the detection limit of our XRD setup. All

powders were found to crystallize in the polycrystalline SnO_2 tetragonal rutile phase. The main vibrational modes of the structure were recorded by the Raman spectroscopy. The RE insertion induces some stress in the lattice and therefore leads to a decrease in the crystallites size. The absorbance spectra by the UV-Vis-NIR spectroscopy showed a shift of the absorption edges to lower energies for the doped powders, indicating absorption of more UV photons. More importantly, some additional absorption bands appeared at different wavelengths for Nd and Yb doped SnO_2 samples, but not in the case of doping with Pr and Tb. Finally, the photoluminescence measurements showed a strong emission band in the visible range for the pure SnO_2 originating from the defects in the structure. When doping with rare earth elements, this "visible" PL dramatically decreased dramatically but it was accompanied with the appearance of additional PL peaks characteristics of rare earths elements. Thus, for Nd a large band takes place at 885 nm while for Tb, a weak peak is recorded at 541 nm and for Yb, two strong peaks are visible at 973 and 1004 nm. Such results give an experimental evidence of the optical activity of the RE elements embedded in the SnO_2 matrix. Finally, no additional PL features were detected for Pr doped SnO_2 powder, considering the detection limit of our PL setup.

As a main conclusion of this part, it can be stated that efficient NIR photons are emitted from Nd and Yb doped SnO_2 powders after excitation under UV photons. This result demonstrates the possibility of UV photon conversion via RE-doped SnO_2 system produced by the precipitation method.

In the following, new RE-doped SnO_2 structures will be synthesized by the sol-gel method and their properties will be presented and then compared to those produced by the precipitation process. Given the results above, we have focused on Nd and Yb doping.

3.3 RE-doped SnO₂ powder by the sol-gel method

3.3.1 Synthesis

Undoped and Nd doped SnO_2 as $[SnO_2]_{(1-x)}Nd_x$ solutions were provided by the RBnano company [251] where x was set to 0, 1, 3% and 5 at %. It consists of metal-organic tin precursor in solution in propionic acid (product RBnano RBN119). For doping, Nd was added in the previous solution as neodymium (III) acetate hydrate 99.9% (Alfa Aesar). The sol-gel solutions were then annealed at 700°C for 3h in air in order to get SnO_2 crystallization. Small crystals were obtained and further thoroughly grounded in an agate mortar to obtain a fine powder. In the following, the samples will be labelled SnO_2 and SnO_2:Nd x with x =1, 3 and 5%.
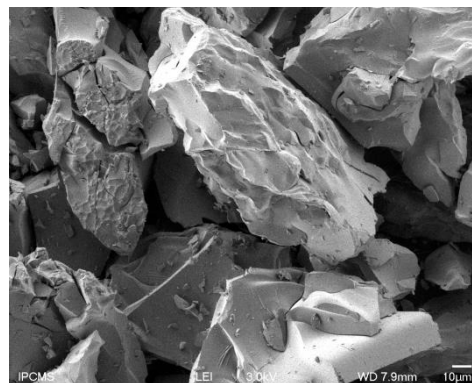
Similarly to Nd case, $[SnO_2]_{(1-x)}Yb_x$ solutions were also provided by RBnano and the same fabrication process was applied. However, higher RE concentrations were tested in this case.

3.3.2 Structural and morphological properties

3.3.2.1 Morphology

Figure 3.7 displays the SEM images of undoped and doped powders produced by the sol-gel method. The images reveal that the powders are composed of nano-aggregates with round shaped grains whose the size is found to decrease when increasing Nd content. This is particularly visible for the sample doped with 5 at. % of Nd (Figure 3.7d). A similar trend is observed in the SEM images of the Yb-doped SnO_2 powders reported in Figure 3.8.

It turns out that the Yb doped SnO_2 powders exhibit smaller grains than that of the Nd-doped ones, especially at high doping level (4 and 6 at.%). This indicates a clear effect of the rare earth elements' insertion and can be understood in terms of effect of the dopant' ionic radius. This will be more thoroughly discussed in the following section.
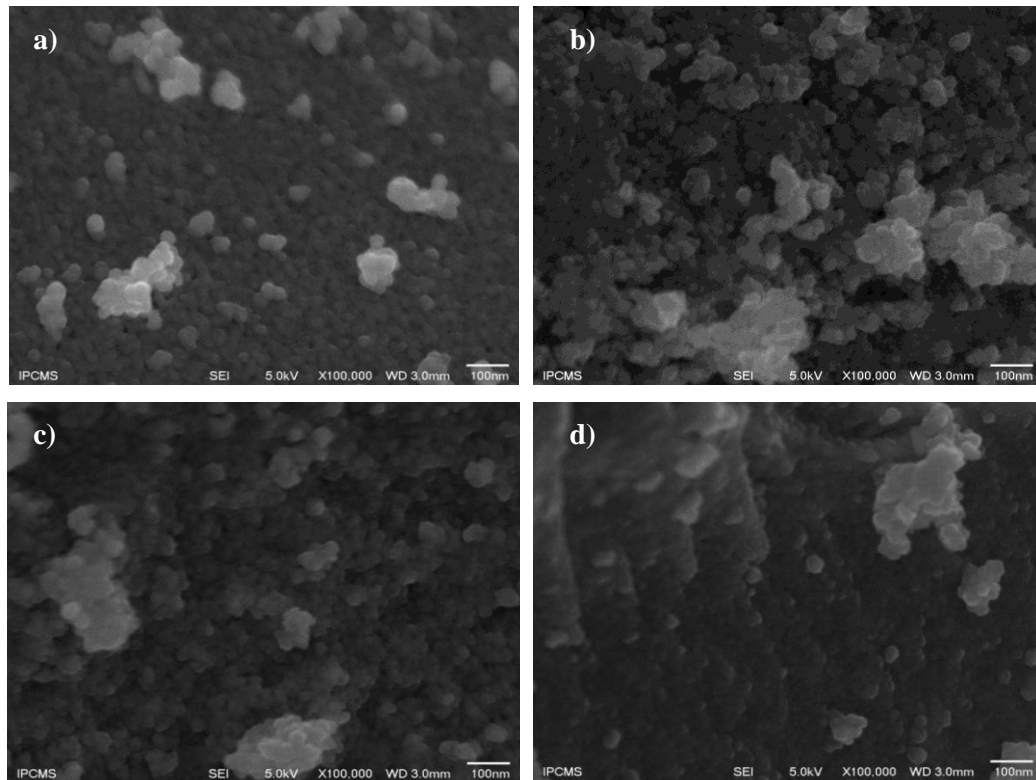
Figure 3.7. SEM images of (a) SnO$_2$, (b) SnO$_2$:Nd 1%, (c) SnO$_2$:Nd 3% and (d) SnO$_2$:Nd 5 %
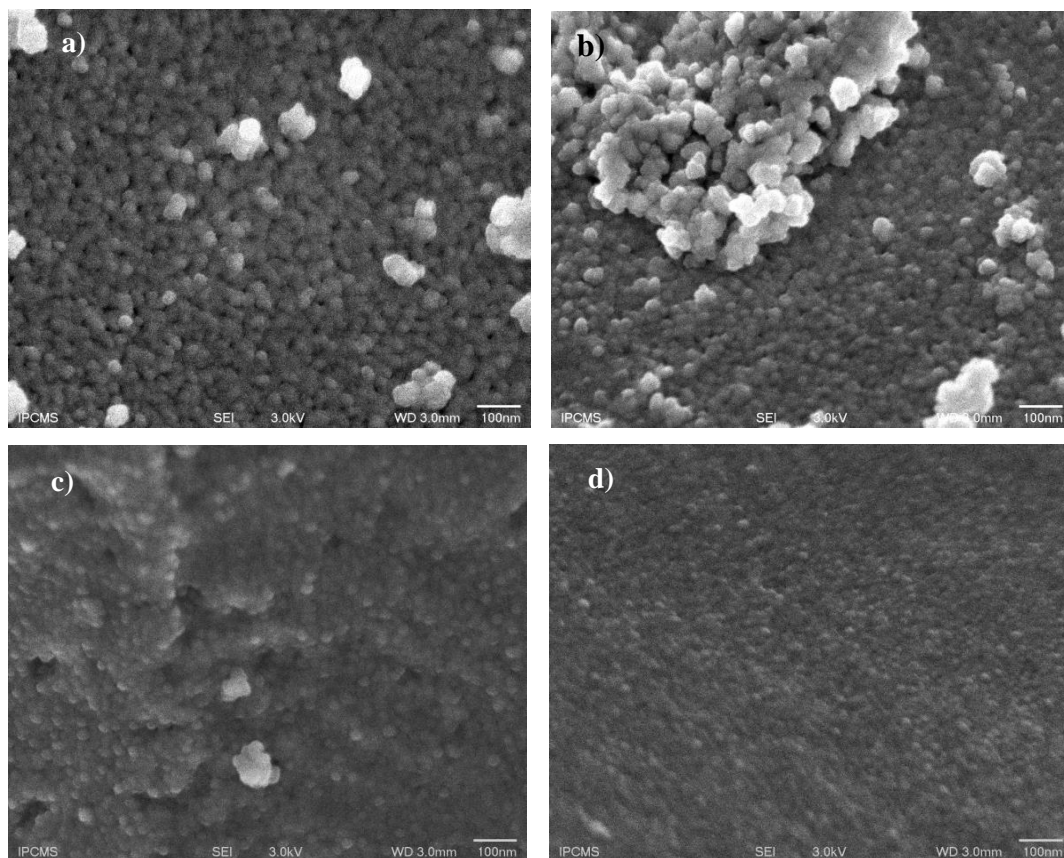
Figure 3. 8. SEM images of (a) SnO$_2$:Yb 1%, (b) SnO$_2$:Yb 2%, (c) SnO$_2$:Yb 4% and (d) SnO$_2$:Yb 6 %.

Data extracted from EDS analysis performed on the different Nd and Yb doped SnO_2 powders are summarized in table 2.1. The measured Nd concentrations are in line with the nominal values. Surprisingly, this is not the case for the Yb doped powders; a considerable difference between the nominal and measured Yb content values can be noticed.

Table .2.1. Nd and Yb measured concentrations as extracted from EDS analysis.

Sample	Nd %	Sample	Yb %	Sample	Yb %
SnO₂:Nd 1%	1.09 % ± 0.43	**SnO₂:Yb 1%**	0.69 % ± 0.24	**SnO₂:Yb 4%**	2.46 % ± 0.69
SnO₂:Nd 3%	2.45 % ± 0.41	**SnO₂:Yb 2%**	1.23 % ± 0.32	**SnO₂:Yb 5%**	3.51 % ± 0.33
SnO₂:Nd 5%	3.43 % ± 0.38	**SnO₂:Yb 3%**	2.07 % ± 0.17	**SnO₂:Yb 6%**	4.12 % ± 0.63

Moreover, the analysis in the COMPO mode did not reveal any presence of Nd (resp. Yb) oxides aggregates or other impurities, giving a first indication of the insertion of all tested Nd (resp. Yb) contents into the SnO_2 matrix. In the following sections, the samples will be labelled as follow: SnO_2: Nd x with x=1, 3 and 5% and for SnO_2:Yb x, x will value 0.69, 1.23, 2.46 and 3.51 %

3.3.2.2 TEM observations

To get a more precise estimate of the particles size and to have a deeper insight on the effect of Nd & Yb doping on the structural as well as the morphological properties of the powders at the nanoscale scale, TEM analysis have been performed on selected powders. Figure 3.9 compares the undoped and SnO_2:Nd 3% using different scales.
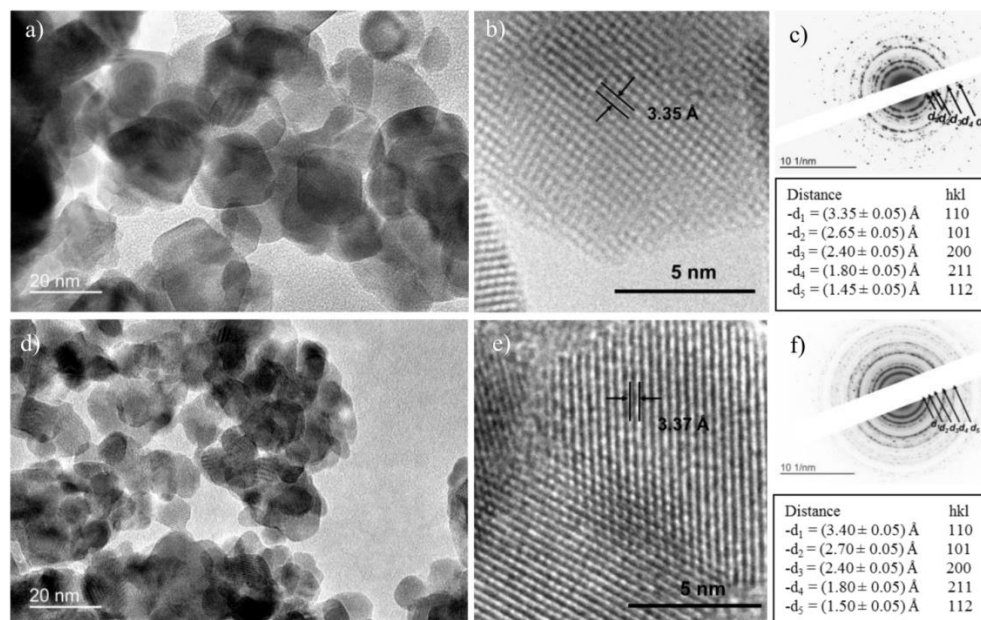
Figure 3. 9. TEM, HRTEM images and SAED patterns of undoped (a, b and c) and 3% Nd doped SnO2 (d, e and f) powders respectively.

The bright field images shown in Figure 3.9a and 9d shows that the powders are composed of agglomerated nanometric particles with round shape, and revealed a particles size decrease when

doping with Nd. Indeed, the nanoparticles size was found to range between 14-24 nm with an average value of about 20 nm for the undoped powder while for the 3at.% Nd-doped one, the mean size is of about 9 ± 2 nm. The data for all Nd-doped samples are reported in Table 2.2. High-resolution images were recorded for further investigations of powders crystallinity and the results are shown in figures 2b and 2e for the undoped SnO_2 and SnO_2: Nd 3at.%, respectively.

Table.2.2 Mean size, standard deviation and Min-Max values of the Nd and Yb doped SnO_2 nanoparticles.

	Doping	**Mean size**	**Standard deviation**	**Min**	**Max**
Undoped	0%	19.64	2.75	14.58	24.76
Nd	1%	16.53	2.09	11.84	22.98
	3%	9.08	1.30	6.10	11.87
	5%	6.23	0.90	4.07	9.38
Yb	1 %	12.43	2.63	5.65	22.15
	4%	7.18	3.30	2.69	20.59
	5%	6.61	1.70	3.19	12.13

As it can be clearly seen from the HRTEM images, the particles look well crystallized, thus, the atomic planes can be unambiguously defined. Moreover, the lattice parameter 'a' can be deduced from the (110) inter-plane distance and is estimated to be 3.35 ± 0.05 Å and 3.37 ± 0.05 Å for the undoped and SnO_2: Nd 3at.%,, respectively. This increase in the lattice parameter suggests an increase of the unit cell volume for the doped powder, which can be considered as a second proof of Nd insertion in the host matrix. Moreover, SAED patterns shown in figures 2.10.c to f assess the polycrystalline nature of the nanoparticles as proven by the numerous circular diffraction rings. These latter are well indexed in the tetragonal rutile phase. The tables below each SAED pattern give the d_{hkl} of the most intense orientations. In overall, the diffraction rings are more continuous for the doped samples (fig. 2d), suggesting better statistic (and therefore smaller crystallites) relative to the undoped SnO_2.

Similar observations have been noticed for the Yb doped powders as shown in Figure 3.10; the powder consists of round shaped particles with a nanometric size. The nanoparticles become progressively smaller and smaller by increasing the Yb doping concentration. However, the Yb doped nanoparticles exhibit relatively smaller sizes when compared to the case of doping with Nd, which supports the SEM observations. This is expected since the ionic radius of Yb is smaller than that of Nd. Therefore it is likely that the doping with Yb will result in smaller particles. Such behaviour was also observed with the powders synthesized by the co-precipitation method. For more statistics, TEM images taken at different scales were used to extract valuable information on the particles size distribution. Figures 2.11 and 2.12 give the size distribution for the different doped sol-gel powders. The results highlight the decrease of the nanoparticles size arising from Nd and Yb doping. It is interesting to notice that at high nominal doping level (5 at.% of Nd and Yb) the particles size

distribution is quite similar indicating that Nd and Yb induce the same effect once inserted into the matrix at a high dose. EDS analysis were also performed on the synthesized powders and satisfactory found to fit with the measured concentrations with SEM-EDS, indicating the homogeneity of the rare earth distribution within the powders.
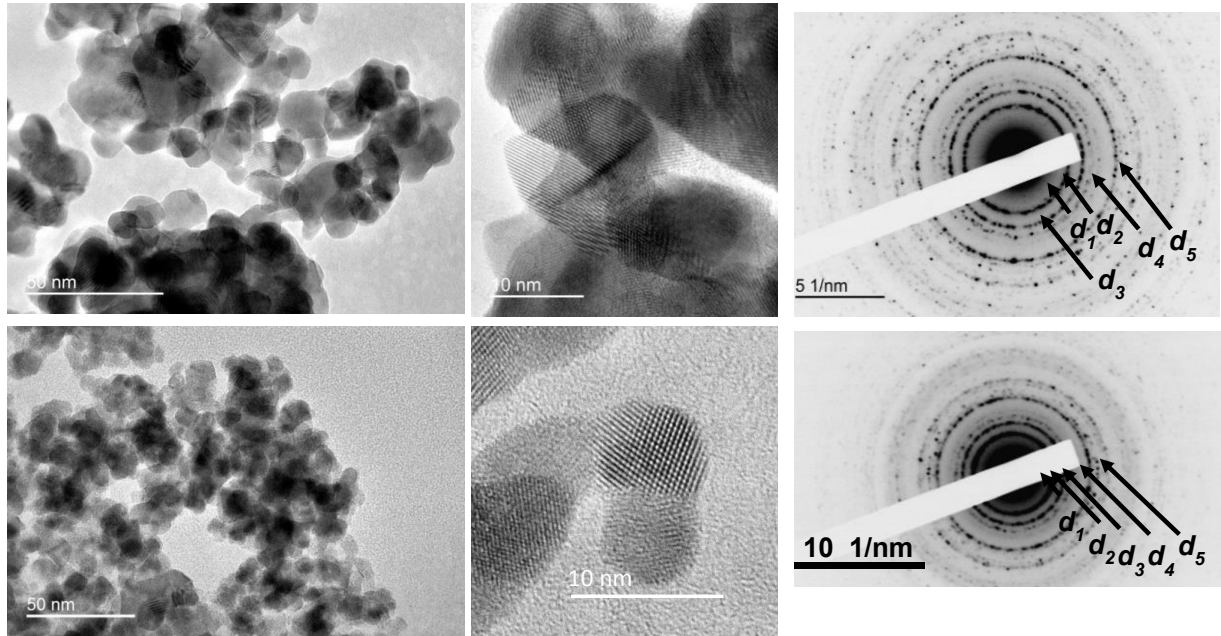
Figure 3. 10. TEM (a-d), HRTEM (b-e) images and SAED patterns (c-f) of 1 and 5 at. % of Yb doped SnO₂ powders respectively
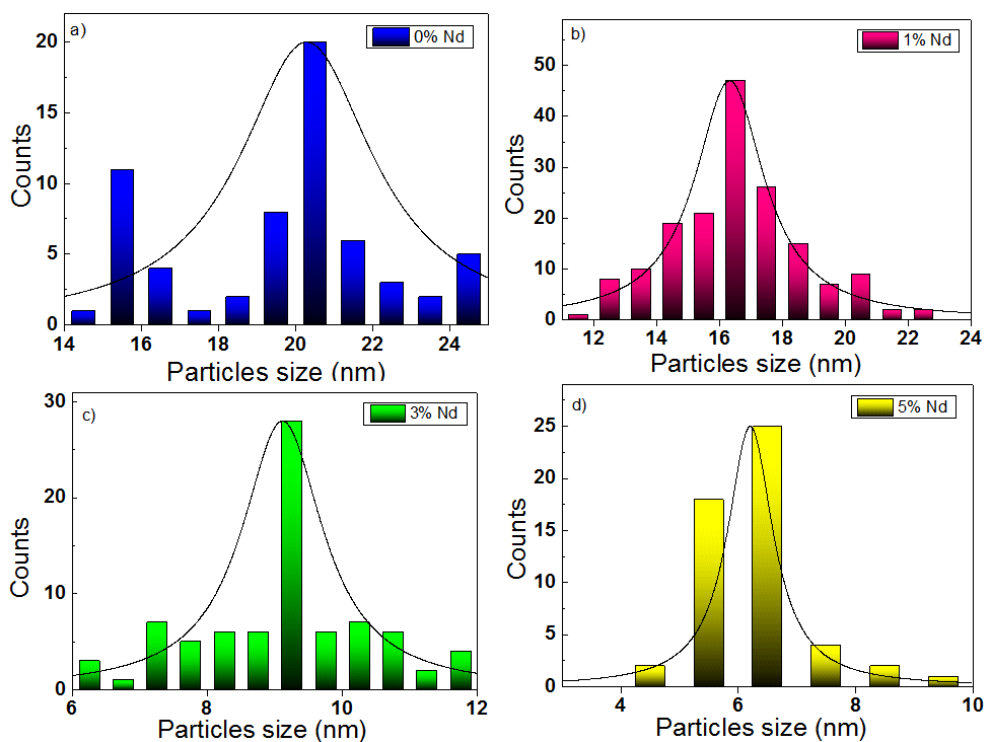
Figure 3.11. Nanoparticles size distribution of the Nd-doped SnO₂ powders with x= 1, 3 and 5% of Nd
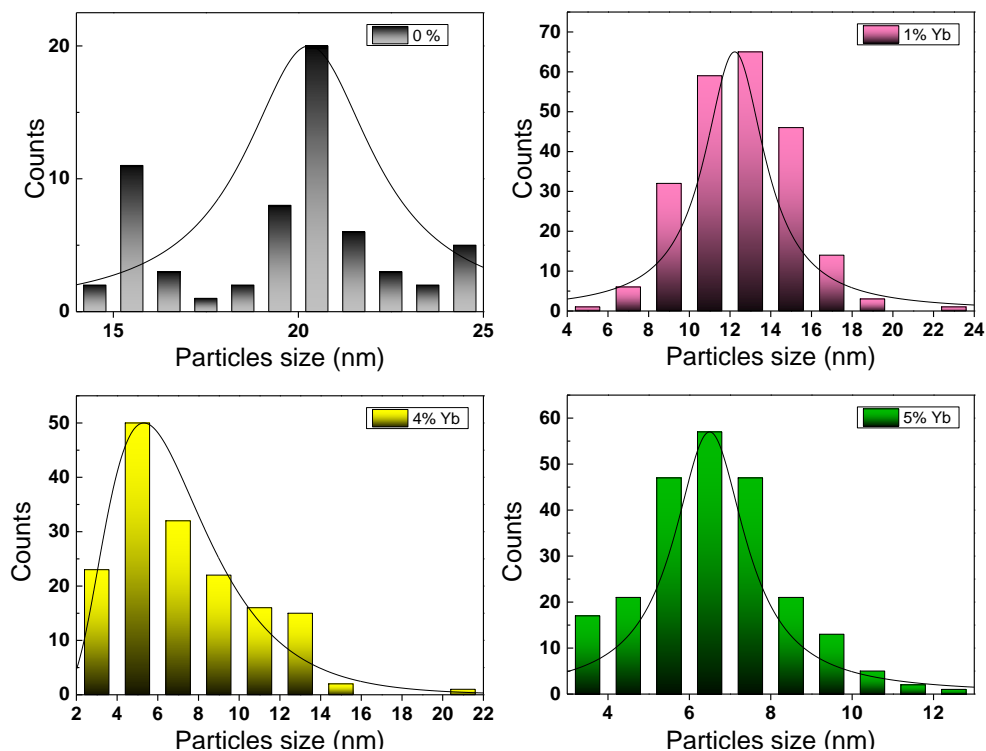
Figure 3.12. Nanoparticles size distribution of the Nd-doped SnO$_2$ powders with x= 1, 3 and 5% of Yb.

3.3.2.3 XRD analysis

In the section above, the structural analyses of the synthesized powders were performed at a very small range and have therefore a local character. To complement, structural properties of the powders have been also investigated at a larger scale using the X-ray diffraction (XRD) technique. Figure 3.13.a shows the X-ray diffraction patterns for SnO$_2$:Nd samples with Nd concentrations of 0, 1, 3, and 5% . All diffraction peaks can be assigned to the tetragonal rutile phase of SnO$_2$ (reference card JCPDS 00-041-1445 of ICDD). It can be noted that the Nd doping does not affect the tetragonal structure of SnO$_2$ whatever the Nd concentration (in the limit of the studied contents). No secondary phases such as SnO nor Nd$_2$O$_3$ were detected within the limit of the XRD technique. This is in agreement with SEM and TEM observations which showed a homogeneous distribution of Nd within the samples. By increasing the Nd content, a slight peak shift towards lower angles is observed, which suggest an increase of the lattice parameters due to tensile stress on the lattice. This behaviour is mainly due to the rare earth element incorporation and less to the presence of defects. On the other hand, the full-width at half maximum (FWHM) of SnO$_2$:Nd x% peaks gradually increases when the Nd content increases, indicating a decrease of the average crystallites size. This is in accordance with the TEM results reported above. The average crystallites size of the SnO$_2$:Nd powders is usually determined using the Scherrer formula:[252] $D = 0.9\,\lambda/\beta\cos(\theta)$ where λ is the X-ray wavelength, β is the FWHM of the (h k l) peaks and θ is the Bragg angle. Only (110), (101) and (211) peaks were used in the calculations.

Figure 3.13.b confirms that the calculated average crystallites size decreases continuously as a function of the Nd concentration. The average crystallites size is found about 16 nm for the undoped SnO$_2$ and decreased down to 5 nm for the 5% Nd doped SnO$_2$ powder. The unit cell volume plotted in Figure 3.13.b was calculated using both the relation: $d = 1/\sqrt{(h^2 + kh^2)/a^2 + l^2/c^2}$ and the Bragg law. We found that the unit cell volume is proportional to the Nd content witnessing the rare earth insertion into the structure. In fact, the insertion of impurities can occur in two ways, in the ideal case, the rare earth will prefer either substitute tin atoms in the host matrix or to occupy the interstitial sites. Since the ionic radius of the Nd^{3+} (0.11 nm) is larger than the ionic radius of Sn^{4+} (0.069 nm), incorporating Nd^{3+} ions into the matrix leads most likely to some distortion and stress in the elementary cell and the crystal lattice. As a consequence, the grains might break which causes a decrease in the crystallites size with respect to the Nd addition.

Concerning the case of the Yb-doped SnO$_2$ powders, the recorded diffraction patterns are plotted in Figure 3.13.c for powders with Yb concentration of 0.69, 1.23, 2.46 and 3.51 at.% .The Yb doping also seems to cause some stress in the lattice without modifying the crystalline nature of the powders. Indeed, all Yb-doped powders were identified as being polycrystalline with tetragonal rutile structure. The intensities of the diffraction peaks were found to decrease with the doping up to 2.46 at.% giving a first indication of the RE insertion. At 3.51 at.% the intensity increases; this could be explained by the density of the powder used for the measurement. Figure 3.13.e) shows the peak position of the (110) plane (the most intense direction referring to the JCPDS card of SnO$_2$) for all investigated Yb concentrations. According to each Yb content value, a shift towards lower or higher diffraction angles is observed, relative to the pure SnO$_2$. No tendency as a function of Yb doping was evidenced. In fact there is a competition between the RE insertion, which lead to a shift toward lower angles, and the structural defects characterized usually by a shit to higher diffraction angles.
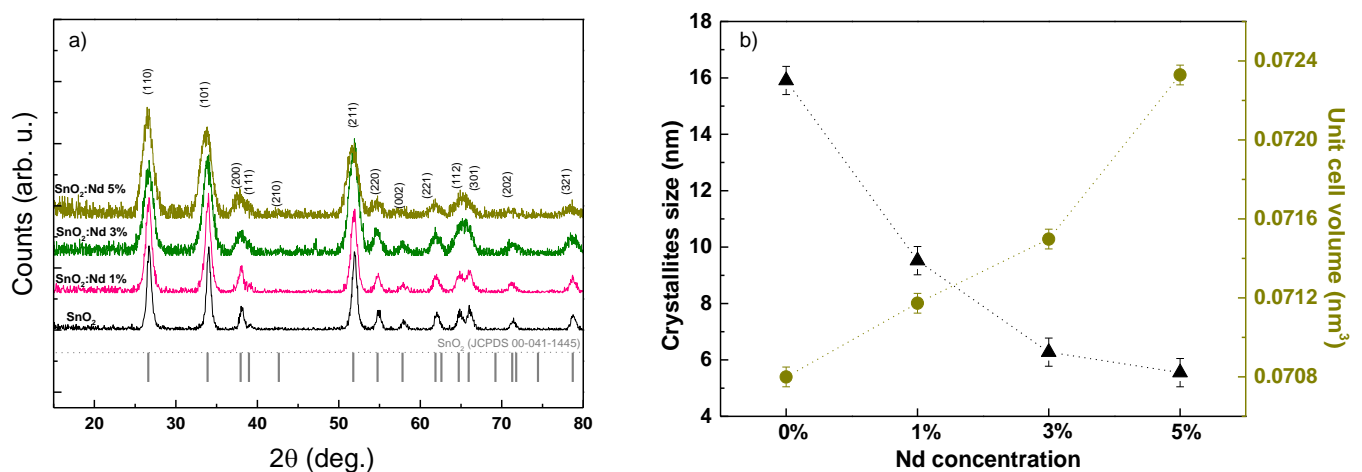
Figure 3.13.a) X-ray diffraction patterns of Nd-doped SnO$_2$ powders with Nd concentration (0, 1, 3 and 5 %). Vertical bars correspond to SnO$_2$ JCPDS card n° 00-041-1445. **b)** Dependence of the crystallites size of SnO$_2$:Nd powders and the unit cell volume as a function of Nd-doping.
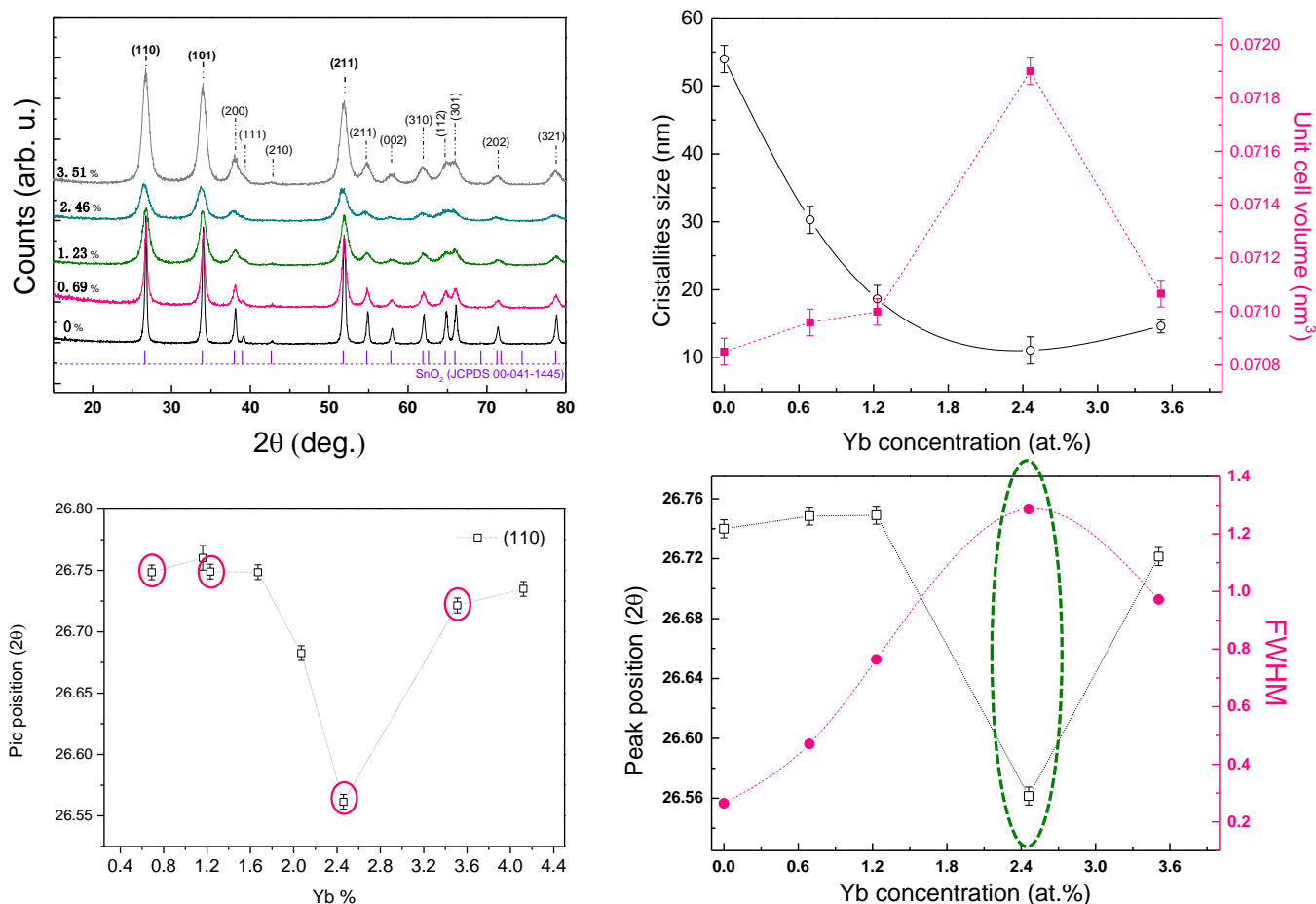
Figure 3.13.c) X-ray diffraction patterns of Yb-doped SnO_2 powders with Yb concentration (0, 0.69, 1.23 and 2.46 and 3.51.at %). correspond to SnO_2 JCPDS card n° 00-041-1445, **d)** Dependence of the crystallites size of SnO_2:Yb powders and the unit cell volume on the Yb-doping, **e)** (110) peak position shift as a function of Yb content and selected samples for the study, **f)** FWHM of the (110)diffraction peak.

The crystallites sizes calculated for the Yb doped samples as well as the unit cell volume are displayed in Figure 3.13.d. As noticed with the Nd-doped powders, the crystallites size of the Yb-doped powders are also found to decrease gradually when increasing the Yb content in the powders, giving a second indication of Yb insertion into the structure. The unit cell volume shows an increase as a function of Yb%. Surprisingly, the unit cell volume reached the highest value of about 0.0719 nm^3 for the SnO_2:Yb 2.46 at.% sample, meaning that all incorporated Yb atoms are well inserted into the SnO_2 structure. However, these values remain relatively smaller compared to Nd-doped powders data; this is expected and quite coherent since it is well known that the Yb^{3+} ionic radius is smaller than that of the Nd^{3+}. At 3.6 at.% of Yb- doping, the mean crystallizt size decreases back but still relatively larger than that of the undoped one, suggesting that a part of Yb ions is located at the grains boundaries sites without affecting the unit cell.

Additional information on the site insertion can be obtained by analysing the cell' parameters. If we assume that the Yb atoms -which have an ionic radius of about 0.086 nm- substitute Sn atoms (ionic radius of 0.071 nm) in the SnO_2 lattice, one would expect a decrease of the cell parameter as Yb^{3+} possess an ionic radius larger than that of Sn^{4+}. On the other hand, if Yb atoms prefer to occupy interstitial sites, the cell parameters should either remains more or less the same or the unit cell volume should increase.

The unit cell parameters of undoped and Yb doped SnO_2 powders are given in table 2.3. Compared to the undoped SnO_2, the Yb doped powders exhibit different values. The parameter 'a' is found to increase gradually by increasing the Yb content. The highest value being obtained with doping at 2.46 at.%. The same remark is underlined with the parameter 'c' which shows larger value also with the 2.46 at.% doped sample, suggesting that the cell at this condition is blended with Yb atoms. The cell parameters show an increase whatever the Yb doping level is, which strongly indicates that the RE is most likely inserted into interstitial sites rather than in substitutional ones. Even if there are some Yb atoms substituting Sn atoms, it is very difficult to distinguish them since there is a competition between the two types of insertion. However, it cannot be ruled out that some Yb atoms are filling some oxygen vacancies or tin vacancies or defects sites.

Table 2.3 the unit cell parameters (a and b) for undoped and Yb doped SnO₂ powders with different Yb at.%

Parameters	Pure SnO₂	0.69 at.%	1.23 at.%	2.46 at.%	3.51 at.%
a	0.47206	0.47321	0.47209	0.47491	0.47248
c	0.31792	0.3181	0.31807	0.31879	0.31834

To sum up, one could consider that for doping at 0.69 at.%, Yb ions are mostly located in interstitial sites (increase of 'a' and 'c'). At doping with 1.23 at.%, the parameter 'a' is comparable to the undoped while 'c' slightly increases, suggesting that Yb is located in both sites. The case of doping at 2.46 at.% is already discussed. Finally for the case of the 3.6 at.% doped sample, we speculate that Yb is in interstitial sites since the cell parameters are weakly affected.

3.3.2.4 Raman analysis

To further investigate the crystalline structure and follow structural changes induced by Nd and Yb doping in sol-gel made SnO_2, Raman spectroscopy measurements were performed and the results are displayed in Figure 3.14. The Raman spectra of the undoped powders confirm the tetragonal rutile phase. The three fundamental vibrational modes characteristics of the rutile structure A_{1g}, E_g and B_{2g} can be distinguished at 632.8, 474 and 775 cm^{-1}, respectively. The definition of each vibrational mode was defined above in the introduction section. The Eu TO and LO vibrational modes are also detected as well as the B_u modes which is characteristics of structural defects, such as oxygen vacancies (V_O)

among others.By doping with Nd, the intensity of all features dramatically decreases indicating that the addition of Nd in the host matrix induces major changes in the structure. The decrease of the oxygen vacancies-related features, particularly with doping at 5at.% suggests that some of Nd atoms fill in the oxygen related defects sites.

In a stark contrast, the Yb doped SnO_2 powders seem to behave differently. When there is no remarkable decrease of the features signal, a continuous blue shift of the main peak position (A_{1g}) is noticed as a function of the Yb content. This translates the strength in the lattice caused by the Yb atoms. The decrease of the Raman shift can be explained by the tensile stress due to the Yb insertion, which is in line with the unit cell volume calculated in the XRD part and showed increasing values. Moreover, an increase of the oxygen vacancies features (B_u) as well as the Eu peaks is noticed for sample 2.46 Yb.% indicating that the density of V_O is much more important in this structure. This can be explained by the fact that when inserting Yb into the structure, Yb^{3+} ions will be bounded to oxygen atoms, which will likely generates V_O. Moreover, the full width at half maximum (FWHM) of the A1g peaks is found to increase by increasing Nd doping indicating poorer crystalline structure.
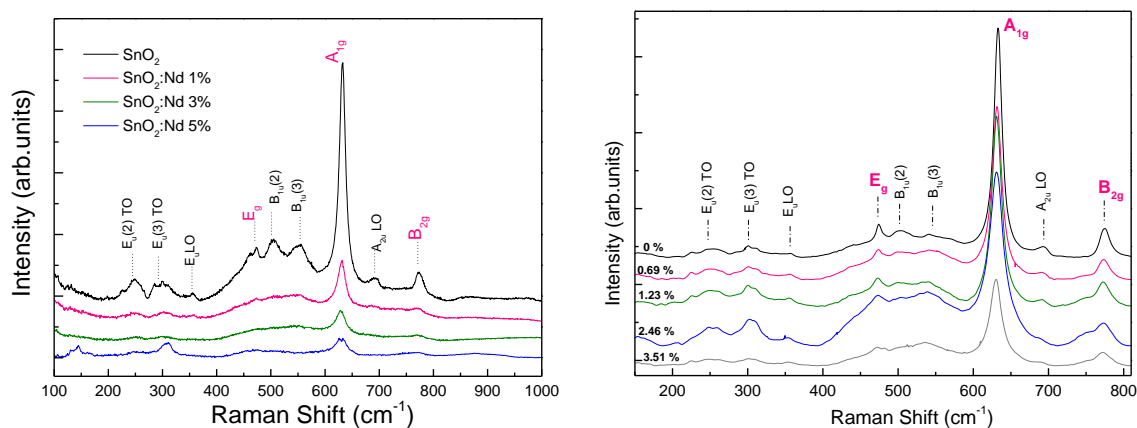
Figure. 2.14 Raman spectra of a) SnO_2: Nd powders with different Nd concentrations (0, 1, 3 and 5%), b) SnO_2: Yb powders with different Yb concentrations (0.69, 1.23, 2.46 and 3.51 at.%)

To resume this part, Raman data confirm that Nd and Yb are well inserted into the SnO_2 structure. Although the insertion of RE leads to some stress on the lattice, and therefore on the crystalline quality of the nanoparticles, the tetragonal rutile phase is preserved, within the limits of the investigated concentrations.

3.3.3 Optical properties

In the sections above, we demonstrated that Nd and Yb atoms are successfully inserted into the SnO_2 host matrix produced by the sol-gel method, similarly to the case of using the precipitation technique. In the following, we will discuss the effect of Nd or Yb doping on the optical properties of the synthesized SnO_2 powders.

Figure 3.15.a plots the UV-visible-NIR absorption spectra of the undoped and Nd doped SnO₂ powders recorded in the 250-1000 nm range. The undoped powder exhibits a strong absorption in the UV-blue ranges of the spectrum with a slope extending over 200 nm. The spectra show a strong absorption in the 250-550 nm wavelength range and an absorption threshold from 480 to 550 nm due the large exciton binding energy. These observations are in good agreement with those reported by Bouaine et al.[199] and are expected for SnO₂.
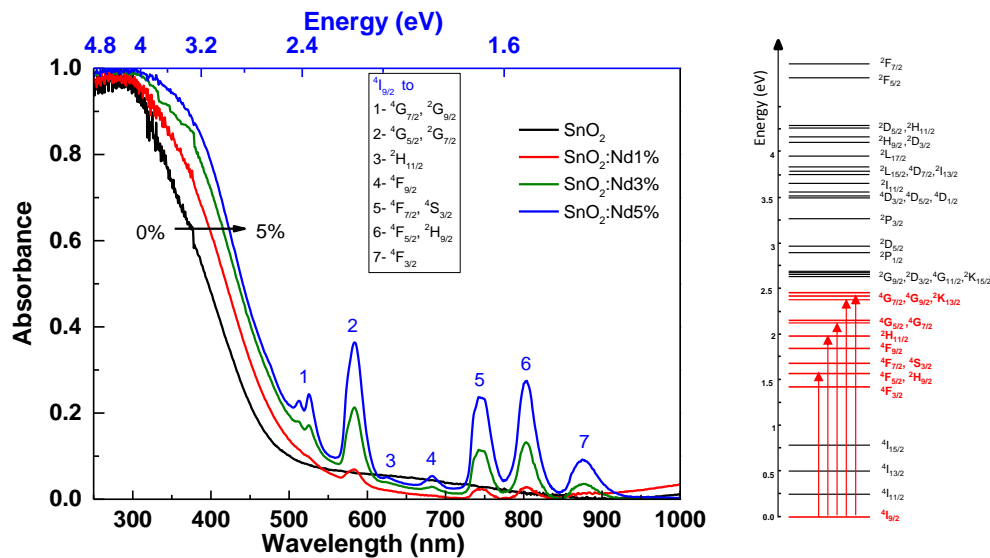
Figure 3.15 *a)* Absorbance spectra of Nd-doped SnO₂ powders versus Nd content, b) excitation mechanisms in the Nd³⁺ energy levels.

While no other features are observed for the undoped SnO₂ sample, the Nd-doped powders spectra exhibit additional absorption bands centred at 513, 524, 583, 680, 744, 802 and 872 nm with variable intensities. These observations will help understanding the excitation mechanisms of the Nd³⁺ ions reported in the following PL section. All these bands are found to match with direct excitation of electrons from the $^4I_{9/2}$ ground state to upper excited states when referring to the electronic level configuration of Nd³⁺ in LaCl₃: Nd crystals [146, 151, 184]. The correspondence of each absorption peak is presented in Figure 3.15.b. The intensity of all peaks is found to increase by increasing the Nd content in the structure suggesting that all incorporated atoms are optically active. Such result is particularly important for applications in solar cells for which SnO₂ can be used as a transparent conducting oxide (TCO). Moreover, Figure 3.15.a reveals a significant shift of the absorption edge towards lower energies as a function of the Nd content. Once again, we have avoided the extraction of the band gap of our materials from these curves since the graph is self-speaking. Some authors consider an indirect transition,[253] while many others suggest a direct transition across the gap [246, 254, 255]. The determination of the Eg is not our main interest of this study but it is worth mentioning this. In all cases, the data suggest a clear decrease in the band gap with Nd addition, which is in favour of Nd insertion into the SnO₂ matrix.

As for Yb doping, the absorption edge of the material was found to shift toward lower energies when increasing the doping level til 2.46 at.%, then it turns back to higher energies (Figure 3.16). Such result might indicate a solubility limit of the rare earth; beyond this concentration level, RE atoms can be inserted into defects sites in the structure such as grains boundaries. Figure 3.16.a shows additional absorption features in the IR region, which are linked to absorption by Yb atoms. A closer look on the Yb absorption is shown in Figure 3.16.b. It appears that the Yb absorption consists of a wide band ranging from 870 to 1040 nm and an intense and symmetric peak centred around 977 nm. The intensity of the last increases by increasing the Yb doping level up to 2.46 at .% and it decreases for higher doping level, meaning that less Yb atoms are optically actives.
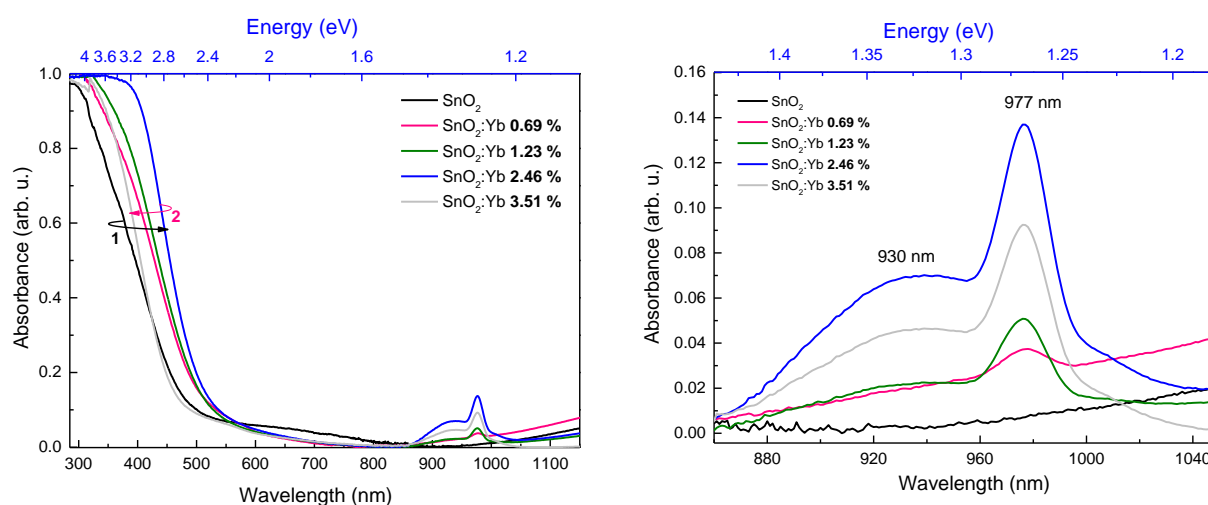
Figure 3.16 *a)* Absorbance spectra of Yb-doped SnO₂ powders versus Yb content, b) Zoom on the absorption region of Yb in SnO₂.

3.3.3 Luminescence properties of the RE doped SnO₂ sol-gel powders

3.3.3.1 Photoluminescence of Nd doped powders

The data above showed that the Nd and Yb doping induces noticeable structural and optical changes in the SnO₂ matrix and as a consequence it is expected to affect the luminescence properties of the doped powders. Figure 3.17 shows the UV-Vis-NIR emission spectra of pure SnO₂ and doped SnO₂:Nd 5% powders recorded under a 325 nm (3.81 eV) laser excitation. These spectra cover a large part of the spectral range useful for applications such as solar cells.

As noticed for the pure powder prepared by the co-precipitation method, the powder synthesised by the sol gel method also exhibits a very strong luminescence band centred at 600 nm, and a much less intense one in the 400-450 nm region. No band-to-band emission at 344 nm (band gap around 3.6 eV) was recorded in the detection limit of our PL setup. It is important to remind the origin of the strong PL coming from the matrix; this will be helping interpreting the PL results of the doped powders.

The large and intense band around 600 nm arises from deep levels within the SnO_2 band gap created by the oxygen vacancies[196] which are present at a high density in such oxide based powder. In fact, oxygen vacancies are one of the dominant defects that form donor levels, which usually play an important role in the PL process [245-247]. Another important source of the luminescence centers in the SnO_2 material can be the presence of tin interstitial atoms resulting either from the preparation technique in the case of pure SnO_2, or from the substitution process occuring in the case of the doped powders. Moreover, it cannot be excluded that the large amount of grains boundaries in the powder led to efficient recombining luminescent centers. Similar observations in quantum nanoparticles systems have been reported in the literature.[247-249]

As for the band situated around 400-480 nm, it consists of two distinct features at 414 and 440 nm whose the origin is already reported by Gu et al.[245] in the case of SnO_2 thin films by sol-gel dip coating method . The peak at 414 nm can be assigned to the electron transitions from the donor levels created by oxygen vacancies to the valence band,[204] while the peak at 440 nm can be ascribed to the luminescent centres of the inter-grains defects.[250]

Figure 3.17 displays also the PL spectrum of the most highly Nd doped sample, namely SnO_2: Nd 5at.%. The two peaks in the UV region are again present and exhibit comparable PL intensities than for the undoped SnO_2 sample. In contrast, the band in the visible region is almost 10 times weaker than that recorded for pure SnO_2. This result indicates that the presence of Nd induces fundamental changes in the defects type and density, and consequently influences the radiative recombination processes. This also could mean that the non-radiative recombinations (such as point defects, dislocations, surface/interface states, and grain boundary states) are increased with the presence of Nd^{3+} ions. Another possibility supported by the XRD analysis is that considerable amount of Nd atoms substitutes Sn atoms in the host matrix. This observation does not exclude the presence of Nd atoms in interstitials sites, which can compensate defects related to the oxygen vacancies.
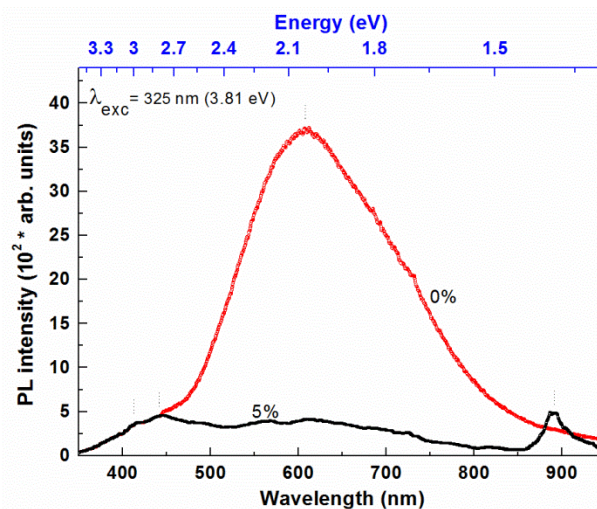
Figure 3.17 Room temperature emission spectra of undoped and 5% Nd doped SnO_2 powders under He-Cd laser excitation wavelength of 325 nm

It can be noticed from Figure 3.17 that the strong decrease of PL band in the visible range is accompanied by an emission line centred at 885 nm and usually attributed to the $^4F_{3/2} => \, ^4I_{13/2}$ transitions of Nd^{3+}. A second, less intense band appears around 820 nm. This strong optical activity of Nd^{3+} ions is a good indication of the Nd insertion into the SnO_2 matrix. In fact, the insertion of Nd atoms in the SnO_2 matrix induced simultaneously strong effect on the defects responsible on the PL in the visible region, as well as a light emission in the NIR region (radiative recombination process). At a first glance, this behaviour can suggests an energy transfer from the SnO_2 band to Nd^{3+}. Similar conclusions were drawn for Nd doped ZnO nanocrystals[181] and Nd doped SnO_2 thin films.[225]

To highlight the role of Nd in a possible transfer process, we have recorded the photoluminescence for all synthesized Nd doped SnO_2 powders. The emission spectra of the powders containing different Nd concentrations (1, 3, and 5%) are shown in Figure 3.18.
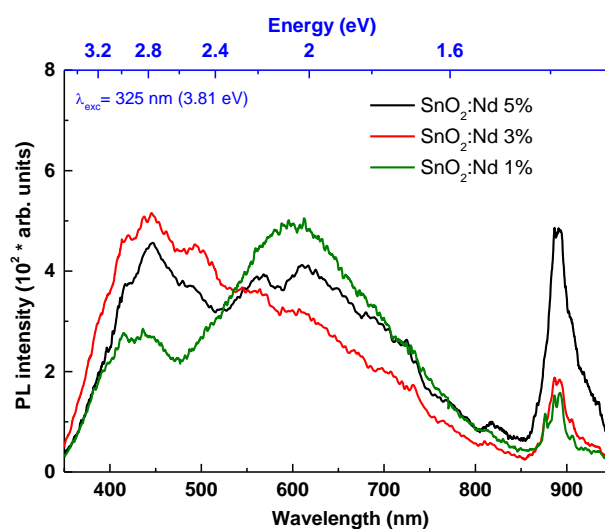
Figure 3.18 Room temperature UV-to-NIR emission spectra of Nd doped SnO_2 powders with different Nd %

It is interesting to note that, while the shape of the two defect emission bands does not present major changes, the intensity of the emission bands is very sensitive to the Nd content in the SnO_2 powder. This is especially the case for the NIR emission (at 885 nm) for which the intensity is found to increase when increasing the Nd concentration thanks to more Nd elements in the powder.

Since Nd^{3+} is expected to emit in the NIR region, additional PL measurements have been performed to have a closer look to the Nd emission using a better resolved and longer wavelength range detector. The PL recorded between 850-1200 nm under a He-Cd laser excitation is reported in Figure 3.19. Three emission groups can be observed. The first peaks are those reported in Figure 3.17, centred at 885 nm, while two more groups appear at 1065 and 1336 nm. These peaks are commonly assigned to the $^4F_{3/2} => \, ^4I_{n/2}$ transitions, with n equal to 13, 11 and 9, respectively[225]. The intensity of these emission groups enhances with Nd addition. No quenching effect was observed meaning that most of the Nd atoms are incorporated into the SnO_2 structure. To explain the PL lines and discuss the

possibility of an energy transfer in our Nd doped systems, we draw in Figure 3.20 the energy levels diagram of SnO_2 and Nd^{3+} ions, in order to clarify the possible transitions.
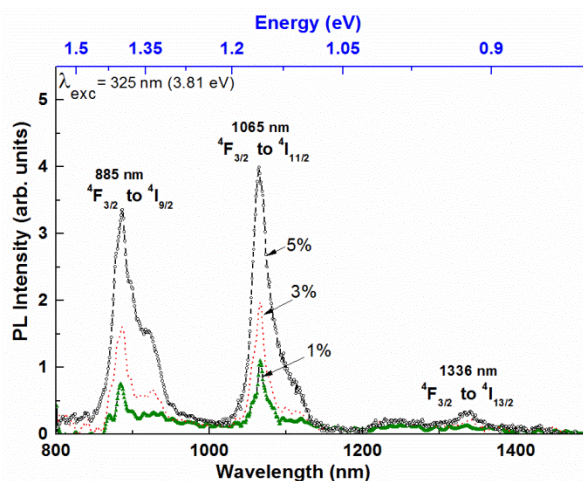
Figure.2.19 Room temperature IR emission spectra of Nd doped SnO_2 powders with different Nd content.

Since the excitation wavelength for the PL measurements was set at 325 nm (3.8 eV, superior to the band gap of our doped powders), the excitation of the Nd^{3+} ions can possibly occur via indirect mechanisms. As a first process, (i) we can consider that the band to band transition of the host SnO_2 transfers all the energy (3.6 eV) to the $4f$ electrons of Nd^{3+}. Another possible energy transfer process is that occurring via transitions throughout the electron trapped states within the band gap (ii), (iii) and (iv). These two possible mechanisms represent the resonant energy transfer process in the ideal case. These processes are schematically drawn in Figure 3.20.
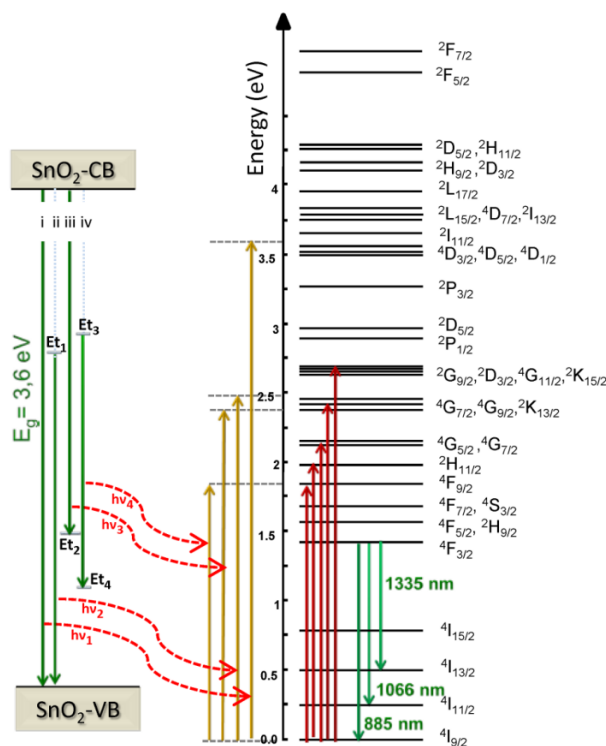
Figure.20 Energy levels diagram of the Nd^{3+} ions observed in $LaCl_3$[146, 151], and the process of potential energy transfer from SnO_2 to Nd^{3+}.

Concerning the process involving the traps, it can be speculated that photons emitted between 500 and 800 nm (process involving traps in SnO_2) can be appropriate to excite the Nd^{3+} ions from the ground state $^4I_{9/2}$ to the $^4G_{5/2}$, $^2F_{7/2}$ excited states. As a matter of fact, we have shown in Figure 3.15 that the SnO_2 powders absorb light in the visible region, particularly at around 600 nm, which corresponds also to the main emission region of SnO_2. The de-excitation of the Nd^{3+} ions to the ground state can result in the appearance of three NIR bands reported above. In other words, the absorption band of SnO_2 in the visible region provides sensitizing band to excite the 4f electrons of the Nd^{3+} ions, which will then relaxes by emitting NIR photons.

3.3.3.2 Photoluminescence of Yb doped powders

Concerning the Yb-doped powders, Figure 3.21a compares the room temperature PL of pure and the 0.69 at.% Yb doped SnO_2 powders under Nd-YAG laser excitation of 355 nm. The same behaviour as that reported for the Nd-doped powders is observed. A dramatic decrease of the defects' band centred at around 650 nm with the appearance of two narrow and intense peaks in the NIR is noticed. Surprisingly, a weak peak at 375 nm comes into view. This peak could be most likely attributed to the band-to-band transitions known as the excitonic peak. In term of energy, the band gap of the bulk SnO_2 is around 3.6 eV; this value can vary versus the structure (thin films, nanocrystals, nano…) and the preparation technique. The presence of such feature at an energy of 3.31ev might represent the band gap value of our material. While the intense features at 972, 1005 and 1019 nm are attributed to the Yb emission, thanks to transition from the $^2F_{5/2}$ excited state to the $^2F_{7/2}$ ground state.
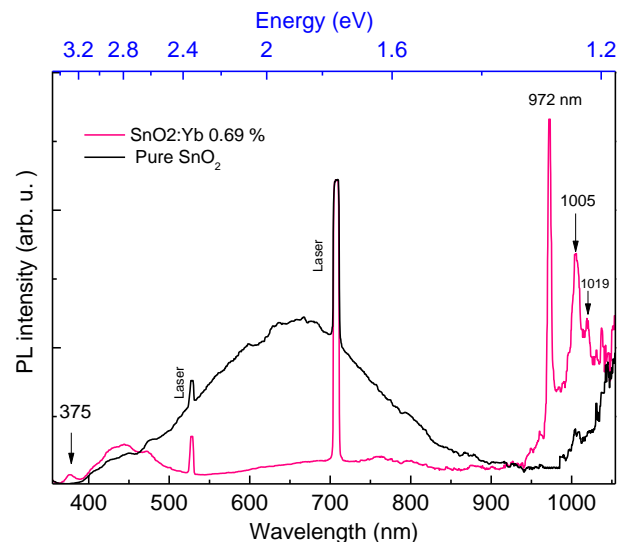
Figure 3.21 Room temperature emission spectra of undoped and 5% Yb doped SnO_2 powders under Nd-YAG laser excitation of 355 nm

Considering the energy levels structures of lanthanides drawn in Dieke's diagram, it can easily be seen that Yb^{3+} possesses a single excited state ($^2F_{5/2}$) approximately at 1.32 eV above the ground state ($^2F_{7/2}$)[146]. Our powders exhibit three narrow emissions at 1.27, 1.23 and 1.21 eV. The existence of more than a single emission band could be explained in terms of the crystal field splitting of the two electronic levels of Yb^{3+}.

We have found that the bands peak positions of Yb are blue shifted when compared to the Yb emission in the Yb-doped ZnO thin films reported by Balestrieri et al[256] . Indeed, these authors have shown the presence of a strong peak at 980 nm (1.26 eV) and a less intense broad band centred around 1030 nm (1.20 eV). One more effect of the crystal field linked to the SnO_2 host matrix is that in place of the broad band, our samples exhibit two well-resolved peaks indicating that the energy levels of Yb^{3+} degenerate differently when embedded in the SnO_2 matrix.

In order to get an insight on the energy levels of the Yb^{3+} in the SnO_2 structure, a closer look on the Yb photon emission under a Xenon excitation ray at 300 nm is displayed in Figure 3.22. It appears that this emission consists of more than four features. The de-convolution of this emission will allow building the electronic levels structure (energy levels diagram) of Yb. About eight Gaussian components were necessary for the de-convolution process to fit the experimental spectrum.

Considering the $(2J+1)/2$[5] Stark splitting of the $^{2S+1}L_J$ energy levels, the $^2F_{5/2}$ can be degenerated into three sublevels that we name as A, B and C; similarly, the $^2F_{7/2}$ levels can be degenerated to four sublevels that we label A', B', C' and D'. The position of each sublevel depends strongly on the crystal field of the host matrix. Figure 3.22 shows three peaks that take place at higher energies, namely at 1.27 eV, 1.29 eV and 1.31 eV and 5 other features at lower energies. This means that the highest energy emitted is originated from transitions occurring between the highest energy level of $^2F_{5/2}$ (A) and the lowest energy ground state $^2F_{7/2}$ E=0 labelled as D', so we can say that the energy level A is located at 1.31 eV from the ground state. According to this hypothesis, the two transitions at 1.27 and 1.29 eV define somehow the position of the B and C sublevels of the $^2F_{5/2}$ multiplet. Now, considering the energies of the three levels of the $^2F_{5/2}$ multiplet, it should be possible to localize the energy positions of the A', B' and C' of the $^2F_{7/2}$ multiplet. After mathematical calculations, we found that the A', B' and C' sublevels are situated at about 0.11, 0.06 and 0.04 eV above the D' (E=0 eV) level. The feature n°= 9 in Figure 3.22 is too wide and weak and do not correspond to any transition in the energy levels of Yb, so it is therefore ascribed to some noise in this part of the spectrum coming from the CCD camera. Table 2.4 summarizes the energy positions and the corresponding optical transitions.

---

[5] J : the total angular momentum
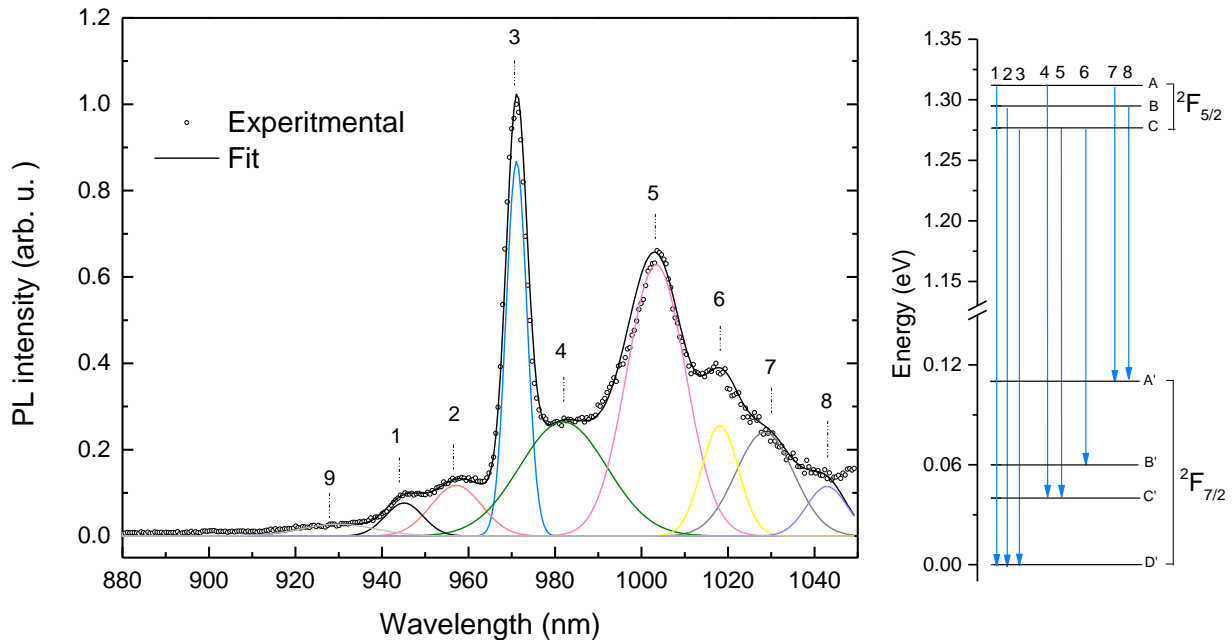
Figure 3.22 a) Gaussian de-convolution of the Room temperature Yb emission spectra recorded under Xenon lamp excitation wavelength of 300 nm, **b)** identification of the electronic transitions recorded in the PL spectra as well as the positions of the $(2J+1)/2$ Stark components of the $^2F_{5/2}$ and $^2F_{7/2}$ multiplet of Yb^{3+} in SnO_2 structure.

Surprisingly, the energy levels positions of the $^2F_{7/2}$ sublevels fits very well with calculated and experimental values of Yb^{3+} in a cubic sesquioxyde host material. Also, the energy values found for the three $^2F_{5/2}$ multiplet do not differ too much from that reported by Fidancev et al. for $Yb:Y_2O_3$ [257]. This means that the local environment of Yb in SnO_2 structure (rutile) is quite similar. In Yb- YAG Lasers the energy levels positions of Yb are found to be around 1.28, 1.31 and 1.32 eV [151].

Table 2.4 Nature of transitions exhibiting the PL of Yb in the NIR region

Peak	Position (nm)	Energy (eV)	Transitions			
1	945.15	1.31	$^2F_{5/2}$	A (1.31 eV)	→	$^2F_{7/2}$ D' (0 eV)
2	957.48	1.29	$^2F_{5/2}$	B (1.29 eV)	→	$^2F_{7/2}$ D' (0 eV)
3	971.34	1.27	$^2F_{5/2}$	C (1.27 eV)	→	$^2F_{7/2}$ D' (0 eV)
4	982.02	1.26	$^2F_{5/2}$	A (1.31 eV)	→	$^2F_{7/2}$ C' (0.04 eV)
5	1003.2	1.23	$^2F_{5/2}$	C (1.27 eV)	→	$^2F_{7/2}$ C' (0.04 eV)
6	1018.45	1.21	$^2F_{5/2}$	C (1.27 eV)	→	$^2F_{7/2}$ B' (0.06 eV)
7	1028.7	1.20	$^2F_{5/2}$	A (1.31 eV)	→	$^2F_{7/2}$ A' (0.11 eV)
8	1043	1.18	$^2F_{5/2}$	B (1.29 eV)	→	$^2F_{7/2}$ A' (0.11 eV)

To study more deeply the energy transfer mechanism in the Yb doped powders by sol-gel, it is important to distinguish between absorption and emission mechanisms.

Figure 3.23.a compares the absorption and the emission spectra of the 1% Yb doped SnO₂ powders. The intensity of the spectra was normalized from 0 to 1. It is clear that the Yb atoms embedded in the powder absorbs strongly photons of wavelengths ranging from 850 to 1050 nm (energies from 1.18 to 1.45 eV); on the other hand the emission consisting in narrow bands (peaked at 945 and 957 nm) is starting at wavelengths above 940 nm. Despite the broad and intense absorption band between 850-960 nm, only two weak emission peaks are collected at 945 and 957 nm.
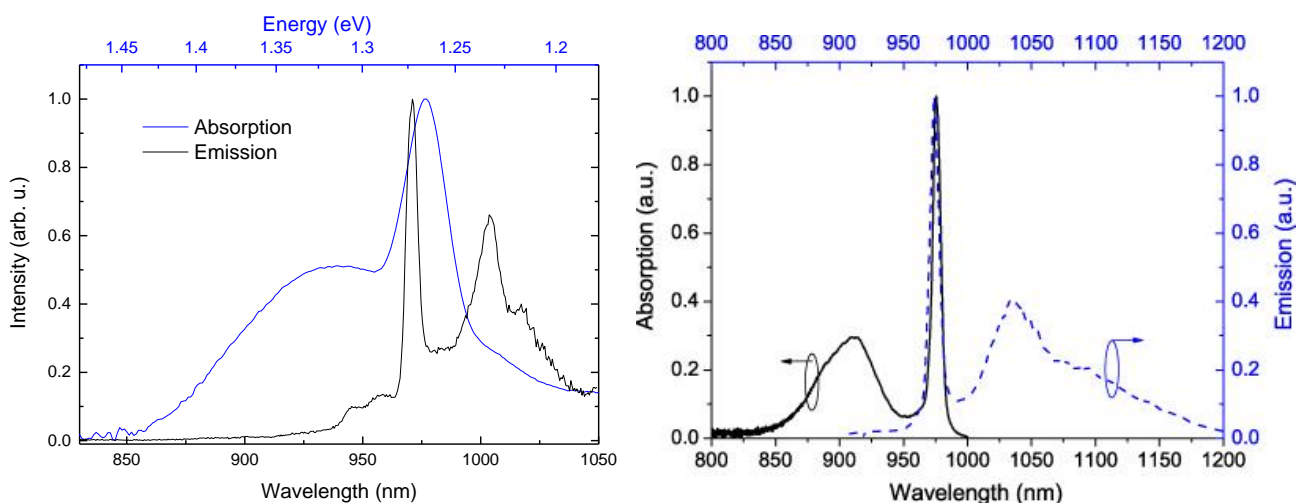
Figure 3.23. The absorption and emission spectra of the 1% Yb-doped SnO₂ powder, b) Yb^{3+} related absorption and emission spectra of pure silica sol-gel-based Ytterbium fiber (from ref [258]).

The presence of the intense and broad emission band at higher energies indicates the presence of high energy levels above 3.31 eV that can be reached3. by the excited electrons. This does not contradict with what we announced just before about the energy levels of Yb but reveals complementary information about the density of states of the electronic levels of Yb. Different mechanisms can be involved for the interpretation of this result. Considering the Franck-condon principle[6], each electronic level has a stack of vibrational levels associated with it. Depending on the shape of the potential energy curve, there may be a large series of vibrational energy levels (deep minimum), very few vibrational levels (shallow minimum), or no vibrational levels (no minimum). In this is case there are no selection rules for vibronic transitions, so every vibronic state can be final/initial state. The probability transition between these vibronic states is dictated by the wave function overlap at the initial and final states (combined electronic and vibrational

---

[6] This principle states that when an electronic transition takes place, the time scale of this transition is so fast compared to nucleus motion that we can consider the nucleus to be static, and the vibrational transition from one vibrational state to another state is more likely to happen if these states have a large overlap. Also, it successfully explains the reason why certain peaks in a spectrum are strong while others are weak (or even not observed) in absorption spectroscopy.

wave functions). The maximum transition probability occurs when two vibrational states are connected through vertical transitions.

In our case, we speculate that the broad absorption band is most likely originated from the vibronic coupling[7]. A simplified schema illustrating vibronic transitions as well as the origin a broad absorption band is presented in Figure 3.24
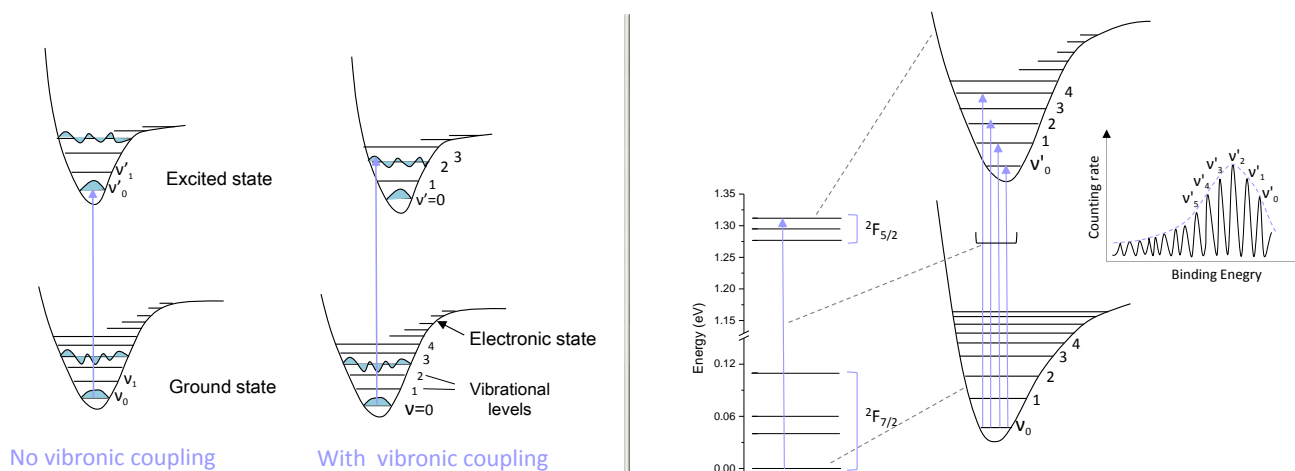
Figure 3.24 a) pure electronic transition and the electronic transition couples with the vibrational transition. b) Diagrammatic illustration of absorption lines of the Yb^{3+} ions.

The intensity of the vibronic transitions is proportional to the square of the overlap integral between the vibrational wave functions of the two states involved in the transition. In fact, after electronic excitation, nuclei remain in vibrational excitation. The larger the change in molecular conformation, more pronounced becomes the intensity of vibronic peaks which can explain the strong intensity of the broad peak centred at 977 nm.

When superimposing the emission together with the absorption spectrum (Figure 3.22.a), a blue shift between the intensity maxima of the absorption and emission is noticed. This is starkly different with earlier reports on Yb-doped silica materials, for which, the maximum of the Ytterbium absorption superimpose perfectly with that of its emission. Such behaviour is commonly known as the anti-Stokes shift, for which the absorption occurs from a vibrational state of the ground electronic level to a higher excited state, then, the excited electrons decay to the zero-phonon level of the electronic ground state via photon emission. A diagram illustrating this phenomenon is presented in Figure 3.25

---

[7] The word "vibronic" is the combination of the words "vibrational" and "electronic." Because the energy required for one electronic state to another electronic state (electronic transition, usually in the UV-Vis region) is larger than one vibrational state to another vibrational state (vibrational transition, usually in the IR region), sometimes energy (a photon) can excite a molecule to an excited electronic and vibrational state
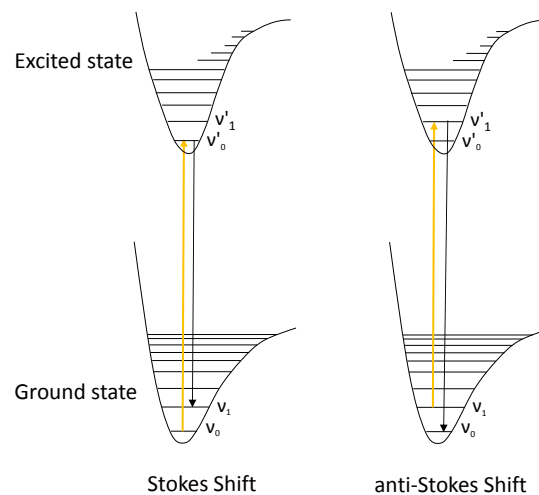
Figure 3.25. Schematic representation of Stokes and anti-Stokes shifts.

In addition to the anti-stokes shift, the Yb emission peak around 971 nm is much narrower than the absorption peak. We speculate that this narrow peak most likely originates from zero-phonon transitions. Such result is very original and belongs only to the effect of the SnO_2 crystal field effect.

The effect of the Yb doping concentration on the photoluminescence properties was also investigated. Figure 3.26 reports the room temperature PL spectra of the Yb-doped SnO_2 powders under Nd-YAG laser excitation wavelength of 355 nm.
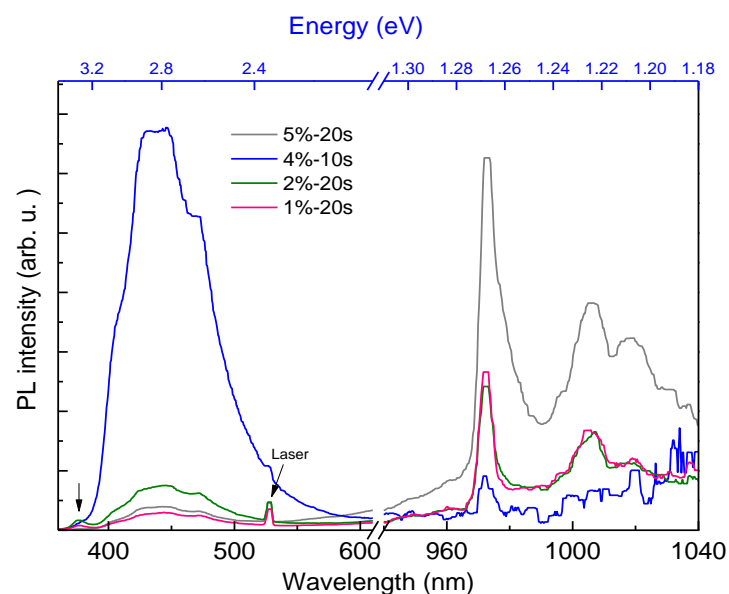
Figure.2.26. Room temperature UV-to-NIR emission of the Yb-doped SnO_2 powders for different Yb content. The excitation was provided by mean of a YAG laser (excitation wavelength of 355 nm)

A decrease of the defects-related band at 650 and the appearance of the Yb emission in the NIR region is noticed for all powders, including the 1 at.% Yb doped powder reported above. In particular, the PL

intensity of the Yb signal is found to increase by increasing the Yb content, except for the 4 at.% doped powder which exhibit a poor Yb signal and a very strong emission in the visible (380-600 nm). The dramatic decrease of the defects-band at 650nm indicates that the presence of Yb induces important changes in the density and type of defects. The explanation given in the case of the Nd-doping could be also valid for the Yb case: the Yb atoms are compensating the defects' sites in the lattice and the excitons relax via non-radiative paths. Finally, it is possible that the visible photons are involved in an efficient energy transfer from the SnO_2 host matrix to the rare earth ions, as discussed in the following section.

Besides, the presence of the Yb emission clearly proves the optical activity of the Yb ions incorporated within the SnO_2 matrix. However, the decrease of the Yb emission for the case of the 4 at.% doped powder does not mean that less Yb atoms are not optically active but might suggest that Yb atoms cannot efficiently emit under 355 nm excitation otherwise a decrease of the absorption band should be noticed.

It is important to note that at this experimental condition the PL intensity arising from structural defects in SnO_2 is too strong compared to the other powders which confirm our assumption: the energy which is not transferred to Yb (weak signal) is emitted as visible photons. The second hypothesis can be supported by the non-radiative transitions in the Yb. Since the structural analysis has shown a largest unit cell volume for this powder, we think that the structure is blended by Yb ions. This means that the interatomic distance between the Yb ions is too small, and it is likely possible that the transferred electron jumps from an ion to another until it losses its energy (quenshing effect).

3.3.3.3 Photoluminescence Excitation (PLE) experiments

Figure 3.27 plots the PLE spectrum of the SnO_2:Nd 3% powder recorded by monitoring the near-infrared (NIR) $^4F_{3/2}$ ➔ $^4I_{11/2}$ emission at 1066 nm in the 450-700 nm range. The PLE was performed at room temperature using an optical parametric oscillator (OPO) laser. The average laser power was around 30 mW.

The PLE spectrum exhibits numerous Nd^{3+} excitation lines centred at 470, 530, 585 and 611, 628 and 685 nm which correspond to the direct excitation of electrons from the ground state $^4I_{9/2}$ of Nd^{3+} to the upper excited states $^2G_{9/2}$, $^4G_{11/2}$ and $^4G_{9/2}$, $^4G_{7/2}$ and $^4G_{5/2}$, $^2G_{7/2}$, and $^2H_{11/2}$ and $^4F_{9/2}$ respectively (see Fig. 10). It is interesting to notice the increase of the background of the spectrum when the excitation is increased towards lower wavelengths (represented by the dashed line in Fig. 2.27).

The fact that the increase of background occurs in a region where the SnO_2 matrix absorbs can indicate that some energy transfer might occur through one of the mechanisms described in Fig. 10.

The absorbance of SnO₂: Nd 3% sample is also reported in Figure 3.27 for complementary information. The overlap between the absorption of the SnO₂ matrix and the different energy levels of Nd³⁺ ions is favourable for the energy transfer process. However, it is difficult to quantify the real efficiency of such a process. Further studies are needed to estimate the energy transfer efficiency.
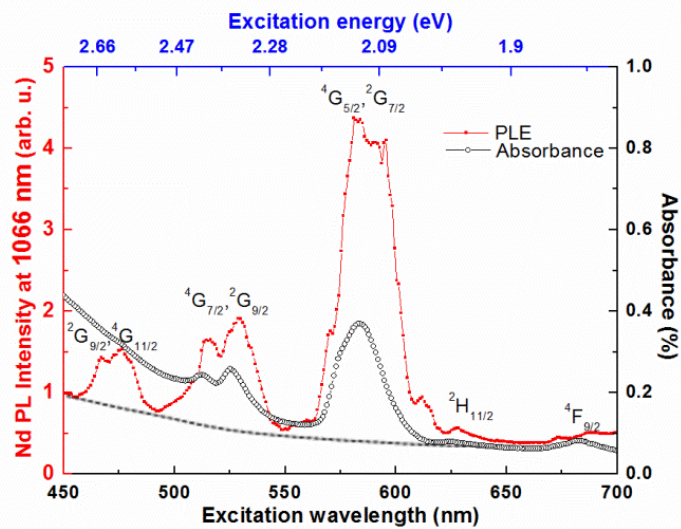
Figure 3.27. PLE spectrum at 1066 nm for the 3% Nd doped SnO₂ powder

Concerning the Yb doping case, a complete excitation spectrum is presented in Figure 3.28. The excitation was performed by means of a Xenon lamp. The PL intensity of Yb recorded at 971 nm is carefully followed when varying the excitation wavelength from 250 to 625 nm.
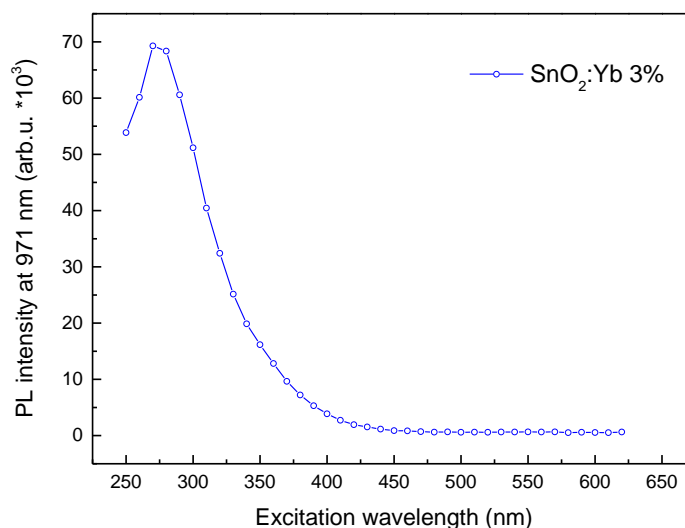
Figure 3.28. PLE spectrum of the 2 at.% Yb doped SnO₂ powder. The detection is fixed at 971 nm while the excitation wavelength is varied from 250 to 625 nm.

As it can be clearly seen from the above spectrum, efficient photoluminescence of Yb is obtained when exciting in the deep UV. The maximum of PL is recorded under excitation of 275 nm (4.5 eV). It is important to remind that Yb possesses only one excited state with an energy around 1.3 eV. Consequently, the PLE spectrum indicates that Yb can be indirectly excited using the UV light. Moreover, it appears that the shape and range of Yb excitation spectrum fits very well with the absorption spectrum of the SnO_2 host matrix, meaning that when the SnO_2 absorbs the UV light, Yb emit NIR photons. Such mechanism is denoted "down-shifting", therewith an efficient energy transfer occurs from the SnO_2 to the Yb^{3+} ions.

Different transfer mechanisms can be proposed as shown in Figure 3.29. The excited electrons in the conduction band of SnO_2 can relax to lower energy states and therefore excite a 4f electron of the Yb. A second process can be identified as electronic transfer, in case where Yb atoms are very close to the excited atoms, and therefore the electrons will jump directly to an excited state of Yb, thanks to the crystal field effect of the matrix which is responsible of states mixing from different parities. Furthermore, the probability of the presence of electrons traps within the band gap cannot be excluded. In such case, resonant transitions after electron relaxation could result in a 4f electron excitation in the Yb structure. The different possibilities of radiative transitions through the Yb enegy levels were already discussed above.
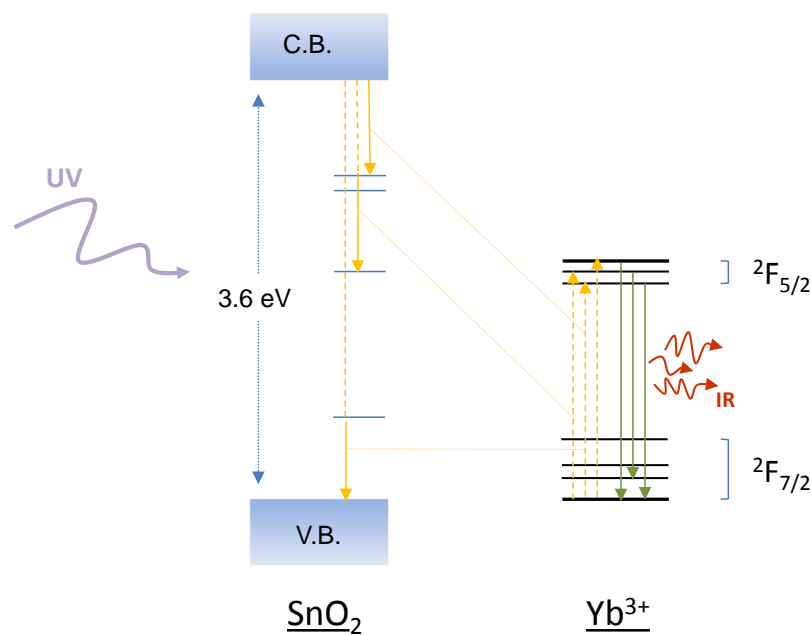
Figure 3.29. Possible energy transfer mechanisms occurring between SnO2 and Yb^{3+} ions

3.3.4 Summary

Undoped SnO_2, Nd-doped and Yb-doped SnO_2 (Nd: SnO_2 and Yb:SnO_2) powders were synthesized by the sol-gel method and annealed at 700°C. SEM observations indicate a high agglomeration factor at a

Macroscopic level, and a uniform distribution of the particles size. TEM images showed that the particles size is decreasing with increasing RE content. The Yb-doped nanoparticles have shown smaller values than that doped with Nd. The crystallinity, structure and crystallites size for the powders were determined by XRD and SAED measurements. A tetragonal crystalline phase is demonstrated for all samples. A slight diffraction angle shift to lower angles is observed with increasing RE content, indicating effective RE incorporation. The insertion of RE atoms in the host matrix as well as the crystallinity of the grains in the powder were also confirmed by Raman spectroscopy analysis. Doping with Yb in contrast to Nd, have shown a solubility limit of 2.4 at.%, beyond which larger cell parameters have been reported.

On the other hand, the effect of the RE doping on the matrix absorption have been investigated. More incorporated Nd atoms is found to decrease the band gap while for Yb a solubility limit was noticed at 2.4 at.% ; above this concentration the absorption edge shifts to higher energies indicating an increase of the band gap. More interestingly, we demonstrated Nd and Yb related absorption bands in the visible and NIR regions, respectively.

Finally, PL and PLE spectroscopies have shown the optical activity of both rare earths in SnO₂. Intense and well-defined Nd peaks have been recorded at 885, 1060 and 1334 nm; these peaks are found to increase linearly with the Nd content. Yb ions in the other hand have shown wide emission band from 850 to 1050 nm. De-convolution of the Yb-PL spectra resulted in more than 7 components. Such analysis allowed us building the energy levels of the SnO₂:Yb structure with exact positions of the $^2F_{5/2}$ and $^2F_{7/2}$ multiplets as well as identifying the transition of each band. The Yb PL is found to be independent on the insertion site. Finally, an energy transfer from the SnO₂ to Yb has been experimentally demonstrated using the PLE spectroscopy. The same conclusion has been drawn for doping with Nd.

3.4. (Nd, Yb) co-doped SnO₂ powder by the sol-gel method

3.4.1. Synthesis

(Nd, Yb) co-doped SnO₂ powders by the sol gel technique have been synthesized using the same procedure described above for Nd or Yb doped SnO₂ powders.. Nd and Yb acetate hydrate have been added to SnO₂ solution with different masses to obtain different doping levels. For this study we have chose to set the Yb content at 2 % and vary Nd amount to 0, 2, 4 and 6 %. The aim of this study is to investigate whether SnO₂ allows incorporation of both RE elements with strong optical activity. Moreover, we would like to check if, in an addition to possible energy transfer from the matrix to the RE element, there is a possible energy transfer between the RE ions, namely here from Nd to Yb. If

The photoluminescence of one of them is beneficial to solar cells, the PL of both is of a potential interest, especially when being incorporated in a TCO host.

In the following the powders will be labelled as a function of their nominal doping: SnO_2:Yb2 %, Nd x%, with x= 0, 2, 4 and 6.

3.4.2. Morphology

The SEM images of the different co-doped powders in the SEI mode are shown in figure 3.4.1 As in the case of the powders reported in the section 2.2, the (Nd, Yb) co-doped powders also consist of nano-aggregates with round-shaped grains with homogenous and regular distribution. The co-doping at this stage did not affect the physical aspect of the powders. Analysis by the EDS spectroscopy did not reveal any presence of impurities in the material.
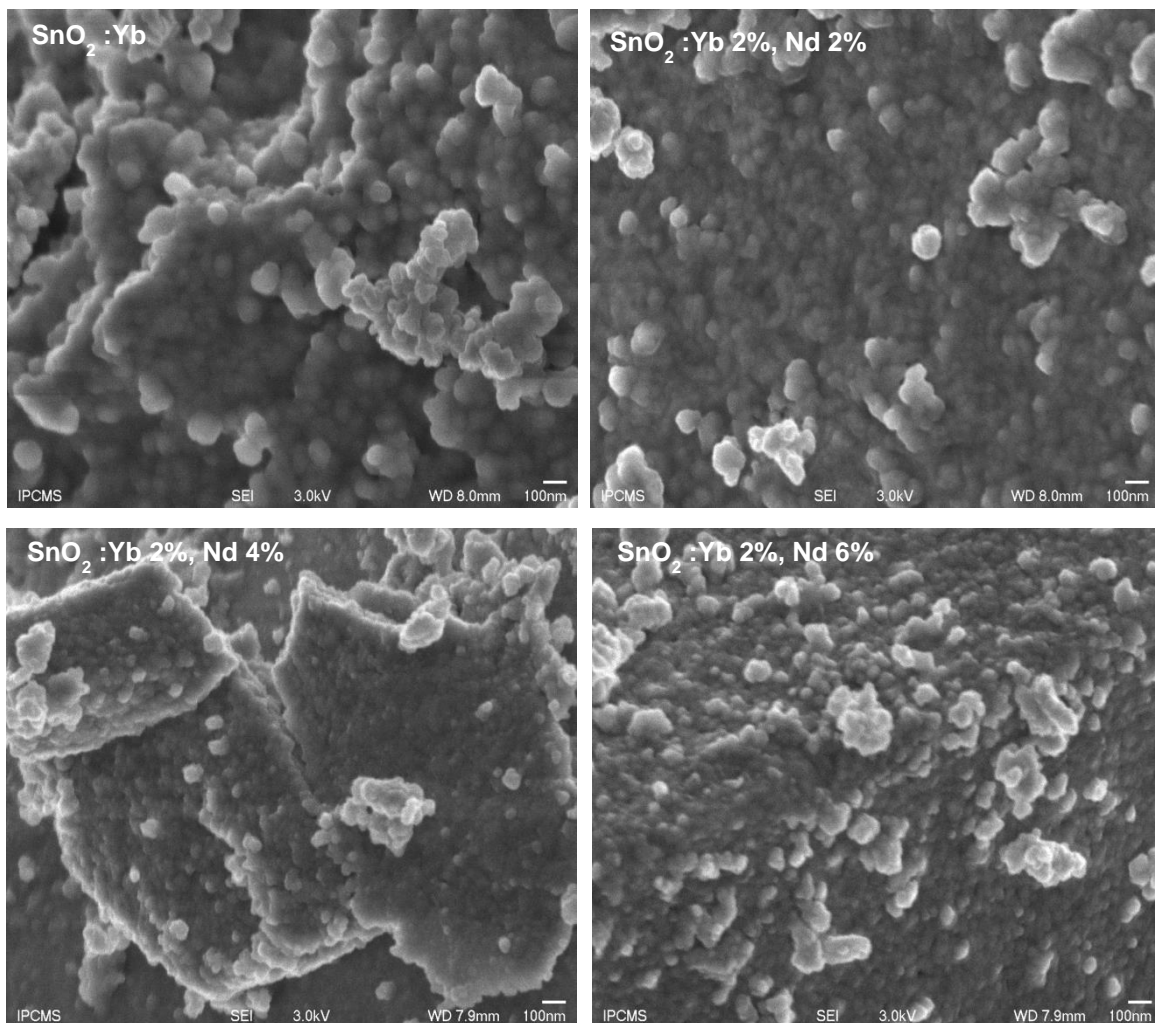
Figure 3.4.1. SEM images of (a) SnO_2:Yb 2%, (b) SnO_2: Yb 2%, Nd 2%, (c) SnO_2: Yb 2%, Nd 4% and (d) SnO_2: Yb 2%, Nd 6 %

3.4.3. TEM observations

Nanoscale anamysis of the (Nd, Yb) co-doped grains is performed by the TEM and HRTEM microscopy techniques. Figure 3.4.2 displays the TEM, HRTEM images and SAED patterns of the co-doped powders as a function of the Nd-doping.
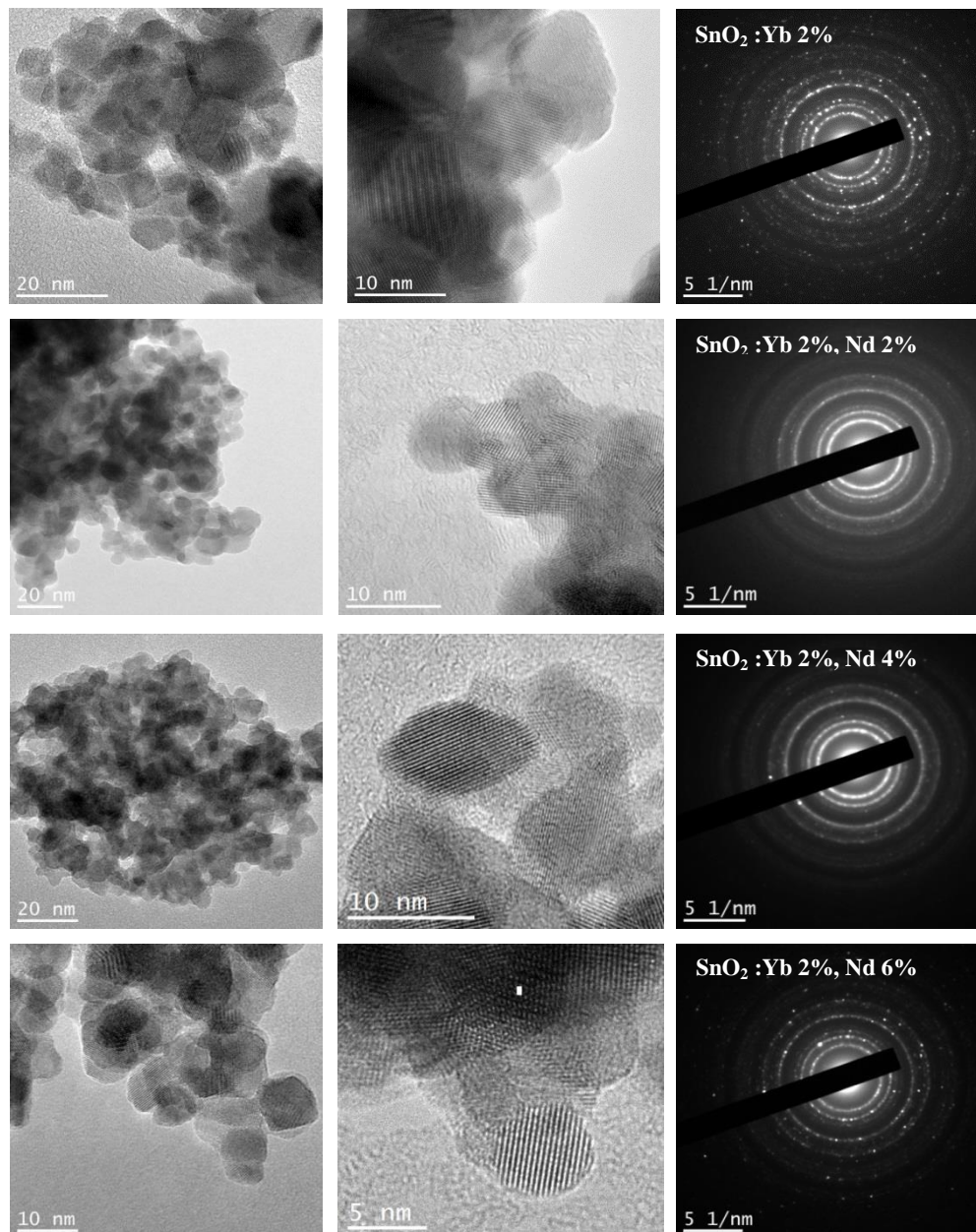
Figure 3.4.2. TEM, HRTEM images and SAED patterns of (a) SnO₂:Yb 2%, (b) SnO₂: Yb 2%, Nd 2%, (c) SnO₂: Yb 2%, Nd 4% and (d) SnO₂: Yb 2%, Nd 6 %

The bright field images show the aspect of the powders and reveal their compositions of round-shaped nanoparticles whose the size vary from a sample to another. At first glance the (Nd, Yb) co-

doped nanoparticles are of smaller sizes than the Yb-doped one. The average nanoparticles size with Yb 2% doping is found to be around 16-20 nm. That of the Yb2%, Nd 2% doped ones are in the range 8-12 nm. Doping with Yb2%, Nd 4% results in nanoparticles size of 8-10 nm while that of Yb2%, Nd 6% exhibits the smaller sizes, about 5 ± 2nm. This decrease of the nanoparticles size clearly seen from the TEM images, gives a first indication on the insertion of the RE elements into the matrix.

The HRTEM images shown in the middle range unveil the atomic plans of the nanoparticles, giving a first indication on their crystallinity. The latter is checked by the SAED technique whose the patterns are shown in the right part of the figure 3.4.2. The SEAD patterns of the different samples show diffraction rings characteristics of polycrystalline SnO₂ phase. Additional data treatments are needed to extract quantitative information on the d_{hkl} as well as the lattice parameter of the samples.

The presence of Yb and Nd in the nanoparticles is checked by EDS analysis on local nanoparticles agglomerates. Data extracted from EDS-TEM are shown in table 3.4.1. Indeed, different Yb and Nd concentrations have been detected. Here we present the mass and the atomic concentrations of both REs. Since their molecular weight is different, the atomic % were deduced from the mass %. The mass concentrations are found to fit with the nominal values. The atomic concentration of Yb is found to approach 1.4 ± 0.2 %.

Table .3.4.1. Nd and Yb measured concentrations as extracted from EDS analysis.

Sample	Nd mass %	Yb mass %	Nd atomic %	Yb atomic%
SnO₂: Yb 2%	/	1.77 % ± 0.04	/	1.22 %
SnO₂: Yb 2%, Nd 2%	1.99 % ± 0.03	2.04 % ± 0.04	1.65 %	1.42 %
SnO₂: Yb 2%, Nd 4%	3.23 % ± 0.07	2.21 % ± 0.09	2.70 %	1.54 %
SnO₂: Yb 2%, Nd 6%	7.18 % ± 0.12	2.36 % ± 0.12	6.03 %	1.65 %

3.4.4. XPS analysis

Two samples have been selected for chemical analysis by XPS, namely the Yb2%-doped and (Nd2%, Yb2%) co-doped SnO₂ powders. The powders were compacted into pellets in order to collect maximum of signal and to obtain qualitative information when using high density of the nanoparticles. Conductive carbon films are placed in the bottom of each sample to ensure charges evacuation during measurement. The survey spectra (recorded in the 0-1300 eV binding energy range) of the selected samples are displayed in figure 3.4.3. The identified main peaks are 3s, 3p, 3d, 4s, 4p, 4d, 5s and 5p core levels of tin, the 1s, 2s and 2p core levels of oxygen; the 4s, 4p and 4d core levels of ytterbium and finally the 3d core level of neodymium. Quantitative analysis of

the latter element might be very complicated since its signature overlaps with the O KLL peaks. Moreover, no other element or impurities have been recorded in the survey spectra of the two samples except C, which is usual for any XPS measurements. C1s binding energy position is used as a reference to determine binding energies of the other elements.
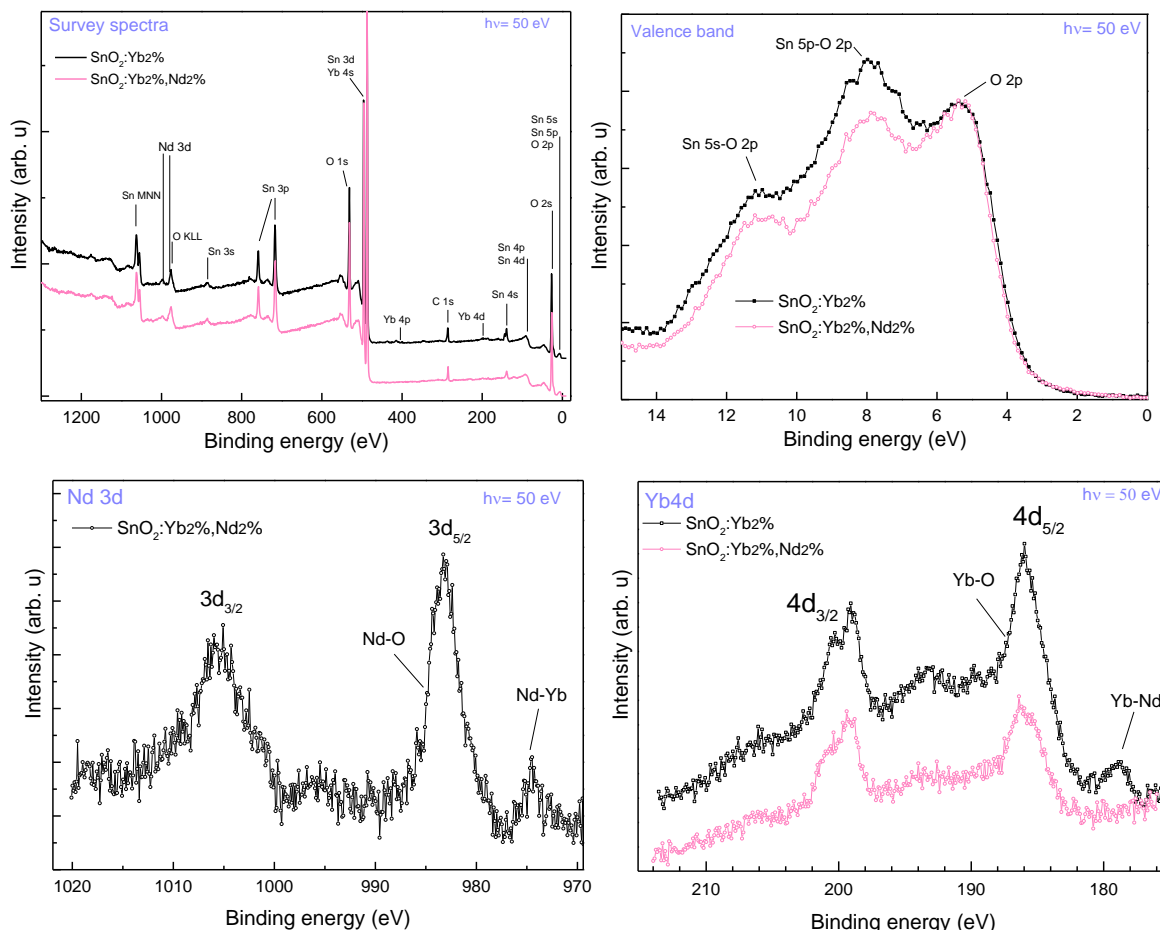
Figure 3.4.3. XPS spectra of the Yb-doped and (Nd, Yb) co-doped powders

A closer look to the valence bands shown in fig. **3.4.3.b** allows rapid identification of the dominant oxide in the structure. Both samples are exhibiting three bands at 5, 8 and 11 eV that are generally arising from the hybridization of the atomic orbitals of tin and oxygen. The band at 5 eV corresponds mainly to the O 2p derived levels. The contribution at 8 eV is due to the *ppσ* hybridization between Sn *5p*- O *2p* orbitals [259]. Finally, the band at 11 ev is mainly derived from Sn *5s*- O *2p* bonding states. The simultaneous presence of these three bands indicates that the structure is primarily SnO₂, confirming TEM observations. Moreover, it is interesting to notice that the intensity of the O 2p band is the same with both samples while that of the Sn *5p*- O *2p* and Sn *5s*- O *2p* decrease with the co-doped powder. The only difference between the two samples is the additional doping of 2 at.% of Nd which is likely responsible on this decrease. Since the two bands arise essentially from interaction between Sn and O

in the SnO_2 structure, the addition of Neodymium, especially in substitutional sites, will reduces the number of oxygen atoms bounded to Sn, resulting in the decrease of the intensity of these hybridized bands.

The Yb 4d core levels of the Yb 2% and (Yb 2%, Nd 2%) co-doped powders are displayed in figure **3.4.3.b.** We can easily recognize the Yb $4d_{5/2}$ and $4d_{3/2}$ spin-orbit doublet peaks at 186 and 199 eV for both samples, characteristics of the oxidation state of 3+. This indicates that Yb ions are bounded to oxygen. The Yb-doped SnO_2 powder exhibits additional peak at the lower part of the binding energies (at 179 eV). This peak could be attributed to Yb-Yb bonds due to the presence of non-dissociated metallic Yb clusters in the material. Its doublet appears at 191,5 eV. This reveals that even at a relatively low Yb-doping level, some Yb atoms are not inserted into the matrix and being aggregated in metallic clusters. This result supports our interpretations concerning the Yb-doped powders (case of the 2.4 at.% Yb-doped sample) presented in the above section 3.3.

The absence of Yb-Yb signature for the co-doped sample suggests that either all incorporated Yb atoms are bounded to oxygen or the excess of Yb is bonded to Nd. In the latter case, Yb-Nd bonds should be detected somewhere in the core levels spectra of Yb or Nd. Overall, considering the relatively small contribution of Yb-Yb bonds against the Yb-O bonds in the core level spectra, we can conclude that Yb is mainly bounded to oxygen, indicating their successful insertion within the SnO_2 host matrix. In both samples, Yb ions are found to be optically active (3+ valency).

To avoid the overlap between the Nd 3d core levels and the O KLL peaks, the Nd signal was extracted by subtracting the (Nd, Yb) co-doped signal from that of the Yb-doped sample (without Nd). The Nd 3d core level peaks are shown in figure **3.4.3.c.** Intense and well-defined peaks were recorded at 983 and 1005 eV corresponding to the Nd $3d_{5/2}$ and $3d_{3/2}$ spin-orbit doublet of Nd ions bounded to oxygen and possessing the 3+ oxidation state[260]. This indicates that Nd ions are well inserted into the SnO_2 structure and possess an energy level structure as that in $LaCl_3$ crystal with permitted intra 4f transitions. This also supports the result observed for the valence bands. When Nd substitutes Sn in the matrix, less Sn atoms will be bounded to oxygen, resulting in the decrease of their hybridization bands. Moreover, it is interesting to notice a second contribution that appears at lower binding energies, mainly at 974 eV. This signature highly supports our assumption about the formation of Nd-Yb bonds in the structure, since the Yb-Yb signature was not observed in the Yb core level spectrum. Another hypothesis can be advanced: one can consider that the addition of Nd within the structure makes all Yb ions bonded to oxygen; thereby the excess of Nd remains agglomerated in separated clusters. Moreover, the presence of Cl signature in the XPS spectra of Yb is suspected at 201 eV most likely coming from contamination during analysis.

3.4.5. Crystal structure

The diffraction XRD patterns of the (Nd,Yb) co-doped powders in the 20-80 2θ range are displayed in figure **3.4.4a**. All the powders are found to be polycrystalline with the tetragonal rutile phase. The increase of the dopant concentration did not affect the crystalline phase of the powders; however, it has an impact on their crystalline quality. In fact, the diffraction peaks positions are found to shift toward lower diffraction angles with the increase of the Nd content with an optimal at 4 at% where it turns back to the initial position. This shift indicates an increase of the lattice parameter and therefore a dilatation of the lattice. This phenomenon is a signature of the insertion of the dopants into lattice. The shift back to the initial positions might indicate that we reached the solubility limit of the rare earth into the matrix. It could also be caused by the increase of structural defects into the structure, for which a shift toward higher diffraction angles have gained the competition. On the other hand, no additional diffraction peaks, particularly those linked to Nd or Yb based compounds, have been recorded within the detection limit of our XRD setup.
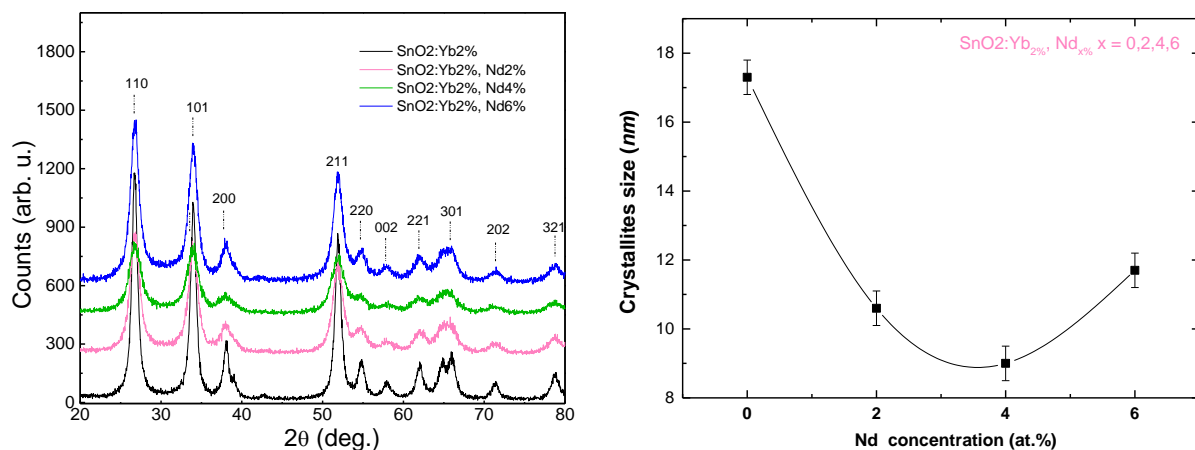
Figure 3.4.4. XRD diffraction patterns of the (Nd,Yb) co-doped powders with Yb concentration of 2 at% and Nd of 0,2,4 and 6 at%. **b)** crystallites size as a function of the Nd concentration.

Figure **3.4.4**b shows the crystallites size of the (Nd,Yb) co-doped powders with Yb concentration of 2at% and Nd of 0,2,4 and 6 at%. The figure clearly shows a decrease of the crystallites size by increasing the Nd content up to 4 at%, confirming the XRD results. Similarly to the the case of the Yb or Nd doped powders, we do think that when the dopant is well inserted into the lattice (the case of substitutional insertion), especially when the dopant have a larger ionic radius than the lattice ions (Sn^{4+}), it causes stress in the lattice which induces grains breakage resulting in smaller grains size. At 6 at.% the crystallites size increases. This does not means that Nd is not inserted within the matrix, but We speculate that the additional Nd ions are present in other lattice sites such as grains boundaries. We admit however that we do not have any experiment that

support such statement as it is difficult to quantitatively determine the quantity of dopants inserted in interstitial, substitutional or at grains boundaries sites.

3.4.6. Optical properties of the Yb:Nd co-doped powders

The absorbance spectra of the (Nd,Yb) co-doped powders are presented in figure **3.4.5**. The first information that can be extracted from the graph is that both Nd and Yb ions are inserted into the matrix and they are optically active. This is deduced from the typical absorption peaks in the visible and NIR range that correspond to direct excitation transitions in the Nd and Yb electronic structures. The intensity of theses peaks is found to increase as a function of the Nd content and reaches a pseudo-plateau at 4 at%, meaning that the number of the Nd ions optically active in the 4 and 6 a.% doped samples is comparable. On the other hand, additional information on the band gap can be obtained from the UV part of the absorption spectra. The increase of the Nd content in the powders leads to a continuous shift of the absorption edge of the material toward lower wavelengths (higher energies), indicating an increase of the band gap. This can be explained by the moss Burstein effect, in which the increase of the dopant concentration leads to the increase of the carriers concentration (in the case of substitutional sites) and therefore to the shift of the Fermi level above the conduction band. In this case the electrons need more energy to jump to empty states in the conduction band resulting in the increase of the measured optical band gap. To be more precise, when the ionic dopant (here Nd^{3+} or Yb^{3+}) substitutes the Sn^{4+} ion in the lattice, it will generate one free electron. This should be compensated by an oxygen vacancy, mostly responsible for the generation of n-type carriers in electronic structure of the semiconductor.
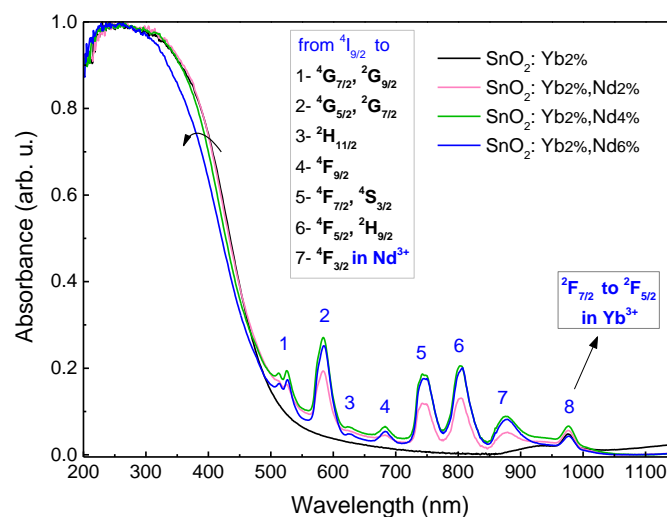
Figure 3.4.5. Absorbance spectra of (Yb, Nd) co-doped powders as a function of the Nd content.

3.4.7. Photoluminescence properties and Energy transfers

The photoluminescence spectra of the Yb2%-doped and (Yb 2at%, Nd 6at%) co-doped SnO_2 powders are presented in the figure **3.4.6.** The excitation wavelength was fixed at 275 nm in order to excite high levels in the SnO_2 band gap. The 2 at% Yb-doped powder exhibits typical Yb-PL in the NIR. By adding 6 at% of Nd into the structure, additional Nd PL takes place in the emission spectrum at 855 nm accompanied with an increase of the Yb PL at 976 nm. It is interesting to notice that the Nd emission peak at 885 nm is quite large and less defined when compared to that recorded for the Nd-doped SnO_2 powders presented before.

Moreover, the co-doped sample exhibits a shift in the peaks positions of Yb toward higher wavelengths (to lower energies). This is obviously due to the crystal field effect on the electronic structure of the rare earths. The increase of the Yb emission by incorporating 6 at.% is a good indicator of the interaction between Yb and Nd, as it will be investigated in the following part.
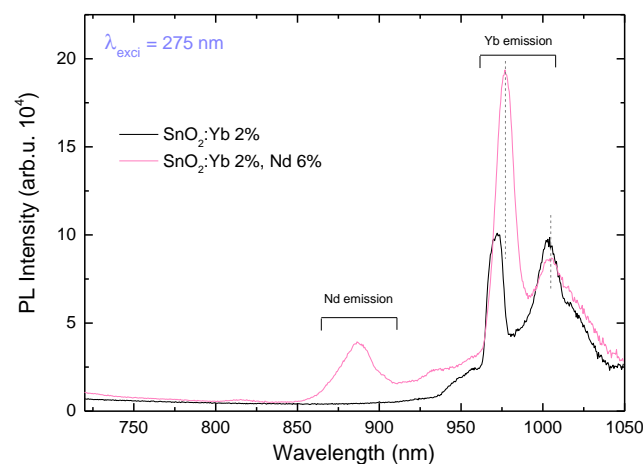
Figure 3.4.6. Photoluminescence spectra of the Yb 2at% doped and (Yb 2at%, Nd 6at%) co-doped SnO_2 powders under a xenon lamp excitation of 275 nm.

To gain insight on the photoluminescence process, PL excitation spectroscopy has been performed on the synthesized samples. Figure **3.4.7** compares the photoluminescence maps of the Yb 2at%-doped and (Yb 2at%, Nd 6at%) co-doped SnO_2 powders. The maps are visually speaking by themselves: the Yb-doped sample shows one energy transfer type while the (Nd, Yb) co-doped displays two.

In map 1, efficient photoluminescence of Yb can be achieved by exciting deep in the UV from 250 nm to 380 nm with maximum efficiency at 275 nm; this region perfectly corresponds to the absorption zone of the SnO_2 host matrix, which here plays the role of the intermediate medium, namely it absorbs

the UV light and thereby excites indirectly the Yb ions via band-to band transitions or through intermediate states in its large band gap.

In map 2, one can notice that the Yb emission can be obtained by exciting at different wavelengths of the spectrum: (i) through the UV light which corresponds to the excitation via the host matrix, (ii) through the excitations in the visible, namely at 530 and 550-600 nm. It happens that these later excitation wavelengths coincide perfectly with those at which Nd ions optically absorb. This means that the observed Yb emission (under excitation in these regions) comes essentially from Nd^{3+} ions, indicating an energy transfer between the two rare earth ions. Moreover, the intensity of Yb-PL obtained through Nd sensitization is 5 times higher that that obtained via the host sensitization. Moreover, Nd is also found to be excited directly at 580 nm and indirectly via the host at 275 nm. However, the intensity of the Nd-PL is relatively small when comparing with Yb-PL (for the sample under consideration)
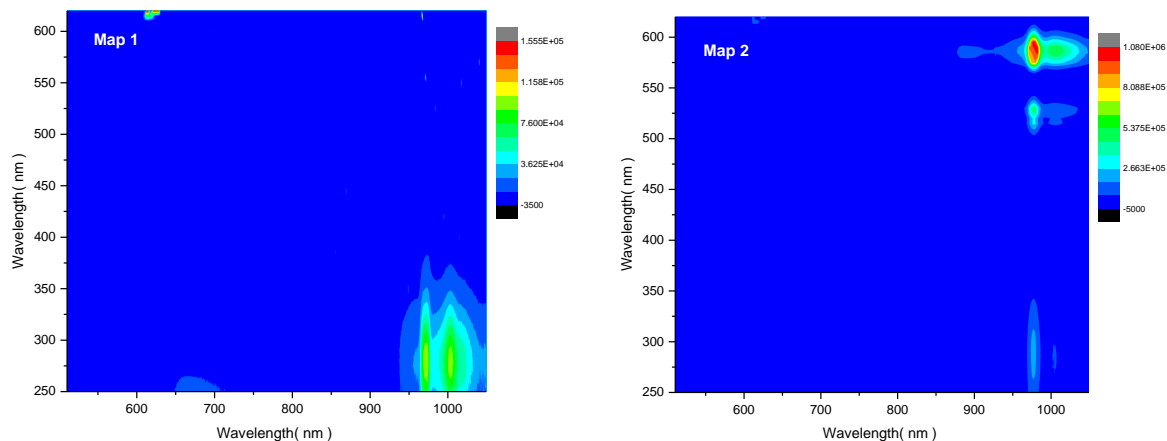
Figure 3.4.7. Photoluminescence maps of the Yb 2at%-doped and (Nd 6at%, Yb 2at%) co-doped SnO₂ powders. The X-axis represents the emission wavelength and the Y-axis represents the excitation wavelength

Based on the PL and PLE results detailed above, we display the possible energy transfer mechanisms that can occur in the Yb,Nd doped SnO₂ structures. They are schematically drawn in figure **3.4.8.**

(i) For Yb-doped SnO₂: the absorption of an incident UV photon in SnO₂ generates an electron from the valence band to the conduction band; its stepwise de-excitation along the discrete levels in the band gap can excite three 4F electrons in the Yb^{3+} ions. (3 ions in the ideal case)

(ii) SnO₂ transfers its energy to both Yb^{3+} and Nd^{3+} ions that will emit NIR photons.

(iii) SnO₂ transfers its energy only or mostly to one rare earth.

(iv) SnO$_2$ transfers its energy to both Yb^{3+} and Nd^{3+} ions and simultaneously, a part of Nd^{3+} ions transfer their energies to Yb^{3+}ions.

(v) SnO$_2$ excites directly one Nd^{3+} ion that emits a NIR photon. The excess of energy is simultaneously used to excite at least two Yb^{3+}.
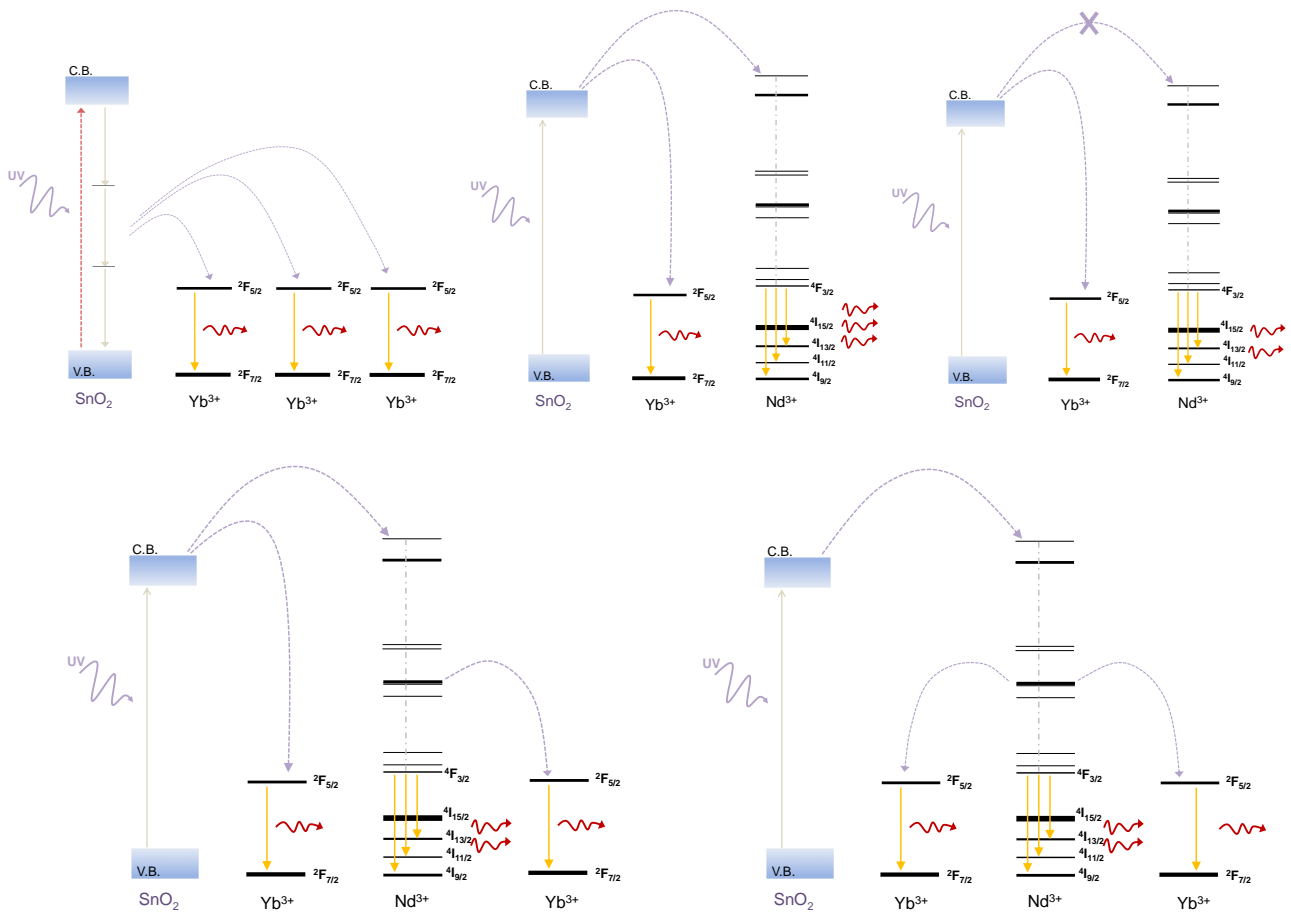
Figure. 3.4.8 Possible principal energy transfer mechanisms occurring in (Nd,Yb) co-doped SnO$_2$ system.

3.4.8. Discussion on the energy transfer

From the PL maps presented in the previous section, one can distinguish between two types of energy transfer processes: (i) Excitation from the host matrix, and (ii) Excitation from the Nd^{3+} ions. In the following, we will consider separately each of these possibilities.

3.4.8. 1. Sensitization from the host

Figure **3.4.9** summarizes the photoluminescence intensities of Nd and Yb at 885 and 972 nm, respectively, as a function of the Nd concentration in the (Yb, Nd) co-doped powders.
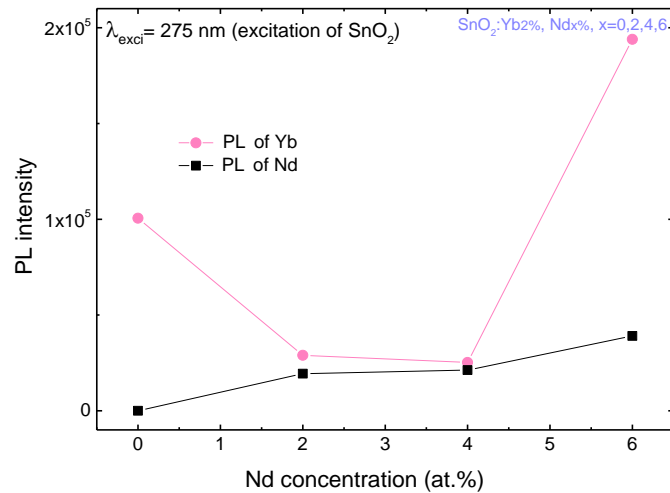
Figure 3.4.9. PL intensity of Yb at 972 nm and Nd at 885 nm as a function of the Nd concentration in the powders. The excitation wavelength here is about 275 nm

The excitation wavelength is fixed at 275 nm for which a maximum energy transfer from SnO_2 to the REs takes place. When no Nd is present (0 at%), SnO_2 transfers all its energy to the Yb^{3+} ions. The Yb-PL characteristic under excitation at 275 nm was shown in figure 3.4.7a and the energy transfer process here corresponds to the case (i) of figure 3.4.8. When incorporating 2 at% of Nd in the structure (nominal concentration), the Nd-PL signature appears at 855 nm with slightly the same intensity as that of Yb-PL. The latter is strongly affected by the presence of Nd ions. In this sample, the energy supplied by the host matrix is shared by the two ions Nd^{3+} and Yb^{3+} as schematically drawn as case (ii) in figure 3.4.8. The same behaviour is found for the 4 at% doped sample. However, the powder with 6 at% of Nd is found to behave differently. While the PL intensity of Nd slightly increases, that of Yb spectacularly increases (5 times stronger than Nd). This enhancement of PL might be due to several phenomena, mainly based on energy transfer processes. One can consider that either one of energy transfer mechanisms denoted (iii), (iv) and (v) in figure 3.4.8 is dominant or two of them or all three:

- Indeed, SnO_2 can transfer its energy to both ions but possibly preferentially to Yb^{3+} ions, in spite of the considerable amounts of Nd.

- we cannot exclude that SnO_2 sensitize both ions and simultaneously, a part of Nd^{3+} ions excite the Yb^{3+}ions (process iv). This energy transfer process is supported by the decrease of the interatomic distance between Nd^{3+} and Yb^{3+} ions when increasing the impurity concentration.

- Finally, it cannot be ruled out that SnO_2 transfers most of the energy to Nd^{3+}, which in turn, excites several Yb^{3+} ion located around.

3.4.8. 2. Sensitization by the Nd³⁺ ions

The PL intensities of Nd and Yb under direct excitation of Nd (at 885 nm) are reported in figure **3.4.10** as a function of the Nd content. The photoluminescence of Yb is found to increase gradually with the increase of the Nd content in the structure, indicating an efficient energy transfer occurring between the Nd^{3+} and Yb^{3+} ions. In this case, the efficiency of the energy transfer can be correlated to the interatomic distance between the two ions Nd^{3+} (sensitizer) and Yb^{3+} (activator), which decreases by increasing the Nd content in the structure. In the other hand, the PL intensity of Nd is found to increase with the increase of Nd% up to 4 at% and then slightly decreases because of the efficient energy transfer to Yb^{3+} ions. This result confirms our assumption. Figure **3.4.10** shows clearly that Yb^{3+} ions are the most affected element by the increase of the Nd content.
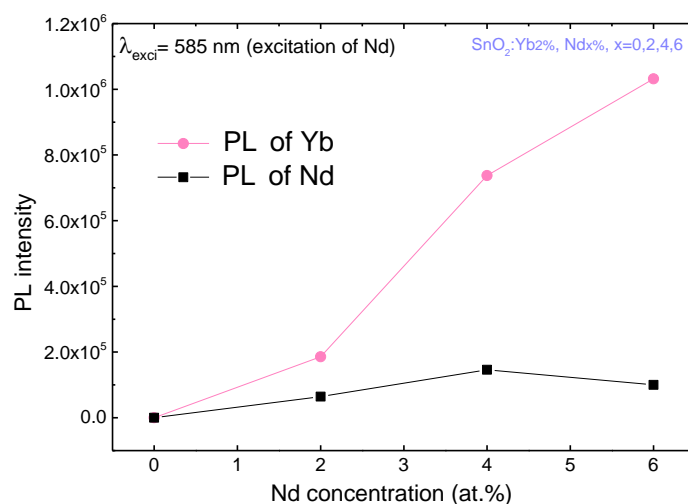
Figure 3.4.10. PL intensity of Yb at 972 nm and Nd at 885 nm as a function of the Nd concentration in the powders. The excitation wavelength here is about 585 nm (direct excitation of Nd)

Finally, it is important to underline that the Yb sensitization via Nd is found to be 6 times stronger than the sensitization by the host matrix. This difference can be understood in terms of a higher efficiency of the energy transfer. It is likely that the energy transfer between Nd and Yb involves energy levels of both ions which are in resonance, while the energy transfer from the host to Yb requires an assisted phonon process, in which energy dissipation losses rate can be important. 3.4.9. Summary

(Nd, Yb) co-doped powders with different Nd concentrations have been synthesized by the sol-gel method. The SEM and TEM observations assessed the nano-metric aspect of the nanoparticles

with values around 20 to 5 nm. Deep chemical analysis of their valances bands as well as the core levels of

Yb and Nd, revealed the successful functionalization of the SnO$_2$ with optically active Yb and Nd ions, mostly present in the 3+ oxidation state. The crystallinity of the powders was checked by SAED at small scale and by XRD analysis at larger scale. All powders are found to be polycrystalline with a tetragonal rutile phase. A shift of the diffraction peaks as well as a decrease of the crystallites size have been noticed, indicating the RE insertion into the structure. The absorption spectra measured by the UV-visible spectroscopy have shown a shift of the absorption edges toward higher energies as a function of the Nd content, suggesting an increase of the band gap. The co-doped powders have shown large spectra with emission ranging from 850 to 1050 nm, including Nd and Yb photoluminescence. Careful analysis of their PL maps conduct to propose two possible energy transfers mechanisms. The host matrix is found to transfer the UV energy to both Nd^{3+} and Yb^{3+} ions. Also, an energy transfer process from Nd^{3+} ions toYb^{3+} ions has been highlighted. Investigating the Yb-PL intensity as a function of the Nd content have shown a linear increase, which sustain the idea of the efficiency of their interaction. The Yb-PL resulting from Nd sensitization is found to be 5 times stronger than that arising from the host sensitization (using 6 at.% of Nd-doping)

3.5. Chapter Conclusions

In this chapter, we have presented the properties of RE-doped SnO$_2$ powders (nanoparticles) synthesised by two chemical routes. We have used the co-precipitation technique to check the possibility of doping SnO$_2$ with different rare earth elements, namely: Pr, Nd, Tb et Yb. The powders have been analysed by means of several characterization techniques. Information about the rare earths insertion within the matrix has been reported. Nd and Yb have particularly exhibited intense PL in the infrared region compared to the other REs. Thanks to these first results, we have investigated the effect of the RE concentration on the optical properties of the material. For this purpose we have synthesised Nd and Yb- doped SnO$_2$ powders by the sol-gel technique that offers better dopant insertion. Different RE concentrations have been studied. A variety of characterization techniques have been employed to check the insertion of the REs into the structure. We have found that SnO$_2$ matrix allows incorporation of Nd and Yb up to respectively 3.6 at% and 2.4 at.%. The insertion of the RE did not affect the crystalline quality of the nanoparticles but it is found to strongly influence their absorption. RE-doping have resulted in a decrease of the band gap, accompanied with the appearance of the RE absorption peaks. Thus, Nd is characterized by numerous absorption peaks in the visible while Yb is found to absorb in the infrared. The incorporated rare earths were optically active and gave rise to intense photoluminescence in the NIR region. An energy transfer from SnO$_2$ to the RE has been

demonstrated through the PLE spectroscopy measurements. Finally, we report on co-doping the SnO$_2$ nanoparticles with Yb and Nd. Analysis of the REs core levels by XPS revealed the insertion of

the RE elements within the matrix and their srong binding to oxygen. In this functionalized powder, we have determined two possibilities of photons conversions processes: (i) The UV photons can be converted into infrared through energy transfer from the host to both Yb^{3+} and Nd^{3+} ions; (ii) The visible photons can be also converted into infrared through energy transfer from Nd^{3+} to Yb^{3+} ions. We conclude that SnO$_2$ as a host material is a very good sensitizer for down-shifting functionality, particularly when using Nd and Yb infrared RE emitters.

These results are the prelude for our study of Nd and Yb doped SnOx films deposited by the magnetron sputering technqiue. Such method is more compatible with application in optoelectronic and photovoltaic technologies. The results of this study are detailed in chapter 4, and the umplementation to solar cells is described in chapter 5.

3.6. References

[228] Y.J. Chen, L. Nie, X.Y. Xue, Y.G. Wang, T.H. Wang, Linear ethanol sensing of SnO 2 nanorods with extremely high sensitivity, Appl. Phys. Lett., 88 (2006) 083105.

[229] J.S. Chen, M.F. Ng, H.B. Wu, L. Zhang, X.W. Lou, Synthesis of phase-pure SnO 2 nanosheets with different organized structures and their lithium storage properties, Cryst. Eng. Comm. , 14 (2012) 5133-5136.

[230] D. Wei, Y. Shen, M. Li, W. Liu, S. Gao, L. Jia, C. Han, B. Cui, Synthesis and characterization of single-crystalline SnO2 Nanowires, Journal of Nanomaterials, (2013).

[231] S. Wu, C. Li, W. Wei, H. Wang, Y. Song, Y. Zhu, L. Lu, Nd-doped SnO 2: Characterization and its gas sensing property, Journal of Rare Earths, 28 (2010) 171-173.

[232] R.S. Katiyar, P. Dawson, M.M. Hargreave, G.R. Wilkinson, Dynamics of the rutile structure. III. Lattice dynamics, infrared and Raman spectra of SnO 2, Journal of Physics C: Solid State Physics, 4 (1971) 2421.

[233] R.S. Katiyar, R.S. Krishnan, The vibration spectrum of rutile, Physics Letters A, 25 (1967) 525-526.

[234] R.J. Betsch, H.L. Park, W.B. White, Raman spectra of stoichiometric and defect rutile, Materials Research Bulletin, 26 (1991) 613-622.

[235] T. Hirata, K. Ishioka, M. Kitajima, H. Doi, Concentration dependence of optical phonons in the TiO2-SnO2 system, Physical Review B, 53 (1996) 8442-8448.

[236] S.H. Sun, G.W. Meng, G.X. Zhang, T. Gao, B.Y. Geng, L.D. Zhang, J. Zuo, Raman scattering study of rutile SnO2 nanobelts synthesized by thermal evaporation of Sn powders, Chemical Physics Letters, 376 (2003) 103-107.

[237] H.L. Ma, J.Y. Yang, Y. Dai, Y.B. Zhang, B. Lu, G.H. Ma, Raman study of phase transformation of TiO2 rutile single crystal irradiated by infrared femtosecond laser, Applied Surface Science, 253 (2007) 7497-7500.

[238] L.Z. Liu, T.H. Li, X.L. Wu, J.C. Shen, P.K. Chu, Identification of oxygen vacancy types from Raman spectra of SnO 2 nanocrystals, J. Raman. Spectrosc., 43 (2012) 1423-1426.

[239] J.X. Wang, D.F. Liu, X.Q. Yan, H.J. Yuan, L.J. Ci, Z.P. Zhou, Y. Gao, L. Song, L.F. Liu, W.Y. Zhou, G. Wang, S.S. Xie, Growth of SnO2 nanowires with uniform branched structures, Solid State Communications, 130 (2004) 89-94.

[240] Y.J. Chen, L. Nie, X.Y. Xue, Y.G. Wang, T.H. Wang, Linear ethanol sensing of SnO2 nanorods with extremely high sensitivity, Applied Physics Letters, 88 (2006) 083105.

[241] R. Durman, P. Favre, U.A. Jayasooriya, S.F.A. Kettle, Longitudinal optical-transverse optical (L.O.-T.O.) splitting on internal modes in the Raman spectra of noncentric crystals, Journal of Crystallographic and Spectroscopic Research, 17 (1987) 431-484.

[242] L. Abello, B. Bochu, A. Gaskov, S. Koudryavtseva, G. Lucazeau, M. Roumyantseva, Structural Characterization of Nanocrystalline SnO2by X-Ray and Raman Spectroscopy, Journal of Solid State Chemistry, 135 (1998) 78-85.

[243] L.Z. Liu, X.L. Wu, F. Gao, J.C. Shen, T.H. Li, P.K. Chu, Determination of surface oxygen vacancy position in SnO2 nanocrystals by Raman spectroscopy, Solid State Communications, 151 (2011) 811-814.

[244] L.Z. Liu, T.H. Li, X.L. Wu, J.C. Shen, P.K. Chu, Identification of oxygen vacancy types from Raman spectra of SnO2 nanocrystals, Journal of Raman Spectroscopy, 43 (2012) 1423-1426.

[245] S. Chen, X. Zhao, H. Xie, J. Liu, L. Duan, X. Ba, J. Zhao, Photoluminescence of undoped and Ce-doped SnO2 thin films deposited by sol–gel-dip-coating method, Applied Surface Science, 258 (2012) 3255-3259.

[246] L. Dua, P.K. Biswas, Synthesis and photoluminescence property of nanostructured sol–gel antimony tin oxide film on silica glass, Chemical Physics Letters, 572 (2013) 66-72.

[247] D.J. Norris, A.L. Efros, M. Rosen, M.G. Bawendi, Size dependence of exciton fine structure in CdSe quantum dots, Physical Review B, 53 (1996) 16347-16354.

[248] T. Kim, D. Lee, Y. Yoon, Microstructural, electrical, and optical properties of SnO 2 nanocrystalline thin films grown on InP (100) substrates for applications as gas sensor devices, Journal of Applied Physics, 88 (2000) 3759-3761.

[249] E.M. Wong, P.C. Searson, ZnO quantum particle thin films fabricated by electrophoretic deposition, Applied Physics Letters, 74 (1999) 2939-2941.

[250] F. Gervais, B. Piriou, Temperature dependence of transverse- and longitudinal-optic modes in TiO2 (rutile), Physical Review B, 10 (1974) 1642-1654.

[251] RB nano company, R. Society, http://www.rbnano.fr/.

[252] A.L. Patterson, The scherrer formula for X-ray particle size determination, Physical Review, 56 (1939) 978-982.

[253] P. Mulvaney, F. Grieser, D. Meisel, Electron transfer in aqueous colloidal SnO2 solutions, Langmuir, 6 (1990) 567-572.

[254] F.J. Arlinghaus, Energy bands in stannic oxide (SnO2), Journal of Physics and Chemistry of Solids, 35 (1974) 931-935.

[255] J. Jacquemin, Propiété optiques du SnO2 et du β-PbO2 intrinsèques au voisinage du gap, Le Journal de Physique Colloques, 35 (1974) C3-255-C253-260.

[256] M. Balestrieri, G. Ferblantier, S. Colis, G. Schmerber, C. Ulhaq-Bouillet, D. Muller, A. Slaoui, A. Dinia, Structural and optical properties of Yb-doped ZnO films deposited by magnetron reactive sputtering for photon conversion, Solar Energy Materials and Solar Cells, 117 (2013) 363-371.

[257] E. Antic-Fidancev, J. Hölsä, M. Lastusaari, Crystal field energy levels of Eu 3+ and Yb 3+ in the C 2 and S 6 sites of the cubic C-type R 2 O 3, Journal of Physics: Condensed Matter, 15 (2003) 863.

[258] B. Assaad, H. Hicham El, F. Ihsan, B. Géraud, B. Mohamed, B. Laurent, A pure silica ytterbium-doped sol–gel-based fiber laser, Laser Physics Letters, 10 (2013) 055106.

[259] J.M. Themlin, R. Sporken, J. Darville, R. Caudano, J.M. Gilles, R.L. Johnson, Resonant-photoemission study of SnO2: Cationic origin of the defect band-gap states, Physical Review B, 42 (1990) 11914-11925.

[260] F. Rivera-López, M. Pérez, X-ray photoelectron spectroscopy: surface and depth profiling studies of glasses doped with Nd and Yb ions, Surface and Interface Analysis, 44 (2012) 927-930.

Chapter 4: Rare Earth doped SnO$_X$ thin films by Sputtering

Introduction

This chapter aims at producing RE-doped SnO$_x$ thin films serving as TCOs and photon converter layers for solar cells. Although RE-doped SnO$_x$ nanoparticles have been successfully synthesized by chemical routes in chapter 3, the study of thin films remains more important, particularly from the application point of view since further implementation to solar cells is performed by thin films. The work reported in this chapter aims at investigating the possibility of doping of SnO$_2$ layers with rare earths and check whether an energy transfer from the host to REs is occurring. Our films are elaborated by reactive magnetron sputtering, this technique provides quite good RE insertion and good crystalline quality of the films. This chapter reports on the structural and optical properties of undoped, Nd-doped and Yb-doped SnO$_x$ thin films. These elements exhibit infrared PL useful to solar cells. We will show that the combination of both Yb and Nd is of potential interests, thanks to multiple photon conversion processes.

In a first part, we discuss the properties of the undoped SnO$_x$ films versus several experimental parameters such as the Ar/O$_2$ gas flow rate and the deposition temperature. Indeed, our films being synthesized starting from tin targets under Ar bombardment in the sputtering system, Ar gas is somehow responsible of the deposition rate while the oxygen gas plays a key parameter for the tin oxidation. Strong changes in the structure of the SnO$_x$ matrix are therefore expected. The substrate temperature during deposition is also an important parameter as it controls the staking coefficient of the sputtered atoms as well as their surface mobility. The thermal annealing of the deposited films can also modify the crystalline structure, the morphology and the conductivity of the final SnO$_x$ films. The objective of this part is to know to which extend is it possible to modify the properties of the deposited SnO$_x$ films versus some operational parameters.

In a second part of the chapter, we study the effect of the presence of Nd atoms on the structural, optical and electrical properties of deposited Nd-doped SnO$_x$ films. In particular, we focus on the photoluminescence properties of the grown doped films versus the A/O$_2$ gas flow, the substrate temperature and annealing temperature. We also demonstrate the positive effect of the Nd content on the light emission properties. The aim of this study overall is to look to the best local environment for

the Nd ions in order to reach the highest PL emission that will be useful for photon conversion in solar cells for instance.

The properties of Ytterbium doped SnOx films are reported in the third part of this chapter. The applied methodology is the same than that of Nd doped SnOx films. The similarities and particularities between the two rare earth elements will be outlined. Finally, the effect of co-doping SnO$_x$ films by Nd and Yb on the emission properties is detailed in the last paragraph of the chapter. The benefits and the limitations are thoroughly discussed.

4.1. Synthesis and Properties of Undoped SnO$_2$

4.1.1. Effect of the Ar and O$_2$ gas flow on SnO$_x$ films

4.1.1.1. Synthesis

Table 4.1.1 gives the deposition parameters used to deposit undoped SnO$_x$ thin films on silicon or quartz substrates. The deposition is carried out under different oxygen gas flows while that of the Ar was kept constant. Parameters such as the pressure, the radio frequency power (P), the substrate temperature (T)/rotation/distance to target, and deposition time (t) were kept constant for this serie of samples. The Ar/O2 flow varies from 1.7 to 4. The [O]/[Sn] ratio data as deduced from RBS fit and reported in table 4.1.1 show no change for samples grown with oxygen flow above 4. This result will be commented later. The resulting thicknesses as extracted from the XRR analysis and ellipsometry data are also reported in table 3.1 for the case of 30min deposition time. A typical XRR curve of an undoped SnO$_x$ film is displayed in figure 4.1.1. All techniques have given comparable values which support the reliability of the measurements. We found that the thickness of the films is decreasing when the oxygen flow increases. This means that the introduction of more oxygen content in the deposition chamber decelerates the deposition process. In addition, the average roughness was found to be around 1.11 ± 0.27 nm indicating a very good quality of the films.

Table.4.1.1. Deposition parameters, thickness using XRR fit, Tauc gap deduced from ellipsometric data, band gap calculated from the transmission data and stoichiometry ([O]/[Sn]) by RBS of the SnO$_x$ undoped films by sputtering. The RF power, pressure and deposition time were kept constant as follow: 50 W, $3.3.10^{-4}$ m.torr, and 30 min, respectively

Table.4.1.1. Deposition parameters and stoichiometry by RBS of the undoped SnO$_x$ films as a function of the O$_2$ gas flow during deposition by sputtering. The deposition temperature was set at 100°C.

Film	Ar : O2 (sccm)	Thickness by XRR (nm)	Band gap by ellipsometry	Eg by tauc plot from Transmittance	[O]/[Sn] BY RBS
A	12:3	320 (by RBS)	2.8 ± 0.72	3.19 ± 0.2	0.16 ± 0.2
B	12:4	303	4.23 ± 0.86	4.15 ± 0.2	2.1 ± 0.2
C	12:5	248	3.78 ± 0.54	3.84 ± 0.2	2.1 ± 0.2
D	12:6	148	4.15 ± 0.66	4.15 ± 0.2	2.1 ± 0.2
E	12:7	117	3.83 ± 0.52	4.26 ± 0.2	2.1 ± 0.2
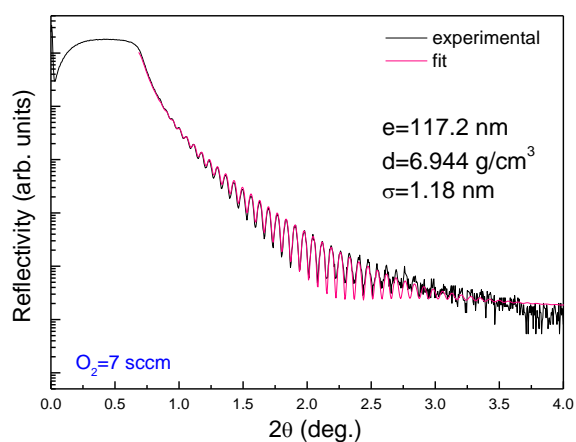
Figure 4.1.1. Typical X-ray reflectivity (XRR) of an undoped SnO$_x$ film (deposited with O$_2$=7sccm)

4.1.1.2. Crystalline structure

Figure 4.1.2 displays the typical θ-2θ scan of SnO$_x$ films deposited on silicon substrate under different O$_2$ gas flows and using Sn as a target. The XRD peak positions of pure SnO and SnO$_2$ as given by their JCPDS cards are also given in Figure 4.1.2 as a reference. At first glance, the oxygen content seems to play a key role on the crystallization of the films.

For the lowest oxygen content (3sccm) the film exhibits a broad diffraction band at lower diffraction angles centred around 30°. This signature is commonly attributed to amorphous SnO. However, this does not exclude the presence of nano-crystalline SnO$_2$ structure, since the band is covering a large part of diffraction angles where some SnO$_2$ diffraction peaks could be present. Similar diffraction patterns have been reported by Rinnert et al.[225] .

By increasing the oxygen gas flow to 4 sccm (Ar/O$_2$ = 3), the structure is completely switching to a polycrystalline SnO$_2$ structure; the different atomic orientations can be easily identified according to the JCPDS card n°= 00-41-1445. By increasing more the oxygen gas flow, the growth becomes favoured along the (110) and (200) plans/directions. It even results in the appearance and

disappearance of some growth directions. Except for the film deposited under O_2 gas flow of 6 sccm, although its diffraction peaks are hardly visible, its crystalline structure can be approximately identified as a mixture of amorphous SnO and crystalline SnO_2. This is deduced from the large diffraction band characteristics of SnO and the weak diffraction peaks belonging to SnO_2 structure.

Besides, a weak diffraction peak is observed at lower diffraction angles mainly at 24.6° for the all SnO_x films. We speculate that this feature is most likely due to the presence of a $SiSnO_x$ interface between the SnO_2 films and the Si substrate. To our best knowledge, no earlier reports explaining the origin of this peak exist in the literature; also no JCPDS card of such compounds could matches with the position of this peak.

As a summary of the XRD results, the increase of oxygen during deposition of the undoped SnO_x films does not seem to modify strongly the crystalline nature of the films.
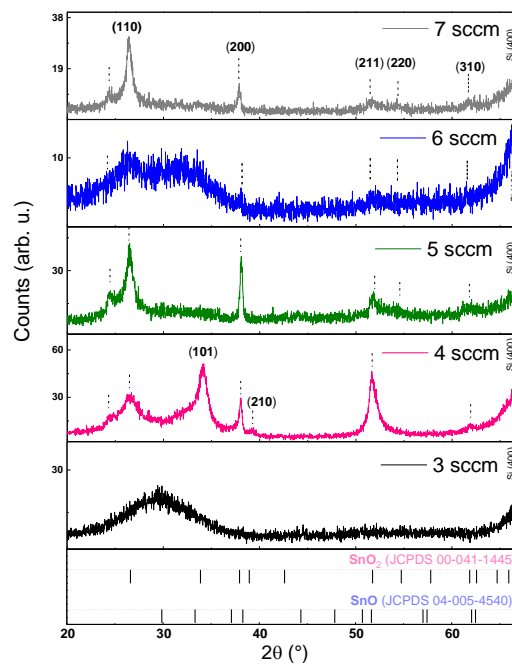
Figure 4.1.2. X-Ray diffraction patterns of undoped SnO_x films deposited with increasing the O_2 gas flow ratio during deposition from 3 up to 7. The main peaks are indexed in the rutile SnO_2 structure.

4.1.1.3. Chemical analysis by RBS

RBS analysis were performed on the undoped SnO_x thin films in order to determine the oxygen concentration in the films since the latter have been elaborated under different O_2 gas flows. Typical

RBS spectra of an undoped SnO$_x$ film and the best fitting curve are presented in figure 4.1.3. Similar spectra were obtained for the other deposition conditions.

The presence of tin and oxygen atoms in the structure can be witnessed by the presence of two peaks at high and low energies, respectively. The width of each peak corresponds to the thickness of the film. It is worth noting that from the peaks' shape the two elements seem homogeneously distributed along the growth direction. The same conclusion can be underlined for all the samples of this serie. Figure 4.1.3.b shows how the growth rate is strong ly dependent on the O$_2$ gas flow during deposition; the deposition rate is found to decrease when more oxygen is injected in the deposition chamber which is in agreement with the XRR and ellipsometry values reported above. Despite the difficulty of calculating the oxygen content, all spectra were simulated with an error value of 0.05.
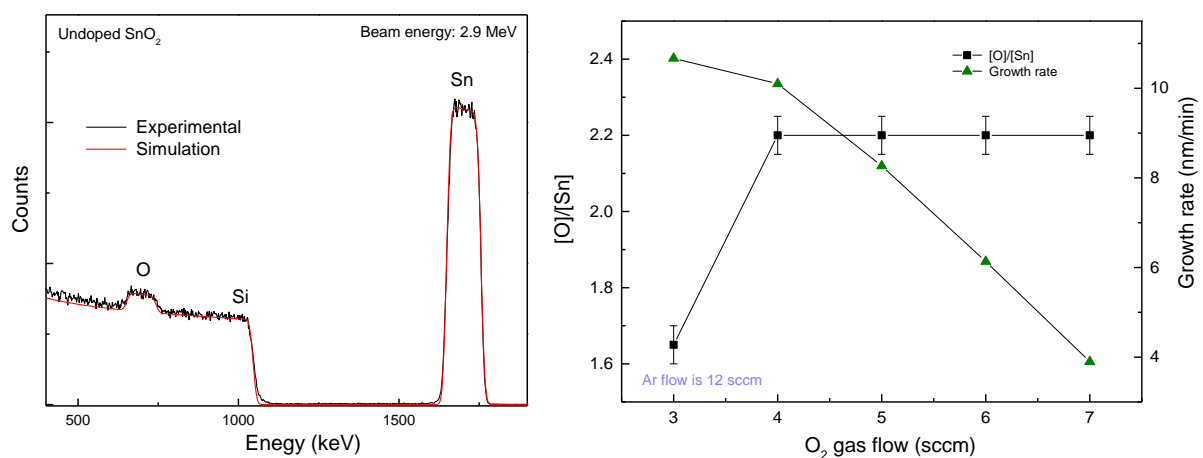
Figure 4.1.3. **(a)** Experimental and simulated RBS spectra of an undoped SnO$_x$ film of 105 nm, **(b)** Variation of the [O]/[Sn] atomic ratio and the growth rate with the oxygen gas flow during deposition.

Figure 4.1.3.b presents also the stoichiometry of the films extracted from the chemical analysis by RBS and reveals a constant [O]/[Sn] ratio of 2.1±0.2 for samples produced with an O$_2$ gas flow above 4sccm with Ar flow set at 12sccm. This means that no further oxygen atoms can be incorporated into the structure beyond 4 sccm of O$_2$ gas flow during deposition. At this stage, the SnO$_x$ structure contains oxygen atoms either in tetragonal crystalline or interstitial sites. It seems that flowing more oxygen in the chamber does not affect the crystalline structure of the films. In line with the XRD results, the film deposited under O$_2$ flow of 3 sccm is an oxygen poor film, the tin and oxygen atomic ratio being at about 1.65 ± 0.05. In this case, the crystalline structure can be identified as a nanocrystalline SnO with an excess of oxygen or an oxygen deficient-nanocrystalline SnO$_2$. The wide diffraction band in figure 4.1.2 is most likely resulting from the high density of defects in the structure including oxygen vacancies.

4.1.1.4. Optical properties

The transmission spectra of the undoped SnO$_x$ films are plotted in figure 4.1.4. The spectra are reported in the 200-850 nm to highlight the spectacular change of the absorption edges. The optical properties are found to be strongly sensitive to the oxygen gas flow during the deposition and therefore to the oxygen content in the films.
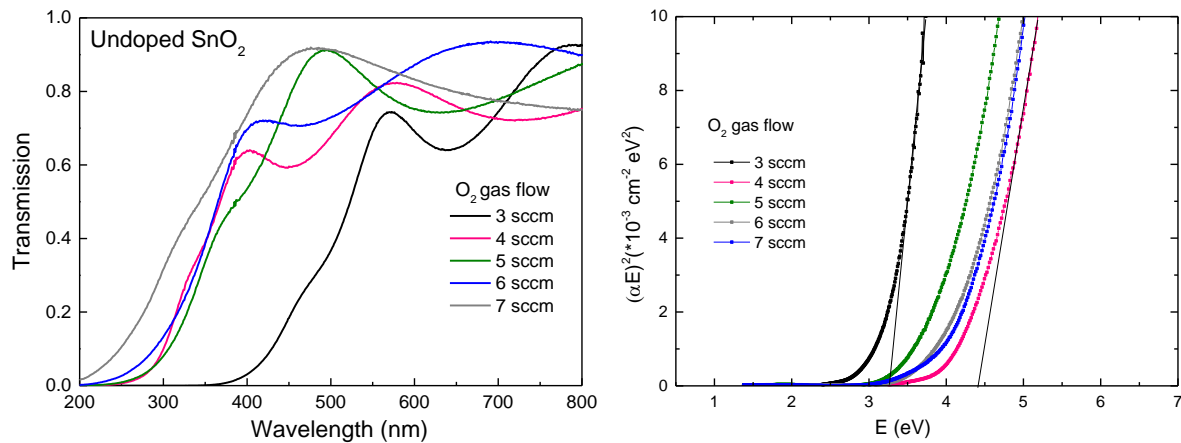
Figure 4.1.4. (a) Transmission spectra of the undoped SnO$_x$ films deposited under different O$_2$ gas flows; **(b)** Tauc plots as deduced from the transmittance data versus the O$_2$ gas flow of the undoped SnO$_x$ films

The spectra clearly show a change in the optical properties of the films when the O$_2$ gas flow increases from 3 to 7. In agreement with the structural analysis reported above, the material is found to rock from a SnO structure for the films with O$_2$= 3sccm to a SnO$_2$ structure with oxygen flows higher than 4 sccm. The absorption edge shifts progressively toward higher energies (shorter wavelengths) by increasing the oxygen flow during the deposition, indicating an increase of the band gap of the material. Besides, the transparency of the films is found to range between 60-90 % in the visible to the NIR ranges. Different fringes in the transmission spectra have been noticed for all undoped samples. That commonly arises from the interference of light reflected by the film substrate, substrate-air interfaces and internal reflections within the films as the SnO$_x$ films' thicknesses exceed 100 nm.

The transmission data were used to determine the band gap values of the different materials using the formula:

$$\alpha = \frac{1}{d} \, ln \left[\frac{1-R}{T} \right]$$

Were α is the absorption coefficient, d the thickness of the films, T the transmittance and R the reflectance. By extrapolating the linear part of the Tauc plots, $(\alpha E)^2$ as a function of the photon energy (see figure 4.1.4.b), it is possible to extract the band gap energy values of the different samples when assuming direct transitions (n=1/2). Up to now there is still a lot of controversy about the nature of

electron transitions in the SnO_2 material whether they are direct or indirect. Calculated E_g data assuming a direct transition are reported in table 4.1.1. The film deposited under O_2 flow of 3 sccm exhibits a lower band gap with a value of 3.15 eV. This finding is coherent with the SnO structure for which the band gap can lay between 2.5 to 3.4 eV. Increasing the oxygen content during deposition leads to an increase of the band gap. The films deposited with O_2 above 4 sccm, which have a polycrystalline SnO_2 structure, exhibit an average band gap value about 4 eV. These values are close to those reported in literature for a SnO_2 structure since its bandgap energy is given to value between 3.6 and 4.6 eV. As it is shown in table 4.1.1, although the films have the same [O]/[Sn] ratio (stoichiometry), they exhibit different band gap values. This is most likely related to the crystalline quality of the films as confirmed by the XRD analyses shown above. One possible origin of the changes of Eg is the disorder in the structure. Indeed, it is often found in literature that the structural disorder rather reduces the band gap of the semiconductor as a consequence of the formation of band tails (multiple energy level states) close to the valence or conduction bands. Such phenomenon is more pronounced for strongly disordered structures such as amorphous materials. This is probably the case for sample A produced with an O_2 flow of 3sccm.

We have also attempted to determine the optical properties of the produced SnO_x films from spectroscopic ellipsometry measurements. Different simulation models have been tested to estimate the thickness of the films as well as the refractive index n and the extinction coefficient k. From the last, we have also extracted the optical band gap.

The measured n and k of the sample A were better fitted using the Adachi-new Forouhi model. In contrast, the ellipsometric data of the crystalline SnO_2 samples (B to F) were rather well fitted using the Adachi dispersion model. The fit was realized with an average standard deviation of 2. An example of typical experimental and fit curves of the ellipsometry measurements is given in figure 4.1.5 for one selected undoped film. .
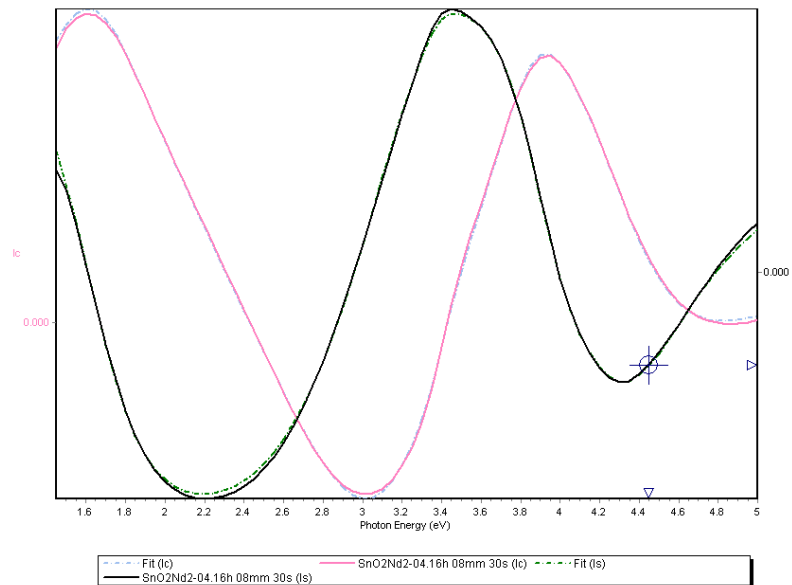
Figure 4.1.5. Example of typical fit with ellipsometry to extract optical properties of the films

The extracted values of the band gap rom the ellipsometric measurements are also reported in Table 4.1.1. The Tauc plots were drawn from the absorption coefficient of the films calculated using the measured extinction coefficient values k where $\alpha = 4\pi k/\lambda$. The amorphous sample having a SnO structure is exhibiting a low band gap value equal to 2.8 eV against 3.15 eV which was found using the transmittance data. We speculate that this value is more appropriate given the structure since the band gap calculated from the transmission spectra is based on the thickness measured by RBS that lacks some accuracy. Moreover, the extraction of large thicknesses values from the XRR technique is quite difficult. Therefore we consider that 2.8 eV is closer to the right band gap energy value for sample A. For the other samples, the bandgap energies calculated from the ellipsometry measurements are found to be lower than those extracted from the transmittance data (Table 4.1.1). Yet, the optical bandgap energy values extracted either by ellipsometry or transmission is just an approximation given the complexity of the deposited SnOₓ films being amorphous or polycrystalline.

Figure 4.1.6 reports the refractive index of the pure SnO_2 films as a function of the photon wavelength. At first glance it can be easily understood that the samples belong to different families of SnOₓ based materials. Sample A (deposited under 3 sccm of O_2) which is amorphous and has a SnO structure exhibits a higher refractive index compared to the other samples (B to F). In the other hand, the crystalline samples which have a SnO_2 structure (4, 5 and 7sccm) have almost the same refractive index. Sample E deposited with 6 sccm of O_2 gas flow is however behaving differently. Thanks to the XRD results, this SnO_2 film was found to be partially amorphous, which might explain the increase of the refractive index values within the measured photon wavelength range. Considering the comparison in figure 4.1.6, it is worth noting that the refractive index of our deposited tin oxides (SnO and SnO_2)

is ranging between 2 and 2.7 which make them relevant as anti-Reflective coating layers for solar cells or photodetection applications.
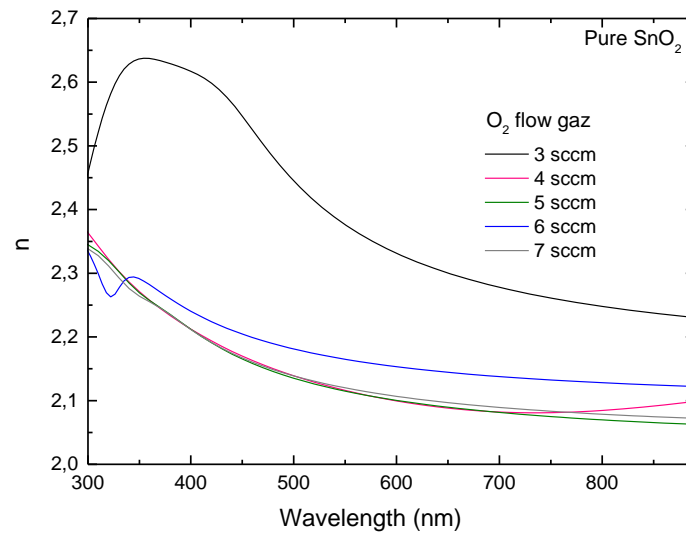
Figure 4.1.6 The refractive index of the different pure SnO$_x$ films as a function of photon wavelength obtained by fitting ellipsometric data.

4.1.1.5. Photoluminescence properties

The photoluminescence spectra of the as deposited SnO$_x$ films are displayed in figure 4.1.7 after excitation with a Nd: YAG laser emitting at 355 nm.
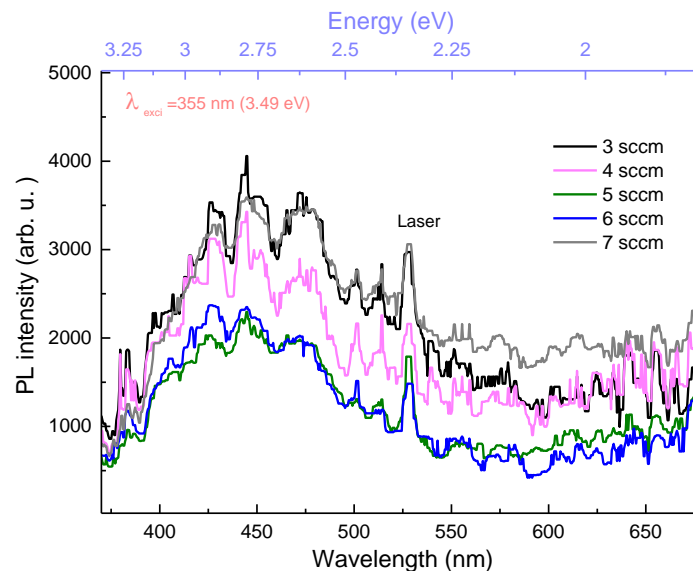
Figure 4.1.7 PL spectra of the undoped SnO$_x$ films deposited with different oxygen gas flows

The SnO$_x$ films exhibit a very weak PL band in the UV-Vis part of the spectrum and centred at about 440-450nm nm. The position and intensity of this band are slightly the same for all samples, whatever is the stoichiometry or the deposition conditions. In contrast to the reported work of Rinnert et al

[225] on SnO$_2$ films which showed a strong PL band centred around 600 nm, our samples seem to have a very small density of radiative defects in the structure. As already explained in the chapter 1 (case of powders), the origin of these radiative recombination centres is most likely related to the oxygen vacancies, the interstitial sites and grains defects. The fact that all samples display the same emission band whatever the crystalline structure suggests that the films possess comparable populations of radiative defects and most of electron relaxation/transitions occur non-radiatively.

4.1.2. Effect of deposition temperature

4.1.2.1. Structural properties

This study was conducted in order to get an insight on the influence of the substrate temperature during deposition on the growth process of the undoped and sputtered SnO$_2$ films. To do so, the argon to oxygen gas flow ratio was fixed targeting a pure SnO$_2$ structure. The sputtering parameters were kept constant. The deposition time was monitored so as to obtain a fixed thickness of about 100 nm. Table x gives the measured thickness as determined using the XRR or ellipsometry measurements for the undoped films grown at different temperature. The values are quite close and the final film thickness is indeed around 100nm $\pm$ 10. Based on our experiments, we have found that higher deposition temperatures delay the deposition process. In the following, the structural, optical and electrical properties of these sputtered films will be discussed.

Figure 4.1.2.1 displays the XRD patterns of the undoped SnO$_x$ films deposited with different substrate temperatures. The sample deposited at room temperature (15°C) is found to have an amorphous structure, witnessed by the wide diffraction band ranging from 20° to 38°. In fact, this signature is usually attributed to an amorphous SnO structure; however it is difficult to decide the nature of this film simply from a diffraction pattern. As a matter of fact, we expect a formation of SnO$_2$ phase from the Ar and O$_2$ gas mixture used during the growth. Increasing the deposition temperature to 100°C leads to the appearance of some diffraction peaks located at 26.48, 38.09 and 51.7° with in addition the wide diffraction band found at 15°C. According to the JCPDS card number 00-41-1445, these peaks are characteristics of a polycrystalline SnO$_2$ phase. From the intensity point of view, the (110) and (200) directions exhibit much intense peaks against the (211) direction. This means that some preferential planes are favoured during the growth. Apart from this, a weak peak at 24.37° comes into view whose the intensity increases by increasing the deposition temperature. We attribute this signature to a SnSiO$_x$ composite phase that might appear at the surface between the SnO$_2$ film and the silicon substrate. At 200°C, the wide diffraction band is still visible which indicates the presence of an amorphous component. The intensity of the SnO$_2$ diffraction peaks is found to increase indicating a better crystalline structure. The same observations have been noticed for the film deposited at 300°C.

A closer look to its pattern reveal that the (110) peak intensity is stronger than that of (200) meaning that the growth along the (110) becomes prominent against the other directions. This structure evolution is even more visible for the samples deposited at high temperature, especially <u>at</u> 400 and 500°C for which the ratio between the peaks intensities is quite obvious.

Figure 4.1.2.1.b compares the (110) and the (200) diffraction peaks of the different undoped SnO_x films and highlights the shift of the peaks positions toward higher diffraction angles. This indicates that increasing the substrate temperature during deposition leads to a compressive stress on the crystal lattice of the films. Additionally, as it can be clearly seen from the diffraction patterns, the (110) peak intensity is increasing when the deposition temperature increases while the intensity of the (200) peak stabilises above 300°C.

For deeper insight on the structure evolution, the crystallites sizes along the (110), (200) and the (211) directions were calculated using the Scherrer formula. Moreover, we could extract the Lattice constant 'a' values for the (200) direction from the XRD patterns. These results are summarized in table 4.1.2.1

Table 4.3.5 *gives the crystallites size along the (110), (200) and the (211) directions and the lattice constant calculated from the (200) peak (as deduced from the XRD analysis) versus the deposition temperature*

T	Thickness (nm)		Crystallites size (nm)			Lattice cons. 'a' (Å)	Band gap	
(°C)	XRR	ellipsometry	(110)	(200)	(211)	(200)	Trans.	ellipsometry
15	91.5	97.6 ± 6.5	/	/	/	/	3.8 ± 0.2	4.0 ± 0.2
100	110.4	114.8 ± 3.08	5.56	29.53	3.51	4.7283	3.8 ± 0.2	3.7 ± 0.2
200	109.8	112.6 ± 2.3	10.10	28.62	4.76	4.7218	3.9 ± 0.2	4 ± 0.1
300	109.4	109.3 ± 3.5	12.282	28.08	6.06	4.7169	3.9 ± 0.2	4.1 ± 0. 1
400	98.5	98.9 ± 3.5	17.245	28.12	16.41	4.7199	4.04 ± 0.2	4.16 ± 0.2
500	106.7	108.7 ±2.4	18.986	25.47	18.713	4.7170	4.07 ± 0.2	4.10 ± 0. 2

Obviously, it is impossible to calculate the crystallites size for the amorphous sample deposited at 15°C. Overall, when increasing the deposition temperature, the crystallites size of the (110) and (211) increases gradually and substantially while that of the (200) decreases slightly. Moreover, given the lattice constant values shown in table 4.1.2.1, the deposition temperature seems to affect strongly the crystallites size but not the lattice parameters. It we consider the third decimal, we can notice that the "a" parameter decreases when increasing the growth temperature. The calculated a values are close to that of the SnO_2 bulk material whose the constants are: a=b=4.7374 Å, c=3.1864 Å. A tentative calculation of the second lattice parameter "c" has been done but the obtained values were far from the data found in literature. This is most probably due to the large error coming from the calculations since

it involves fitting the (211) peak which have a very weak intensity, especially for the samples grown at 100°C and 200°C.
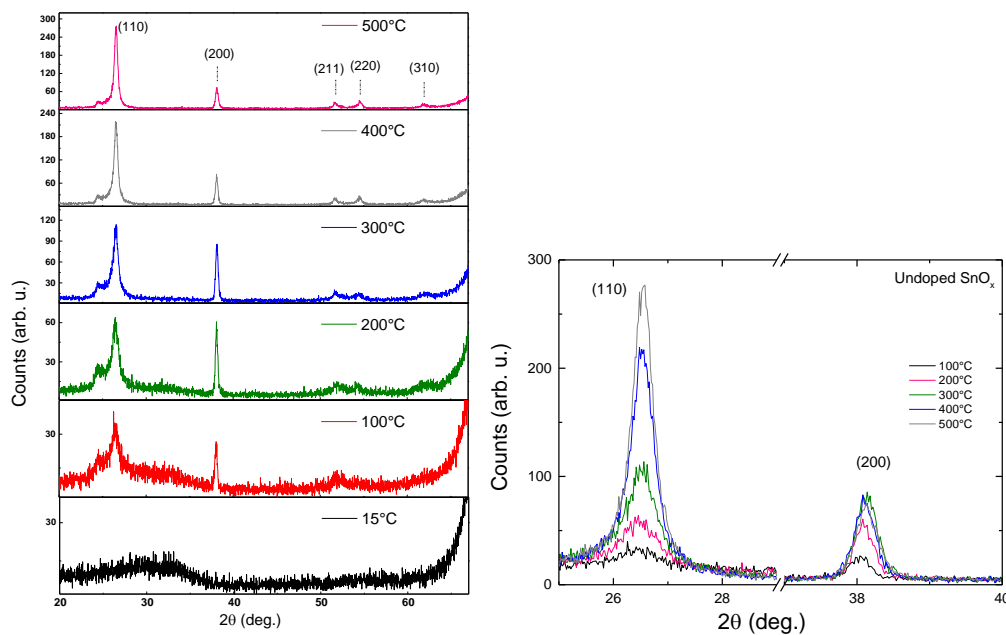
Figure 4.1.2.1. **a)** Diffraction patterns **b)** Overlays of the diffraction patterns of the undoped SnO$_x$ films (8:4), as a function of the deposition temperature. The diffraction peaks are indexed in the SnO$_2$ rutile structure

4.1.2.2. Optical properties

The transmission spectra of the sputtered films are presented in figure 4.1.2.2 versus the deposition substrate temperature. The films exhibit a transmittance of about 80 % for wavelengths above 700 nm, which is remarkable. Furthermore, all films exhibit an absorption edge around 200 nm, which is a typical signature of a SnO$_2$ structure. However, the absorption edge seems to be steeper when increasing the deposition temperature leads. Thanks to the Tauc plot procedure, values of the band gap Eg of the different films were determined and they are reported in Table 4.1.2.1. The effective band gap values slightly increase when the deposition temperature increases, which is indicative of a better structured materials. A similar trend is obtained with the bandgap values deduced from the spectroscopic ellipsometry measurements as reported in Table 4.1.2. The ellipsometric data were fitted with χ^2 of less than 1. Considering the error bar when extracting the Eg values, we assume that both techniques give roughly comparable band gap values. We think that the reported values are very close to the real band gap of these SnO$_2$ materials since
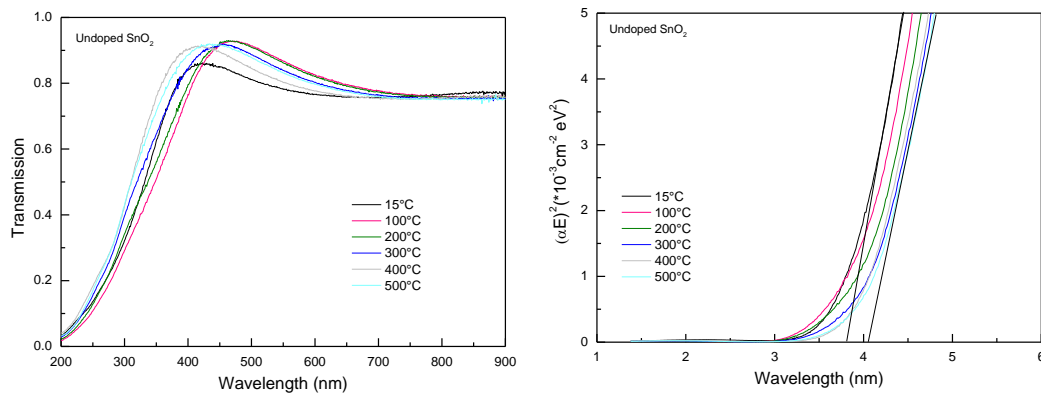
Figure 4.1.2.2 a) UV-to NIR transmission spectra, **b)** Tauc plots of the unddoped films (8:4) as a function of the deposition temperature.

The spectroscopic ellipsometry measurements allow also extracting the refractive index of the deposited films. The data are reported in Figure 4.1.2.3 as a function of the photon wavelength for the undoped layers deposited at different temperatures. The amorphous sample grown at room temperature exhibits the lowest n values; its refractive index is equal to 2 at 650 nm. Increasing the deposition temperature leads to an increase of the n values in the limit of the investigated wavelengths range, particularly for the sample deposited at 500 nm for which the variation of n is markedly visible. Overall the refractive index of this set of sample is ranging somewhere around 2.x with $0 \leq x < 4$. This variation is reasonable and the thickness of the film can be adapted in order to use such layers for antireflection coating.
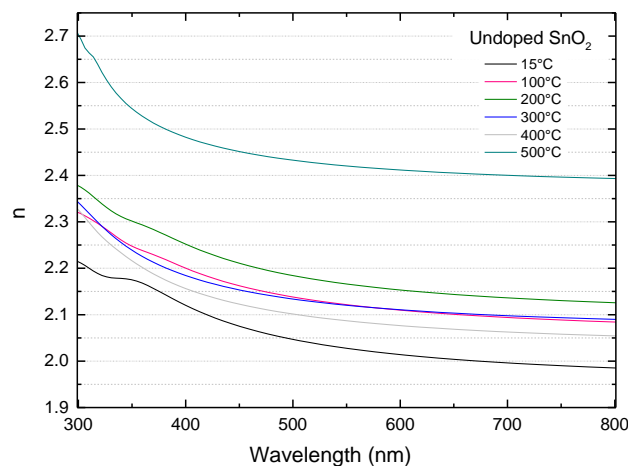
Figure 4.1.2.3. Refractive index if the undoped SnO$_x$ films (8:4) as a function of the deposition temperature

4.2. Nd doped SnO$_x$

4.2.1. Effect of gas flows

4.2.1.1. Synthesis of Nd doped SnO$_x$

In order to produce Neodymium doped SnO$_2$, two discs of pure Nd metal (99.99%), about 70 mg each, were placed on top of the tin target. The study on the effect of the gas during deposition was realised by varying both O$_2$ and Ar gas flows resulting in different Ar/O$_2$ gas flow ratios (R). For these experiments, the substrate temperature was set at 100°C. Table 4.2.1 summarizes the experimental conditions and some measured or calculated physical parameters. In the following, the ratio R will be the variable.

Table.4.2.1. Deposition parameters, thicknesses by XRR and ellipsometry, Tauc gap by ellipsometry and transmission, stoichiometry by RBS of the Nd-doped SnO$_x$ films by sputtering. The deposition temperature was set at 100°C.

Sample label	Ar :O$_2$ (sccm)	R	Thickness /XRR (nm)	Thickness / ellipsom. (nm)	E$_{gopt(E)}$ (eV)	E$_{gopt(T)}$ (eV)	[O]/ [Sn] by RBS
Nd-A	12:3	4	156.2 ± 2	159.6 ± 1.33	2.84 ± 0.1	3.20 ± 0.2	1.8 ± 0.1
Nd-B	14:4	3.5	146.1 ± 2 151.8 ± 2	148.3 ± 2.28	3.44 ± 0.3 2.80 ± 0.2	3.47 ± 0.2	2 ± 0.1
Nd-C	12:4	3	124.8 ±2	122.5 ± 6.9	4.08 ± 0.2	4.08 ± 0.2	2.1 ± 0.1
Nd-D	8:4	2	105.5 ± 1	108.9 ± 3.8	3.91 ± 0. 2	3.95 ± 0.2	2.1±0.1

4.2.1.2. Crystal structure

Figure 4.2.1 displays the typical θ-2θ scan of Nd-doped SnO$_2$ thin films elaborated at 100°C as a function of the gas flow ratio ranging from 2 to 4. The Nd content was estimated to be about 0.62 at. % ± 0.02 for all doped samples.

The film Nd-A produced with R =4 (flowing low oxygen in the chamber) exhibits a broad diffraction band at around 30° , a feature commonly assigned to amorphous or nanocrystalline SnO structure[261, 262] [263] [19] [225]. This spectrum is very similar to that reported above for the undoped SnO$_x$ deposited with O$_2$=3 sccm. However, the spectrum of Nd-A sample does not exclude the presence of SnO$_2$ phase since some diffraction peaks of SnO$_2$ might be present at this range of diffraction angles; therefore it is quite difficult to conclude about the exact composition of this film simply from such

pattern. A similar diffraction pattern is obtained for the film Nd-B deposited at R=3.5 with however the appearance of a narrow peak at 2θ=33.9 assigned to the (101) plane of the rutile SnO$_2$ phase; this is indicating that the film is a mixture of polycrystalline SnO and SnO$_2$. As for the sample deposited with an Ar/O$_2$ ratio of 3 (Nd-C), its XRD pattern displays many well-defined peaks, which are characteristics of a polycrystalline tetragonal rutile SnO$_2$ (according to the JCPDS card no. 00-041-1445 of ICDD). The peak located at 26.44° is attributed to the (110) diffraction, and the peaks at 37.98°, 51.74°, 53.92° are assigned to the (200), (211) and (220) planes, respectively.
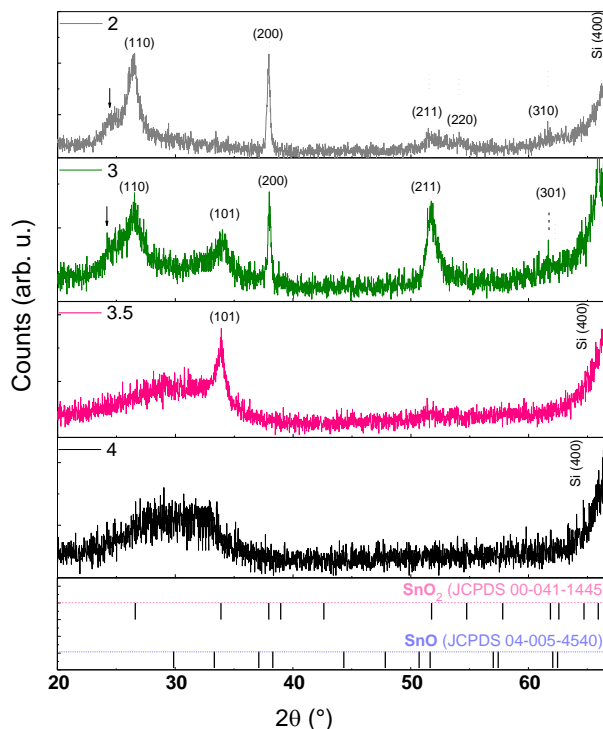
Figure 4.2.1. X-Ray diffraction patterns of Nd: SnO$_x$ films deposited with increasing Ar/O$_2$ gas flow ratio from 2 up to 4. The main peaks are indexed in the rutile SnO$_2$ structure.

Finally, the XRD pattern of the sample made with R=2 (Nd-D) also shows a polycrystalline character of SnO$_2$ with a strong texture along (110) and (200) preferential planes. These XRD data show that crystalline SnO$_2$ rutile phase can be obtained at a quite low deposition temperature (100°C) and by simply tuning the Ar/O$_2$ flow ratio during the sputtering process. This is an interesting result as compared to previous work by Rinnert *et* al.[225] and Pan *et* al.[19] who stated that SnO$_2$ rutile phase could only achieved after a thermal annealing as high as 700°C.

Moreover, the X-ray diffraction data of the Nd-doped SnO$_x$ films also revealed the presence of the weak peak at 24.56° (for the crystalline samples), like in the case of the undoped SnO$_x$ films, and which corresponds to the signature of a ternary phase of SnSiO$_x$. This is most likely resulting from the

inter-diffusion of Si and Sn at the film/silicon substrate interface. This assessment is partially coming from the observation that this peak is not be detected for our films deposited at 100°C on quartz substrate (diffraction pattern not shown here),

Finally, no additional diffraction peaks corresponding to Sn_3O_4, nor metallic Sn, nor other Nd-based spurious phases were identified within the detection limit of our XRD technique. The absence of Nd-related compounds in the XRD patterns suggests that Nd atoms are successfully incorporated into the SnO_x lattices probably thanks to the low doping level (< 1 at. %).

4.2.1.3. Chemical analysis of Nd doped SnOₓ

Besides the tin and oxygen content in the films, it is important to determine the RE concentration present in the films as well as its distribution along the thickness of the layer. Simulation of the RBS spectra was used to determine the effective atomic concentrations. It worth to notice that is quite difficult to extract accurate values of the oxygen content with techniques such as RBS and EDX. For this reason Nd content is evaluated here with respect to the tin content. Therefore the films will have a stoichiometry as $Sn_{(1-y)}O_xNd_y$.
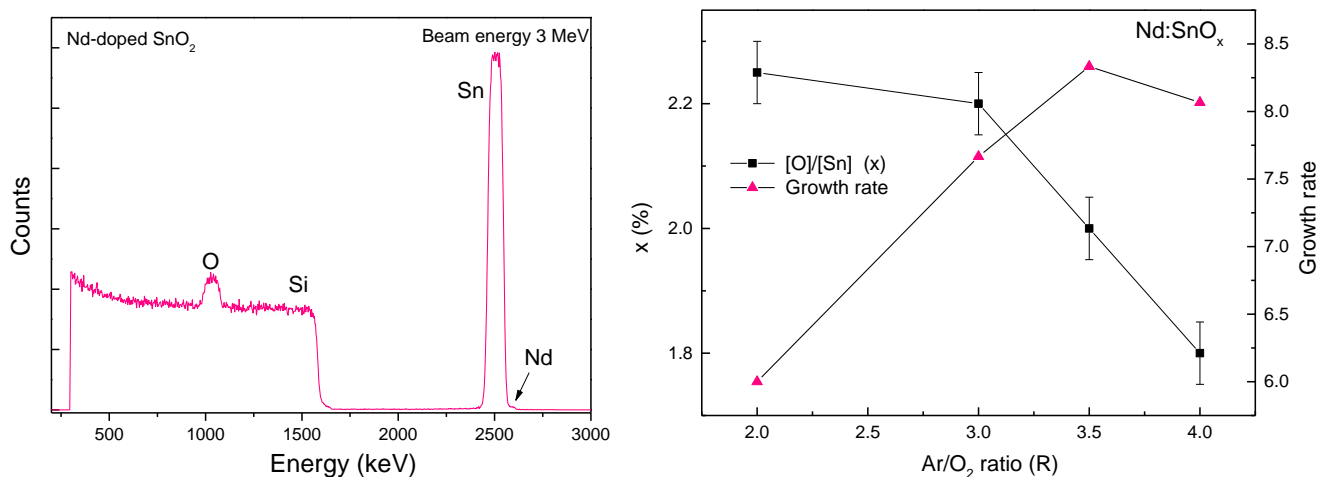
Figure 4.2.2. a). Example of an experimental RBS spectra of Nd-doped SnO_x films of 115 nm, b. Variation of the [O]/[Sn] atomic ratio and the growth rate with the Argon to oxygen gas flow ratio during deposition.

Figure 4.2.2.a displays the RBS spectrum of the Nd-doped SnO_x film produced with R=4 (thickness of 115 nm). This is a typical example of RBS spectra of this serie. Since the Sn and Nd have comparable atomic numbers (50 and 60, respectively), It was very difficult to extract the Nd concentration from the RBS data. Nd peak being located at the tail of the Sn signal, it is impossible to determine the Nd atomic distribution within the film. Yet, we have simulated the RBS spectrum of Figure 4.2.2 .a using SAM software, and we estimated the Nd concentration to be about 0.6 at.%. A comparable Nd content is found for all films whatever is R value.

The chemical composition and therefore the stoichiometry of the films have been successfully identified and presented in figure 4.2.2.b. The oxygen poorer structure exhibited an [O]/[Sn] ratio of 1.6, which is consistent with the XRD results. It is difficult to decide if the film possesses a SnO or SnO$_2$ structures from an atomic ratio. We can easily have a SnO$_2$ structure rich with oxygen vacancies or SnO structure with some oxygen excess in the interstitial sites or both structures with a lot of defects. Anyway, the [O]/[Sn] ratio is found to increase by increasing R (incorporating more oxygen atoms into the structure). This result is totally coherent with what we reported above. The structure is trending from an oxygen poor to oxygen rich film just by changing the Ar/O$_2$ gas flow ratio during deposition. With R=2, the stoichiometry of the films is written as $SnO_{2.25\pm0.05}Nd_{0.62\pm0.06}$.

To cast inner light on the real composition of the films in term of oxides, XPS analysis was carried out on the sputtered SnO$_x$:Nd samples. XPS analyses is offering valuable information on the chemical environment of the atoms and therefore, help in the identification of their valence from their binding energies. Usually a careful look to the high resolution XPS valence-band (VB) spectra provides a rapid identification of the most abundant oxide in the films. For instance, SnO and SnO$_2$ can be unambiguously distinguished through very distinct signals [264, 265].

Figure 4.2.3 plots the valence-band photoemission spectra of our Nd-doped SnO$_x$ thin films as a function of the gas ratio R. The films deposited with low Ar/O$_2$ ratio (R=2 and 3) present three distinguished bands: The most prominent one located around E_B = 5eV noticed B in the figure 4.2.3 is originated from the O *2p* derived levels (bonding or nonbonding); The feature around E_B = 8 eV labelled C is due to the *ppσ* hybridization between Sn *5p* and O *2p* orbitals; The band around E_B = 11 eV (noted D) is mainly derived from bonding Sn *5s*-O *2p* states[259]. An additional feature around E_B = 3 eV (named A) appears for the film deposited with R=3,5 commonly assigned to antibonding Sn *5s*-O *2p* states[265]. Increasing further the ratio R to 4 (less incorporated oxygen in the film) leads to enhancement of the intensity of band A as well as to the decrease in the intensity of the other bands. In addition, a shift of band D towards lower binding energies is observed.
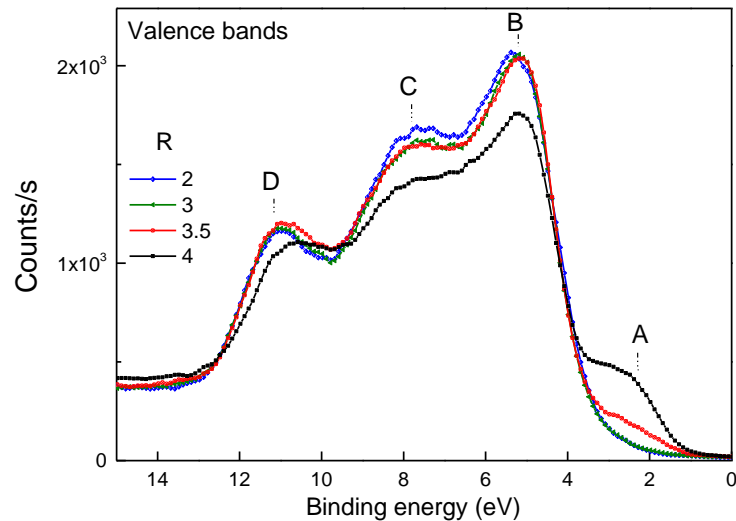
Figure 4.2.3. XPS spectra of the valence-band of the Nd-doped SnO_x sputtered thin films versus the Ar/O_2 gas flow ratio (R).

The XPS valence-band (VB) spectra of films made with R=2 and R=3 fit that of a pure SnO_2 structure. This is expected as these films are oxygen rich. At the opposite site, given the XPS signatures for the film grown with R=4, it can be conclude that this film has a SnO structure. Indeed, previous reports by Themeline *et* al.[265] showed that the most notable difference between SnO and SnO_2 in the VB spectra is the appearance of the peak at lower binding energy of the VB (band A), characteristic of SnO[22]. In fact, these Sn 5s derived levels that form the bottom of the conduction band in SnO_2 become a part of the occupied states in the top of the valence band in SnO.

Interestingly is the XPS response of sample made at R=3,5 where both features of SnO_2 and SnO structures are observed. This behaviour indicates the formation of a structure composed of a mixture of SnO_2 and SnO oxides. Our results show that a decrease of the Ar/O_2 flow ratio R from 4 to 2 leads to a structure change from SnO to SnO_2.

Additional surface analyses by the Near Edges X-ray Absorption Fine Structure spectroscopy (NEXAFS) can provide information about local bonding environment of the oxygen and tin constituent elements. Figure 4.2.4.a displays the O 1s and Sn $M_{4,5}$ NEXAFS spectra of the Nd doped films, obtained in the total electron yield (TEY) mode. The plotted O 1s absorption lines of the films with R= 4 and R= 3,5 are found to match spectacularly with that of the SnO reference, whereas those of the films with R= 2 and R= 3 exhibit SnO_2 signal as compared to the reference. This is unexpected for R=3.5 comparing to XPS results shown above.
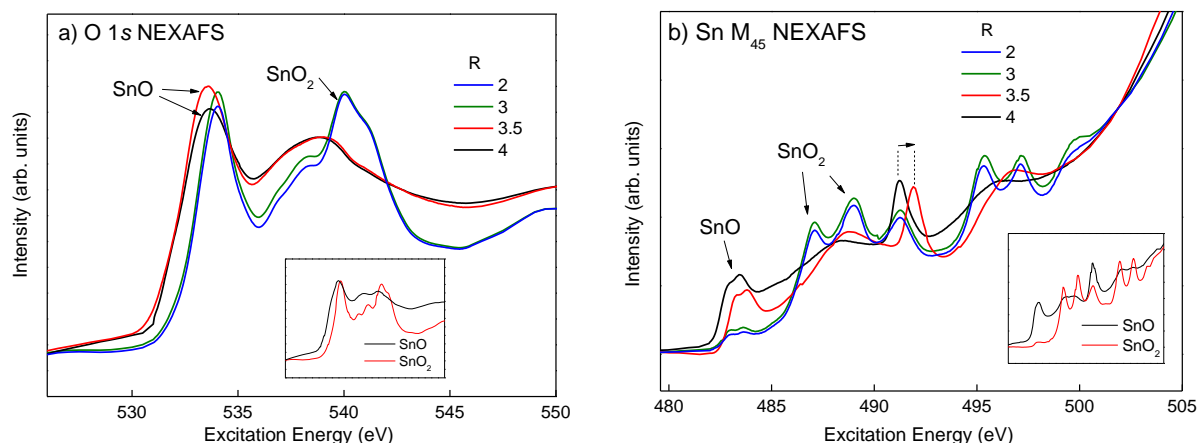
Figure 4.2.4. **(a)** O$_{1s}$ and Sn M$_{4,5}$ **(b)** NEXAFS measurements of Nd-doped SnO$_x$ samples versus the Ar/O$_2$ gas flow ratio. The spectra of SnO and SnO$_2$ powder shown in the inset of each graph were added for comparison.

The Sn M$_{4,5}$ absorption spectra shown in figure 4.2.4.b confirm a SnO structure for R=4 and a SnO$_2$ structure for R=2 and 3. The data for the film at R=3.5 is found to behave differently. A chemical shift about 0.7 eV in the Sn M$_{4,5}$ absorption peak at 491 eV is clearly noticed relative to the other films, most likely due the presence of secondary SnO$_2$ phase oxide.

To complete our study on the local configuration within the Nd-SnO$_x$ fims, the NEXAFS analyses were performed to determine the coordination and the oxidation degree of Nd atoms into the different matrices. The Nd M$_{4,5}$ NEXAFS experimental spectra are reported in Figure 4.2.5 for the different ratios R. MLFT calculations for Nd^{3+} and Nd^{4+} are also plotted for comparison.

At first glance, by comparing to Nd^{3+} and Nd^{4+} calculated spectra, the shape of the experimental spectra matches more closely to Nd^{3+}, particularly the M4 absorption peaks. These simulated spectra were calculated for atomic Nd^{3+} and Nd^{4+} ions in isolated space without considering any crystal field effects from the SnO$_x$ lattice. One can remark that the energy positions of peaks in calculated and measured spectra do not line up exactly. This could be due that the calculation does not take into account the M4-5 peak splitting. Therefore, it is more appropriate in this case to consider only the spectral shape and number of peaks, mainly at the M4 edge. In the calculated spectra, Nd^{4+} exhibits four main bands with a sharp large band in the centre, while Nd^{3+} has three main bands. On the other hand, the measurements show clearly three band structure at the M4 edge, suggesting that the samples are in primarily Nd^{3+} oxidation state. If there was a significant fraction of Nd^{4+} in the samples, we would expect to see some evidence of the prominent middle peak in the measurements, unless its concentration is too small to be detected.
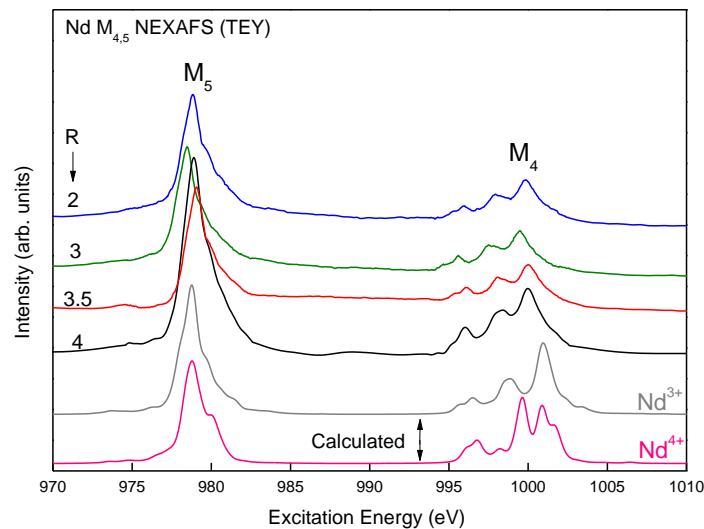
Figure 4.2.5. Nd M4,5 NEXAFS measurements of Nd-doped SnOx samples versus for different gas flow ratios. MLFT calculations for Nd^{3+} and Nd^{4+} are included for comparison.

Figure 4.2.5 clearly shows a chemical shift of the M4,5 lines while the line shapes remain unchanged. Since Nd M4,5 NEXAFS measures electron transitions from $^3d_{10}{}^4f_n$ to $^3d_9{}^4f_{n+1}$ state, this chemical shift with similar line shape can be caused by (i) a compensating effect of the shift of Nd 3d level due to different Madelung potential on Nd ion in SnO and SnO_2, and (ii) the screening of the Nd 3d core-hole potential by free charge, possibly due to oxygen vacancies[266]. Indeed, XAS measurements are subject to a core hole in the final state, meaning the energy position of the unoccupied states is affected by a Coulomb interaction with a positive hole in core electronic states. The effect of this interaction is a shift of the XAS absorption edge. The importance of the shift is also affected by the number of the other electrons in the system, which has a screening effect to reduce the Coulomb interaction. As stated above, the number of electrons may change due to the number of oxygen vacancies, which behave as free charges. The different Madelung potential refers to a differing electrostatic energy that is binding a particular Nd site to its SnOₓ lattice. Nd ions in different SnOₓ lattices will be affected by a different electrostatic binding which may shift the M4,5 peak position. The NEXAFS data confirm then that decreasing the Ar/O₂ gas flow ratio from 4 down to 2 results in the structural change from amorphous SnO to polycrystalline SnO_2. This can tune the local bonding environment around Nd dopants without changing their ionic valency. These results will help understanding the photoluminescence results presented below.

4.2.1.3. Optical properties of Nd doped SnOₓ

As shown in the section above, changing the oxygen flow during deposition induces radical changes on the structural properties; the material can be tuned from SnO to SnO_2 for both undoped and Nd-

doped. As the final application of these layers is as transparent windows in solar cells, it is important to determine their optical properties such as transmittance, optical band gap and refractive index. Moreover, the doping with rare earth elements is expected to induce a significant impact on the density states at the band edges and therefore on the absorption of the films. From the antireflection point of view, it is important to get a glimpse on how the refractive index varies with the oxygen content in the films. Finally, for the photon conversion, it is crucial to identify the wavelengths domain where the films absorb. In the following the transmittance recorded in the UV-VIS-NIR region as well as the refractive index of the Nd doped layers are presented.

Spectroscopic ellipsometry measurements were carried out on the Nd-SnOx films produced by sputtering. The refractive index, the extinction coefficient and the absorption coefficient of the films were then extracted versus the gas ratio R. Figure 4.2.6 gives the data for the refractive index. A strong change is clearly observed. At first sight, two types of materials can be distinguished. The sample Nd-A deposited with R = 4 exhibits high the refractive index values over the UV-visible range. A similar curve is reported in the section 3.1.3 concerning the undoped films. Such high n can be a signature of a material with a SnO phase. For the films deposited with R= 2 and 3, having a SnO$_2$ structure, much lower refractive index values are obtained. For instance, n at 600 nm is about 2.14-2.15 for Nd-C and Nd-D while it is close to 2.3 for Nd-A. When comparing these data with those of the pure SnO$_2$ films, it seems that doping with Nd enhances the n values in the visible region. On the other hand, the refractive index curve of sample Nd-C (R=3.5) is located just in between the other curves most probably because the sample is composed of a mixture of SnO and SnO$_2$.
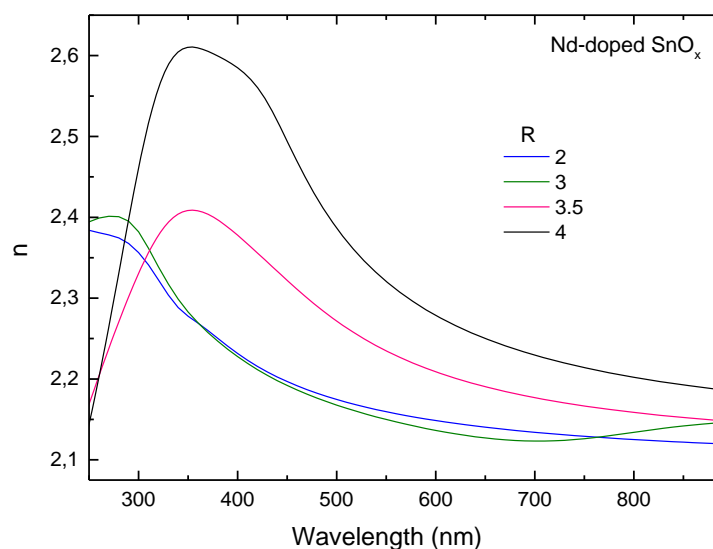
Figure 4.2.6. Refractive index of the Nd-doped SnO$_x$ thin films as a function of the photon wavelength deduced from the ellipsometric data

The extinction coefficient and consequently the absorption coefficient of the Nd-SnOx films were also deduced from the ellipsometric measurements. The band gap values for the different films were then calculated using the Tauc plot procedure as described in chapter 1. The extracted values $E_{gopt(E)}$ are summarized in Table 4.2.1. The sample Nd-A containing less oxygen content is exhibiting a low band gap equal to 2.84 eV. This is well in line with the structural analysis reported above for this sample that demonstrated the formation of a SnO structure known to have a low bandgap. by decreasing the Ar/O$_2$ gas flow ratio to 3, the sample exhibit an amorphous and crystalline structure, so, the film was fitted with two models, the AnF to fit the amorphous part which had a value of 2.80 close to the film with R=4. When using the Ad model to fit the crystalline part, we found a value of 3.4 eV which is more close to a SnO$_2$ material. We do think that both results are correct since each model fits a different part of the structure. For application of the doped layers as antireflection coating, the optimization of the film thickness is required in order to have a better optical window around 600 nm where the maximum of the incident solar spectrum intensity is. For example, Nd-SnO$_2$ films of about 75 nm in thickness give the best choice for 0 % reflectance at 600 nm.

The transmission spectra of the deposited Nd-SnO$_x$ films are plotted in figure 4.2.7a versus the gas ratio R. The spectra were measured using a spectrophotometer lambda 19 over a large wavelength range but we report only the part in the 200-850 nm range, as no particular features were found for wavelengths larger than 850 nm. Once more, the data show that the optical absorption is very sensitive to the oxygen content in the deposited films.

Figure 4.2.7. Transmission spectra of Nd-doped SnO$_x$ films synthesized with different Ar/O$_2$ gas flow ratios R

For the film deposited with R= 4, the transmittance spectrum suggests an absorption edge at about 400 nm indicative of a low band gap oxide. At the opposite side, the films elaborated with R=2 and 3 show an absorption edge in the 275 nm range, approaching that of a wide band gap SnO$_2$ oxide. For R=3,5

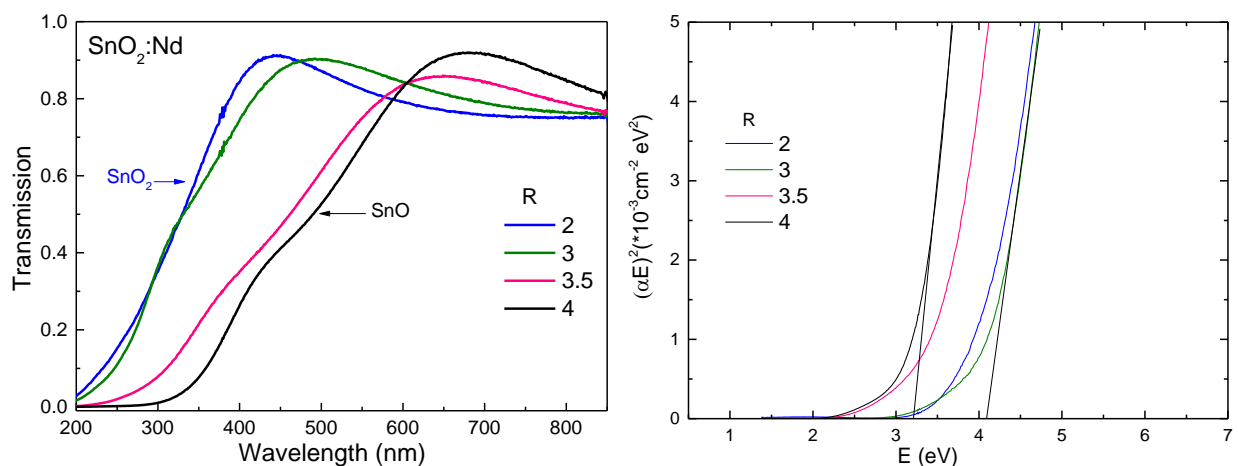the transmission spectrum is lying between the two cases mentioned before, and suggests a bandgap of a material with a SnO$_2$ secondary phase present in the SnO film. Extraction of the optical band gap from the transmittance was attempted after conversion into absorbance and the use of the conventional Tauc plot. However, it is important to underline that the absorption edges of this series of samples are laying in wide ranges of wavelengths; in consequence the extrapolation of the linear part of the Tauc plots is very delicate. Yet, we have calculated E$_{gopt(T)}$ from the plots in Figure 4.2.7b and the values are also given in Table 4.2.1. The E$_{gopt(T)}$ values are quite consistent with the ellipsometric data (E$_{gopt(E)}$).

Overall, these findings unveil that SnO films are able to absorb photons with energy higher than 2 eV (< 600nm), while the SnO$_2$ films are transparent to photons with energy lower than 3 eV (> 410nm).

As a summary of this part, the structural and optical properties carried out so far on the Nd doped SnO$_x$ films allow to conclude that Nd atoms can be inserted into three different SnO$_x$ matrices by simple change of the Ar/O$_2$ gas flow ratio R during the sputtering process. Namely SnO (R=4), SnO$_2$ (R= 2 and 3) and a mixture of SnO and SnO$_2$ (R=3.5) can be produced. The question is what about the optical activity of Nd atoms within these different matrices ?

4.2.1.4. Photoluminescence properties

In order to get a glimpse on the optical activity of the rare earth Nd embedded into the different SnO$_x$ matrices, Photoluminescence (PL) spectroscopy were performed. The UV-Vis-NIR room temperature PL spectra recorded under a He-Cd laser excitation of λ = 325 nm (3.81 eV) for films with R ranging from 2 to 4 are displayed in Figure. 4.2.8.

It is interesting to underline that, regardless of the matrix' structure, all Nd doped SnO$_x$ films exhibit a broad luminescent band covering a large part of the UV-Visible spectrum ranging from 350 to 700 nm with however variable intensities. This UV-Vis emission is originated from the host matrix. On the other hand, only the SnO$_2$ oxygen richer film deposited with R=2 has demonstrated optical emission In the Near Infrared (NIR) spectral region where three intense and well-defined peaks are recorded. This NIR emission features are commonly assigned to radiative transitions of the 4f electrons of Nd rare earth. Similar emission spectra were reported in the case Nd doped SnO$_2$ nanoparticles as shown in chapter 1 [267].
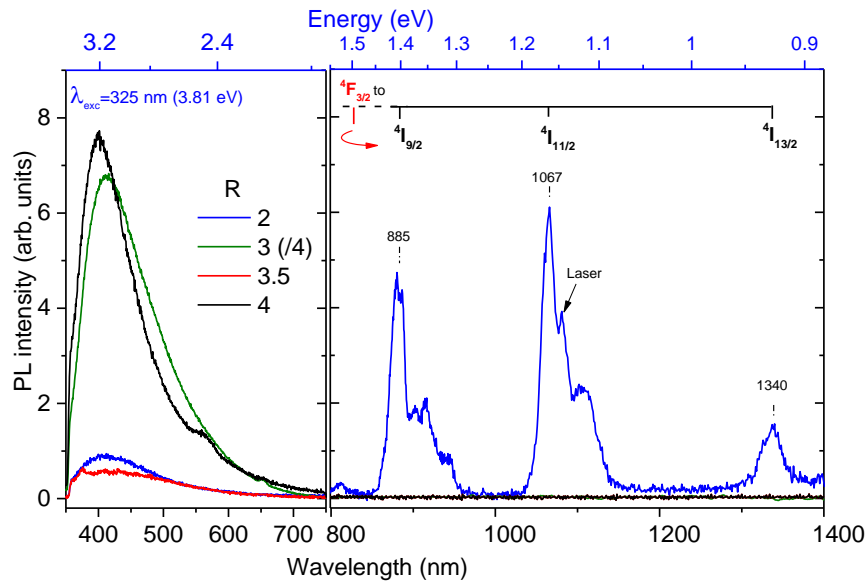
Figure 4.2.8. Room temperature UV-to-NIR photoluminescence spectra of Nd:SnOₓ thin films for different gas flow ratios: 2, 3 3.5, and 4 under an excitation wavelength at λ=325 nm.

Let's first focus on the UV-Visible photoluminescence of the Nd doped synthesized layers.

A closer look to the broad emission band of the SnO film (R=4, sample Nd-A) indicates the presence of two contributions, one strong band centered around 430 nm and a second less intense centred around 560 nm. It is found that both of the bands are arising from oxygen vacancies together with tin interstitial atoms and inter-grains related defects [200, 245]. In fact, oxygen vacancies, which are present with a high density in such structure, represent the most prominent defects in SnO that can form localized deep levels around the Fermi level. The electrons transitions from these intermediate states to the valence band induce efficient radiative recombinations resulting in the strong emission band recorded in the UV-to-Visible part of the spectrum. Surprisingly, by increasing the oxygen content (R=3.5, sample Nd-B)), the intensity of this band dramatically decreases suggesting fundamental changes in the defects type. This behaviour is however fully consistent with the film structure composed of a mixture of SnO and SnO$_2$ phases. This means that the non-radiative recombinations whose the origin are multiple such as point defects, dislocations, grain boundaries, surface/interface states are prominent relative to the radiative recombinations. By increasing further the oxygen content (R=3, sample Nd-C), the defects-band increases spectacularly. The signal' intensity of this spectrum was divided by 4 for a better clarity. It is worth reminding that at this deposition condition, the structure switched to SnO$_2$. Since the UV-Vis emission for samples R=4 and R=3 have similar shape and peak position, we speculate that the radiative recombinations have the same origin (oxygen vacancies) in SnO and SnO$_2$ structures, with however different densities.

For the case of the SnO$_2$ made with R=2 (the most oxygen richer in this study), a dramatic decrease of the UV-Vis emission accompanied with the appearance of three strong bands in the NIR region is

noticed. The group emissions located at 885, 1067 and 1340 nm is usually attributed to the 4f electron transitions form the $^4F_{3/2}$ energy level to the $^4I_{n/2}$ levels of the Nd^{3+} ions with n equal to 9, 11 and 13, respectively. Moreover, it is interesting to notice that the Nd emission peaks at 885 and 1067 nm are followed by a second less intense band indicating the splitting of the $^4I_{9/2}$ and $^4I_{11/2}$, respectively, particularly due the SnO$_2$ crystal field splitting effect. Such narrow and intense photoluminescence peaks give an experimental evidence of the good insertion and the efficient optical activation of the Nd^{3+} ions into this structure. The absence of Nd-related features for the other structures (R= 3, 3.5 and 4) in the NIR domain suggests that either Nd atoms are not inserted into site position or they are not optically active.

The presence of the 3+ oxidation state feature of Nd assessed by the NEXAFS analysis shown above indicates that Nd^{3+} ions are well inserted within the deposited layer regardless of R value and furthermore they possess an energy level structure as that in LaCl$_3$ crystals. However this observation does not mean that the impurity ions are optically active. The local environment of the rare earth ion plays a dominant role on the optical emission of the Nd^{3+} ions.

In fact, the electric dipole transitions between the intra-4f states are naturally forbidden for the isolated rare earth ions [176, 184]. However, this selection rule can be relaxed if one considers the effect of the crystal field, which is responsible for states mixing with different parities. In Judd's work[159], it is shown that the electric dipole transitions within the 4f shells of the RE ions can be permitted only if the RE ions are not positioned in the inversion centre of the lattice. Moreover, due to the parity forbidden of the 4f-4f transitions, the optical absorption cross section of lanthanides Ln^{3+} is quite small, typically in the order of 10^{-21} cm^2. When exciting the luminescent lanthanide ions, their absorption is limited to narrow lines. One effective way to overcome this problem is sensitization by/via a host matrix through an energy transfer. In this context, large bandgap semiconductors such as ZnO, TiO$_2$, In$_2$O$_3$[268-271] and here SnO$_x$ are very good candidates. The overall process is somehow complicated and involves several mechanisms and energy levels. Clarifying the sensitization process and identifying the exact origin of the efficient photoluminescence lines, particularly those recorded for the SnO$_2$ oxygen richer film are tackled below.

In order to have a deeper insight on the optical activity of the rare earth versus the host matrix, PL excitation spectroscopy (PLE) was carried out for the two extreme structures, namely for R=4 (SnO structure) and R=2 (SnO$_2$ structure) films. The experiment consists in recording the Nd emission intensity measured at 885 nm while varying the excitation wavelength from 250 to 650 nm. The PLE spectra are displayed in figure 4.2.9.
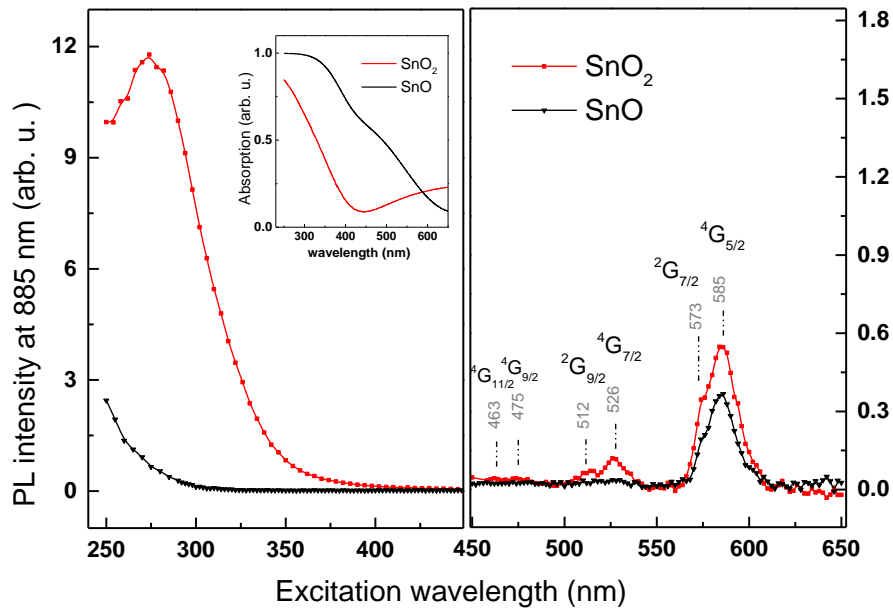
Figure 4.2.9. Room temperature photoluminescence spectra of Nd: SnO$_x$ thin films with R=2 (SnO$_2$) and R=4 (SnO) as recorder at 885nm and under excitation wavelengths from 250 to 650nm.

The PL emission under excitation in the 250-450 nm range exhibits spectra with strong difference in intensity for samples SnO$_2$ (R=2) and SnO (R=4) in addition to a blue shift. In contrast, the emission spectra obtained under excitation in the visible (450-650 nm) show comparable peak positions for SnO$_2$ and SnO samples accompanied with a slight reduced PL intensity for the second one. The bands correspond to emissions resulting from direct excitation of 4f electrons of Nd^{3+} from the $^4I_{9/2}$ ground state to higher energy levels (Figure 4.2.10). The emissions centred around 463, 475 nm corresponds to the $^4G_{11/2}$ and $^4G_{9/2}$ energy levels, while the emission group at 512 and 526 nm coincides with the $^2G_{9/2}$ and $^4G_{7/2}$ levels. Finally the emission under excitation at 573 and 585 nm translates the $^2G_{7/2}$ and $^4G_{5/2}$ levels, respectively. Yet, the energy level positions of these emissions are found to be slightly shifted when compared to the expected ones for an ideal LaCl$_3$ crystal. This can be understood in term of the crystal field effect since the position of the rare earth electronic levels are influenced by the spin-orbit interactions[184].

Given the PLE response in the visible range (450-650 nm), it is obvious that Nd^{3+} ions are optically active in both SnO and SnO$_2$ matrixes. However the overall recorded PL intensity in this region is much weaker than that collected under UV excitation (250-450 nm) especially for the SnO$_2$ sample. Furthermore, we have found that that emission spectrum of Nd in SnO$_2$ structure matches with its optical absorption at wavelengths below 450 nm (see insert in figure 4.2.9).

The detection of the PL emission in both UV and visible parts for sample Nd-D (R=2) suggests an efficient resonant energy transfer from the host SnO$_2$ matrix to the Nd^{3+} ions. Such process is

schematically illustrated by the left part of Figure 4.2.10. The energy transfer can occur in different ways: a 4f electron of Nd^{3+} can be efficiently excited from the $^4I_{9/2}$ ground state to higher energy levels thanks to the exciton recombination resulting from (i) the band to band transitions, or (ii) through transition from localized states created by oxygen vacancies near the conduction band to the valence band. In the case of Nd doped SnO$_2$, the indirect excitation is markedly 22 times stronger relative to the indirect one, indicating the importance of the sensitization through the SnO$_2$ host matrix.
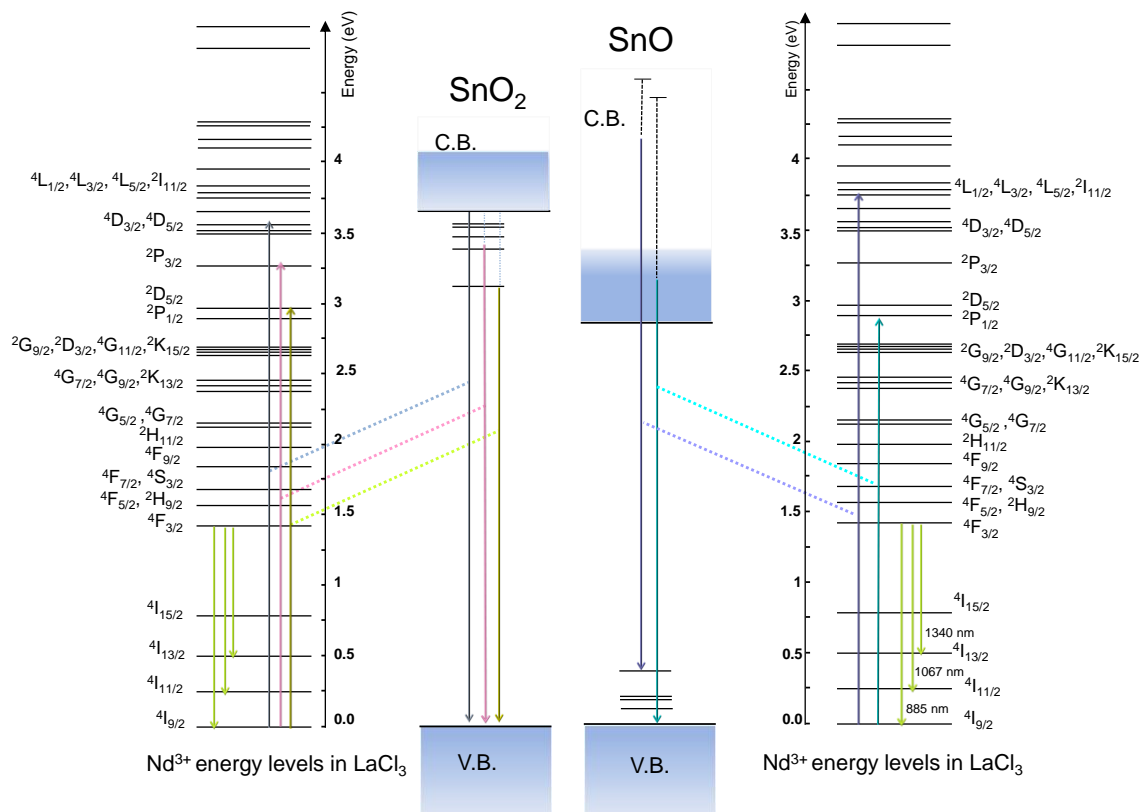
Figure 4.2.10. Energy transfer mechanisms and transitions occurring between SnO$_2$ left) and SnO (right) matrix and Nd^{3+} ions

As for the SnO sample, despite the strong absorption of the structure in a wide wavelengths range (see insert of Figure 4.2.9), only a weak Nd emission was collected under excitation with high-energy UV photons (λ < 300 nm). Presently, such result explains the absence of Nd response in the PL spectra recorded under 325nm excitation wavelength (figure 4.2.8). Noteworthy, the comparable emission intensities for sample Nd-A over the whole wavelengths range suggest that both the direct and indirect excitations of Nd^{3+} ions in SnO structure have almost identical probabilities;Since the SnO host matrix has a small band gap with a p-type character, the recombination of excitons during the UV excitation step will involve high energy levels above the conduction band and some localized defect states near the valence band.

As a summary, thanks to PL and PLE measurements, we demonstrate that UV photons are successfully converted into NIR photons as a consequence of inta-4f transitions of the RE ions present in the SnO_2 host matrix. The quantification of the conversion efficiency via this energy transfer process is underway.

4.2.2. Effect of deposition temperature

4.2.2.1. Structural properties

The Nd doped SnO_2 films were deposited at different temperatures ranging from 15 to 400°C. Table 4.2.2.1 gives the films thickness of these films as deduced from the XRR method. Thanks to the control of deposition rate, the films were produced to have comparable thicknesses.

In the following the structural properties of these films will be discussed as well as the determination of phase composition and Nd ionic state.

Figure 4.2.2.1 displays typical X-ray diffraction patterns of the Nd-doped SnO_2 thin films grown at different temperatures. As can be observed, the film deposited at 15°C exhibits a broad diffraction band that covers a wide diffraction angles range (from 25° to 38°) which could suggest at first glance an amorphous structure. Furthermore, it is quite difficult to distinguish whether there are different SnO_x phases as numerous diffraction peaks of SnO and SnO_2 can be present in this range. To get a deep insight on this structure, a measurement by Transmission electron microscopy (TEM) was performed (not shown here) which revealed a strongly fine-grained polycrystalline film in addition to be randomly oriented grains. At a deposition temperature of 100°C, two sharper peaks appear at 26.32° and 37.94° meaning that the film has a SnO_2 polycrystalline structure. By referring to the JCPDS card n°= 00-45-1445, the films are found to be highly textured and preferentially oriented along the (110) and (200) planes, respectively, with comparable intensities. By increasing the deposition temperature to 200°C, the relative intensities of the (110) and (200) peaks remain comparable but three small peaks corresponding to the (211), (220) and (310) directions appeared at 51.56°, 54.38°, 61.64°, respectively. At 300°C no additional diffraction peaks were detected, however the intensities of the peaks increase, meaning that the film has a better crystalline quality. More interestingly, the (110) plane becomes prominent against the (200) plane suggesting that the texturing along this direction is more favourable. The same behaviour is observed for the film prepared at 400°C. Furthermore, It is important to point out that by increasing the deposition temperature, the full width at half maximum (FWHM) for the (110) plane is found to decrease while it increases for the (200) direction one. As the FWHM is translating the crystallites size, this result means that the growth along the (110) plane is prominent when increasing deposition temperature resulting in larger grains

(see table 4.2.2.1). In contrast, grains with (200) direction are getting smaller with increasing deposition temperature.
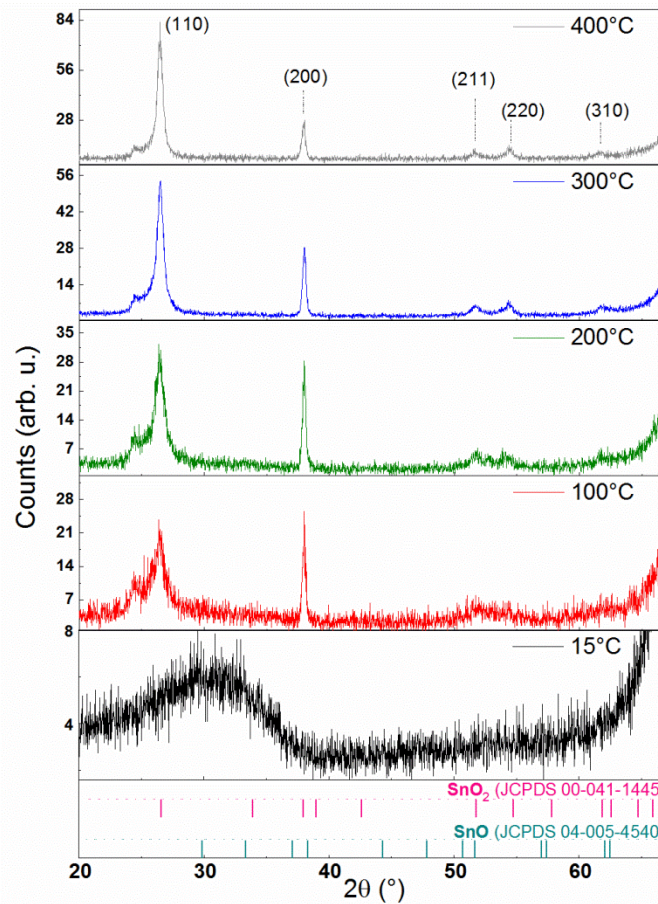
Figure 4.2.2.1. XRD diffraction patterns of Nd-doped SnO$_2$ thin films for different deposition temperatures

It can be noticed that a spurious peak appears at $2\theta = 24.36°$ whose the intensity is found to increase with respect to the deposition temperature. At first glance, this peak can be attributed to the formation of Sn and Si composite at the film-substrate interface. Films deposited on quartz substrates were also analysed by XRD (not shown here) but no such diffraction feature was found which confirms our assumption. On the other hand, neither secondary SnO phase nor Nd oxides have been observed in the detection limit of our XRD setup suggesting that Nd atoms are well inserted into the SnO$_2$ host matrix.

In order to have further insight on the crystalline structure evolution with the deposition temperature, transmission electron microscopy (TEM) observations were carried out on the samples deposited at 15 and 200°C. Figure 4.2.2.2 show the cross section bright field images of the two layers. Both samples are homogeneous, with a columnar like growth mode and have thicknesses of about 67 and 96 ± 2nm for 15 and 200°C deposition temperature, respectively. Although the surfaces are rather flat, a slightly larger roughness is observed on the sample grown at 200°C, in agreement to what already observed on high temperature deposited ZnO [256]The same observations can be also made from the

corresponding high resolution images. Both samples show a clear polycrystalline character, with columns well visible, especially in the high temperature deposited sample. Their width is about 15 nm. It is noteworthy to underline the well visible atomic planes in the low temperature film suggesting that the large peak in the corresponding XRD diffractogram is mainly due to a small crystallite size. The polycrystalline character is also unambiguously evidenced by the electron diffraction patterns (figure 4.2.2.3). At low temperature however, the intensity of the SnO$_2$ diffraction rings is weak suggesting small crystallites. Few more intense spots on these rings are observed mainly out of the growth axis (blue arrow in figure 4.2.2.3). These rings are much more visible in the 200°C deposited sample, in agreement with the XRD pattern

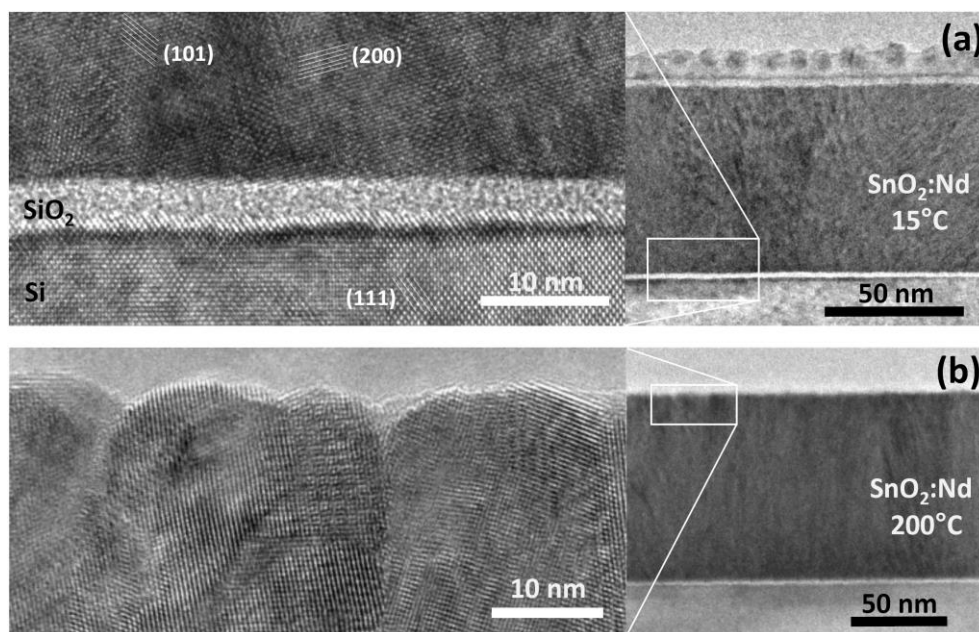**Figure 4.2.2.2.** Cross section TEM image of the Nd-doped SnO$_2$ films grown at 15°C (a) and 200°C (b). The insets show details of the layer/substrate interface and the top of the layer, respectively.
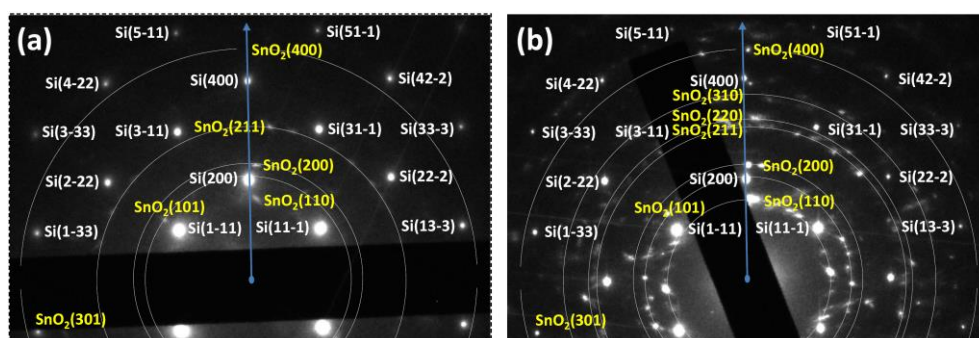

Figure 4.2.2.3. Electron diffraction patterns recorded on the Nd-doped SnO$_2$ films grown at 15°C (a) and 200°C (b). The dotted white circles are a guide for the eyes. The blue arrow stands for the growth direction.

To get more insight on the bonding of atoms within the Nd-doped SnO_2 films, high XPS experiments were applied on the deposited films. This analysis will provide us information on the local bonding environment and thereby the oxidation states of the different atoms with the layer. It is well-known from literature that Sn might exist in two oxidation states: Sn^{2+} in SnO and Sn^{4+} in SnO_2 [264]. And the best way to distinguish between the two structures using this technique is to have a closer look on the valence band (VB) spectra, characterized by very different binding energies features[22, 264, 272].

The high resolution XPS valence band spectra of the Nd-doped films at different deposition temperatures are given in Figure 4.2.2.4.a. As it can be clearly seen from the spectra, all samples exhibit similar binding energy (E_B) signals whatever is the growth temperature. Three main features can be distinguished, which are characteristics of SnO_2, translating the spin-orbit interactions between Sn and O atoms. The most intense band situated at E_B= 5 eV (i) originates from bands that have O $2p$ bonding or non-bonding character while the second band around 7.9 eV (ii) results from $pp\sigma$ hybridization between Sn $5p$ and O $2p$ orbitals. The intermediate states between E_B= 10 and 12 eV (iii) originate mainly from strong interactions between Sn $5s$ and O $2p$ (bonding) orbitals[259]. Similar VB spectra were reported by Lau and Wertheim [264]and by Themeline *et* al. in a detailed XPS study on tin oxides [265]. The fact that all samples exhibit similar features and positions indicates that all our films are mainly composed of SnO_2 structure whatever the degree of crystallization.

Concerning the Nd oxidation state, the XPS experiments were recorded in the 960-1050 eV region where Nd levels are expected to occur [260, 273]. Figure 4.2.2.4.b shows the Nd $3d$ spin-orbit doublet recorded from the high-resolution XPS spectrum, which corresponds to the $3d_{3/2}$ and $3d_{5/2}$ peaks positioned around 1004 and 982 eV, respectively. To avoid the overlap between the Nd $3d_{5/2}$ and OKLL Auger emission peaks that have a very close positions, the signal of the 3d core level was subtracted from the main signal.
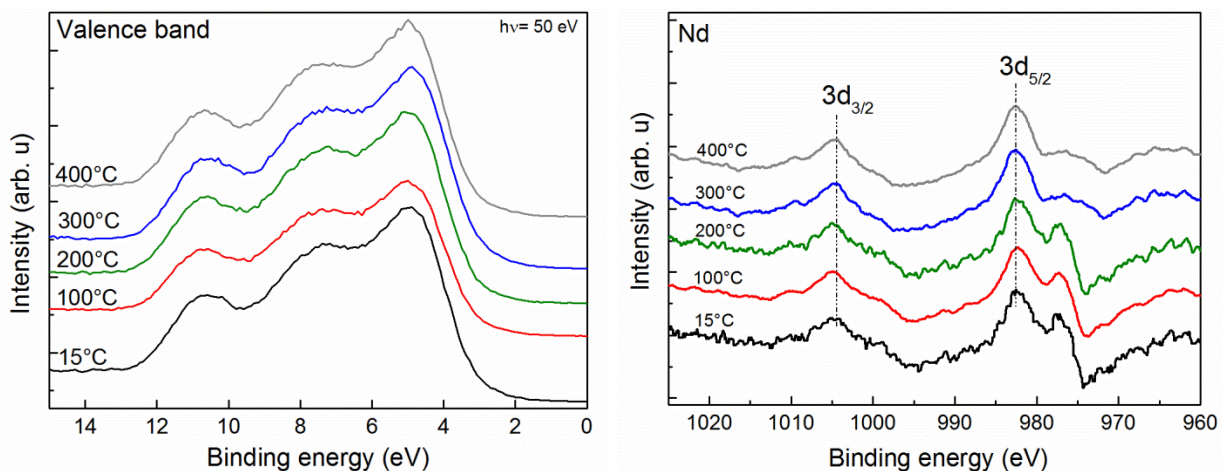
Figure 4.2.2.4. Valence band spectra **(a)** and high resolution Nd 3d core level XPS spectra **(b)** of the Nd-doped SnO_2 films deposited at different temperatures.

As in the case study of the valence bands (Figure 4.2.2.4a), the Nd 3d spin-orbit doublet also exhibits features with comparable intensities for all samples. It is found that the Nd 3d spectra have similar shape and same binding energy positions as that of an Nd$_2$O$_3$ [274] which strongly suggests that the 3d core level of the Nd atoms is bounded to oxygen, and reveals their presence in the +3 valence state[260]. This means that the Nd atoms possess an energy level structure as that in LaCl$_3$ crystal[146, 151]. In the following, this state will be labelled Nd$^{3+.}$

4.2.2.2. Optical properties

We have investigated the optical transmission in the UV-Visible-NIR region of the Nd-SnO$_2$ layers deposited on quartz substrates. The aims are to check the transparency of the layers to be used as TCOs, to evaluate the absorption in the UV region for possible photon conversion and also to deduce the optical energy bandgaps of the films. Figure 4.2.2.5.a shows the optical transmission of the Nd-doped SnO$_2$ thin films for different deposition temperatures.
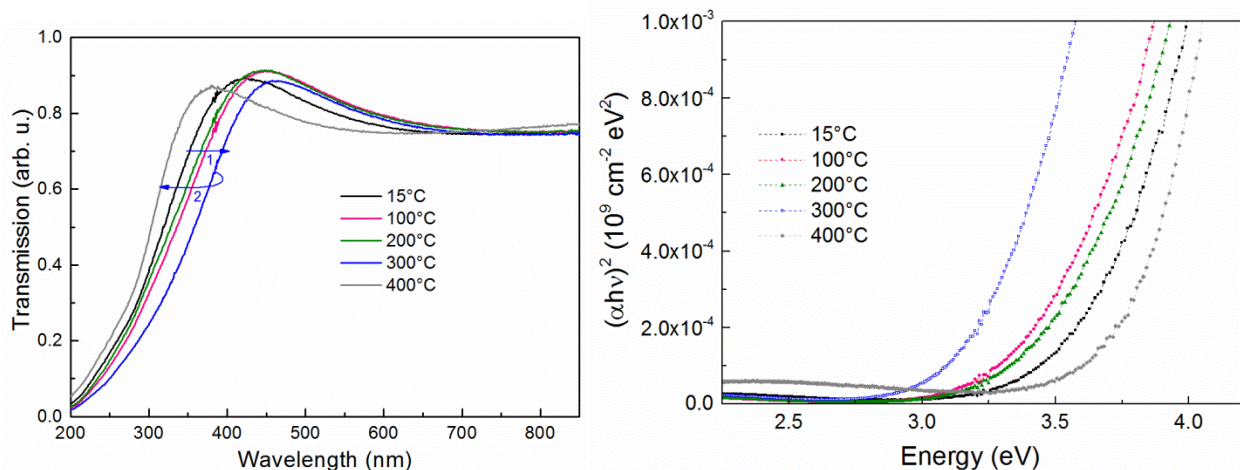
Figure 4.2.2.5. a. UV-Vis optical transmission of Nd-doped SnO$_2$ doped thin films for different deposition temperatures b. Influence of the deposition temperature on the Tauc-gap of the layers

In general, the films exhibit a good transparency in the visible-NIR range since the average optical transmittance for wavelengths above 500 nm is in the 70-80 % range. More important for the photon conversion process, the absorption edge is found to shift toward lower energies by increasing the growth temperature from 15 to 300°C. It is then clear that the films become less transparent to UV (250-400 nm range) with increasing deposition temperature. This can be correlated to the crystallinity of the film as the layers become better crystallised with a preferential orientation as the deposition temperature increases. The transparency then increases for the 400 °C film in the UV region as compared to the other films. These results mean that the optical band gap is varying with deposition temperature with a break for T>300°C.

The optical energy band gap E$_g$ can be determined by plotting $(\alpha h v)^{1/n} \propto (hv)$ using the formula:

$$\alpha = B(hv - Eg)^n \ (1)$$

Where α is the absorption coefficient, B is constant that depends on transition probability; n can have different values depending on the nature of the transition, mainly 1/2, 2, 3/2, and 3 for allowed direct, allowed indirect, forbidden direct and forbidden indirect transitions, respectively. The absorption coefficient was calculated from the transmittance (T), reflectance (R) and the thickness (d) data, using the equation:

$$\alpha = \frac{1}{d} ln \left[\frac{1-R}{T} \right] \ (2)$$

The E$_g$ can then be obtained by extrapolation of the linear part of the curves. The character of the SnO$_2$ band gap is still controversial. Some authors assume indirect transitions[253], while others suggest a direct transitions across the band gap. In this work, the E$_g$ of the Nd-doped SnO$_2$ films were calculated by considering the direct transitions (n=1/2) between the valence and the conduction bands [246, 254, 255].

The resulting Tauc plots for the Nd-SnO$_2$ films are displayed in Figure 4.2.2.5.b as a function of the deposition temperature. It is found that the absorption edge shifts toward lower energies with increasing temperature until 300°C, and then it increases dramatically at 400°C. The extracted Eg values using Equations 1 and 2 are reported in Table 4.2.2.1. Eg decreases dramatically from 3.53 eV at 15°C down to 3.15 eV at 300°C, and then enhances substantially to 3.66 eV at 400 °C. In fact, the variation of Eg is believed to arise from the energy levels created by the dopant near the conduction or the valence band depending on the doping type. Herein, the red shift of the absorption edge can be due to better insertion of Nd atoms into the SnO$_2$ matrix when the temperature increases up to 300°C whereas the blue shift at 400°C suggests that less Nd atoms are inserted into the structure.

From the application point of view, the Eg data say that for instance the film deposited at 300 °C will absorb photons of wavelengths above 390 nm while the film made at 400°C is transparent to photons of wavelengths below 340 nm.

Table 4.2.2.1. Thickness, Crystallites Size and Energy Band gap values for the SnO$_2$:Nd layers deposited at different temperatures

Deposition temperature	Film thickness (nm)	Crystallites size (nm)		Tauc gap (eV)
		(110)	(200)	
15°C	101.3	/	/	3.53 ± 0.25
100°C	102.1	7.1	51.5	3.35 ± 0.3
200°C	103.3	14.4	50.1	3.38 ± 0.3
300°C	92.54	21.1	48.5	3.15 ± 0.3
400°C	81.58	25.7	44	3.66 ± 0.25

4.2.2.3. Luminescence properties

In the paragraphs above, we have shown that the Nd atoms are successfully inserted into the polycrystalline SnO$_2$ structures. Moreover the Nd atoms were found to be in the 3+ ionic state meaning that they possess an energy/electronic level structure as that in LaCl$_3$ crystal [146, 151]. To check the optical activation of the RE ions, analysis by photoluminescence spectroscopy (PL) were performed.

Figure 4.2.2.6 displays UV-Vis-NIR emission spectra of Nd-doped SnO$_2$ layers as a function of the deposition temperature. The room temperature PL spectra were recorded under 325 nm (3.81 eV) He-Cd laser line excitation and the emission was collected from 350 to 1450 nm. For sample grown at 15°C, a large intense and asymmetric emission band is observed in the UV-Vis range, originating most likely from the SnO$_2$ matrix (the signal for this sample was divided by 2 for clarity). The deconvolution applied to this large band resulted in the identification of three major contributions: a first band centred around 415 nm and assigned to radiative transitions of free electrons from the intermediate donor levels created by oxygen vacancies to the valence band; a second band around 440 nm which can be ascribed to luminescent centers originating from inter-grain defects[200, 245]; the third broad band centred around 580 nm is commonly attributed to radiative transitions through the deep levels present in the band gap. The origin of these radiative transitions can be multiple[267]: First is oxygen vacancies (V$_O$) which usually play a dominant role in the PL process as they can generate important amounts of trapped states within the band gap of SnO$_2$ material; second is the grain-boundaries defects which represent efficient recombination centers that are highly present in the case of amorphous structures (similar to powders) and lead to significant visible emission, and the last is the tin interstitial atoms which form a good part of defects that induce efficient radiative transitions[245, 246].
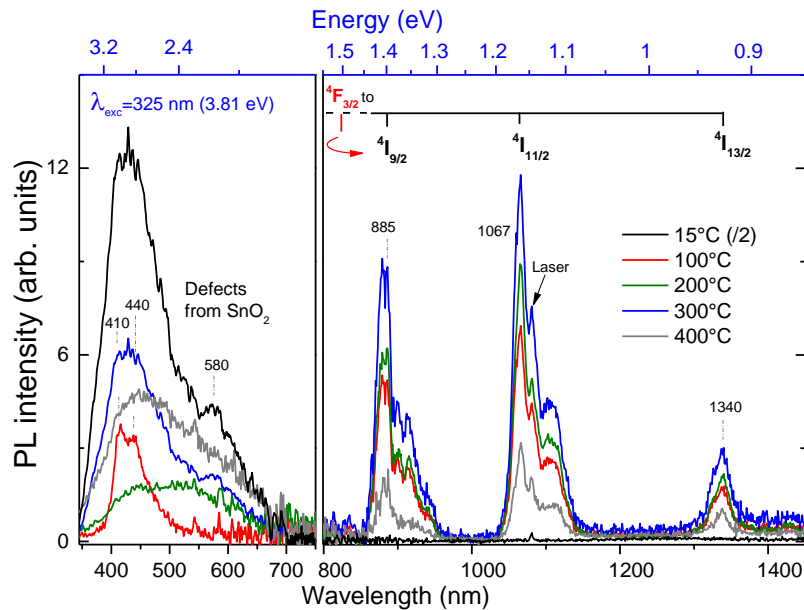
Figure 4.2.2.6. Room temperature UV-Vis-NIR Photoluminescence (PL) spectra of Nd-doped SnO$_2$ thin films deposited at different temperature

It should be noticed that no Nd-related emission peaks was detected in the 800-1450 nm range for the sample, grown at 15°C. By increasing the deposition temperature to 100°C, the PL spectrum exhibit three intense emission lines in the NIR region accompanied with a dramatic decrease of the emission in the UV-visible region coming from the SnO$_2$ matrix. Similar observations were reported for Nd doped TiO$_2$ nanocrystals [181]. The strong features at 885, 1067 and 1340 nm are commonly assigned to the $^4F_{3/2} \rightarrow ^4I_{n/2}$ radiative transitions in the Nd^{3+} energy levels, with n equals to 13, 11 and 9, respectively [225, 267]. The appearance of this emission group gives an experimental evidence of the optical activation of the Nd^{3+} ions. It is important to note that the intensity of the Nd-related PL is stronger than that originates from the host matrix. Moreover, while the peaks at 414 and 440 nm become distinguishable, the band centered at 580 nm seems to vanish.

The decrease of the SnO$_2$ related PL emission is due to many factors, among others, the reduction of radiative recombination paths because of the better crystalline order and therefore the increase of the non-radiative recombinations like dislocations, point defects and inter-grain boundary states. Also, Nd atoms can be responsible of this bend down because of the insertion process. In fact, when Nd atoms are inserted into the matrix, they prefer occupying different sites. The insertion can occur via interstitial sites which compensate Vacancy-Oxygen (VO) related defects. This however does not exclude that some Nd atoms will prefer to substitute some Sn atoms into the matrix. Another explanation could be supported by an energy transfer between the SnO$_2$ emission band centered at 580 nm to Nd^{3+} ions since there are numerous absorption bands of the Nd^{3+} ions in this region as reported by Bouras *et al.* in case of Nd-doped SnO$_2$ powder [267]. When increasing the deposition temperature

further up to 200°C, a large band from 350 to 700 nm is collected, indicating fundamental changes of type and density of radiative defects, but the intensity of Nd emissions increases only slightly, suggesting that little more Nd^{3+} ions are optically active. At a deposition temperature of 300°C, the photoluminescence intensity due to Nd^{3+} is enhanced as well defined $^4F_{3/2} \rightarrow {}^4I_n$ transitions are identified. In contrast, the Nd emission of the sample deposited at 400°C dramatically decreases while the emission of its matrix is still comparable to that of the sample made at 300°C. This result indicates that the insertion of Nd atoms into the matrix and their presence in the 3+ oxidation state are not sufficient conditions to insure a strong luminescence emission. The observed behaviour for this sample can be due to the crystal field effect which is less appropriate. This is also probably the case for the sample deposited at 15°C which exhibited a poor crystallinity and for which no Nd emission was recorded. It is likely that an efficient energy transfer from the matrix to the RE ions is the needed condition.

To assess this last assumption, PL excitation spectroscopy (PLE) experiments were performed on our Nd-SnO$_2$ samples. The aim is to investigate the possibility of an energy transfer from the SnO$_2$ matrix to the Nd^{3+} ions and to understand the different mechanisms occurring behind Nd emission. PLE experiment here consists in recording the intensity of the PL emission at 885 nm while varying the excitation wavelength.

Wide range room temperature PLE spectra is presented in Figure 4.2.2.7 in which the excitation wavelength was varied from 250 nm to 650 nm. It appears that Nd emission can be obtained when exciting at different wavelengths in the UV and visible regions. Thereby, two parts of the spectra can be distinguished. Except for the film grown at 15°C, the excitation in the UV from 250 to 350 nm gives rise to a strong Nd related PL. On the other hand, other PL emissions are collected under excitation at several wavelengths, mainly 530, 550, 570, 560 and 625 nm.

It can be noticed that the large response in the excitation spectra at wavelengths below 400 nm for samples deposited at temperatures higher than 100°C matches with the absorption of the SnO$_2$ matrix in this wavelength range. This means that exciting directly the host matrix leads to strong PL of the Nd^{3+} ions, which give us an experimental evidence of a resonant energy transfer from the host SnO$_2$ to the Nd^{3+}ions. Thus, the UV photons are successfully converted into NIR photons, thanks to the intra 4f transitions in the RE. However, it is quite difficult to quantify the real efficiency of such process using PLE.

The excitation spectra in the 450-650 nm range show that Nd^{3+} ions can be directly excited. The comparison to the energy levels diagram of Nd^{3+} in LaCl$_3$ crystals[146, 151] allows us identification of some energy levels corresponding to each excitation (absorption) peak in the visible region. It is interesting to notice that the intensity of the absorption peaks of the Nd^{3+} ions decreases by increasing

the deposition temperature meaning that the absorption cross-section of the rare earth decreases with temperature most likely due to the crystal field effect. However, the direct excitation remains fairly negligible as compared to the huge PL resulting from the indirect excitation via the matrix (70 times stronger). Such result reveals the importance of the sensitization of the Nd^{3+} ions by the SnO$_2$ host matrix.

As far as the mechanism of transfer is concerned, different options are possible. As illustrated in figure 4.2.2.8, a 4f electron of Nd^{3+} can be efficiently excited from the $^4I_{9/2}$ ground state to a higher energy level via energy transferred from the matrix either (i) via exciton recombinations resulting from the band to band transitions or (ii) through some localized intermediate defect states within the SnO$_2$ band gap. The 4f electrons will then relax via different energy levels until the $^4F_{3/2}$ excited state, where a deexcitation will occur to the $^4I_{n/2}$ with n=13, 11 and 9 respectively and therefore give rise to the three emission lines in the NIR region.

Figure 4.2.2.7 shows that the optimum energy transfer is achieved for the sample made at 300°C which explain the stronger Nd PL observed in Figure 4.2.2.6. At 400°C the less efficient indirect excitation is due to non-resonant exciton recombinations across the band gap.

Although the photon conversion process was demonstrated, it is difficult to distinguish the down-conversion functionality from the quantum-cutting or the down-shifting using solely the PLE spectroscopy analysis since only the radiative recombinations can be detected. Yet, the PL and PLE experiments allowed identifying the energy levels responsible for the resonant energy transfer.
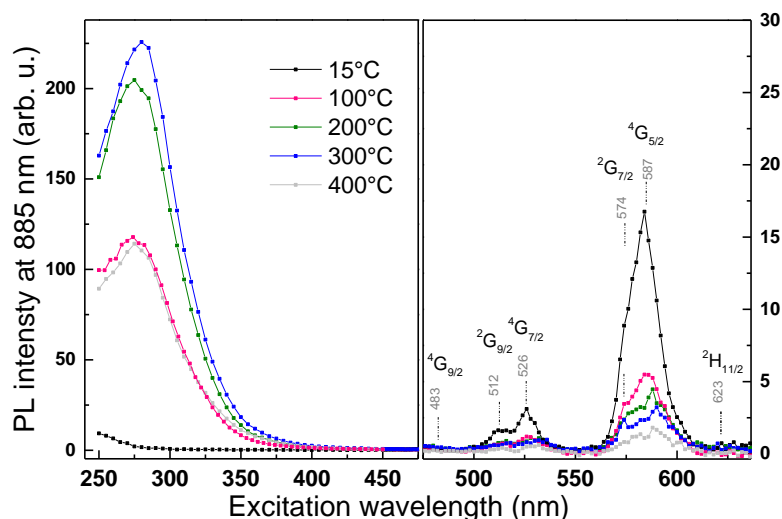
Figure 4.2.2.7. Room temperature Photoluminescence excitation (PLE) spectra of the 885 nm Nd emission line of Nd-doped SnO2 deposited at different temperatures
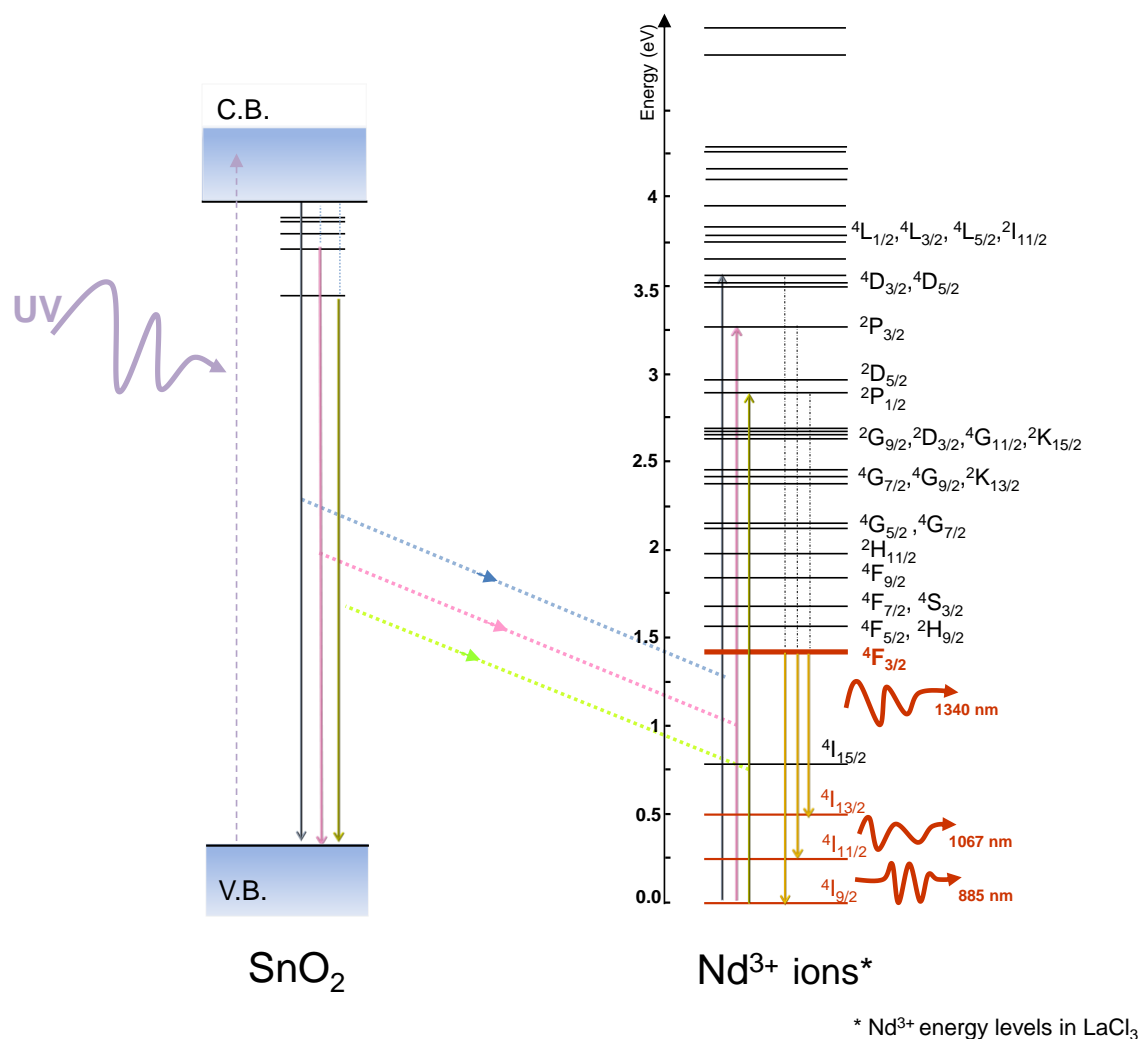
Figure 4.2.2.8. Different energy transfer mechanisms from the host SnO$_2$ to the Nd^{3+} ions

4.2.3. Summary

Nd doped SnO$_x$ thin films were fabricated by RF magnetron sputtering by varying first the Ar/O$_2$ gas flow R. Experiments such as XPS, NEXAFS, XRD and UV-Vis-NIR have revealed that the crystalline structure and composition can be easily modulated by tuning R values. Thus, different Nd hosting SnO$_x$ matrices can be synthesized: SnO, SnO$_2$, or a mixture of SnO$_x$. Thanks to the PLE measurement, we demonstrate experimentally that the strong Nd^{3+} PL originates from an efficient resonant energy transfer from the host matrix; in this study we found that SnO$_2$ is better and efficient sensitizer than SnO. When the host matrix SnO$_2$ absorbs UV light, it efficiently sensitizes the Nd^{3+} ions. Playing on the substrate temperature during the growth process has significantly enhanced the PL properties of the films, particularly the efficiency of the energy transfer (ET) from the host matrix to Nd^{3+} ions. Different ET mechanisms were proposed.

4.3. Yb-doped SnO₂

4.3.1. Effect of gas flows

4.3.1.1. Synthesis

The doping has been performed by placing two pieces of pure Yb metal discs (99.99%, about 70g each), on the top of the tin target. The study was conducted following the same procedure as for the undoped and Nd-doped samples. Since the oxygen plays an important role on the rare earth activation, the Yb-doped films were deposited under different oxygen gaz flows (from 2 to 6 sccm). The Argon flow was set at 8 sccm while varying the oxygen flow from 2 to 6 sccm; this leads to a R=Ar/O2 flow ranging from 4 down to 1.3. The deposition temperature was fixed to 100°C. Table 4.3.1 summarizes the deposition parameters, namely the thickness of the films obtained by XRR and ellipsometry, band gap Eg values extracted from transmission and ellipsometry data, and the stoichiometry determined by RBS.

Table.4.3.1. Deposition parameters of the Yb-doped SnOₓ films as a function of the O₂ gas flow during deposition by sputtering. The deposition temperature was set at 100°C.

Film	Ar:O₂ (sccm)	R	Thickness (nm)		Eg	
			XRR	Ellipsometry	Ellipsometry	Transmission
Yb-A	8:2	4	238 ± 2	186.7 ± 5.3	4.02 ± 0.15	4.06 ± 0.1
Yb-B	8:3	2.7	236 ± 2	209,6 ± 4.4	3.93 ± 0.14	4.06 ± 0.2
Yb :D	8:5	1.6	119.2± 1	118.5 ± 6.4	4.12 ± 0.2	3.95 ± 0.1
Yb :E	8:6	1.3	91.4 ± 1	95.47 ±3.2	4.12 ± 0.1	3.88 ± 0.2

4.3.1.2. Crystal structure

Figure 4.3.1 presents the typical θ-2θ scans of the Yb-doped SnOₓ thin films deposited at 100°C under different oxygen gas flows. All the diffraction patterns seem to fit with the response of a polycrystalline SnO₂ tetragonal rutile structure. This result is quite different from that observed with the undoped and Nd-doped films. In those cases, low oxygen flows have led to SnO structure (R=4). In the present case, the lowest oxygen flow (2sccm) introduced into the deposition chamber resulted in a well crystallized film exhibiting a SnO₂ structure. The growth is found to be preferential along (110) and (200) planes, according to the JCPDS card n°00-041-1445. By increasing of the O₂ flow during deposition, the intensity of the diffraction peak along the (200) plan decreases gradually with the

increase of oxygen content during deposition. Moreover, the position of this diffraction peak is shifting toward low diffraction angles, indicating an increase of the lattice parameter. This means that more oxygen in the chamber did not affect the polycrystalline nature of the films but their crystalline quality. For the highest oxygen flow used in this study (6 sccm), the resulting film shows weaker XRD signal, confirming a low crystalline quality. This is expected from such high oxygen content during deposition.

It is important to point out at this stage that the positions of the diffraction peaks of tetragonal SnO and SnO$_2$ are quite close to each other (see figure 4.3.1). Therefore, it is difficult to extract valuable and reliable information on the oxides present in the films. Overall, the SnO$_2$ phase is witnessed by the presence of the (110) diffraction peak and some other peaks. Thus we can simply suggest that the films are preferentially SnO$_2$. Figure 4.3.1 reveals also the presence of an additional diffraction peak at 24.27° recorded for all samples. Above, we have attributed this contribution to a possible phase of SnSiO$_x$, which can be formed at the interface between the Si substrate and the SnO$_x$ films during deposition. Unfortunately, the peak position of this feature corresponds exactly to the (111) diffraction peak of the orthorhombic SnO; this coincidence reinforces our suspicions about the presence of SnO phase in the films. Let's remind that our purpose behind investigating the variation of the oxygen flow during the deposition is the synthesis of films with different stoichiometry, mainly oxygen poor and rich films and to correlate the RE activation with the chemical environment. Only chemical analysis can allow us identification of oxygen atoms and oxygen vacancies in the deposited structures. XPS spectroscopy data will be presented later.
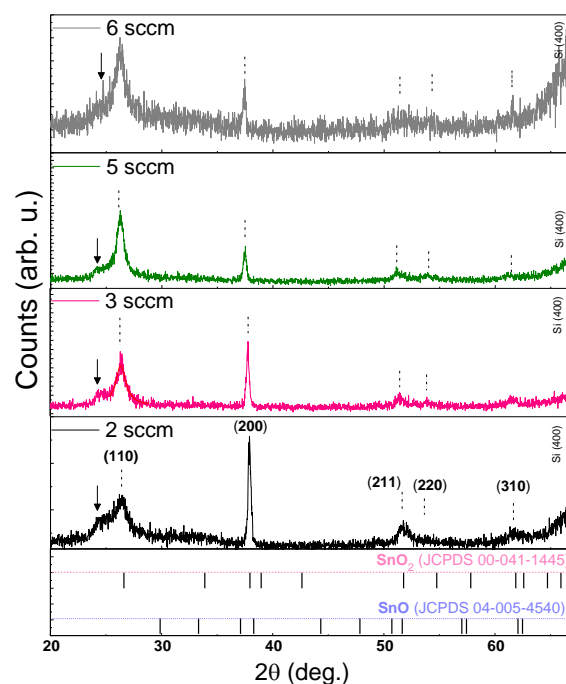
Figure 4.3.1. X-Ray diffraction patterns of Yb : SnO$_x$ films deposited with increasing O$_2$ gas flow during depos-

-ition from 2 up to 6. The main peaks are indexed in the rutile SnO$_2$ structure.

Table 4.3.2 gives the crystallites sizes along the (110), (200) and (211) directions calculated from the diffraction patterns using the Bragg's low. The lattice parameters along (200) and (110) directions are also reported. The crystallites along the (200) have the largest size against the crystallites along the (110) and the (211) directions which exhibit comparable sizes. This behaviour is noticed for all the Yb-doped films whatever is the oxygen gas flow used during deposition. Besides, given the crystallites values reported in table 3.6, the oxygen gas flow is found to strongly affect the growth process. The lattice parameter 'a' of the rutile structure was calculated for all samples using the Scherer formula. Overall, the 'a' values of the different samples are comparable to that of the bulk SnO$_2$ material (a=b=4.73 Å), particularly the sample deposited under O$_2$=2 sccm for which a value of 4.74 A is found. This parameter a increases by increasing the oxygen content in the film for the (200) plane. Along the (110) plane the 'a' values are more or less constant, about 4.78 ± 0.01 Å. This is in agreement with the XRD observations for which the increase of the oxygen content has a clear effect of the crystalline quality along the (200) plane. The increase of the lattice parameter indicates a larger unit cell volume. This suggests that more oxygen atoms are incorporated into the structure. Only chemical analysis can confirm this hypothesis

Table 4.3.2. Crystallites size of the Yb-doped SnO$_x$ films along the (110), (200) and the (211) directions, the lattice parameter 'a' and the stoichiometry by XPS of the films as a function of the O$_2$ gas flow during deposition by sputtering.

Film	Ar:O$_2$ (sccm)	Crystallites size			Lattice parameter 'a'	
		(110)	(200)	(211)	(200)	(110)
Yb-A	8:2	5.30	31.6	6.7	4.74 ± 0.02	4.78 ± 0.02
Yb-B	8:3	7.89	32.7	13.6	4.75 ± 0.02	4.77 ± 0.02
Yb-C	8:5	11.36	27.9	7.8	4.79 ± 0.02	4.79 ± 0.02
Yb-D	8:6	8.08	30	1.8	4.80 ± 0.02	4.79 ± 0.02

4.3.1.3. Chemical analysis by XPS

The valence-bands (VB) of the Yb-doped SnO$_x$ films as a function of the oxygen gas flow during deposition are displayed in figure 4.3.3. The 3d$_{5/2}$ and 1s core levels photoemission spectra of Sn and O, respectively, are reported as well. All VB spectra of the Yb-doped films at the left side of the figure display three-peaked curves featuring a SnO$_2$ structure (consistent with XRD results). This is in

agreement with earlier XPS studies [22, 259, 264, 265, 275-277] of SnO$_2$ oxide. In fact, as explained before, the valence bands spectra allow rapid identification of the most abundant oxide in the structure but do not provide quantitative analyses on the real contribution of each oxide phase (in the case of two oxides or more).
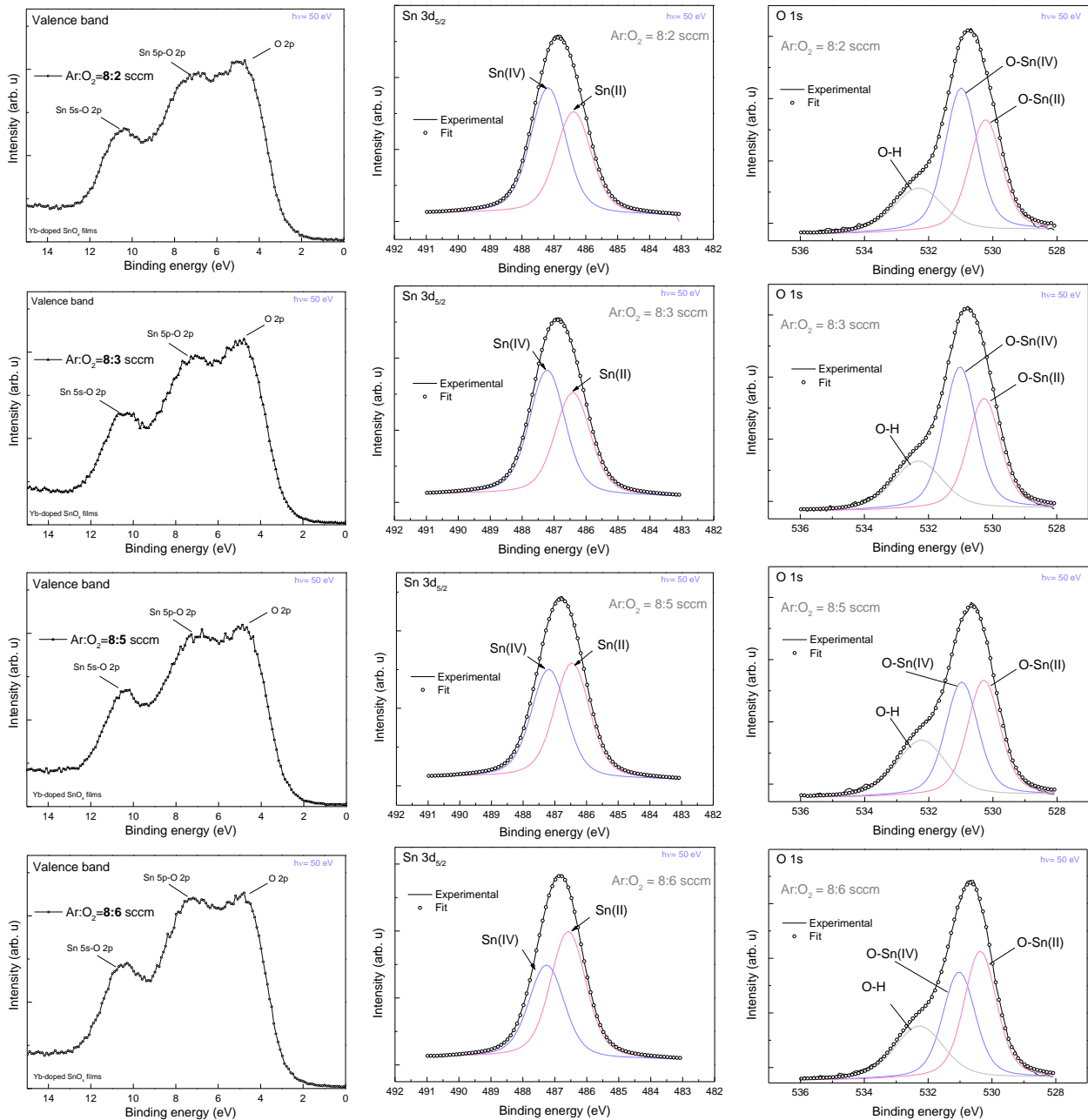

Figure 4.3.3. (a) Valence bands, (b) Sn 3d$_{5/2}$ and (c) O 1s core levels spectra of the Yb-doped SnO$_x$ films as a function of the oxygen gas flow during films elaboration.

Each photoemission peak noticed in the spectra corresponds to hybridization between Sn and O atomic orbitals; their assignments are reported in the spectra. Detailed studies on the valence bands of tin

oxides (SnO and SnO_2) have been reported in literature. Sherwood (1990) [277] have determined the orbital energies and atomic populations for the valence levels of SnO and SnO_2. In the same year, Themlin et al.[259] have reported the VB energy distribution curve (EDC) and shallow core levels of SnO_2. They discussed them in terms of density of state (DOS) and surface electronic theory. Their study was in agreement with theoretical bulk DOS derived by Robertson et al.(1979)[55]. This latter have in fact calculated the bulk electronic structure of SnO_2 using tight-binding (TB) method based on O 2s and 2p orbitals and Sn 5s and 5p orbitals. (Electronic structure of SnO_2 reported by Robertson et al. was discussed in chapter 1). Few years later, Kövér et al. (1995)[276] have studied the valence bands of metallic Sn, SnO and polycrystalline SnO_2 using high resolution XPS, Auger spectroscopies and DV-Xα (discrete variational Xα) MO method. They have identified the different Sn and O related orbitals in the VBs. The Sn-Sn and Sn-O bonds lengths in Sn, SnO and SnO_2 have been reported as well (in a.u.). Figure 4.3.3a does not allow a real differentiation between the films as the spectra look similar. Additional analyses are needed.

In order to insight the oxide structure and to extract valuable information about the element's surroundings, fine analysis of the $3d_{5/2}$ and 1s core levels of Sn and O, respectively, have been performed. The treatment of data and de-convolution of peaks were carried out using Average software. The results are shown in Figure 4.3.3b and c for Sn and O respectively. Surprisingly, although the valence bands suggested a SnO_2 structure, the core levels of Sn and O reveal the presence of two oxide phases, mainly SnO and SnO_2 with more or less comparable amount. The ratio between them is found to vary from a sample to another, but a gradual evolution of the contribution of each oxide can be easily seen, thanks to the deconvolution process. The presence of SnO oxide is witnessed by the presence of the Sn (II) element at low binding energies (around 486.42 eV), while the SnO_2 oxide is characterised by the presence of the Sn (IV) element at high binding energies (around 487.21 eV). Despite the small energy difference between Sn (II) and Sn (IV), about 0.7 eV, the deconvolution of the Sn $3d_{5/2}$ peak has been successfully done. These peaks positions are in line with previous reports enabling distinction between SnO from SnO_2 oxides using XPS. Themelin et al.[265] have reported that Sn (II) component is located at 0.73 eV from the Sn (IV) in SnO_2 single crystals. Akgul et al. [278] have also reported 0.7 eV of energy gap between the two chemical states in SnO_2 thin films deposited by spray pyrolysis.

If one looks to the Sn3 $d_{5/2}$ core level spectra of the samples versus the oxygen flow, one can directly notice the increase of the SnO contribution with the O_2 flow. The samples deposited under 2 and 3 sccm exhibit roughly the same structure, with a dominant SnO_2 phase (55,12%). At 5 sccm, the sample shows comparable amounts of SnO and SnO_2 (50:50). Finally, the sample elaborated under 6 sccm of oxygen shows a SnO rich structure with 57.83 % against 42.17% of SnO_2. The Sn $3d_{5/2}$ core level

spectra clearly show the reduction of Sn (IV) to Sn (II) when increasing the oxygen content during elaboration.

Interestingly, the observations noticed with Sn 3d$_{5/2}$ core level spectra are exactly the same than those found with the O 1s core levels as shown in figure 4.3.3c. This result confirms the consistency of these analyses. The oxygen bound to Sn (II) is found to lay around 530.30 eV while that bound to Sn (IV) to form SnO$_2$ is detected at 531.40 eV.

To sum up, the SnO and SnO$_2$ proportion extracted from the Sn 3d$_{5/2}$ and O 1s peaks are now reported in table 4.3.3. At first glance one could directly notice the reduction of SnO$_2$ oxide to SnO when increasing the oxygen content during deposition. The percentages of SnO$_2$ and SnO calculated from O1s data are slightly different from those found using Sn 3d$_{5/2}$ data because of the additional contribution of the chemisorbed oxygen in the peak.

The main feature of these results is that, unlike our expectations, the oxygen gas flow seems to increase the SnO oxide in the structure (reduction of SnO$_2$). For better understanding, we have calculated the stoichiometry of the films whose the values are also reported in table 4.3.3. It appears that the sample deposited at 2 sccm is a poorer oxygen film when compared to the other samples. Above 3 sccm, the stoichiometry of the films does not change any more. This result means that the excess of oxygen introduced into the deposition chamber is not incorporated into the structure of the film but pumped out or reacting differently within the structure. Such finding is of great importance to interpret the optical properties of the synthesized Yb-SnO$_x$ films as detailed below.

Table 4.3.3 SnO and SnO$_2$ contents and stoichiometry of the Yb-doped SnO$_x$ films extracted from Sn 3d and O 1s core levels spectra.

Samples	From O 1s		From Sn 3d$_{5/2}$		Stoichiometry SnO$_x$
Ar-O$_2$ (sccm)	SnO$_2$	SnO	SnO$_2$	SnO	x = [O]/[Sn]
8-2	56.60	43.40	55.12	44.88	1.57 ± 0.01
8-3	56.53	43.47	54.83	45.17	1.63 ± 0.01
8-5	49.83	50.17	48.41	51.59	1.62 ± 0.01
8-6	45.73	54.27	42.17	57.83	1.63 ± 0.01

The increase of the SnO concentration in the Yb-doped SnO$_x$ films can partially be explained by the presence of the Yb atoms in the structure. Indeed, it is well known that the key parameter for the rare earth activation is its binding to oxygen to form rare earth sesquioxide, in which the metal atoms are particularly present in the 3+ oxidation state. Thereby, we do think that some Yb atoms pumps the

oxygen bounded to Sn (IV), which impoverish the structure from oxygen, resulting in the reduction of Sn (IV) to Sn (II).

To check our assumption, we monitored the Yb 4d core levels in our films using the XPS analysis again. The Yb 4d$_{5/2}$ photoemission spectra as a function of the oxygen gas flow during deposition are shown in figure 4.3.4
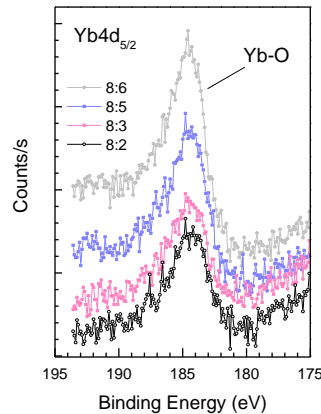

Figure 4.3.4. Yb 4d$_{5/2}$ core level spectra of the Yb-doped SnO$_x$ films as a function of the oxygen gas flow during elaboration.

Figure 4.3.4 gives spectra of the Yb-doped films exhibiting a typical 4d$_{5/2}$ peak of Yb ions bound to oxygen. The peak position of the 4d$_{5/2}$ component (around 184,6 eV for all samples) indicates that Yb ions have a 3+ oxidation state [260, 279-281]. This means that the Yb atoms are successfully inserted into the structure and they are optically actives. Moreover, it is important to notice the increase of the peak area with the increase of the oxygen flow, which indicates that more Yb ions are bounded to oxygen (more Yb^{3+} ions optically active). This explains in turn the reduction of SnO$_2$ and the increase of SnO phase in the films. Moreover, it known that Yb might exist in the 2+ oxidation state. XPS Yb^{2+} signature have been reported by Schmidt et al.[282]. It turns out that the binding energies of Yb2+ and Yb^{3+} are very close each other[283], so it is quite difficult to distinguish them, particularly at low concentrations.

4.3.1.4. Optical properties

The optical transmission of the Yb-doped SnO$_x$ films elaborated under different O$_2$ gas flows is presented in figure 4.3.5a. The spectra are reported in the 200-800 nm range. Figure 4.3.5.b plots the Tauc curves used for the extraction of the band gap values reported in table 4.3.1.
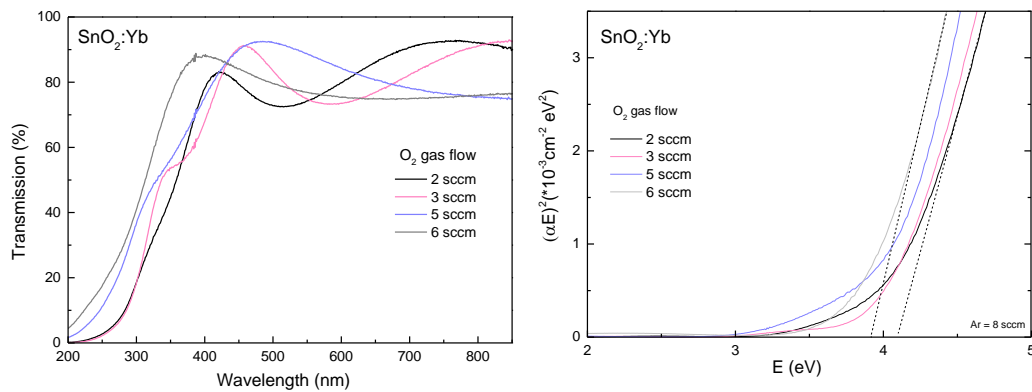
Figure 4.3.5. UV-vis-NIR transmission spectra of the Yb : SnO$_x$ films as a function of the O$_2$ gas flow during elaboration.

The Yb- doped films exhibit transparency varying between 75 and 90 % in the visible and infrared range but clearly they absorb in the UV region, mainly from 200 to 400 nm. The absorption thresholds were found ranging between 200 and 280 nm. Such high-energy threshold values are a signature of SnO$_2$ structure, which is consistent with the XRD data and valence bands.

Interestingly, the samples deposited at 2 and 3 sccm of O$_2$ gas flow have comparable absorption edges indicating probably the same band gap energy. Moreover, in spite of similar films thicknesses, the sample elaborated at 3 sccm exhibits more interference fringes than that deposited at 2 sccm. This behaviour is most likely due either to different refractive index of the layers or to the presence of secondary indirect band gap in the structure. Further increase of the O$_2$ flow during deposition up to 6 sccm leads to a shift of the absorption edge toward shorter wavelengths (higher energies) indicating much higher optical band gap. Figure 3.16.b shows the Tauc plots of the Yb-doped SnO$_x$ films as a function of the gas flow during elaboration. If one looks to the curves, one could notice the shift of the absorption edge toward lower energies when increasing the oxygen content during deposition. This is at first glance in contradiction with the transmission data. The extracted band gap values are reported in table 4.3.1 and compared to values calculated using ellipsometry. The samples elaborated under 2 and 3 sccm exhibit comparable band gap energy values, about 4.02 ± 0.05 eV. This value is confirmed by ellipsometry and Tauc plots, and consistent with the absorption edges in the transmission spectra. However, in the case of the 5 and 6 sccm, different values are calculated. The Tauc plots give band gap energies decreasing down to 3.88 ± 0.02 eV while ellipsometry data show increasing values up to 4.12 ± 0.01 eV. We believe that ellipsometry data are more reliable and it supported by the shift observed in the transmission data. Overall the change of the optical band gap energy is moderate. Moreover, it is interesting to notice that the extracted band gap values for all samples are close to SnO$_2$ structure while XPS Sn 3d$_{5/2}$ and O 1s core levels have shown the presence of minimum of 40% of

SnO. These band gap values are more consistent with the RBS, XRD and valence bands results which shown a SnO$_2$ structure. We do think that the structure of the films is mostly SnO$_2$ with some local environments which are oxygen deficient resulting in the formation of some local SnO amounts detected in the XPS spectra.

4.3.1.5. Photoluminescence properties

The photoluminescence properties of the Yb-doped SnO$_x$ were investigated using an Nd-YAG laser with an excitation wavelength of 355 nm. The emission spectra of the films as a function of the O$_2$ gas flow deposition are displayed in figure 4.3.6 .

The sample deposited using the lowest O$_2$ gas flow (2 sccm) exhibits a weak emission band in the UV-Vis and a strong three-peaked photoluminescence in the infrared region. The band centered at 440 nm is originating from the host matrix as discussed earlier in the sections related to PL in Nd-doped films. The PL in the infrared region is located at 956, 972 and 1004 nm and assigned to the 4-f electrons transitions from the $^4F_{5/2}$ to the $^4F_{7/2}$ energy levels in Yb. Such signal indicates that Yb atoms are successfully inserted into the host matrix and are optically active, in line with the XPS results. When comparing the Yb-related emission to the matrix-related PL, one could notice that Yb PL is 10^5 stronger than that of the host matrix.
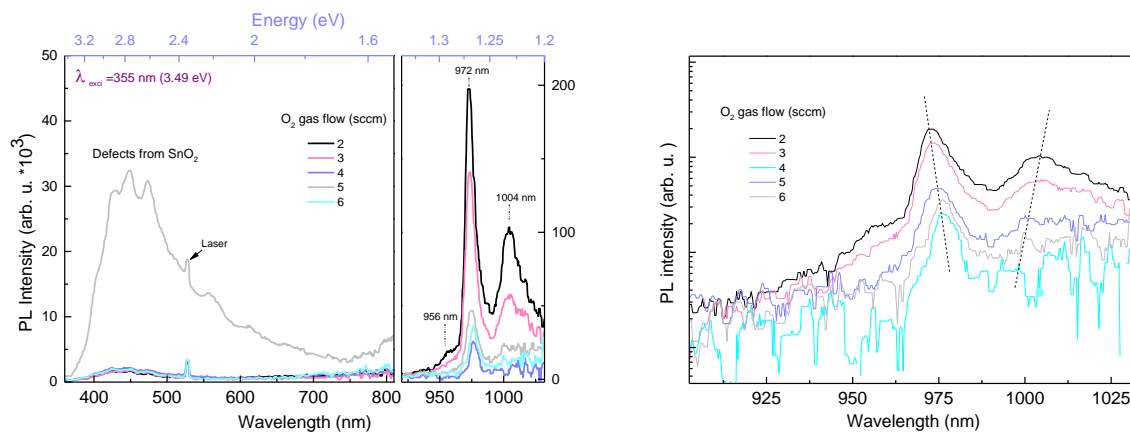
Figure 4.3.6. a) PL spectra of Yb-doped SnO$_x$ thin films as a function of the O$_2$ gas flow during deposition, b) Zoom on the Yb emission for same samples in logarithmic scale.

Increasing the O$_2$ gas flow during deposition seems to affect drastically the Yb emission. The latter is found to gradually decrease as a function of the oxygen flow. One could speculate that either less Yb atoms are inserted within the matrix and therefore fewer atoms are optically active, or a change in the electronic structure at the band gap edges has occurred. In both cases the efficiency of the energy transfer from the matrix to the rare earth is expected to be less efficient. Interestingly is the film

deposited under O$_2$ flow of 5sccm as its PL in the UV-vis resolves in four features located mainly at 424, 448 and 475 nm, in addition to an emission band vanishing at 700 nm. These features are most likely originating from radiative defects in the host structure.

The unexpected decrease of the Yb-related PL when increasing the oxygen gas flow during deposition can be correlated to the oxide structure, thanks to the XPS data. Indeed, we have shown that the excess of oxygen incorporated into the deposition chamber is not incorporated within the structure but it is pumped out (stoichiometry of the films doesn't change). On the other hand, we suggested the oxidation of Yb (that pumps the oxygen related to Sn (IV)) resulting in the increase of the SnO phase. In other words, the oxygen present within the layer has activated more and more Yb atoms present in the structure. From the Yb 4d$_{5/2}$ core level presented in figure 4.3.4, we have noticed an increase of the Yb^{3+} ions (bound to oxygen and optically active) proportionally to the oxygen flow, which should be in favour of a higher PL signal. As a result, we propose that the decrease of Yb emission -in spite of the increase of Yb^{3+} amounts- is due to a quenching effect induced by a high concentration of Yb emitting centers. In this particular case, the numerous Yb^{3+} ions are too close to each other; consequently the excitation energy absorbed by one Yb^{3+} ions is immediately transferred to another Yb^{3+}ion; Consequently the energy supplied by the host matrix is lost non-radiatively. The higher is the concentration of Yb^{3+} the lower is the PL emission (up to certain density).

In figure 4.3.7 we summarize the evolution of PL of Yb at 972 nm when increasing the oxygen flow, and correlation to the SnO content into the structure
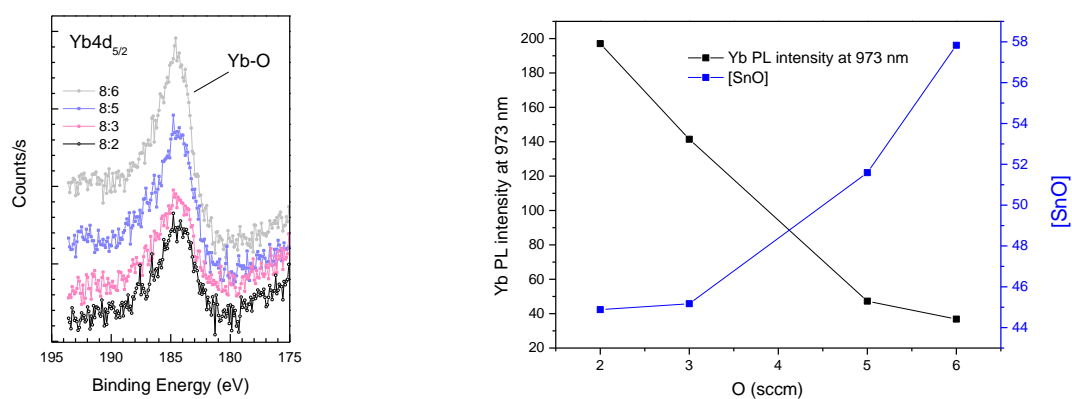
Figure 4.3.6.7a) 4d$_{5/2}$ core levels of Yb and b) its PL at 972 nm as a function of SnO oxide content in the structure

The figure clearly shows that increasing the SnO phase is somehow responsible on the decrease of Yb PL signal. This is indirectly indicating the increase of the density of the density of Yb^{3+} optically active as revealed by XPS. One could imagine different interaction in the structure with increasing the oxygen flow during films elaboration as follow:

1- $Yb + SnO \rightarrow Yb\text{-}O + Sn$

2- $Sn + SnO_2 \rightarrow 2\ SnO$

3- $Sn + O_2 + Yb \rightarrow Yb\text{-}O + SnO$

Figure 4.3.6.b illustrates the correlation between the photoluminescence intensity of Yb and SnO phase when varying the oxygen flow. The PL peak position recorded at 972 nm shifts toward lower energies by increasing the O_2 gas flow during the films deposition, while the peak situated at 1004 nm is found to shift toward higher energies. At first glimpse, it turns out that the sublevels of the $^2F_{5/2}$ are getting closer by adding more oxygen in the structure (increase of the SnO phase). We can conclude that oxygen atoms are a key parameter that plays an important role on the activation of the RE, its energy levels positions and splitting.

In order to cast light on the PL mechanisms and possible energy transfer occurring from the host matrix to the Yb^{3+} ions, PLE spectroscopy was performed on the synthesised Yb-doped films. The PL intensities recorded at 970.53 nm as a function of the excitation wavelength for the different samples are presented in figure 4.3.8

As expected from the PL results, the Yb emission essentially arises from an energy transfer from the SnO_2 matrix. This is witnessed by the strong PL response at 970 nm when exciting in the UV, a region where our SnO_2 has been shown to absorb this wavelengths.
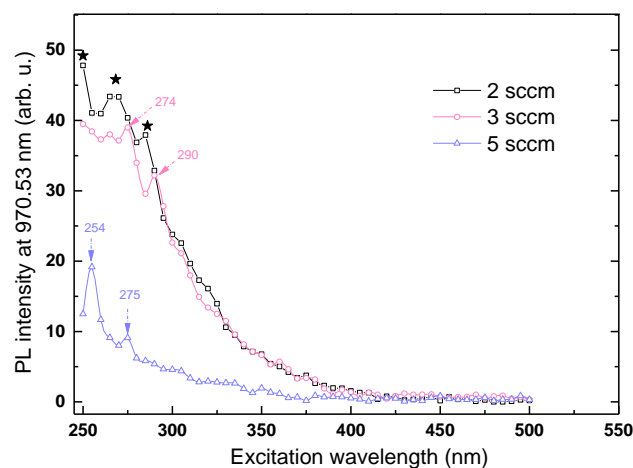
Figure 4.3.8. PLE spectra of the Yb-doped SnO_x thin films deposited at 2, 3 and 5 sccm, respectively.

Despite that the absorption edges of the films shifts toward higher energies (indicating an increase of the band gap), the energy transfer is found to occur in the same wavelength range whatever is the band gap of the material. This means that the energy transfer does not fully involves the band-to-band transitions in the host matrix, but occurs through the intermediate deep levels present within the SnO_x band gap. On the other hand, the intensity of the Yb-related PL (which translates the down shifting

efficiency) dramatically decreases by increasing the Yb^{3+} ions content, indicating less energy transfer. This result confirms the effect of concentration quenching in which only few Yb^{3+} atoms can participate to the radiative emission process. It is not excluded that the decrease of the Yb-PL can be related to the significant amounts of SnO in the structure. We have shown in the case of Yb-doped powders that deep levels in SnO$_2$ structure are very important for the energy transfer process.

In Figure 4.3.8, the PLE spectra of Yb at higher energies can be resolved into three peaks at 250, 268 and 284 nm (4.96, 4.62 and 3.64 eV respectively) for the sample deposited at 2 sccm and into two peaks at 275 and 289 nm (4.50 and 4.29 eV, respectively) for the 3 sccm, and finally into 254 and 275 nm (4.88 and 4.50 eV, respectively) for the 5 sccm sample. This is translating somehow to the presence of well-defined deep levels (originating from oxygen vacancies) within the SnO$_2$ band gap, from which, more transitions are participating to the energy transfer.

It is interesting to notice that the films deposited at 2 and 3 sccm of oxygen have almost the same thickness, as well as a comparable crystalline structure and similar absorption edges. Despite all of these common characteristics, the two films exhibit different Yb-PL intensities under an excitation wavelength of 355 nm (figure 4.3.8). The difference is much less obvious when comparing the PLE spectra of the same films for which the exponential decay curves are quite comparable,. This can be explained as due to the type of excitation source, which is an intense laser for the PL setup while it is a xenon lamp for the PLE experiment. Also, the detection equipment is not the same neither.

4.3.2. Effect of annealing

This study aims at optimizing the PL properties of the best photoluminescent sample of the above set. The purpose here is to anneal the Yb-doped SnO$_x$ film under Ar atmosphere at different temperatures; mainly 500, 700 and 900°C during 10 min in order to answer the question wether annealing has an effect on the Yb activation or rather affects the efficiency of the energy transfer occurring from the host oxide matrix to Yb^{3+} ions. The structural changes occurring through the annealing process were investigated by XPS and MEB, while the light emission properties and energy transfer were checked by PL and PLE experiments.

4.3.2.1. XPS analysis

a) Valence bands

The valence bands of the Yb-doped films deposited at 8:2 sccm of Ar and O$_2$ (100°C) and separately annealed at 500, 700 and 900°C are presented in figure 4.3.9. At first glance, one could easily recognize the 3 bands characteristics of the SnO$_2$ structure for the samples annealed at 500 and 700°C. At 900 °C,

a radical change in the structure can be witnessed by the deformation of the valence band of the sample. The O2p contribution seems to completely vanish while that of the hybridization between Sn and O shifts toward higher binding energies. The same but relatively smaller shift of the valance bands edges toward higher binding energies have been recorded for the samples 500 and 700°C due to charges effect. We can conclude then that annealing up to 700°C can preserve the SnO_2 aspect of the structure.
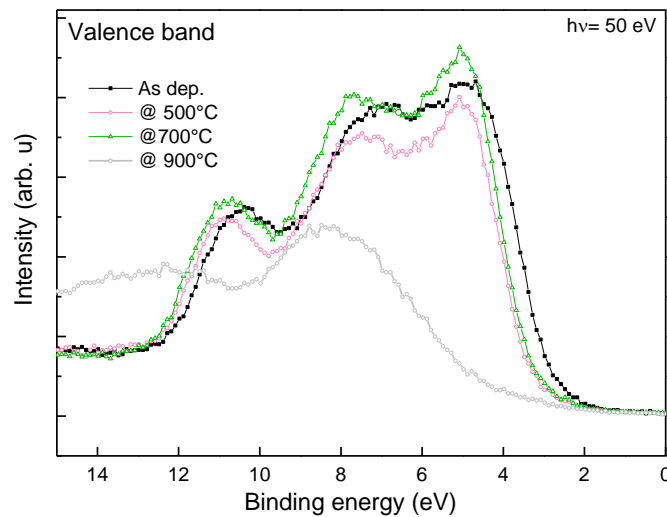

Figure 4.3.9. Valence band spectra of the 8:2 Yb-doped SnO_x sample annealed at different temperatures.

b) Sn3d$_{5/2}$ and O1s core levels

The Sn 3d$_{5/2}$ and O 1s core levels as well as their peaks deconvolution are displayed in figure 4.3.10. Interestingly, the annealing temperature seems to deeply affect the SnO/SnO_2 oxides proportion in the films. It can be clearly seen from the Sn 3d$_{5/2}$ core levels spectra of the samples that the SnO phase becomes prominent against SnO_2 for annealing temperatures of 500 and 700°C. This behaviour is confirmed by the O 1s core level spectra. For the sample annealed at 500°C, contribution of O bound to carbon is also detected. At 900°C a third component appears at high binding energies, confirming the change in the structure at this condition. This peak is as intense as the one related to SnO. Such peak can be attributed to the presence of Sn atoms bound and to Si atoms from the substrate. Scaning electron microscopy (SEM) analysis has been applied on the annealed samples. The images are reported in Figure **4.3.11.** While the surfaces of the un-annealed sample and those annealed at 500 and 700°C look smooth, the surface of the sample annealed at 900°C exhibits a high density of pitches which suggest that the film went through a melting phase. It is most likely that some Sn diffuses to the Si surface (forming an Sn-Si eutectic) and some others move towards the surface. The non-conventional XPS data of this sample are therefore not surprising.
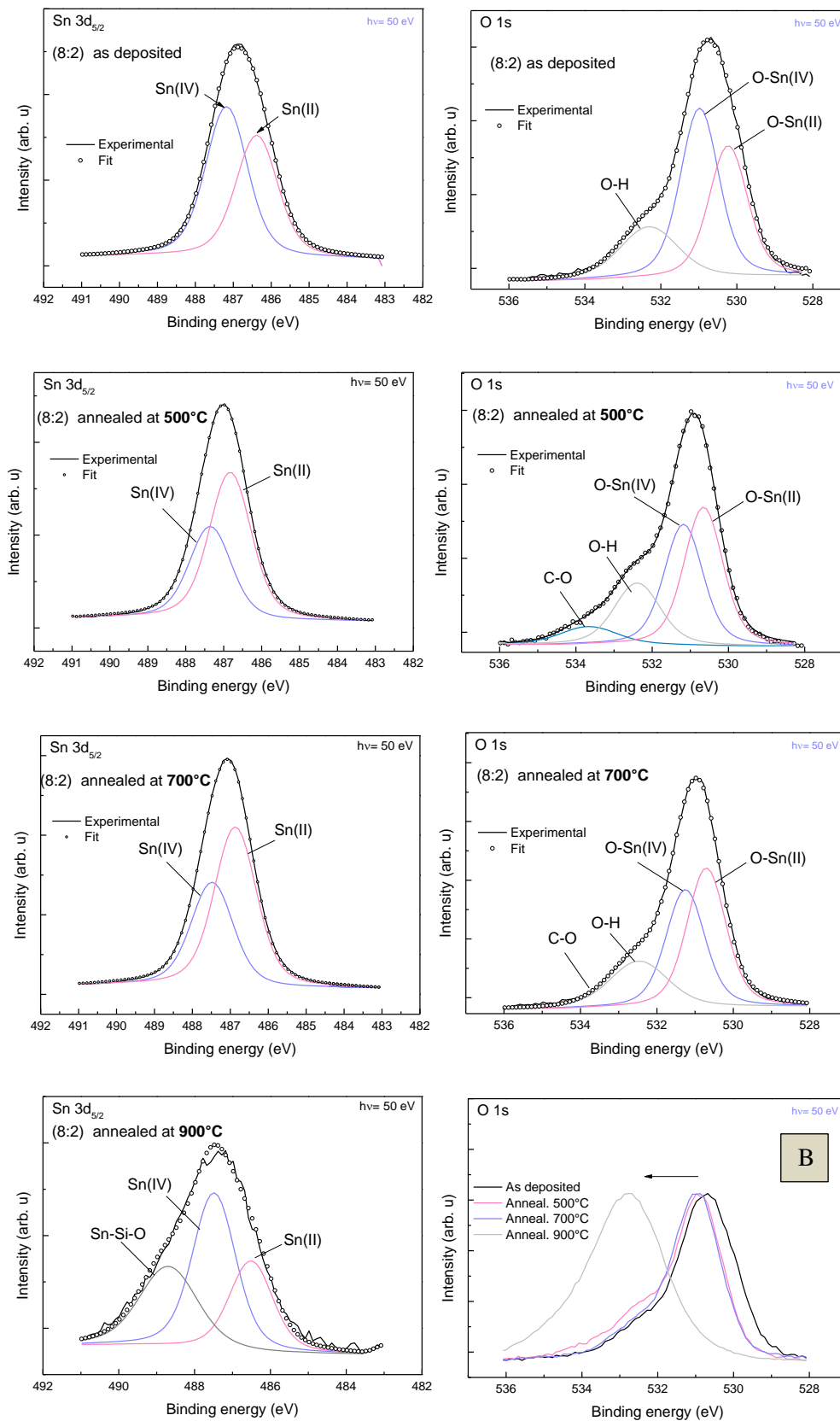
Figure 4.3.10. Sn 3d$_{5/2}$ and O 1s core levels spectra of the Yb-doped SnO$_x$ samples deposited at 8:2 sccm at 100°C and annealing in air at 500, 700 and 900°C.
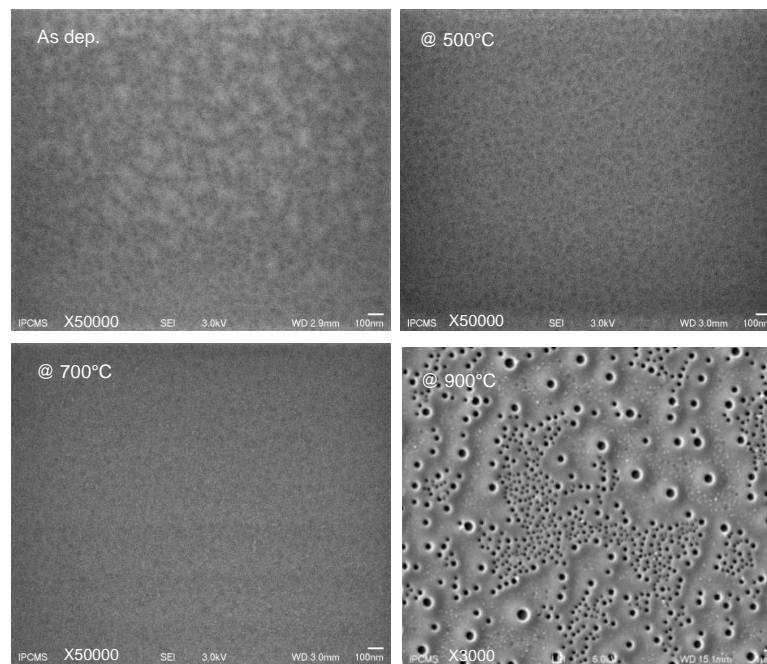
Figure 4.3.11 SEM images of the Yb-doped SnO$_x$ films elaborated at 8:2 sccm at 100°C and annealed at 500, 700 and 900°C.

Back to the XPS data of figure 4.3.10 and focusing on the O 1s spectra reported at the right side, one could notice the presence of the contribution of chemisorbed oxygen atoms at high binding energies present at the surface of the films. In figure 4.3.10 named 'B', we have compared the O 1s core levels of the different un-annealed and annealed samples. A gradual shift about 0.2 eV toward higher binding energies is measured as a function of the annealing temperature. The same behaviour has been noticed with the Sn 3d$_{5/2}$ core levels (not presented here). At 900°C, the O 1s peak completely shifts to higher binding energies confirming the deformation of the structure.

The SnO and SnO$_2$ proportions extracted from Sn and O peaks deconvolution are presented in table 4.3.4. The increase of SnO phase as a function of the annealing temperature is clearly evidenced. The concentration of SnO in the films increases from 43.40 % for the as deposited sample to 60.75 % for the 700°C annealed one. We have not given the value for the 900°C annealed samples since the third observed component can induce fault interpretations. On the other hand, the contribution of the chemisorbed oxygen in the peaks was not taken into consideration while it seems to not be negligeable. Overall, we can conclude from the data that the annealing at high temperatures favours the formation of SnO phase.

Table 4.3.4 SnO and SnO$_2$ proprtions of the Yb-doped SnO$_x$ films deposited at 8:2 sccm of Ar and O$_2$ and annealed at 500,700 and 900°C, extracted from Sn 3d and O 1s core levels spectra.

Samples	From Sn 3d$_{5/2}$		From O 1s	
8-2 (sccm)	SnO$_2$	**SnO**	SnO$_2$	**SnO**
as dep.	56.60	43.40	55.12	44.88
R500°C	38.42	61.58	46.74	53.26
R700°C	39.25	60.75	45.92	54.08
R900°C	44.16	26.11	/	/

In order to understand the origin of this behaviour, it appears crucial to have a look on the Yb 4d core level to see whether Yb is responsible of the decrease of the SnO$_2$ amounts in the films or due to other mechanisms.

c) Yb 4d$_{5/2}$ core level

The Yb 4d$_{5/2}$ spectra of the different samples are presented in figure 4.3.12 as a function of the annealing temperature. The first observation is the shift of the Yb 4d$_{5/2}$ peak toward higher binding energies due to charges effect. This is consistent with the Sn and O peaks that have shown also a similar shift. It is important to mention here that the peak position of the C 1s (used as reference) in all samples is the same. Therefore the shift is an indicator of a change in the environment of the rare earth upon thermal annealing.
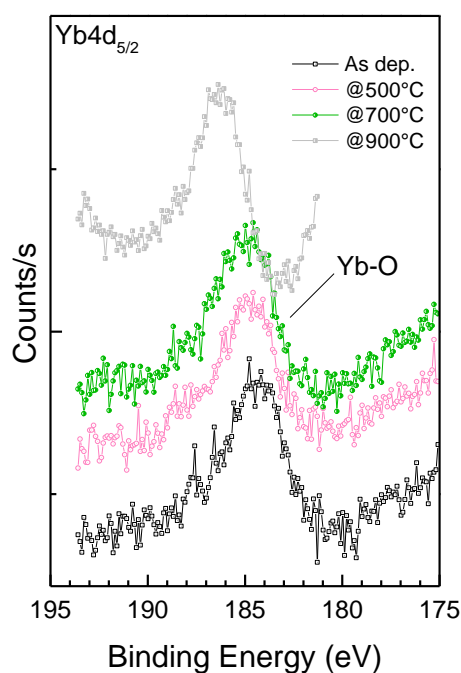
Figure 4.3.12. Yb $4d_{5/2}$ core level spectra of the Yb-doped SnOx films deposited at 8:2 sccm at 100°C and annealed in air atmosphere at different temperatures

It is interesting to notice that the Yb-O peak area does not vary for the samples annealed at 500 and 700°C as compared to the as deposited sample. This means that the density of Yb^{3+} ions bound to the oxygen (Yb_2O_3) is the same for the three samples. We can conclude that the thermal annealing up to 700°C does not affect the oxidation states of Yb. In other words, once a Yb atoms is inserted within the structure, it is very difficult to reduce its valence; It is most likely that Yb oxide is stable at high temperature.

d) Discussion

The Yb atoms already incorporated into the structure seem unaffected by the annealing treatment (excluding annealing 900°C). Thus, no additional Yb^{3+} ions can be formed using this treatment. It results that Yb is not responsible of the increase of the SnO phase within the structure. One explanation can be conducted in terms of dissociation enthalpy. It is likely possible that the annealing treatment leads to the dissociation of Sn-O bonds resulting in the increase of the SnO phase in the structure. To understand this mechanism we need to know the atomization energy or lattice energy of SnO and SnO_2 for which all bonds between atoms in the compound will be broken. Moreover, it is known that the bond energy is inversely proportional to the bond length: the shorter is the bond length the higher is the bond energy. Sherwood et al.[277] in their study of the valence bands of tin oxides by XPS and Xα calculation have determined the bond lengths of Sn-O in SnO and SnO_2. They have reported that the Sn-O bond in SnO_2 is shorter that in SnO (2.054 Å for SnO_2 and 2.224 Å for SnO). The same information has been reported by Kover et al.[276]. Therefore it is easier to dissociate tin from oxygen in SnO than in SnO_2 structure, which is consistent with the lattice energies of the two oxides. In fact, the lattice energy of SnO_2 is higher than that of SnO, namely 11807 KJ mol⁻¹ for SnO_2 and only 3652 for SnO [284, 285]. So propose that the increase/ formation of SnO phase in the films is occurring in two steps:

1- Dissociation of SnO: SnO → Sn+ $\frac{1}{2}$ O
2- Equilibrium: SnO_2 + Sn = 2 SnO

It is highly possible that the oxygen dissociated from tin migrates to the surface and then desorbed while the tin atoms will bond with SnO_2 to form SnO, resulting in fine to the increase of the SnO phase. Tropis[286] have studied in his thesis the adsorption/desorption of oxygen at the surface of SnO_2 as a function of the temperature. He reported different phase changes in SnO_2 versus temperature as illustrated in figure 4.3.13: (i) from ambient temperature to 150°C, the oxygen existing at the surface in the physisorbed $O_{2,phys}$ is easy to dissociate, (ii) At temperatures ranging between 150 and 200°C nm

oxygen lie at the surface in the chemisorbed form $_{ads.}$, (iii) At high temperatures, namely 200-500°C, oxygen could be in the O^{2-} form, which is instable and needs energy to be linked to the lattice. Beyond this temperature, the oxygen of the lattice migrate to the surface and thereby being desorbed when increasing further the annealing temperature. This behaviour corresponds exactly to that observed for our samples upon annealing.
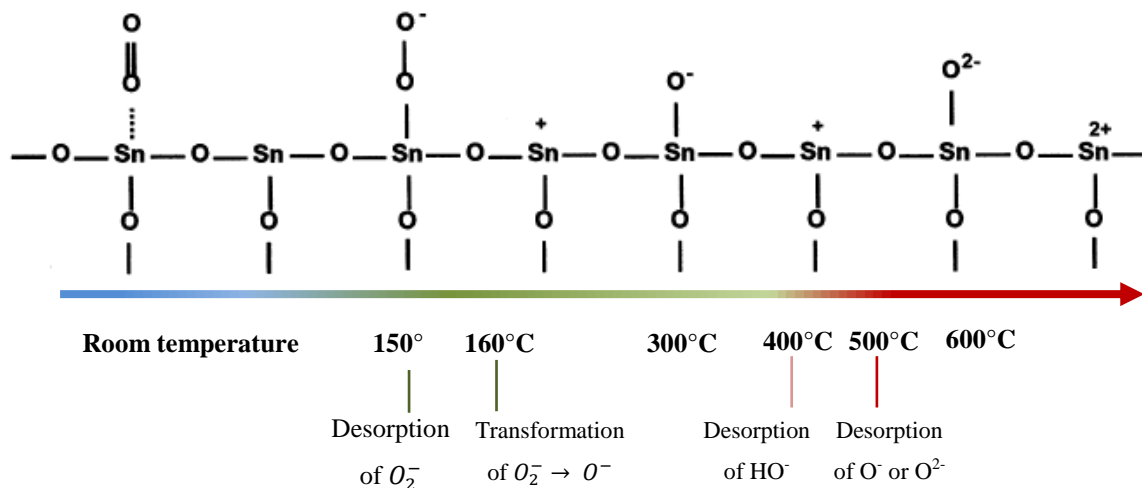

Figure 4.3.13. Physical changes in SnO$_2$ as a function of the temperature[286].

4.3.2.3. PL properties of Yb-doped SnO$_x$ films

The photoluminescence spectra of the Yb-doped films deposited at 8:2 sccm of Ar and O$_2$ at 100°C, before and after annealing at 500, 700 and 900°C are presented in figure 4.3.14. Only Yb-related PL is presented here. For this particular experiment, the excitation was performed by means of a xenon lamp and set at 300 nm wavelength.

The Xenon excitation of the as deposited sample (2 sscm) results in a strong emission peak of Yb at 970 nm and weak emission band at 1004 nm, in addition to a small contribution at 951 nm. Such results are slightly different from the PL recorded under a laser excitation (PL of figure 4.3.6). Increasing the annealing temperature to 500°C leads to the enhancement of the Yb-PL intensity, particularly the band centred at 1001 nm, whose the intensity is comparable to that recorded at 970 nm. Spectacularly, annealing at 700°C favours the emission at 1001 nm but also accentuates that at 980 nm which appears as a distinct peak. The band at 956 nm is also affected by the annealing step. Thus, the thin film sample annealed at 700°C exhibit a PL spectrum with several well-resolved bands. Such spectrum is remarkably similar to that recorded for the Yb doped SnO$_2$ powders annealed at 700°C (see figure.3.22 in chapter 3). A further increase of the annealing temperature up to 900°C results in a PL with a zero

phonon emission peak centred at 974 nm and a wide emission band. Although the PL signatures might say that the Yb are optically active in this sample, the interpretation is not straightforward given the particular results revealed by XPS and SEM experiments for this annealing condition.
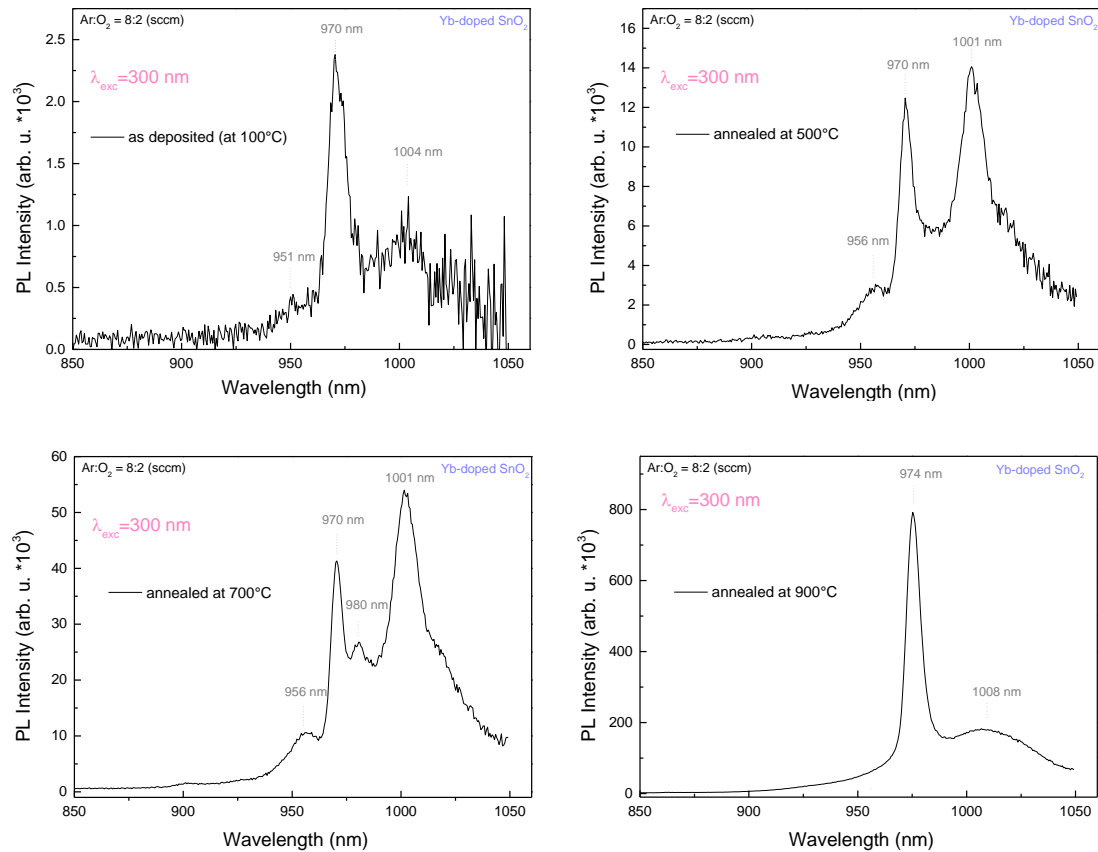
Figure 4.3.14. PL spectra of the Yb-doped SnO$_x$ films deposited at 8:2 sccm at 100°C and annealed at 500, 700 and 900°C. The excitation was performed by Xenon lamp at 300nm

The increase of the PL intensity originating from Yb as a function of the annealing temperature, in spite of the same density of Yb^{3+} ions in the structure, can be interpreted in terms of : (i) higher efficiency of the energy transfer from the host to Yb^{3+}, and/or (ii) higher transition probability between the electronic/vibronic levels in Yb^{3+}.

Concerning the efficiency of the energy transfer, we have seen from the Sn 3d and O 1s core levels an increase of the SnO phase in the structure with the annealing temperature. This means that the structure contains more oxygen vacancies when annealing at high temperature. Moreover, we know that the oxygen vacancies are one of the key parameters responsible on the energy transfer from the matrix to the rare earth. The increase of the SnO density and therefore the increase of the oxygen defects will create some intermediate deep levels in the band gap structure of SnO$_2$ which will favours the energy transfer rate from the host to the rare earth.

As for possibility (ii), we have explained in chapter 3 concerning the case of Yb-doped SnO_2 powders that the intensity of the emission in rare earths depend on the transition probability between two states, which in turn depends on the overlap between the vibrational wavefunctions of the initial and final states. The maximum of transition probability is occurring when the initial and final states are connected with vertical transitions. Thereby, it is highly possible that the crystal field exerted on the Yb^{3+} ions ensures the effectiveness of the maximum of transition probability, which results in an enhanced PL. The effect of the electrostatic crystal field on the Yb^{3+} ions is witnessed by the shift in their $4d_{5/2}$ core levels presented in figure 4.3.11. This shift is in fact revealing the change of the RE's surroundings. If one looks to the emission spectrum of the as deposited sample (100°C), one could notice that splitting of the energy levels of Yb is already done (photoluminescence at different emission bands). We can conclude that the annealing treatment in our case has enhanced the photoluminescence process of the Yb^{3+} ions by favouring the energy transfer rate from the host to the rare earth through transitions along the intermediate levels within the band gap as well as by increasing the transition probability between electronic levels in the rare earth. The deconvolution of the Yb emission of the sample deposited at 8:2 sccm of Ar and O_2 at 100°C and annealed at 700°C is presented figure 4.3.15.a. More than 7 components were needed to deconvolute the emission spectra. The transitions corresponding to each component have been successfully identified and reported in the Yb energy levels diagram drawn in figure 4.3.15.b. We have found that the energy levels structure of Yb in SnO_x in the thin films is the same as that calculated for Yb-doped nanoparticles (chapter 3). However, the final and initial states of the transitions have changed, supporting the assumption of the effect of the crystal field on the host matrix.

Figure 4.3.15. a) Deconvolution of the Yb-related PL for the sample annealed at 700°C. **b)** Energy levels structure of Yb and corresponding transitions of the emission spectrum of Yb.

4.3.2.4. PLE and energy transfer mechanisms

PLE spectroscopy has been performed on the different samples in order to clarify the PL mechanisms of the Yb-doped films under annealing and to investigate the origin of the eff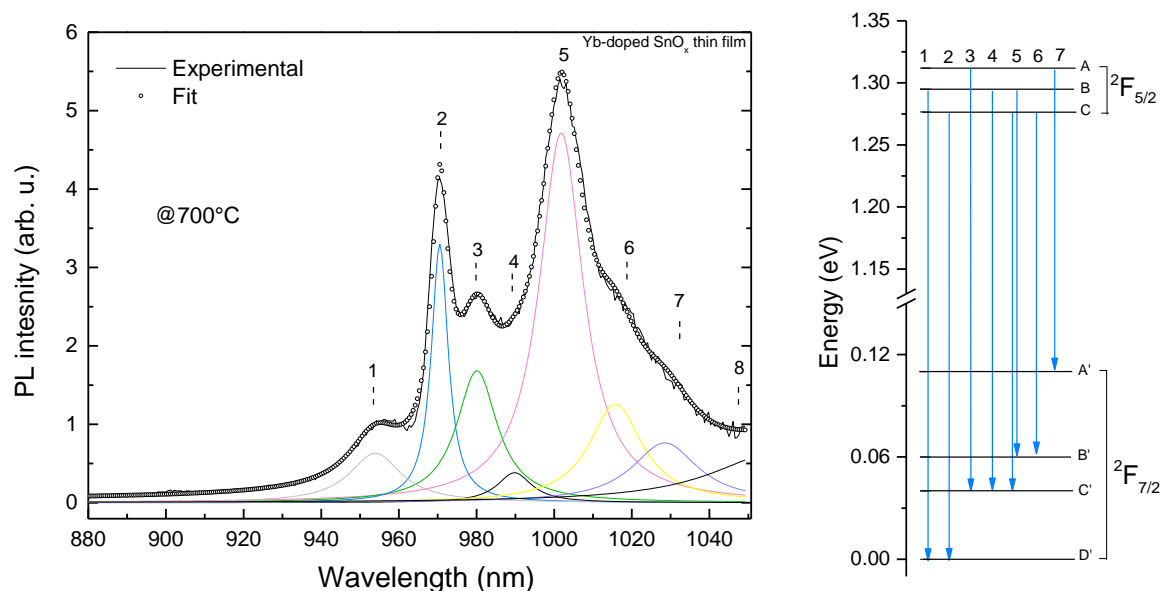icient emissions recorded in the infrared region. Figure 4.3.16 plots the PLE spectra of the Yb-doped SnO$_x$ films deposited under 8:2 sccm of Ar and O$_2$ and annealed at 500°C and 700°C. We deliberately avoided presenting here the case of the 900°C annealed sample as its structure is completely deformed. The PLE spectra reveal that Yb emission in the infrared regions essentially arises from indirect excitation from the host matrix. The Yb-related PL is found to increase when increasing the annealing temperature, particularly at 700°C. At this condition, the efficiency of the energy transfer can be clearly noticed.
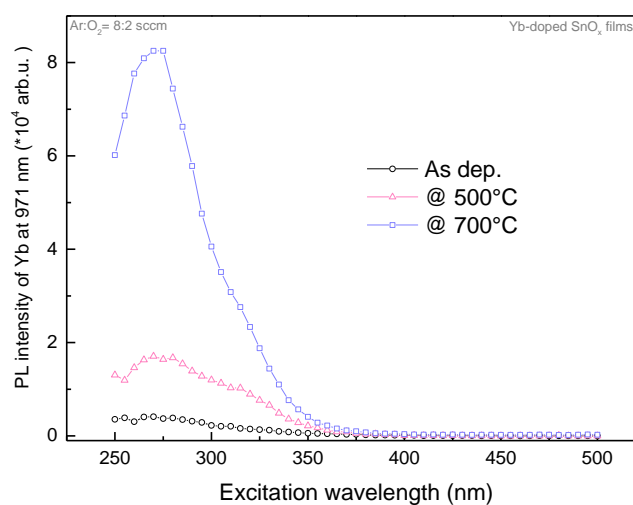
Figure 4.3.16. PLE spectra of the Yb-doped SnO$_x$ films as a function of the annealing temperature.

In this system, the SnO$_x$ host matrix is found to absorb the UV excitation, mainly in the 250-375 nm range, and indirectly sensitize the Yb^{3+} ions, which in turn will emit NIR photons. This process can be identified as down shifting of down conversion. It is likely that one UV photon could be converted into two IR photons, since the energy absorbed by the host is three times larger than the gap between the two electronic levels of Yb. Nonetheless, additional Quantum Yield experiments are needed to identify the process and its real efficiency.

In order to get larger view on the PLE processing involving wide range of wavelengths, PLE maps have been recorded for the four samples. The results are shown in figure 4.3.17.

Figure4.3.17. PL maps of the Yb-doped SnO$_x$ films deposited at 8:2 sccm and annealed at different temperatures

In line with the PL results, The PL map of the as deposited sample consists of a single and weak emission band centred at 970 nm (1.27 eV) arising from excitation in the 250-310 nm range (4.9 - 4 eV, respectively). The PL around 1000 nm also exists but it is too weak to be detected here. The PL map of the sample annealed at 500°C shows addi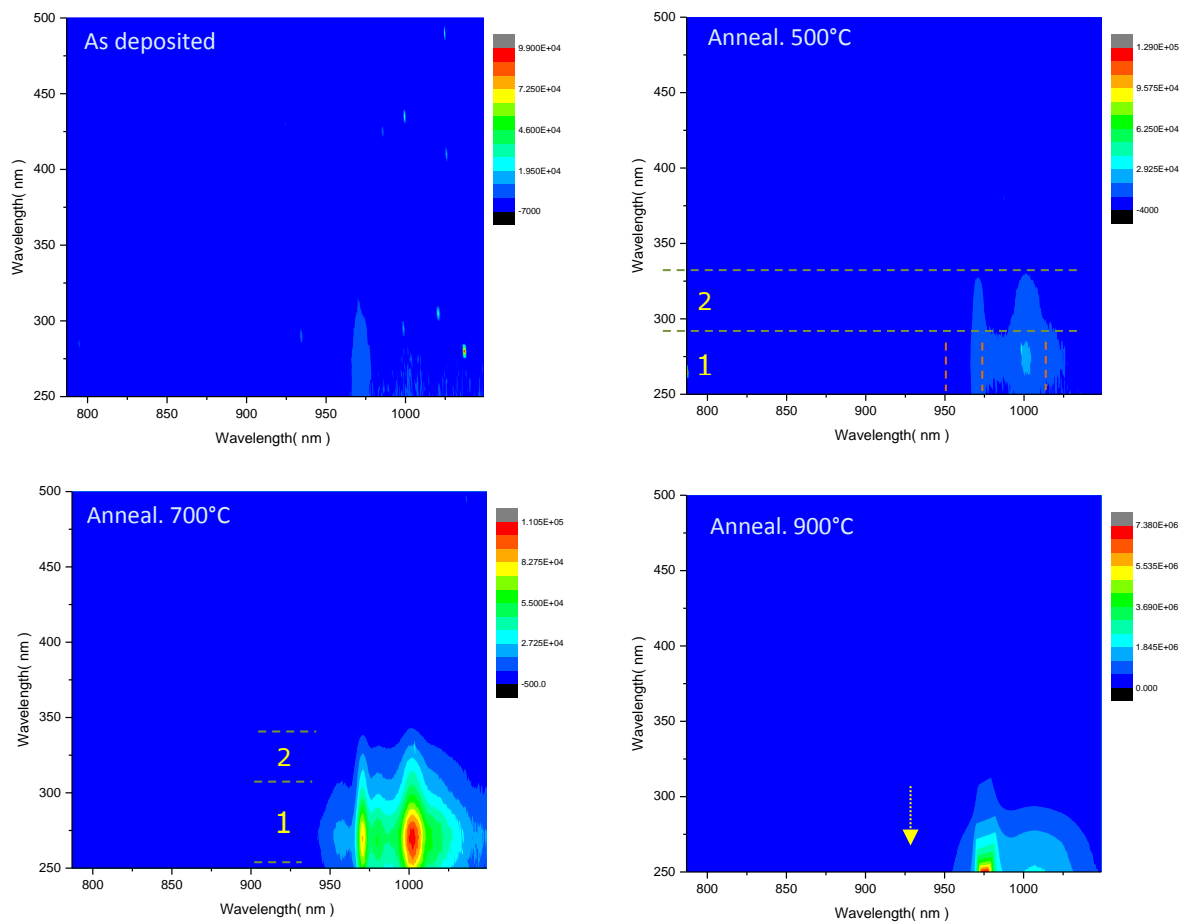tional strong emission band lying from 980 to 1025 nm (1.26-1.20 eV) and centred at 1003 nm (1.23 eV). Moreover, it is worth noting the extension of the excitation range of Yb to 330 nm (3.75 eV). More interestingly, two excitation regimes can be distinguished on the PL map of this sample. (i) The excitation from 260-290 nm (4.7- 4.2 eV) (region 1) gives rise to continuum emission from 965 to 1025 nm with a maximum at 1003 nm , (ii) the excitation from 290 to 330 nm (4.2- 3.75 eV) (region 2) leads only to two distinct and well defined emission bands. This behaviour can be interpreted in terms of resonance of transitions energies within the band gap of the SnO$_2$ host with the energy levels of the Yb $^{3+}$ rare earth.

The PL map of the 700°C annealed sample reveals the presence of third emission at higher energies, namely between 945 and 965 nm (1.28 to 1.3 eV) and arising from excitation in the 250-305 nm (4.9-4.06 eV). The emission band at higher wavelengths is broadened up to 1100 nm. This broadening aspect

indicates the contribution of transitions involving vibronic states of the $^2F_{5/2}$ and $^2F_{7/2}$ electronic levels of Yb^{3+}. Moreover, a very strong emission at each peak centre can be clearly seen by the red color, indicating the intensity of transitions; in other words we can say that the transition probability is at its maximum. Such result sustains the effect of the crystal field on the photoluminescence properties of the rare earth elements. The presence of a band around 945-965nm exclusively under excitation between 250 and 305 nm (excitation 1) indicates the presence of some deep localised states in the host band gap that efficiently sensitize this energy level of Yb. This is not the case for the two other bands that can be excited up to 344 nm.

4.3.3. Effect of the deposition temperature

In the above section, we have investigated the effect of the post-annealing temperature of as-deposited samples on their structural and PL properties. Here, we explore the effect of deposition temperature on the physical properties of Yb-doped SnO$_x$ films, with a focus on the photoluminescence and energy transfer. The doped films were deposited with a ratio R=1,3 corresponding to the condition 8:5 sscm for Ar:O$_2$ respectively. The deposition temperature was varied from 100°C to 500°C. The deposition time was set to 30 min. Table 4.3.5 displays the measured thicknesses of the deposited films as measured by XRR and ellipsometry versus the deposition temperature. The values are quite close.

4.3.3.1. Crystal structure

Figure 4.3.17 displays the XRD patterns of the Yb-doped SnO$_x$ films elaborated with Ar:O$_2$ values of 8:5 sccm at different deposition temperatures, namely 100, 300, 400 and 500°C. The case of the room temperature deposited sample will not be reported here since we have previously shown that no emission lines can be recorded in such amorphous structure. At first glance, the deposition temperature does not provide significant changes in the structure. Indeed, all films exhibit the same number and shape of diffraction peaks indicative of a SnO$_2$ polycrystalline structure. A peak at 24.6° is visible in all diffraction patterns of the samples. As we reported in the case of Nd-doped SnO$_x$ films, we speculate that this signature is corresponding to the Sn-O-Si alloy formed at the interface between the silicon substrate and the SnO$_x$ layer because we did not observe this peak for patterns recorded on quartz substrates. Yet, this peak could possibly also be attributed to the orthorhombic SnO phase according to the JCPDS card n°= 00-013-0111. We therefore cannot exclude the presence of traces of SnO in the structure. This is based partially on the XPS observation reported in the last section where an important contribution of SnO oxide was found within the Yb-doped films. Only analysis by TEM and EDS in this region can allow identifying the exact nature of this component.
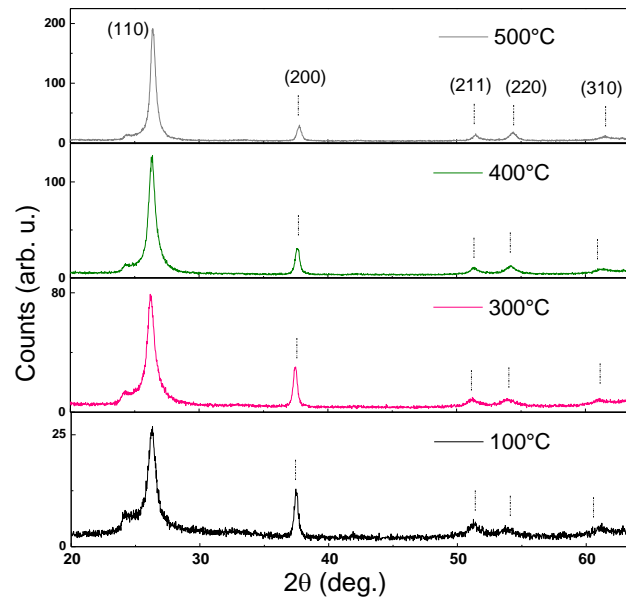
Figure 4.3.17. XRD patterns of the Yb-doped films deposited at 8:5 as a function of the growth temperature

Figure 4.3.17 shows clearly an evolution of the intensity of the diffraction peaks when the deposition temperature increases. The intensity of the (110) peak increases significantly (factor 8) while that of the (200) peak seems to not be seriously modified. A zoom of the diffraction spectra on the 25-40 2θ scan range is given in Figure 4.3.18.a from which the (110) and (200) peaks positions obtained using a lorentzian fit of the diffraction peaks were exctracted and reported in figure 4.3.18.b. At 100°C, the intensity of the (200) peak is more or less comparable to that of the (110) peak. Increasing the deposition temperature to 300°C leads to an intensity increase of the (110) peak relatively to the (200) peak, meaning that more crystallites are grown in this direction. Furthermore, a slight shift to lower diffraction angles is noticed indicating an increase of the lattice parameter resulting from a tensile stress exerted in the material. Increasing further the growth temperature to 400°C results in the increase of the (110) peak intensity while that of the (200) remains constant. However, the diffraction peaks of (200) direction are found to shift towards higher diffraction angles indicating a decrease of the lattice parameter resulting from a compressive stress in the lattice. The same behaviour has been noticed for the film deposited at 500°C, where the (110) peak becomes prominent compared to the (200) peak meaning that the growth is favoured along the (110) direction. As shown in figure 4.3.18.b, increasing the deposition temperature leads to a shift in the diffraction peaks positions to higher diffraction angles which translates a compressive stress exerted on the lattice.

The crystallites sizes, lattice constant 'a' calculated from the XRD data are reported in table 4.3.5. The band gap values calculated by ellipsometry and extracted from transmission spectra are reported as well. As expected, the crystallites size along the (110) direction is found to be an increasing function

of the deposition temperature, but the values are systematically lower as compared to the crystallites size along the (200) direction. The last is found to decrease with temperature. Concerning the lattice parameter, our films exhibit values higher than that reported for the bulk material (4.738 Å). This is particularly expected for the Yb doping. Since the Yb atoms have a larger ionic radius than Sn, their insertion into the SnO$_2$ matrix will induce some tensile stress in the lattice. And since the deposition temperature is known to be a key parameter on the atoms arrangement in the lattice, the larger values of the lattice parameter than that of the bulk is a good sign. Finally, the decrease of the lattice parameter induced by the increase of the deposition temperature can be ascribed to a better crystalline structure and to the presence of few defects in the matrix.
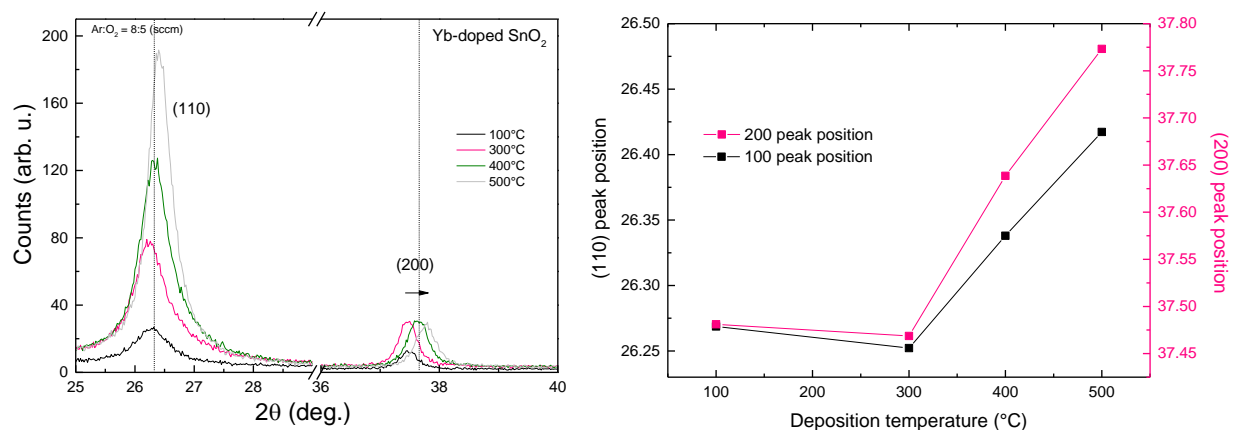
Figure 4.3.18. a) Overlays of the diffraction patterns of the Yb-doped SnO$_x$ films (8:5), **b)** (110) and (200) diffraction peaks positions as a function of the growth temperature

Table 4.3.5 gives the crystallites size along the (110) and the (200) direction and the lattice constant calculated from the (200) peak (as deduced from the XRD analysis) versus the deposition temperature.

T (°C)	Thickness (nm)		Crystallites size (nm)		Lattice cons. 'a' (Å) (200)	Band gap (eV)	
	XRR	ellipsometry	(110)	(200)		Trans.	ellipsometry
100	119.2 ± 1.23	118.53 ±1.12	11.2 ±0.02	26 ± 0.03	4.79 ± 0.03	3.56 ± 0.2	3.99 ± 0.2
300	77 ± 1.02	77.2 ± 1.25	11.7 ±0.04	25.7 ±0.25	4.79 ±0.05	3.76 ± 0.3	4.20 ± 0.2
400	81.5 ± 1.46	80.4 ± 1.21	13.4 ±0.02	23.2 ±0.33	4.77 ± 0.01	3.81 ± 0.2	4.20 ± 0.01
500	86.0 ±2.54	88.22 ± 3.2	17.9 ±0.03	23.1 ±0.33	4.76 ± 0.01	3.82 ± 0.2	4.21 ± 0.01

4.3.3.2. Chemical analysis by XPS

XPS analysis have been carried out on the Yb-doped SnO$_x$ films elaborated at different growth temperatures under 8:5 sccm of Ar and O$_2$, respectively. The spectra of the valence bands (not

presented here) were found to be similar independently of the substrate temperature, and are signature of a SnO$_2$ structure confirming the XRD results. However, we have seen previously that deeper XPS analysis are necessary to evaluate the SnO2-SnO components with the layer. In fact, the reversible dual valency of tin makes it quite particular, complicated and difficult for analysis. Thus, tin and oxygen core levels were determined to extract valuable information. The Sn 3d$_{5/2}$ and O 1s core level spectra of Yb doped films deposited at different temperatures are displayed in figure 4.3.19.
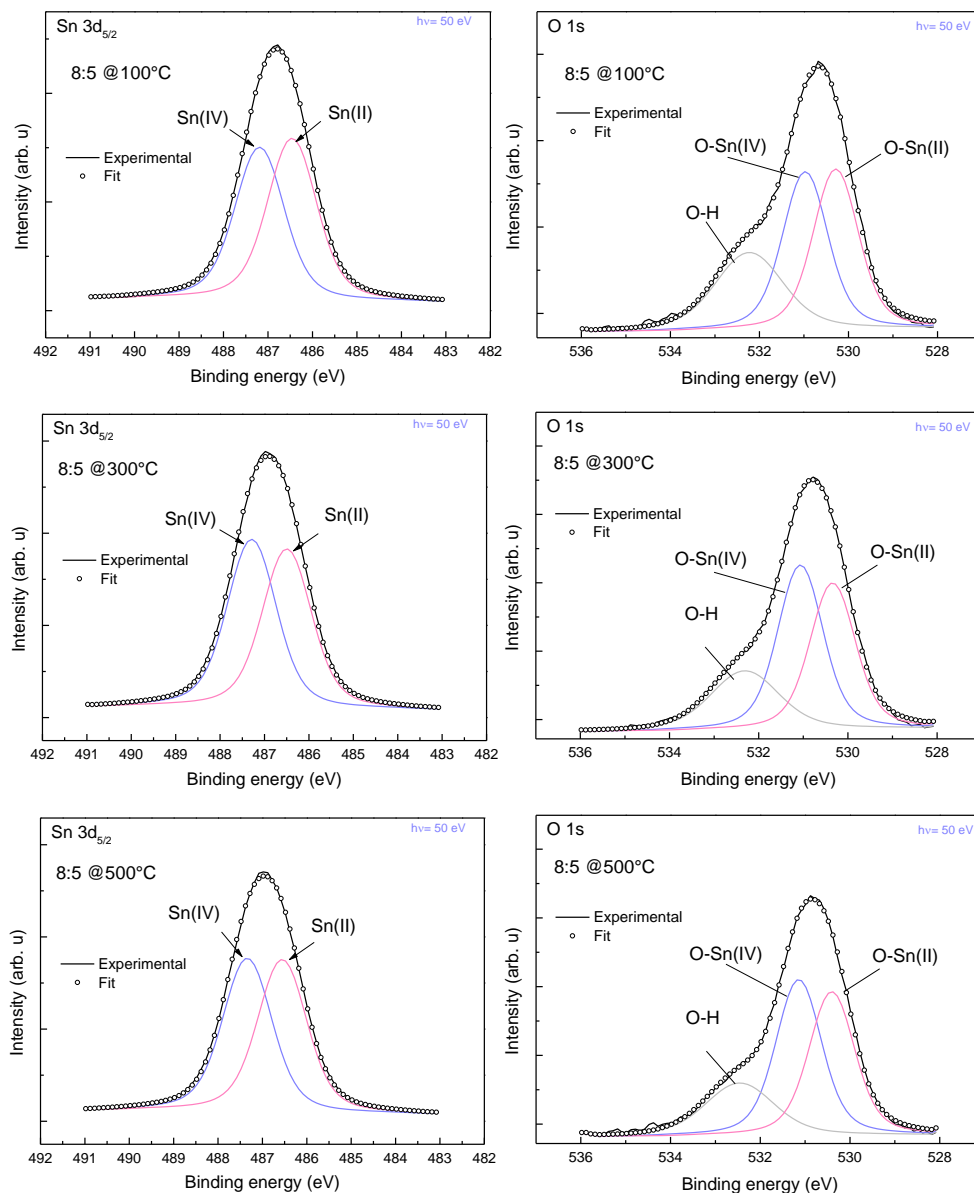
a) Sn 3d$_{5/2}$ and O 1s core levels

Figure 4.3.19. Sn 3d$_{5/2}$ and O 1s core levels in the Yb-doped films (8:5) grown at different T.

The spectra of the sample deposited at 100°C have been already discussed in section 4.3.1.4. This film appears to be composed of 50:50 % of SnO and SnO$_2$ from deconvolution of its tin and oxygen elements. Increasing the deposition temperature to 300°C is found to slightly change the oxides proportions. The values of each component are reported in table 4.3.6. At this deposition condition, the SnO$_2$ phase becomes more prominent than the SnO one. However, the difference between them is too weak to be significant. Further increase of the substrate temperature to 500°C does not affect the film structure as the extracted values are comparable to those of the sample deposited at 100°C. Thereby, we can say that the samples elaborated at temperatures up to 500°C have more or less the same oxidation point level. Table 4.3.6 reports also the oxygen-tin ratio (stoichiometry of the films) which is found to decrease for increasing deposition temperature. This indicates a decrease of the oxygen atoms in the structure induced by temperature. This result will help us understanding the PL properties of the films in the following section.

Table 4.3.4 SnO and SnO$_2$ proportions of the Yb-doped SnO$_x$ films deposited at 8:5 sccm under Ar and O$_2$ at different substrate temperatures (100,300 and 500°C), extracted from Sn 3d$_{5/2}$ and O 1s core levels spectra.

Samples 8-5 (sccm)	From Sn 3d$_{5/2}$		From O 1s		Stoichiometry SnO$_x$
	SnO$_2$	**SnO**	SnO$_2$	**SnO**	x = [O]/[Sn]
100°C	49.83	50.17	48.41	51.59	1.62 ± 0.01
300°C	51.32	48.68	53.13	46.87	1.58 ± 0.01
500°C	49.99	50.01	52.25	47.75	1.56 ± 0.01

b) Yb 4d$_{5/2}$ core level

A closer look to the Yb 4d$_{5/2}$ core level of the Yb-doped films is presented in figure 4.3.20. First, the spectra show that Ytterbium atoms are bound to oxygen whatever is the deposition temperature. Moreover, the area of the Yb 4d$_{5/2}$ peak is quite comparable for all samples, indicating the same density of optically active Yb^{3+} ions. Clearly, the increase of the deposition temperature does not affect that much the oxidation state of Yb, neither its surroundings. When considering the decrease of the oxygen content in the films one would expect the presence of some Yb atoms isolated into the structure or less bounded to oxygen (2+ valence state). However, it is very difficult to detect such small amounts of Yb^{2+} given the detection limit of XPS.
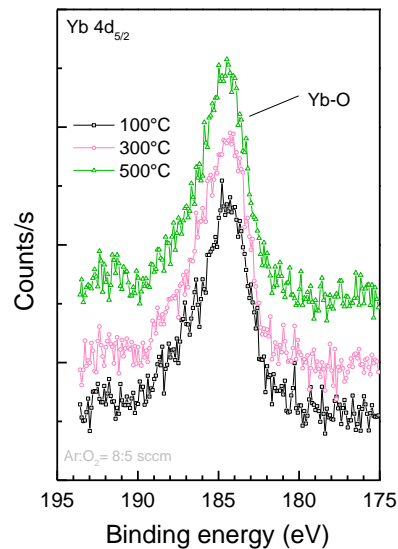
Figure 4.3.20. Yb 4d$_{5/2}$ spectra of Yb in the Yb-doped SnO$_x$ films as a function of the deposition temperature.

4.3.3.3. Optical properties

The UV-Vis-NIR transmission spectra of the samples deposited with the condition 8:5 of Ar:O$_2$ are presented in figure 4.3.21.a as a function of the deposition temperature. Two important information can be extracted here. First, all films have a transparency ranging between 80%-90% in the Visible to NIR ranges, which is of interest to solar cells as transparent oxide material. The second point is the absorption edges of the deposited films which are located at photon wavelengths as low as 200nm. This is once more indicative of a SnO$_2$ structure. It can be noticed that the absorption edge of the film deposited at 100°C is ranging between 200-250 nm while those of the films deposited at 300, 400 and 500°C are similar but have shifted to lower wavelengths (high energies). We have applied the Tauc plot method to the transmittance data of these samples (figure 4.3.21) and deduced the optical band gap energy values.
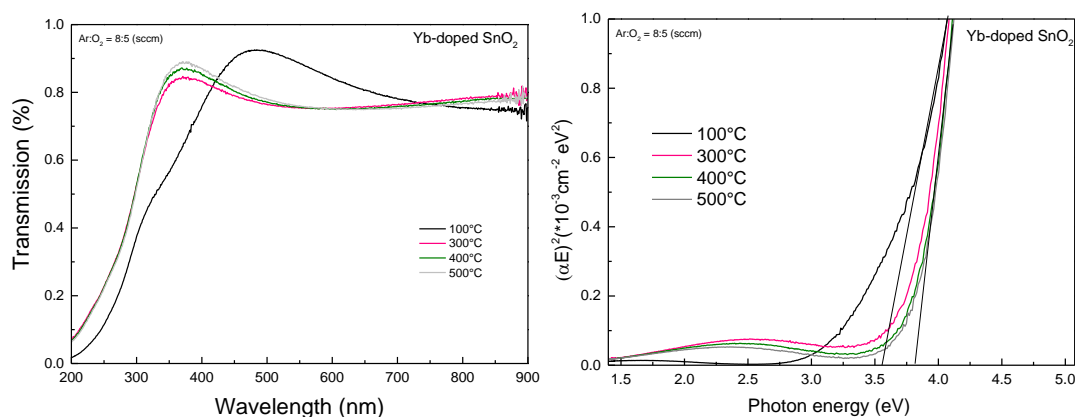

Figure 4.3.21. a) UV-to NIR transmission spectra, **b)** Tauc plots of the Yb-doped films (8:5) as a function of the deposition temperature

It is important to underline that the extraction of reliable values of the band gap energies from the Tauc plots is not straightforward given the complex shape of the curves. Thus the calculated Eg energy values should be taken with care while the trend can trusted.

Table 4.3.5 gives the values of the band gap energies calculated from the transmission data as well as those fitted from the ellipsometric data on the same samples. It turns out that the effective Eg values by transmission and ellipsometry are slightly different, but both techniques show a similar trend (increase of the band gap about 0.3 eV) when increasing the deposition temperature. The film deposited at 100°C has showed the lower band gap values at about 3.56 ± 0.2 eV while the films deposited at higher temperatures exhibit an average band gap in the range 3.8 ± 0.3 eV. It is difficult to explain the origin of this increase of the band gap, since many parameters have to be considered namely the crystalline quality, the preferential growth plans, presence of two oxides phases, deficiency of oxygen, and other structural defects without forgetting the presence of impurities (Yb ions). Yet, the values deduced from ellipsometry data confirm the trend but gives a higher average value about 4.2 ± 0.02 eV. Overall theses values are consistent with the XRD and XPS results for a preferentially SnO$_2$ structure.

4.3.3.3. Photoluminescence properties

Figure 4.3.22 plots the photoluminescence spectra of the Yb-doped SnO$_x$ thin films as a function of the growth temperature under an excitation wavelength of 355 nm of a Nd:YAG laser. The inset shows a zoom of the emission spectra of the films in the visible region.
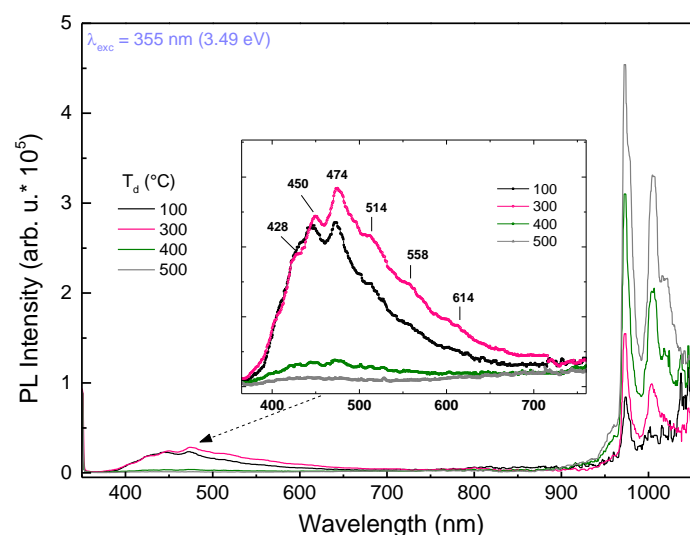

Figure 4.3.22. PL spectra of the Yb-doped SnO$_x$ films (8:5) as a function of the depiction temperature.

The samples elaborated at 100 and 300°C exhibit strong emission spectrum in the visible and NIR when compared to the samples grown at 400 and 500°C. The origin of the visible PL band of the

100°C film has been already discussed in the section 4.3.1.6. This emission ranging between 380 and 700 nm has been attributed to radiative transitions along the defects states localized within the band gap of the host matrix. Moreover, when comparing this PL spectrum to that of undoped or Nd-doped SnOₓ films, one could notice the presence of some narrow peaks in the visible region for the Yb-doped films. These features are particularly more prominent for the 300°C Yb-doped sample. A closer look on this emission region is presented in the inset of figure 4.3.22. At this stage, we do think that these features (more precisely from 480 to 700 nm) can be attributed to the presence of Yb^{2+} ions in the structure. Since XPS analysis showed that these films are oxygen deficient, it is likely possible that some Yb exist in the divalent state. This hypothesis is supported by previous studies [287-290] concerning the photoluminescence properties of Yb in phosphors matrices. Yb^{2+} emission has been identified at different wavelengths, mainly 450, 510, 540, 550, 620 and 630 nm. Moreover, it is important to underline that the emission wavelengths of the rare earth are strongly dependent on its surroundings, in other words, on its energy levels splitting, while the intensity of the PL band is determined by the transition probability occurring between two states. Moreover, in the recent work of Wang et al have [291], the authors have attributed a broad emission band centred on 500 nm and ranging between 400 and 700 nm to the Yb^{2+} ions. In addition to that, as we showed in the last PLE part, the 100°C film is showing some excitation peaks at wavelengths very close to the absorption lines of Yb^{2+} ions. Combining all these information indicates that a portion of Yb^{2+} ions are present in our film produced at 100°C. A similar reasoning can be applied to the sample deposited at 300°C, given its PL emission in the UV-vis range. Thus, given the comparable intensity of the PL in the 380-450 nm wavelengths range, it can be said that the samples deposited at 100°C and 300°C have comparable densities and types of radiative defects within the host band gap. The slight increase of the PL intensity in the 450-700 nm region for the 300°C sample can be explained by the presence of more Yb^{2+} ions in the structure.

The PL features present in the infrared zone are more linked to the existence of Yb^{3+} ions in the structure. Figure 4.3.22 shows intense bands centred at 973 nm and 1005 nm arising from the optically active Yb^{3+} ions for the sample grow at 100°C; the intensity of these band diminish for the 300°C sample.

The enhancement of the Yb^{3+} PL signal in the NIR regions means that either more Yb atoms are oxidized in the 3+ state (and thereby induce more intense PL) or that more efficient energy transfer (RE sensitization) is occurring between the host and Yb^{3+}. The probability of more Yb^{3+} into the structure can be excluded since the 4d core level of Yb analysed with XPS was constant for all samples. So it is rather related to the efficiency of sensitization from the matrix.

Figure 3.3.22 shows that the PL in the UV-vis region of the sample grown at 400°C dramatically decreases while its response in the NIR markedly increases compared to the 300°C sample. Again, the

weak emission arising from the SnO$_2$ structural defects can be recognized at lower photon wavelengths. It is also the case for the emission peak at 472 nm attributed to Yb^{2+}, which remains measurable. In the NIR part of the spectrum the PL intensity of the Yb^{3+} ions is efficiently increased. Different explanations could be possible to understand this behaviour:

The decrease of PL in the UV-Vis translates that most of the electron transitions in the SnO$_2$ bands structure are occurring non-radiatively. This means that either the host structure has reduced density of defects, or this part of energy, is transferred to the rare earth instead of being emitted.

The decrease of PL in this region could also be due to the formation of less Yb^{2+} ions in the matrix, and/or to an efficient energy transfer from the Yb^{2+} to the Yb^{3+} ions, explaining the intense PL in the NIR. The probability of the presence of more Yb^{3+} ions in the structure is ruled out. We have performed additional analysis by means of PLE to help casting light on the energy transfer mechanisms and to quantify if there is a change in the Yb valence and density when increasing the deposition temperature. This will be developed below.

As for the sample deposited at 500°C, it seems that both its crystalline quality as well the Yb emission in the NIR region are enhanced. Less radiative transitions in the UV-vis region have been recorded. We speculate that for this sample the crystal field is favourable for the Yb emission, most likely resulting from an efficient energy transfer from the matrix to the rare earth. We can consider that the intermediate deep levels within the band gap, created by oxygen vacancies, are in resonance with the Yb energy levels. In this case, the RE sensitization via the host is effective. But the energy transfer is not as simple as it looks like. The RE and the transfer centers (structural defects) must be in close proximity to each other. Additional conditions ensuring that the electron transitions within the energy levels of Yb should be fulfilled such as that the wave function overlap at the initial and final states.

In order to insight the origin of the Yb emission in the NIR region and to understand the different energy transfer process, further analyses by means of PLE spectroscopy have been performed on all samples. The PLE spectra of the Yb-doped SnO$_x$ films as a function of the deposition temperature are presented in figure 4.2.23. The PL intensity of Yb^{3+} ions at 971 nm was monitored while varying the excitation wavelength from 250 to 500 nm. The inset in figure 4.2.23 gives a zoom of the PLE spectra for the samples exhibiting a weak PL intensity.
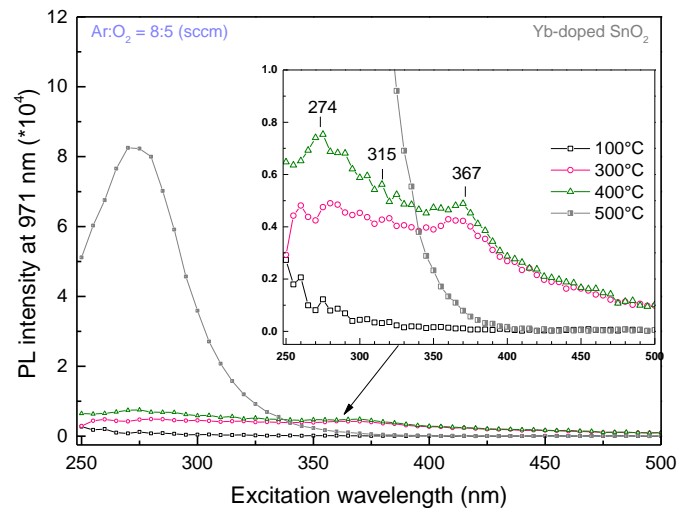
Figure 4.3.23. PLE spectra of the Yb-doped SnOₓ thin films (8:5) as a function of the deposition temperature.

The PLE data show that samples are revealing an Yb^{3+} emission when excited in the UV-Vis range. However, the Yb response is different from a sample to another. The film elaborated at 100°C exhibits Yb emission under excitation in the 205-350 nm range with a maximum intensity at 250 nm. This has been attributed to an energy transfer occurring from the matrix to the rare earth (see section 4.3.16). Moreover, the presence of additional excitation peaks at 274, 315 and 367 nm in the PLE spectrum of this sample intend to suggest the presence of some Yb^{2+} ions in the structure that also transfer energy to the Yb^{3+} ions.

Increasing the deposition temperature to 300°C results in the increase of the Yb emission under excitation in the UV and visible (inset of figure 4.3.23). More interestingly, some excitation peaks at 274, 315 and 367 nm appear more distinctly in the PLE spectrum. This feature can be attributed to an excitation of Yb^{3+} via the Yb^{2+} ions. Kaczmarek et al. [287] have reported the absorption spectrum of Yb^{2+} ions and identified several absorption peaks at 214, 227, 260, 271, 315 and 360 nm. Zhang et al have also reported on the absorption band of Yb2+ in different phosphors[292]. Moreover, Teng et al.[293] have reported a very interesting study, in which they describe an efficient energy transfer between Yb^{2+} and Yb^{3+} ions: After direct excitation of Yb^{2+} ions at 310 nm, they recorded an intense Yb^{3+} luminescence; They have identified this energy transfer as Down Conversion by phonon-assisted two photon cutting process. Three photon cutting process has been also proposed. Thanks to these literature studies, we propose that the excitation peaks identified in the PLE spectrum are Yb^{2+} related.

The film deposited at 400°C is exhibiting roughly the same PLE spectrum, with however a more intense PL when exciting in the deep UV; furthermore the excitation band at 367 nm becomes more prominent, which also indicates the presence of Yb^{2+} ions sensitizing the Yb^{3+} ions.

These results are in good agreement with the PL data reported in figure 4.3.22. For the case of the 300°C sample, one part of the energy is emitted by the Yb^{2+} ions in the visible region, while another part is transferred to the Yb^{3+} ions to be emitted in the NIR. In the case of the 400°C film, the absence of the emission in the visible region in figure 4.3.22 can be explained as following: all the energy absorbed by the Yb^{2+} ions is immediately transferred to the Yb^{3+} ions resulting in a higher Yb^{3+} PL in the NIR region. For these samples (300°C and 400°C), the energy transfer from the Yb^{2+} to Yb^{3+} can be considered as efficient as the transfer from the SnO$_2$ matrix to the Yb^{3+}.

The case of the sample deposited at 500°C is different as its PL shows an intense Yb^{3+} response in the NIR region when exciting the matrix in the range of 250-350 nm. This indicates much more efficient energy transfer from the host SnO$_2$ to the rare earth as compared with the other samples. In this case, the signature of the Yb^{2+} was not clearly detected. From a structural point of view, the highest deposition temperature provides to the atoms a better rearrangement in the lattice with even a decrease in the lattice parameter. It is more likely that the Yb^{3+} ions are now close to the defects centres involved in the energy transfer process. The PL of Yb under excitation of the host is enhanced 8 times by depositing at 500°C.

Complementary analysis of the PLE was conducted via a full PL mapping giving the emission response in the whole NIR range versus the excitation wavelength. This allows us getting a glimpse on the regions where the energy transfer is occurring. The results are presented in figure 4.2.24. The x-axis indicates the emission wavelength while the Y-axis denotes the excitation wavelength (nm). The color indicates the signal intensity (blue for weak signal and red for very intense). The PL map of the sample deposited at 100°C did not show any emission nor excitation region because of the weak signal of the film. The samples deposited at 300°C and 400°C showed different PL maps but remains quite comparable. Wide and continuous Yb^{3+} emission is detected in the infrared region, from 980 to 1050 nm. The PL at 1050 nm is particularly recorded under wide range excitation from 250 to 500 nm. It is also interesting to notice that the PL at 980 arises from excitation from 250 to 360 nm (mostly resulting from Yb^{2+} ions). Such interesting result is in line with the previous PL observations.

The energy transfer at 275 nm is presently ascribed to the matrix while that occurring at 360 nm supports highly the presence of the Yb^{2+} ions in these films. The PL at the 1050 nm is stronger than that at 970 nm and can be explained in terms of efficiency of the energy transfer, which is conditioned by the resonant transitions between the energy levels of the SnO$_2$/Yb^{2+} and the Yb^{3+} ions. The broad PL band can be interpreted by the involvement of the vibrionic levels of the energy levels multiplet resulting most likely from the crystal field splitting effect. Once more, the film elaborated at 500°C is different as it shows clearly two distinct PL peaks at 973 and 1005 nm of Yb^{3+}. Given its PL map, it is obvious that the transitions are involving only the two electronic states (^{2}F$_{5/2}$ and ^{2}F$_{7/2}$). Besides, it is

important to notice that the Yb^{3+} sensitization is occurring at high energies, mainly from 250 to 320 nm, which makes the difference from the samples elaborated at 300°C and 400°C
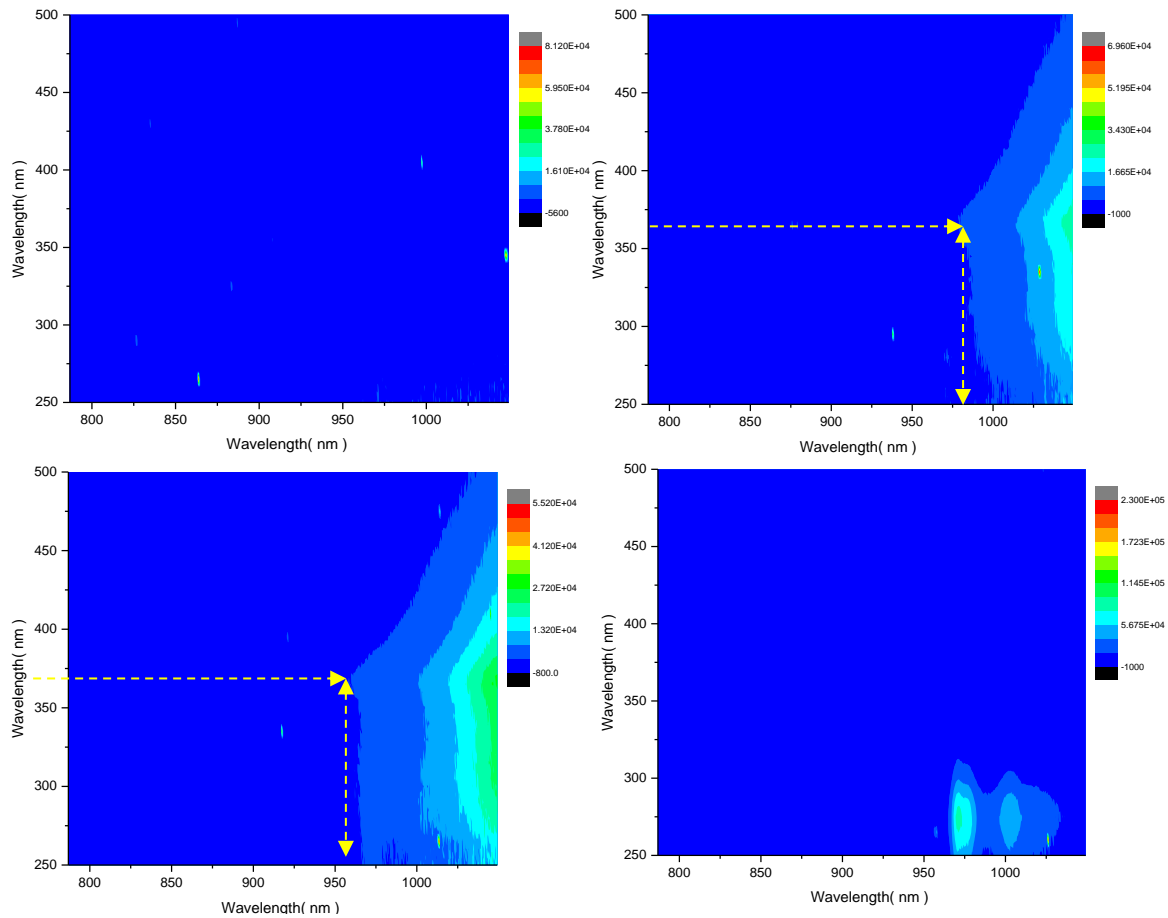

Figure 4.3.24. Full PLE maps of the Yb-doped SnOx films (8:5) as a function of the growth temperature

4.3.3.4. Energy transfer from Yb^{2+} to Yb^{3+}

In the previous section, we have often mentioned the possible energy transfer between Yb^{2+} and Yb^{3+}. The mechanism of the transfer process was proposed by Teng et al.[293]. It is illustrated in figure 4.3.25. To complete the information, the energy levels structure of Yb^{2+} is reported in figure 4.3.26 [294]

In order to demonstrate the cooperative down conversion process occurring between Yb^{2+} and Yb^{3+}, Teng et al. have studied the dependence of the Yb^{3+} luminescence on the excitation power at 325 nm. They have found a sublinear relationship with a slope of 0.43. They reported that for two photon cutting process, the slope should be close to 0.5, while for three photon cutting process, the slope should be around 0.33. In their case, they showed that the energy of an excited Yb^{2+} ion can be

transferred to two or three different Yb^{3+} ions. Thereby they proposed two ways for the energy transfer process:

- one electron in Yb^{2+} falling back to the ground state and three Yb^{3+} are excited to the $^2F_{5/2}$ energy level (figure 4.3.25.a);

- a cooperative down conversion process takes place between one Yb^{2+} ion and two Yb3+ ions (figure 4.3.25.b). This process is phonon-assisted. It is known that the radiative decay and multi-phonon relaxation can compete when the gap between two states is five times the phonon energy of the lattice. In their case, the excited electrons of Yb^{2+} can be easily dissipated in their phosphor matrix.

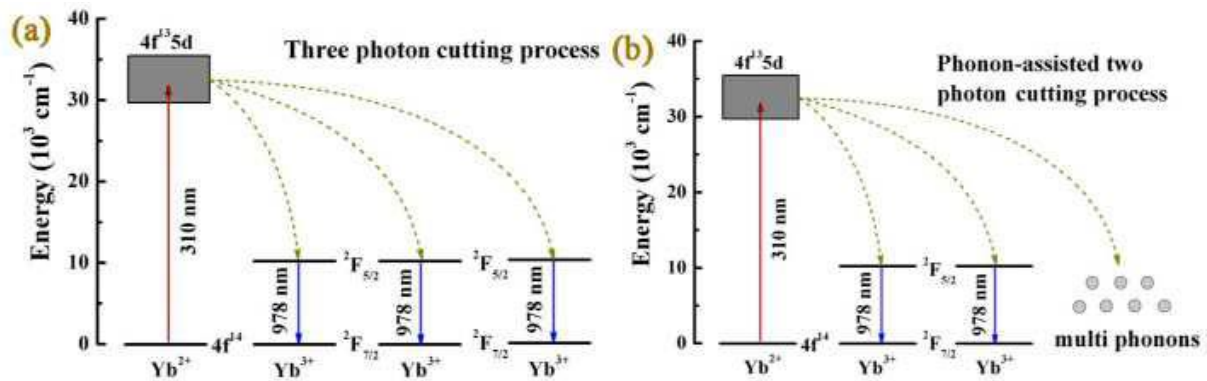They have concluded that both down conversion processes are possible.

Figure 4.3.25. Schematic energy level diagram of Yb^{2+} and Yb^{3+} showing two different energy transfer process, (**a**) three photon cutting process and (**b**) phonon-assisted two photon cutting process[293].

For further investigations, the energy levels structure of Yb^{2+} is reported from in figure 4.3.26 references [294]
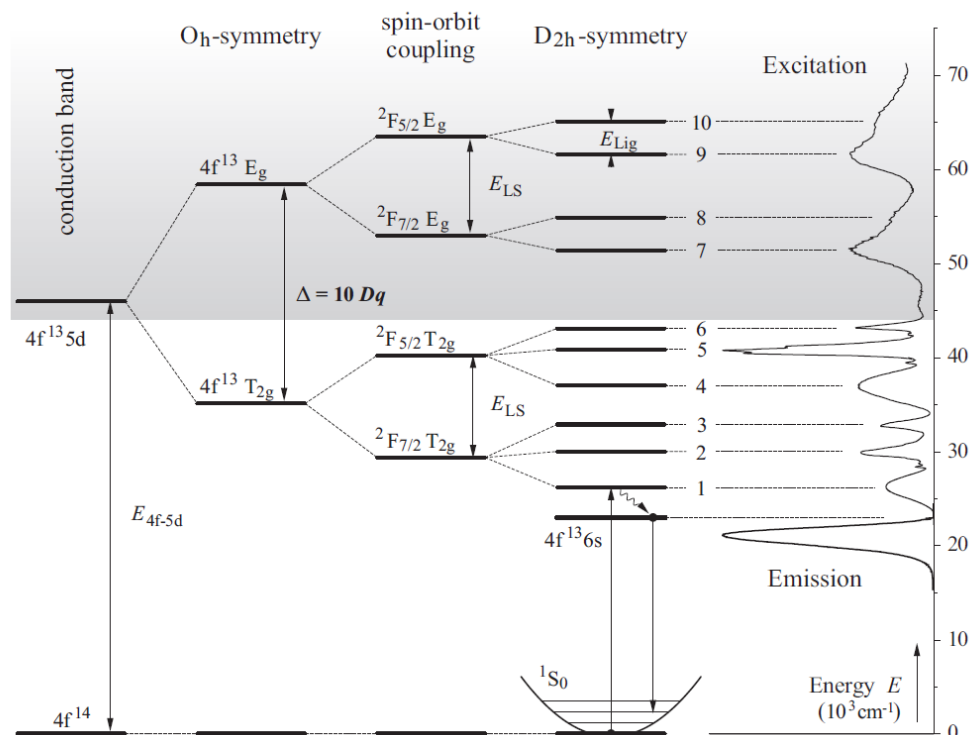
Figure 4.3.26. Energy level scheme of Yb^{2+} on sixfold coordinated D2h-cite in MgF$_2$.[294]

4.3.4. Summary

The Yb-doped SnO$_x$ thin films have been elaborated by reactive magnetron sputtering. Three parameters have been varied, namely the oxygen content, the post-annealing temperature and the deposition temperature, in order investigate the photoluminescence properties of Yb^{3+} ions in the infrared region and the correlation with the structural properties. Different characterization techniques have been employed toward this goal. The XRD for the structure, XPS for the core levels of elements, UV-Vis for transmission and determination of the band gap, MEB for surface analysis, PL and PLE for photoluminescence and energy transfer processes.

The variation of the oxygen content during the elaboration of the films has resulted in the activation of more Yb atoms in the structure and the increase of the SnO phase. Thanks to deep XPS analysis, we have found that our Yb-doped films contain at least 40% of SnO. The Photoluminescence of Yb was correlated to the density of optically active Yb^{3+} ions. We have found that the fewer are the Yb^{3+} ions the stronger is the infrared PL of the films above certain density.

On the other hand, we demonstrated that thermal annealing of the samples up to 700°C does not affect the density of the Yb^{3+} ions but rather it increased the amount of SnO phase in the structure. Thus, in spite of the same Yb^{3+} ions in the structure, the infrared PL spectacularly increases as a function of the annealing temperature and shows several emission lines. The deconvolution of this emission has resulted in more than seven components. The transitions corresponding to each band have been successfully identified, and it has helped in drawing the energy levels diagram of Yb.

Finally, the variation of the substrate temperature during the synthesis of the films did not affect the oxides proportion in the structure, but an important decrease of the lattice parameter has been noticed. This has resulted in an enhancement of the photoluminescence properties of Yb. At deposition temperature of 100, 300 and 400°C, we have revealed the presence of some features that we ascribed to Yb in the divalent state (Yb^{2+}). Supported by other studies in the literature we have identified an energy transfer from the Yb^{2+} to the Yb^{3+} ions.

As a main result of this study, an efficient energy transfer from the host to the Yb^{3+} ions has been experimentally demonstrated. We have noticed that both annealing at 700°C and depositing at 500°C have increased the PL of Yb^{3+} by almost one order of magnitude. However, when comparing their full PLE maps, annealing at 700°C gives rise to more wide and intense PL along the infrared region. Comparison of the Yb-doped SnOₓ system to the Yb-doped ZnO system has clearly shown the effect of the crystal field on the splitting of the energy levels of Yb.

In the next chapter, we demonstrate that Yb-doped films are potentially interesting for UV photons conversion process and can be applied to solar cells.

4.4. (Nd, Yb) co-doped SnO$_2$

4.4.1. Effect of gas flows

4.4.1.1. Synthesis

Co-doping the SnO$_x$ films by Nd and Yb has been performed using two distinct targets. Each rare element has been placed on the top of one target separately (two pure metal discs about 70 mg each). The deposition was carried out by evaporation from both targets simultaneously. The applied power on both targets was the same and fixed at 50 W. The Ar gas flow was set at 8 sccm while that of oxygen was varied from 2 to 8. The substrate temperature was chosen to be 100°C given the RE activation demonstrated above. We further increased the deposition temperature for the best emission sample up to 500°C. Only some selected samples will be presented here.

4.4.1.2. Crystal structure

In figure 4.4.1.a we present the diffraction patterns of the (Nd, Yb) co-doped thin films as a function of the oxygen gas flow during deposition. The low oxygen content (2 sccm) in the deposition chamber results in an amorphous/ nano-crystalline structure characterised by a wide diffraction band extending from 20 to 40°. Similarly to the case of Nd-doped samples (section…), we attribute this XRD feature to the presence of a SnO phase. Increasing the oxygen flow to 3 sccm switches the structure to preferentially SnO$_2$ tetragonal structure. Yet, a significant contribution of the amorphous band is still visible in the diffraction pattern of this sample. At a flow of 6 sccm, the diffraction signal has strongly increased indicating a better crystalline structure. However, the diffraction band (20 to 35°) is still present. As for the 8 sccm sample, it spectrum exhibits more or less the same diffraction pattern than the previous one. For a better observation,of the peak position, the diffraction patterns of the different samples were superimposed, except the amorphous one. The spectra of the 3 and 6 sccm samples were divided by a factor 5 (for clarty of patterns). A gradual shift of the diffraction's peaks positions toward lower diffraction angles is observed. This shift is more pronounced for the (200) plane. Let's remind that the shift in the peaks positions indicates the presence of stress in the crystal lattice, and in the present case this is induced by the presence of two rare earths. The peaks shift toward lower diffraction angles indicates an increase of the crystal lattice parameter, which denotes a tensile stress within the structure. This shift can be considered as a first indicator in favour of the insertion of the rare earth elements into the crystal lattice.
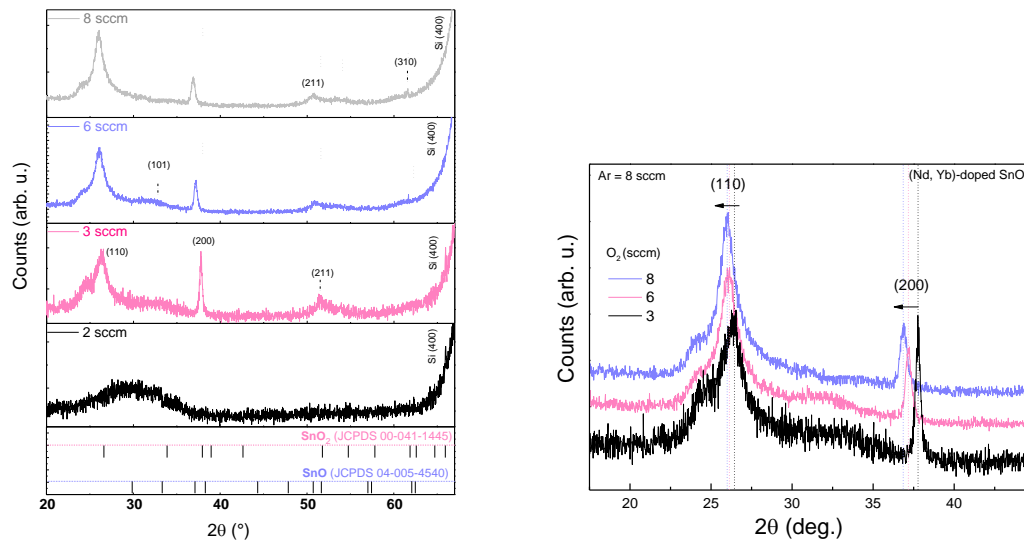
Figure 4.3.1. X-Ray diffraction patterns of (Nd,Yb) co-doped SnO$_x$ films deposited with increasing O$_2$ gas flow during deposition from 2 up to 8. The main peaks are indexed in the rutile SnO$_2$ structure.

4.4.1.3. Chemical analysis by XPS

Further investigations on the structural changes induced by oxygen have been performed by XPS. Precious information about the local environment of the rare earths (Nd and Yb) can be acquired from their core levels spectra. Before it is important to identify the oxides composition within films.

a) Valence bands

Figure 4.4.2 compares the valence bands spectra of the different (Nd, Yb) co-doped SnO$_x$ films as a function of the oxygen gas flow during deposition. Consistent with the XRD result, the 2 sccm film exhibits four-peaked valence band characteristic of SnO phase. The additional band at lower binding energies recorded for the 2 sccm sample corresponds to the Sn 5s states that are located at the minima of the conduction band in SnO$_2$ and becomes a part of states in the top the VB when the structure switches to SnO. More over, it can be noticed that the signal of the 2 sccm sample is shifted toward higher binding energies due to the charge effect.

Concerning the other films (3, 5 and 8 sccm), they all display three-peaked VBs which are typical of a SnO$_2$ structure.

It is important to underline that the valence bands spectra are just indicative of the most abundant oxide in the structure. These spectra provide information about hybridization of Sn and O states in the valence band, density and occupancy of these electronic states. Only analysis of the core levels of each element can allow us determining quantitatively the real oxides present in the films. We have shown in

the previous sections that none of our deposited samples were purely SnO nor SnO₂. By doping with rare earths we are dealing with a mixture of tin oxides phases in the structure.
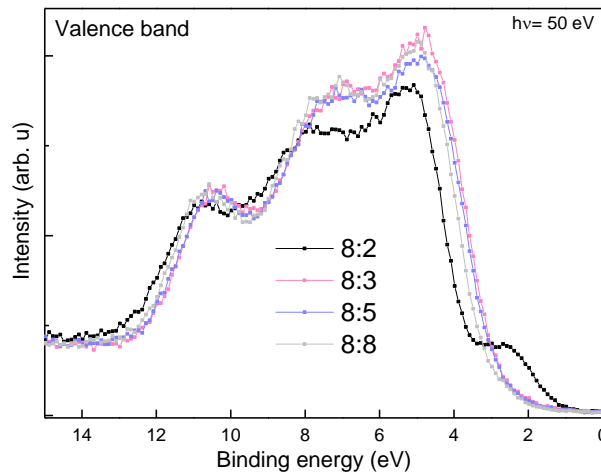

Figure 4.4.2. Valence band spectra of the (Nd,Yb) co-doped SnOₓ sample elaborated under different oxygen contents : 2, 3, 5 and 8 sccm.

b) Sn 3d$_{5/2}$ and O1s core levels

Sn 3d$_{5/2}$ and O 1s core level spectra of the (Nd, Yb) co-doped SnOₓ films as a function of the oxygen gas flow during deposition are displayed in figure 4.4.3. Surprisingly the 2 sccm Sn3d$_{5/2}$ core level reveals that a large part of Sn atoms (78,48%) are Sn (IV) suggesting strongly that this structure is a SnO₂ rich. This is in contradiction to its VB and XRD pattern. In the other hand, its O1s spectrum shows that the amount of lattice oxygen bound to Sn (II) in SnO are slightly larger than that bound to Sn (IV) in SnO₂. In fact, it is very difficult to determine the real parts of SnO and SnO in this particular film because of its amorphous nature. The deconvolution of the Sn3d$_{5/2}$ and O1s of the film deposited at 3 sccm of O₂ is showing quite comparable results. This film contains more SnO₂ amounts (52.58%) than SnO. Increasing the oxygen content during deposition to 5 sccm leads to the increase of the SnO content in the structure. This behaviour was already observed with the case of Yb-doped films. Further increase of O₂ flow seems to favour to the formation of SnO phase with becomes prominent against SnO₂ (54,30 % of SnO vs 45.34% of SnO). It is important to underline here that these films are co-doped with two rare earths that like very much being surrounded by oxygen atoms. It is therefore difficult to rely simply on from the results of the deconvultion of the O1s core level peak since oxygen can be bound to Yb as well as to Nd; Making a difference between them is extremely difficult because of the small and comparable concentration of the rare earths (in the limit of 1.3 at% of Yb and 0.6 at.% of Nd). However, the values of SnO and SnO₂ phases extracted from deconvolution of the Sn3d$_{5/2}$ and O 1s are reported in table 4.4.1. The stoichiometry of the films is reported as well. Overall, a trend in the structure has been noticed as a function of the oxygen gas flow during deposition. The SnO₂ phase is found to gradually decrease while that of the SnO increases by incorporating more oxygen in the deposition chamber.
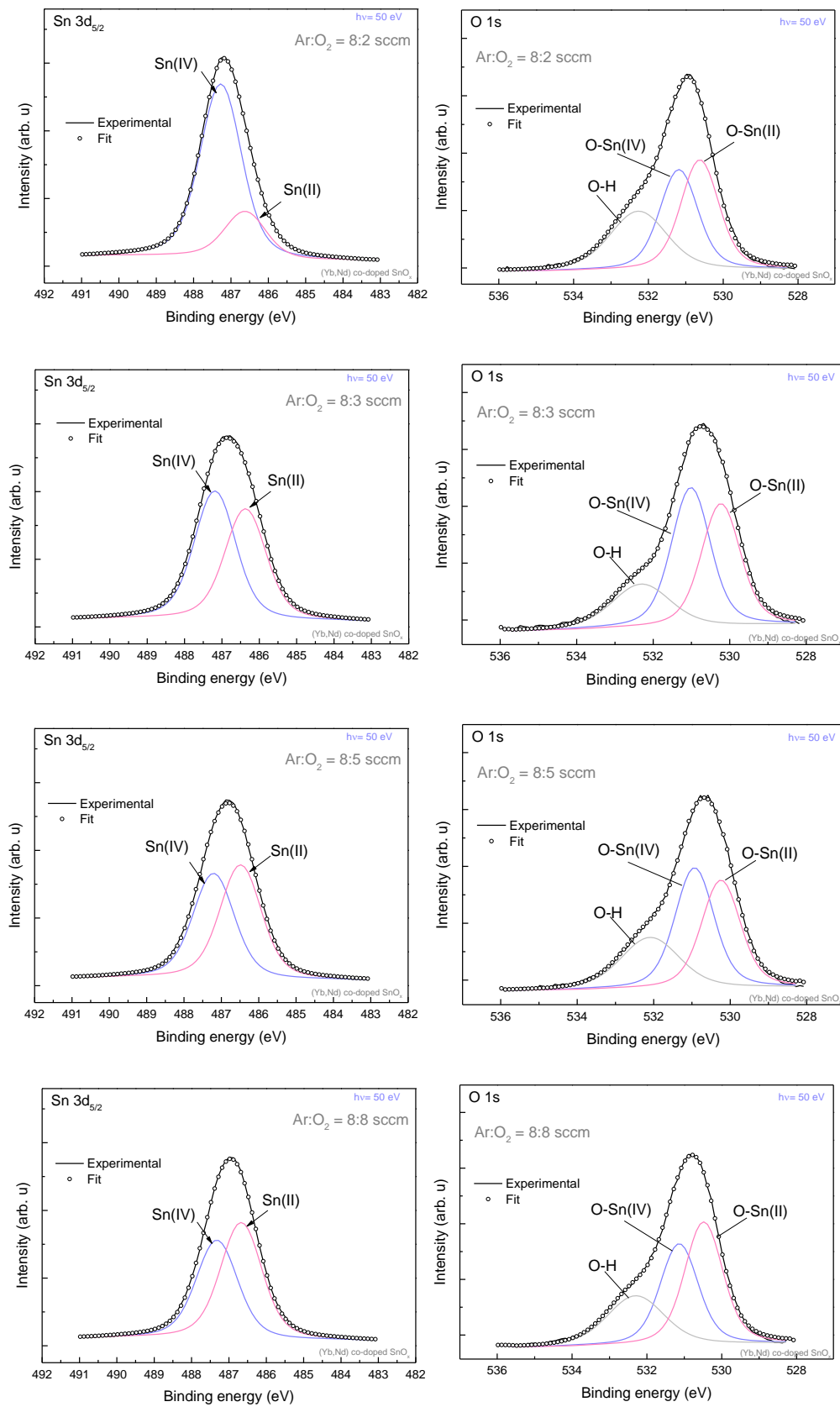
Figure 4.4.3. Sn 3d$_{5/2}$ and O 1s core levels spectra of the (Nd,Yb) co-doped SnOₓ samples as a function of the O$_2$ gas flow during elaboration

The stoichiometry of the films is affected by the variation of the oxygen flow. The 2 sccm film is an oxygen poor film when compared to the other samples for which the oxygen to tin ratio is approaching 1.85. Among all, the 3 sccm deposited sample is the most oxygen richer film.

Table 4.4.1 SnO and SnO$_2$ proprtions of the Yb-doped SnO$_x$ films deposited at 8:x sccm of Ar and O$_2$ with x=2,3,5 and 8, extracted from Sn 3d and O 1s core levels spectra.

Samples O$_2$ flow (sccm)	From Sn 3d$_{5/2}$		From O 1s		Stoichiometry SnO$_x$
	SnO$_2$	**SnO**	SnO$_2$	**SnO**	x = [O]/[Sn]
2	78.48	21.51	47.93	52.06	1.61 ± 0.01
3	53.58	46.41	53.43	46.57	1.87 ± 0.01
5	47.86	52.13	53.00	46.99	1.78 ± 0.01
8	45.34	54.30	45.34	54.65	1.82 ± 0.01

c) Yb 4d$_{5/2}$ and Nd 3d$_{5/2}$ core levels

The Yb 4d$_{5/2}$ and Nd 3d$_{5/2}$ core level spectra of the different samples are presented in figure 4.4.4 as a function of the O$_2$ gas flow. The Yb 4d$_{5/2}$ spectra shows the presence of Yb bound to oxygen (Yb-O) while the Nd 3d$_{5/2}$ spectra reveal the presence some non-bounded Nd atoms which aggregate as clusters (Nd-Nd), in addition to Nd atoms bounded to oxygen (Nd-O). The proportions of these different bounds vary from a sample to another. This result is expected since the Yb^{+3} has an ionic radius (0.086 nm) smaller that that of Nd^{3+} (0.100 nm), so it is much more easier to incorporate Yb in the structure than Nd.
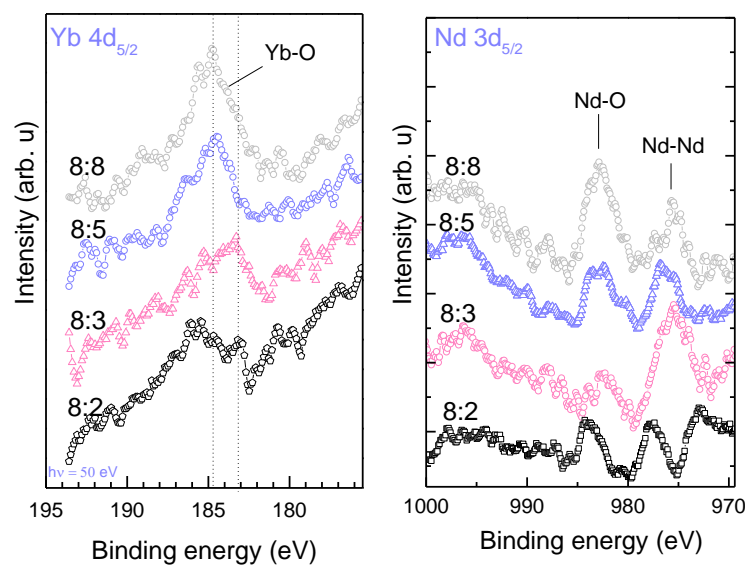
Figure 4.4.4. Yb 4d$_{5/2}$ and Nd 3d$_{5/2}$ core level spectra of the (Nd, Yb) co-doped SnO$_x$ films deposited at 8:x sccm of Ar and O$_2$ respectively, with x= 2,3,5 and 8 sccm

Considering the Yb 4d$_{5/2}$ spectra , the spectrum of the 3 sccm sample is shifted toward lower binding energies indicating a change in the local environment of the rare earth[8]. Besides the intensity of the Yb 4d$_{5/2}$ peak increases with increasing the oxygen gas flow. This means that more Yb^{3+} ions are bounded to oxygen in the structure. This explains somehow the increase of the SnO phase in the structure. The enhancement is more visible with the 5 and 8 sccm deposited samples.

As for the Nd 3d$_{5/2}$ spectra, the metallic Nd (aggregates of Nd-Nd) is present in all films but with a higher density for the 3 sccm film for which a weak signal was recorded for Nd^{3+} ions (Nd-O). The 8 sccm film is showing more Nd^{3+} ions in the structure, like Yb^{3+}. This is consistent with the increase of oxygen content in the films and reduction of SnO$_2$ to SnO. Besides, a shift toward higher binding energies is noticed for Yb and Nd for the 2 sccm sample (see the VB spectrum) because of charge effect.

4.4.1.3. Optical properties

Figure 4.4.5 presents the UV-Vis-IR transmittance spectra of the (Nd, Yb) co-doped films as a function of the oxygen gas flow during samples elaboration. The inset in the figure shows a zoom on the absorption edges in the UV-region. All films are transparent in the visible-IR region and absorb in the UV region. The transmission varies from 75 to 85 % by increasing the oxygen gas flow. This is also due to the decrease of the thickness of the films resulting from the synthesis process. The spectra clearly show a shift of the absorption edges toward higher energies indicating an increase of the band gap. The same behaviour has been noticed for the Yb-doped samples. It was explained by the moss burstein effect. This is consistent with the XPS results, which showed an increase of the optically active Yb^{3+} and Nd^{3+} as a function of the O$_2$ gas flow. Further analysis by the Tauc plots and ellipsometry are needed to determine the band gap values.

Aucune source spécifiée dans le document actif.[8] The Nd 3d$_{5/2}$ peak of this sample is not shifted as compared with the other 3d$_{5/2}$ peaks in the spectra, meaning that only local environment of Yb is affected in this sample
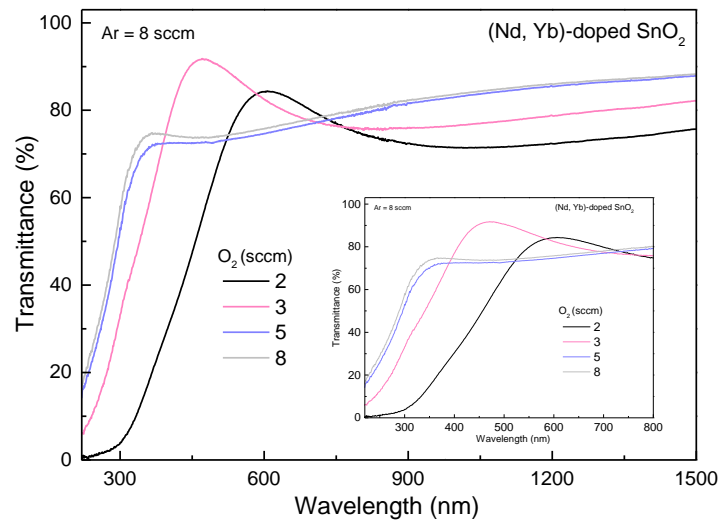
Figure 4.4.5. UV-Vis-IR transmittance spectra of the (Nd, Yb) co-doped SnO$_x$ films as a function of the oxygen gas flow during elaboration.

4.4.1.4. PL properties of (Nd, Yb) co-doped SnO$_x$ films

The photoluminescence spectra of the different samples are presented in figure 4.4.6. The excitation was performed by means of a xenon lamp. In figure 4.4.6.a and 4.4.6.b reports the PL spectra after an excitation wavelength of 275 nm (via SnO$_2$) and 585 nm (via Nd^{3+}) , respectively.
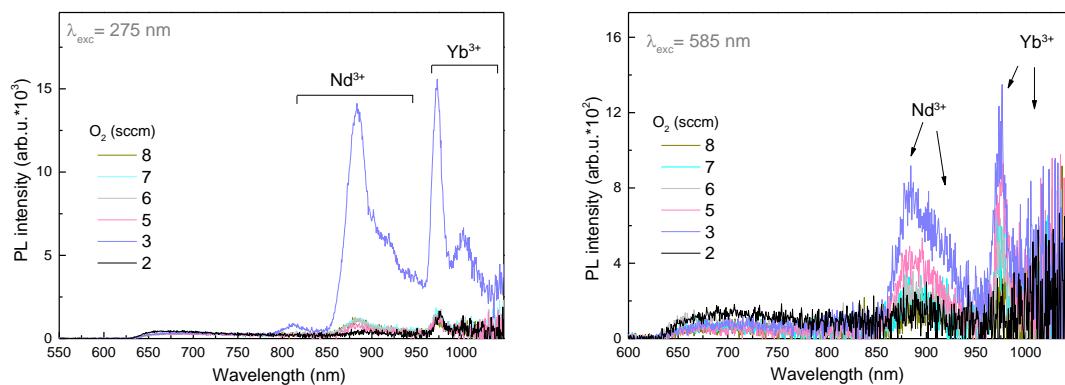

Figure 4.4.6. PL spectra of the (Nd,Yb) co-doped SnO$_x$ films deposited at 8:x sccm of Ar and O$_2$, respectively, with x= 2, 3, 5, 6, 7. The excitation was performed by Xenon lamp at 275nm (a) and 585 nm (b).

The photoluminescence of both rare earths (Nd and Yb) is present in the emission spectra of all samples whatever the excitation wavelength (275 and 585 nm). This is indicating that the inserted Yb and Nd ions are optically active. However, the intensity of their emission varies from a sample to another and depends on the excitation wavelength as well. This is consistent with the XPS results which demonstrated the insertion of both rare earths and their 3+ oxidation state (optically active) with however different contents versus the deposition conditions. The 3 sccm sample particularly shows

strong emissions of Nd^{3+} and Yb^{3+} under 275 nm excitation despite their small amounts recorded in the XPS spectra. The efficiency of the energy transfer from the host to both rare earths is then proven. The weak PL recorded for the samples with more oxygen (5, 6, 7 and 8 sccm) could be explained by a concentration quenching effect, as was the case of the Yb-doped films. In fact, the XRD data of the co-doped films have shown an increase of the crystal lattice parameter indicating a dilatation of the unite cell. This is likely due to the insertion of more and more Yb and Nd atoms in the structure and results in the decrease of the inter-atomic distance between the elements. On the other hand, the XPS data have revealed more optically active Yb and Nd ions (meaning that intra-4f transitions are allowed in their structure, absorption/emission). The fact of presence of more optically active rare earths close to each other will favour the non-radiative energy transfer process between the ions. In other words, the energy/photon or electron emitted by one excited ions is simultaneously re-absorbed/trapped by another identical ion and therefore none or very weak emissions can be recorded. The case of 2 sccm oxygen flow is particular. Indeed, this sample having an amorphous structure is exhibiting weak but considerable emission of Yb^{3+} under excitation of 275 nm, while that of Nd^{3+} seems to be almost vanishing. This is quite consistent with the results of pure Nd-doped films, for which no emission of Nd has been recorded in amorphous SnO structure (case of R=4-oxygen poor film). It is in contrast with the case of Yb with 2sccm oxygen flow for which the crystalline order did not seem to influence the PL signal.

Figure 4.4.6.b presents the PL spectra of Nd and Yb of the different samples under direct excitation of Nd at 585 nm. Interestingly, both Nd^{3+} and Yb^{3+} emission are recorded under Nd excitation. This is an interesting result that strongly underlines an energy transfer occurring between Nd^{3+} and Yb^{3+}. Their PL intensity remains relatively weak because of their small absorption cross-section. In the next section we investigate the excitation mechanisms of Nd^{3+} and Yb^{3+}.

4.4.1.5. PLE and energy transfer mechanisms

The PLE spectra of Nd^{3+} and Yb^{3+} in the (Nd, Yb) co-doped films are shown in figure 4.4.7. The PL of the individual rare earth elements was monitored when the excitation wavelength is varied from 250 to 600 nm.

In figure 4.4.7.a is presented the PLE spectra of Yb^{3+} (PL recorded at 972 nm). It turns out that Yb emission can be measured by exciting at different wavelengths: (i) in the UV region, the PL originates from the host matrix and (ii) when exciting at different wavelengths in the visible, mainly at 529, 581, and 588 nm. The last comes from the Nd^{3+} ions. This result is similar to that found for the co-doped

powders. As expected the 3 sccm sample is exhibiting a better signal, indicating the efficiency of the energy transfer.

Figure 4.47.b plots the PLE spectra of Nd^{3+} (PL recorded at 885 nm). The spectra clearly show that the measured PL is a result of an indirect excitation via the host matrix. Nd can be also excited directly but the efficiency of this emission process remains too weak against the energy transfer supplied by the host matrix. The sample elaborated at 3 sccm is again exhibiting the highest PL associated to Nd. Given the structural properties of this sample, we can conclude that the presence of SnO$_2$ phase is important for the photon emission, particularly for Nd. Therefore, a compromise between the type of structure and the type of RE ions has to been found to reach the highest level of luminescence.
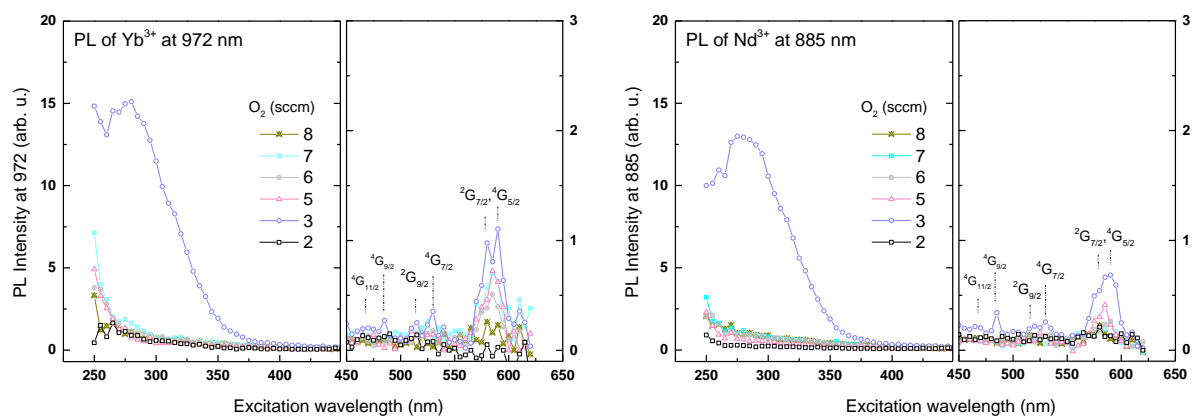

Figure 4.4.7. PLE spectra of the (Nd,Yb) co-doped SnO$_x$ films as a function of the oxygen gas flow during deposition.

4.4.2. Effect of the deposition temperature

In the above section, we have investigated the effect of the oxygen, content during deposition on the structural properties of the films and optical properties of Nd and Yb. In this section we will investigate whether the annealing temperature will enhance the photoluminescence properties. Our choice is focused on the 3 sccm O$_2$ gas flow as it is the only condition that provided significant PL properties.

4.4.2.1. Chemical analysis by XPS

Thanks to the analysis of Yb-doped films, we have shown that the deposition temperature did not affect the structure nor the Yb oxidation but had consequence on the crystalline quality of the films. We have analysed the core levels of Sn, O, Yb and Nd versus the deposition temperature in presence of the two rare elements in the structure.

a) Sn 3d$_{5/2}$ and O 1s core levels

The Sn3d$_{5/2}$ and O 1s of the (Nd, Yb) co-doped samples elaborated at 3 sccm at different temperatures are presented in figure 4.4.8. Similarly to the case of Yb-doped films, the deposition temperature also does not affect the structure of co-doped films as the proportions of SnO2/SnO are not varying that much. Also, the oxygen to tin ratio is same for all samples, (stoechiometry of 1.88).
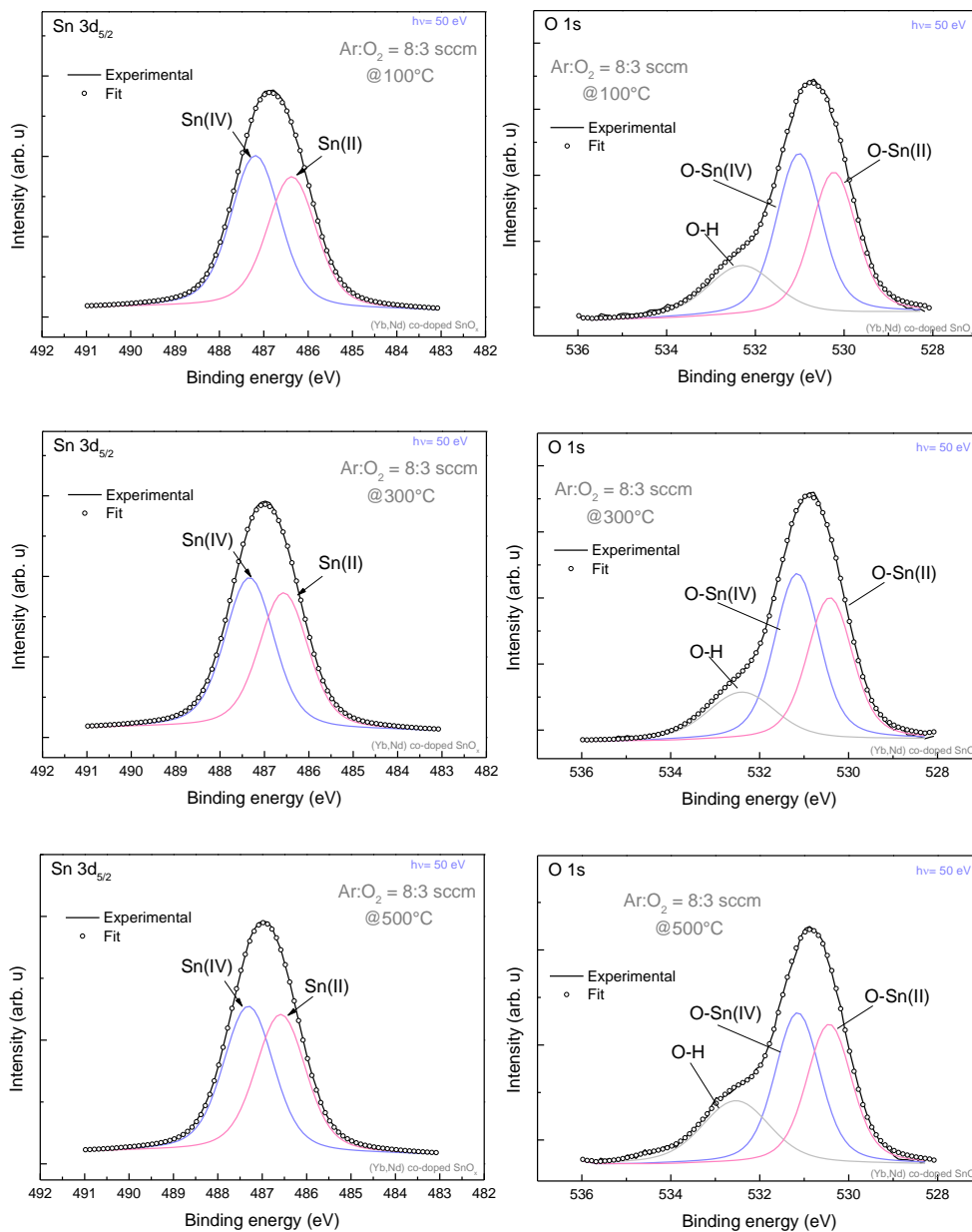

Figure 4.4.8. 3d$_{5/2}$ and 1s core levels of Sn and O elements of the (Nd,Yb) co-doped films (8:3) grown at different T.

b) Yb 4d 5/2 core level

The Yb 4d$_{5/2}$ core level spectra as recorded for the (Nd,Yb) co-doped films are presented in figure 4.4.9. The amount of Yb^{3+} present in the three spectra looks the same; in addition no shift in the peak position is observed; the Yb^{2+} contribution is not detected. The only particularity is the low signal recorded for the sample grown at a substrate temperature of 500°C because of the presence of carbon contamination at the surface which reduces the signal/noise ratio.
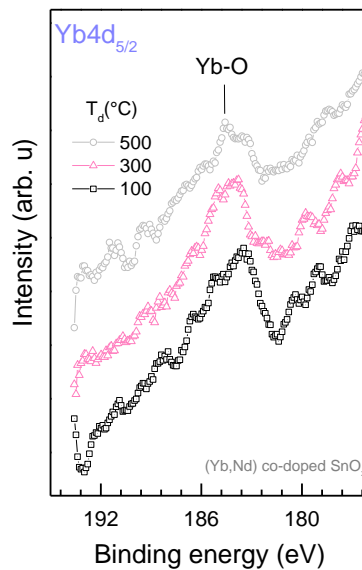

Figure 4.4.9. Yb 4d$_{5/2}$ spectra of Yb in the (Nd, Yb) co-doped SnO$_x$ films as a function of the deposition temperature.

4.4.2.2. Photoluminescence properties

In figure 4.4.10 we compare the Nd^3 and Yb^{3+} emissions at 885 and 972 nm, respectively as recorded under a Nd:YAG laser wavelength excitation operating at 355nm. Interestingly, we could recognize the shape of the curve as that reported in the study of Nd-PL as a function of the Nd concentration. Here Nd^3 and Yb^{3+} are found to behave similarly. The intensity of their PL increases with increasing the deposition temperature up to 400°C. At 500°C it decreases and reaches the same PL intensity as that at 300°C. This results is consistent with XPS results that showed the same structure for the 300 and 500°C grown samples. Now, the increase of the PL up to 400°C can be interpreted in terms of efficiency of the energy transfer from the host matrix and the transition probability in the rare earths structure as explained in the case of the Yb-doped films. Besides, it appears that the PL intensity of Yb is stronger than that of Nd in all samples. However, one has to be careful in interpreting rapidly since this is the intensity of emission at wavelength where maximum of radiative transitions are occurring in each rare earth and does not cover all the emission range.
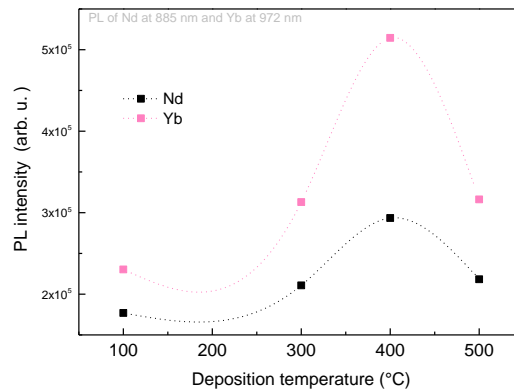
Figure 4.3.10. PL intensity of Yb^{3+} and Nd^{3+} ions in the (Nd, Yb) co-doped films as a function of the deposition temperature.

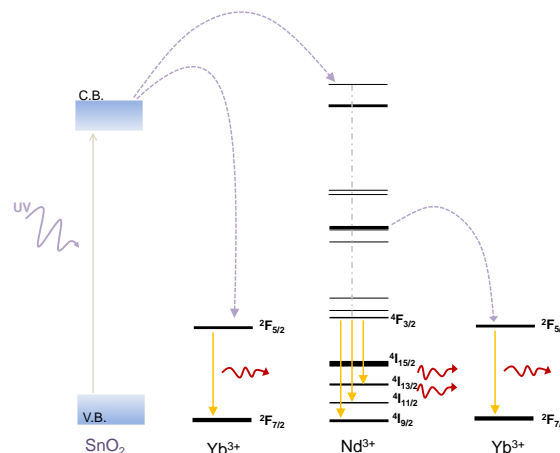A schema of the energy transfer occurring in this system could be imagined as follow

Figure 4.3.11. Energy transfer process in the (Nd, Yb) co-doped films**.** The SnO$_2$ absorbs UV light and thereby sensitizes both Nd^{3+} and Yb^{3+}, Nd^{3+} emits NIR photons but also sensitizes Yb3+ ions with excess of energy

4.4.3. Summary

(Nd,Yb) co-doped thin films have been successfully elaborated by reactive magnetron sputtering. The variation of the oxygen gas flow during deposition has induced many changes in the structure. An increase of the lattice parameter has been noticed. An increase of the SnO phase and a decrease of that of the SnO$_2$ have been reported. In all films different amounts of Yb and Nd with 3+ oxidation states and optically active have been recorded. Small amounts of Nd not inserted into the structure have also been observed as well. The photoluminescence spectra revealed strong emission lines of Yb^{3+} and Nd^{3+} in the infrared region under host excitation. Energy transfer from the host to both Yb^{3+} and Nd^{3+} has been demonstrated. An energy transfer between Yb^{3+} and Nd^{3+} has been also suggested in spite of the small concentrations of the rare earths present in the host. The decrease of the PL of both REs in

for high oxygen flows was attributed to a concentration quenching effect due to an increased content of optically active RE ions. This result have to be confirmed by further XPS analysis

The increase of the deposition temperature resulted in the enhancement of the rare earths' emission in the infrared region with an optimum at 400°C. The decrease of the PL of both REs in all films has been explained by a concentration quenching effect. Such behaviour is explained as due a decrease of the inter-atomic distance between dopants through better crystalline quality.

We finally concluded the potential of co-doping SnO$_x$ thin films with Yb and Nd which exhibit rich emission spectrum including PL of both Res optically active very useful to solar cells and more interesting when comparing to systems with only one RE.

4.5. Elaboration of SnOx films by Sputtering (Experimental)

The Principle of synthesis of oxides thin films by reactive magnetron sputtering is schematically illustrated in figure 4.5.1. In our sputtering system, the substrate is placed in front of the target (top configuration). After attaining high vacuum level in the sputtering chamber, Argon gas is introduced and a voltage between the metallic target and substrate is applied. At the breakdown voltage, neutral Ar atoms are ionized by the electrons (being accelerated by the electric field) flux that flow from the cathode. Subsequently the Ar^+ ions are accelerated toward the target and snatch some metal atoms. It is at this moment that oxygen gas acts to oxidize the metal atoms. The oxygen flux introduced into the deposition chamber can be monitored for desired oxidation degrees. After several collisions of argon ions with the target, they tend to be neutralized by association with electrons from the target. For the metal targets, new electrons are supplied from the underlying cathode. In case of insulating targets it is necessary to use alternate voltage (RF). The term of "magnetron" in the other hand comes from the combination of the radiofrequency and the magnetic field. The latter being around the target can strongly increase the sputtering process and therefore the deposition rate and the quality of the deposited films.
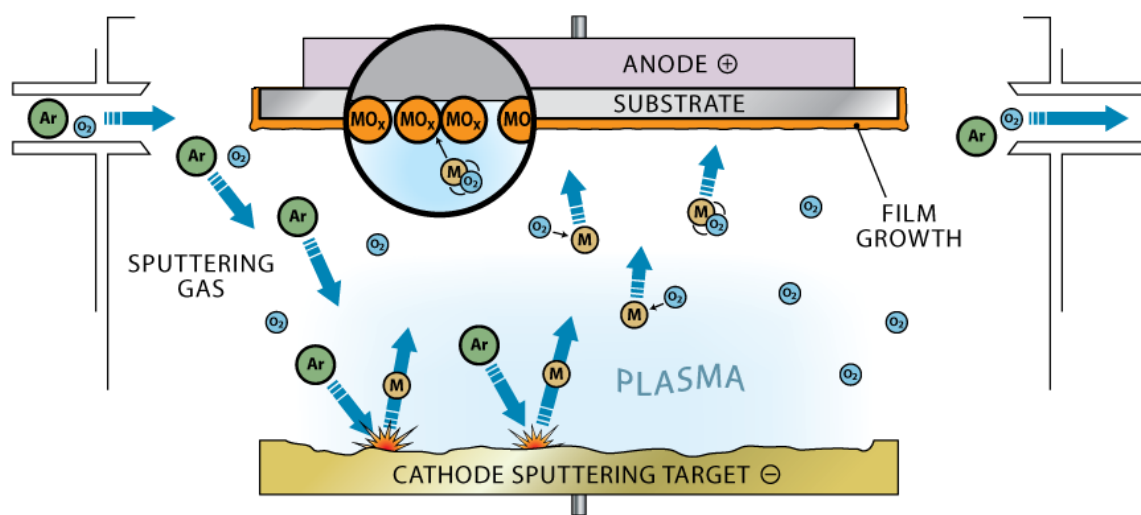

Figure.4.5.1 Operating principle of reactive sputtering[295]

All undoped and REs-doped SnOx films studied in this thesis have been elaborated by means of RF magnetron reactive sputtering using Orion3 sputtering system from AJA international. Up to three targets can be used and allow confocal sputtering. The distance target-to-substrate was about 12 cm for

good uniformity and homogeneity over 2" surface in the substrate holder. All used targets were pure Sn metal targets. The doping with rare earths was performed by placing on the top of the tin target small discs of pure rare earth metal as shown in figure below (4.5.2). With such doping process, contamination is one of the big issues. To avoid this latter, we have used for each RE one distinct tin target. Co-doping was performed by co-sputtering from two targets. The oxygen and argon gas flows were controlled using two massflows while the pressure in the chamber was maintained by means of and electrovalve with feedback control in front of the turbomolecular pump. Standard parameters such as deposition pressure and RF power were fixed to 3.3 mTorr and 50 W, respectively. The other experimental parameters such as oxygen and argon gas flows as well as the substrate temperatures are reported for each study in chapter 4.
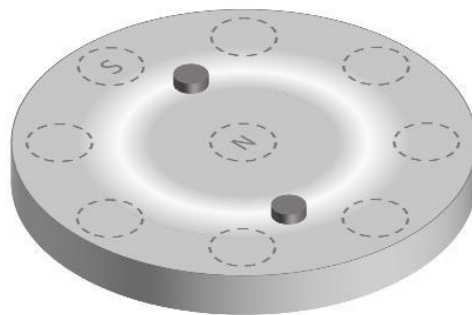

Figure.4.5.2 Placing RE metal discs on the top of targets in our sputtering system. The dashed circles indicate the position of the magnets under the target. The white zone represents where sputtering prevalently occurs because of the magnetic field. [295]

5.6. References

[261] S. Muranaka, Y. Bando, T. Takada, Preparation by reactive deposition and some physical properties of amorphous tin oxide films and crystalline SnO2 films, Thin Solid Films, 86 (1981) 11-19.

[262] H. Yabuta, N. Kaji, R. Hayashi, H. Kumomi, K. Nomura, T. Kamiya, M. Hirano, H. Hosono, Sputtering formation of p-type SnO thin-film transistors on glass toward oxide complimentary circuits, Applied Physics Letters, 97 (2010) -.

[263] M.R. Soares, P.H. Dionísio, I.J.R. Baumvol, W.H. Schreiner, Influence of sputtering parameters on the composition and crystallinity of tin oxide, Thin Solid Films, 214 (1992) 6-16.

[264] C.L.L.a.G.K. Wertheim, Oxidation of tin: an ESCA study, Vac. Sci. Technol., 15 (1979) 622-624.

[265] J.-M. Themlin, M. Chtaïb, L. Henrard, P. Lambin, J. Darville, J.-M. Gilles, Characterization of tin oxides by x-ray-photoemission spectroscopy, Physical Review B, 46 (1992) 2460-2466.

[266] M. Alexander, H. Romberg, N. Nücker, P. Adelmann, J. Fink, J.T. Markert, M.B. Maple, S. Uchida, H. Takagi, Y. Tokura, A.C.W.P. James, D.W. Murphy, Electronic structure studies on the n-type doped superconductors R2−xMxCuO4−δ (R=Pr,Nd,Sm; M=Ce,Th) and Nd2CuO4−xFx by electron-energy-loss spectroscopy Physical Review B, 43 (1991) 333-343.

[267] K. Bouras, J.L. Rehspringer, G. Schmerber, H. Rinnert, S. Colis, G. Ferblantier, M. Balestrieri, D. Ihiawakrim, A. Dinia, A. Slaoui, Optical and structural properties of Nd doped SnO2 powder fabricated by the sol-gel method, Journal of Materials Chemistry C, 2 (2014) 8235-8243.

[268] Y.P. Du, Y.W. Zhang, L.D. Sun, C.H. Yan, Efficient energy transfer in monodisperse Eu-doped ZnO nanocrystals synthesized from metal acetylacetonates in high-boiling solvents, Journal of Physical Chemistry C, 112 (2008) 12234-12241.

[269] C. Fu, J. Liao, W. Luo, R. Li, X. Chen, Emission of 1.53 μm originating from the lattice site of Er3+ ions incorporated in TiO2 nanocrystals, Optics Letters, 33 (2008) 953-955.

[270] A. Kar, A. Patra, Optical and electrical properties of Eu3+-Doped SnO2 nanocrystals, Journal of Physical Chemistry C, 113 (2009) 4375-4380.

[271] J. Vela, B.S. Prall, P. Rastogi, D.J. Werder, J.L. Casson, D.J. Williams, V.I. Klimov, J.A. Hollingsworth, Sensitization and protection of lanthanide ion emission in In 2O 3:Eu nanocrystal quantum dots, Journal of Physical Chemistry C, 112 (2008) 20246-20250.

[272] P.M.A. Sherwood, Valence-band spectra of tin oxides interpreted by X alpha calculations, Physical Review B, 41 (1990) 10151-10154.

[273] Y. Li, S. Zhang, T. Sritharan, Y. Liu, T.P. Chen, Influence of oxygen partial pressure on magnetron sputtered Sr0.8Nd0.3Bi2.5Ta2O9+x ferroelectric thin films, Journal of Alloys and Compounds, 457 (2008) 549-554.

[274] C. Suzuki, J. Kawai, M. Takahashi, A.-M. Vlaicu, H. Adachi, T. Mukoyama, The electronic structure of rare-earth oxides in the creation of the core hole, Chemical Physics, 253 (2000) 27-40.

[275] R.G. Egdell, J. Rebane, T.J. Walker, D.S.L. Law, Competition between initial- and final-state effects in valence- and core-level x-ray photoemission of Sb-doped SnO2, Physical Review B, 59 (1999) 1792-1799.

[276] L. Kövér, Z. Kovács, R. Sanjinés, G. Moretti, I. Cserny, G. Margaritondo, J. Pálinkás, H. Adachi, Electronic structure of tin oxides: High‐resolution study of XPS and Auger spectra, Surface and interface analysis, 23 (1995) 461-466.

[277] P.M.A. Sherwood, Valence-band spectra of tin oxides interpreted by Xalpha calculations, Physical Review B, 41 (1990) 10151-10154.

[278] F.A. Akgul, C. Gumus, A.O. Er, A.H. Farha, G. Akgul, Y. Ufuktepe, Z. Liu, Structural and electronic properties of SnO2, Journal of Alloys and Compounds, 579 (2013) 50-56.

[279] R. Iwanowski, J. Sobczak, Z. Kalinski, X-ray photoelectron study of Yb-doped InP, Acta Physica Polonica-Series A General Physics, 91 (1997) 809-814.

[280] Q. Yin, X. Jin, G. Yang, C. Jiang, Z. Song, G. Sun, Biocompatible folate-modified Gd3+/Yb3+-doped ZnO nanoparticles for dualmodal MRI/CT imaging, RSC Advances, 4 (2014) 53561-53569.

[281] L.W. Yang, Y. Li, Y.C. Li, J.J. Li, J.H. Hao, J.X. Zhong, P.K. Chu, Quasi-seeded growth, phase transformation, and size tuning of multifunctional hexagonal NaLnF4 (Ln = Y, Gd, Yb) nanocrystalsvia in situ cation-exchange reaction, Journal of Materials Chemistry, 22 (2012) 2254-2262.

[282] S. Schmidt, S. Hüfner, F. Reinert, W. Assmus, X-ray photoemission of Yb:Cu4, Physical Review B, 71 (2005) 195110.

[283] E. Flage-Larsen, S. Diplas, Ø. Prytz, E.S. Toberer, A.F. May, Valence band study of thermoelectric Zintl-phase SrZn 2 Sb 2 and YbZn 2 Sb 2: X-ray photoelectron spectroscopy and density functional theory, Physical Review B, 81 (2010) 205204.

[284] B. Darwent, Bond dissociation energies in simple molecules, NSRDS-NBS NO. 31, U. S. DEPT. COMMERCE, WASHINGTON, D. C. JAN. 1970, 48 P, (1970).

[285] V. Vedeneyev, L.V. Gurvich, V. Kondrat'Yev, S. Technica, Bond energies, ionization potentials and electron affinities, Edward Arnold London, 1966.

[286] C. Tropis, Analyse et Optimisation des performances d'un capteur de gaz à base de SnO2 nanoparticulaire: Application à la détection de CO et CO2, in, Université Paul Sabatier-Toulouse III, 2009.

[287] M.K. Sławomir, T. Taiju, I. Masahiko, B. Georges, L. Grzegorz, Optical study of Yb 3+ /Yb 2+ conversion in CaF 2 crystals, Journal of Physics: Condensed Matter, 17 (2005) 3771.

[288] L. Lihong, X. Rong-Jun, H. Naoto, T. Takashi, Z. Chen-ning, L. Jiguang, S. Xudong, Photoluminescence properties of β-SiAlON:Yb 2+ , a novel green-emitting phosphor for white light-emitting diodes, Science and Technology of Advanced Materials, 12 (2011) 034404.

[289] H. Okamoto, K. Kasuga, Y. Kubota, N. Nishimura, H. Kawamoto, K. Miyauchi, Y. Shimotsuma, K. Miura, White emission of Yb 2+: fluoride glasses efficiently excited with near-UV light, Optics express, 21 (2013) 22043-22052.

[290] Z. Zhang, M. Otmar, A.C. Delsing, M.J. Stevens, J. Zhao, P.H. Notten, P. Dorenbos, H.T. Hintzen, Photoluminescence properties of Yb 2+ in CaAlSiN 3 as a novel red-emitting phosphor for white LEDs, Journal of Materials Chemistry, 22 (2012) 23871-23876.

[291] S. Wang, F. Lou, C. Yu, Q. Zhou, M. Wang, S. Feng, D. Chen, L. Hu, W. Chen, M. Guzik, G. Boulon, Influence of Al3+ and P5+ ion contents on the valence state of Yb3+ ions and the dispersion effect of Al3+ and P5+ ions on Yb3+ ions in silica glass, Journal of Materials Chemistry C, 2 (2014) 4406-4414.

[292] Z. Zhang, O.M. ten Kate, A.C.A. Delsing, M.J.H. Stevens, J. Zhao, P.H.L. Notten, P. Dorenbos, H.T. Hintzen, Photoluminescence properties of Yb2+ in CaAlSiN3 as a novel red-emitting phosphor for white LEDs, Journal of Materials Chemistry, 22 (2012) 23871-23876.

[293] Y. Teng, J. Zhou, X. Liu, S. Ye, J. Qiu, Efficient broadband near-infrared quantum cutting for solar cells, Optics Express, 18 (2010) 9671-9676.

[294] S. Kuck, M. Henke, K. Rademaker, Crystal Growth and Spectroscopic Investigation of Yb2+ Doped Fluoride Crystals, LASER PHYSICS-LAWRENCE-, 11 (2001) 116-119.

[295] M. Balestrieri, Transparent conductive oxides with photon converting properties in view of photovoltaic applications: the cases of rare earth-doped zinc oxide and cerium oxide, in, Université de Strasbourg, 2014.

Chapter 5 : Application to solar cells

5.1. Principal loss in single junction solar cells

In 1961, Shockley and Queisser [296] have demonstrated that the efficiency limit for a single-junction with an optimal band gap around 1.3 eV is around 31% for 1-sun spectrum. This was done using the principle of detailed balance between incident and escaping photons and extracted electrons, assuming voltage drops across the contacts and junction. This limit originates comes mainly from the spectral mismatch between the incident photons of solar spectrum and the band gap (absorption) of the semiconductor on which is based the solar cell. Two main mechanisms are responsible of about 80% of the losses: 1) the thermalization loss where the excess of energy provided up-on excitation by high energy UV incident photons is transformed into kinetic energy and then converted into heat This process is denoted (1) in the illustration of figure 5.1.1; (2) The sub-band gap transmission loss where photons with energy lower than the band gap of the semiconductor cannot be absorbed. This process is denoted as process 2 in figure 5.1.1. In addition to those losses, they are other limitations for high efficiency in single junction solar cell. Thus, process 3 illustrates loss mechanisms through excitons recombination. Processes 4 and 5 describe the voltage drops across the p-n junction or across contacts.

Concerning the evolution with the optimum of the conversion efficiency versus the band gap energy, this is because the maximum photovoltage is proportional to the bandgap of the semiconductor, V_{CO}^{max} = Eg / q (in fact, only 2/3 of this value can be reached at the best), while its generated photocurrent decreases because all the photons of energy below the bandgap are not collected. Such opposite behaviors result in the presence of an optimum in efficiency. For crystalline silicon-based solar cells (band gap of 1.12 eV) it is about 30%.
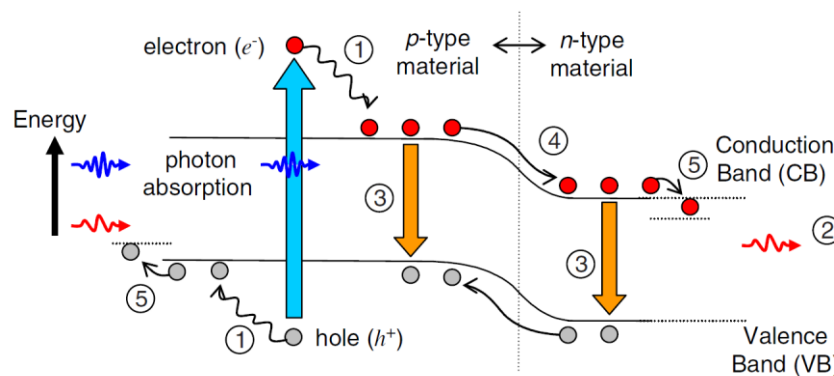

Figure 5.1.1. Principal loss mechanisms in a single junction solar cell: 1 lattice thermalization, 2 transparency, 3 recombination, 4 junction loss and 5 contact voltage loss [4].

Besides the fundamental losses, there are numerous technological limiting factors to reach the optimal efficiencies: Recombination at the back and front surface of the cell, ligh reflection which reduces the amount of absorbed photons, and contacts resistances. As for the reflectance issue, it is handled for silicon cells through a combination of surface texturing and an anti-reflecting coating film such as SiN layers, and for chalcogenide based cells by using a transparent conducting oxide such as ZnO. To date, the best one-Sun efficiencies obtained for Si and CIGS solar cells at the laboratory-scale are about 25.6% and 21.7% respectively.

Nowadays, more emphasis is focused on new concepts to reduce the main losses and/or to increase the solar cell efficiency beyond the theoretical limit. Most of them are dealing with the main problem of the spectral mismatch between the incident solar spectrum and the cell absorption, which is about 48 % of optical losses. One route to avoid these losses is adapting the absorption of the solar cell to the incident spectrum via Tandem solar cells. They consist in a series-connect stack of two to five junctions of semiconducting materials that absorb at different wavelengths. Green et al [297, 298] have estimated the theoretical limit efficiency of tandem cells with infinite number of band gaps to be about 68% for one-Sun spectrum. Interesting but have a big disadvantage, this technology is quite complex and expensive. The second route is adapting the incoming spectrum to the solar cell absorption via photons conversion, which is the subject of this thesis work. This topic is promising and well-investigated in physics and chemistry. Down Conversion (DC), Down Shifting (DS) and Up Conversion (UC) are the different mechanisms used for photons conversion. These processes are schematically described in figure 5.1.2.
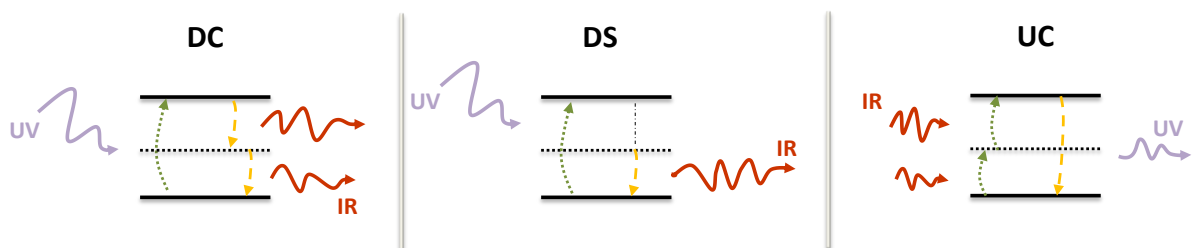
Figure 5.1.2. The three principal photons conversion mechanisms: Down conversion, Down-Shifting and Up conversion.

The DC process, also known as quantum-cutting (QC) or quantum splitting (QS), consists of converting one high energy photon (mainly UV photons) into at least two lower energy photons. The ideal quantum yield (QY) of this process is 2. On the opposite side, combination of two low energy photons (IR) can generate one single high energy photon (it could be visible or NIR) through UC, which is particularly useful to recover transparency losses. Maximum QY of this process is 0.5. The DS in the other hand consists in red-shifting of the incoming high energy photons.

In other words it decreases the high energy of the absorbed photons by re-emitting lower-energy photon. This process is conceptually the simplest photon conversion mechanism and usually occurs in semiconductor materials. Dissipation losses in large band-gap semiconductors are already an example of down shifting. Because of the discrete levels created by structural defects, the de-excitation is often done by a relaxation (thermalization losses) followed by a low-energy photon emission. The QY of this process is less than or equal to 1.

It is important to mention that, even if DS can improve the efficiency of the solar cell by converting one higher energy photon into one lower energy, the cell will be more efficient in the UV part but it will never overcome the Shockley-Queisser limit. However, DC and UC are able to provide efficiencies beyond this limit.

In contrast to the other new concepts developed in third generation solar cells that deals with improving the absorber and cell structure; the spectral modification by photon conversion is a fundamentally optical process and do not depend on the physics of solar cells. In fact, these conversion layers can be directly applied on the top or the back of the solar cell. Typical coupling of photon conversion layers to the solar cell are schematically described in figure 5.1.3
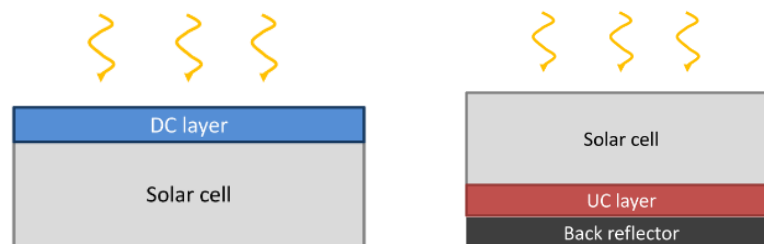

Figure 5.1.3. Association of the photon conversion layers (DC and UC) to the solar cell.

DC or DS layers are placed in front of the solar cell in order to convert the high-energy photons to low-energy photons to be absorbed by the solar cell. The UC in the other hand are placed on the rear side of the cell because of its transparency to low energy photons. DS layers actually reduce energy losses originated from surface recombination, Auger effect and Shockley-Read-Hall recombination, which increase the spectral response of the cell at higher energies range. Associating DC and UC layers to the solar cell will generates more electron-hole pairs, resulting in the increase of the short-circuit current and efficiency of the solar cell [176].

Assuming that most of generated photons by the conversion layers are efficiently absorbed by the solar cell, the maximum energy fractions recovered by DC and UC are presented in figure 5.1.4 in case of a conventional silicon solar cell. Theoretical efficiency limit determined using detailed balance calculations predict maximum conversion limit around ~ 40% [299-302]. Richards et al. have

published several studies on lanthanides doped materials with UC and DC properties applied to solar cells [178, 179]. Since then, pioneering works have been done and continuously intensified [303-306]
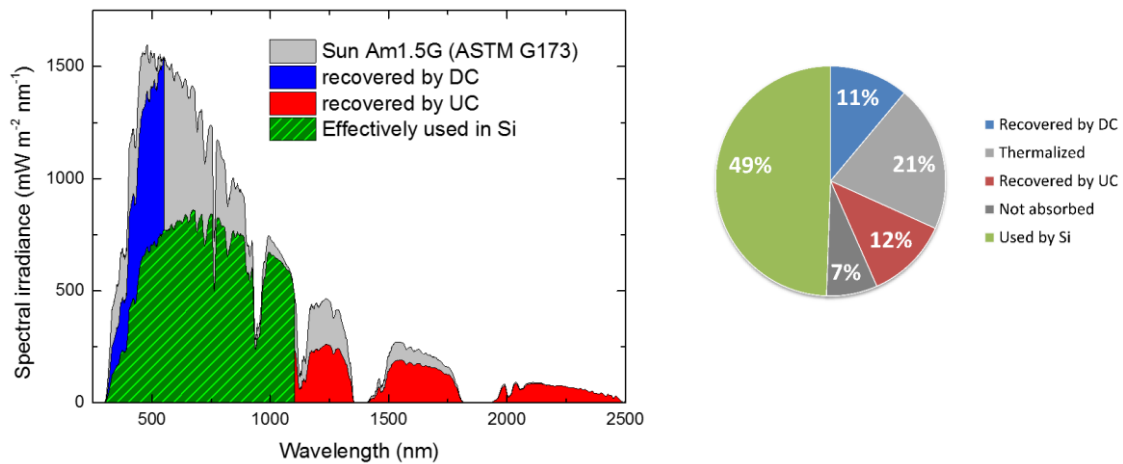

Figure 5.1.2. The fraction of solar spectrum absorbed by typical silicon-based solar cell (green), part of the spectrum recovered by DC (blue) and UC (red)[295].

The mechanisms studied in this thesis are identified as DC or DS. In the following a brief description of this process will be reported.

5.2. Down conversion mechanisms

As mentioned before, down conversion process consist in converting one high energy photon to two low-energy photon better adapted to the solar cell absorption. An interesting report on down conversion can be found in ref [179]. In fact, DC process can be distinguished via three mechanisms: (i) quantum cutting (QC) via host lattice states, (ii) using single ions, (iii) down conversion using ion pairs. The QC term usually describe the generation of multiple photons with a single activator system. DC in the other hand involves energy transfer between a sensitizer and an activator.

a) Quantum-Cutting using host lattice states

This process is illustrated in figure 5.2.1. The QC mechanism is performed by involving host lattice states as shown below. It results in the generation of two electron-hole (e-h) pairs with an energy E_g (for each) from incident photons using an excitation energy where $E_{exc} > 2E_g$. This process is known as interband Auger effect, in which upon excitation an electron is excited from the VB to energy states far in the CB. The excess of energy is enough to excite another electron over the band gap so as one exciting photon produces two e-h pairs. The recombination of the e-h pairs on the luminescent centre

(deep levels within the band gap) results in an emission of two photons. By this way, two photons are yielded from absorption of a single photon. This process concerns solid hosts with luminescent centres such oxide semiconductors with structural defects.
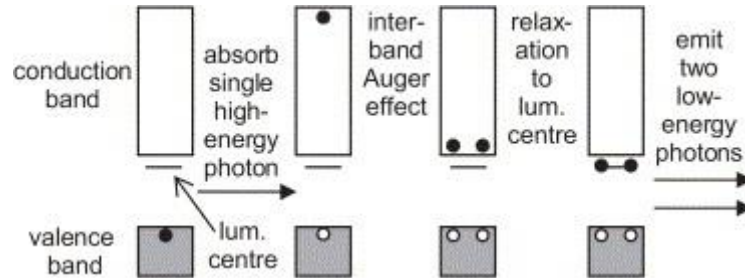

Figure 5.2.1. Inter-band Auger mechanism for generation of two-low energy photons from each incident high-energy photon[179].

b) Quantum-Cutting using single rare earth ion

This process is schematically presented in figure 5.2.2 through the example of praseodymium ions in a YF_3 host lattice. Up-on absorption of one high-energy photon, the well separated energy levels of the rare earth ion can be used to generate more than one visible or NIR photon. In the mid-1970s, two have reported an example of this process using praseodymium ions in YF_3 host lattice. The research groups in [307, 308] reported that the initial absorption is supplied by the matrix at 185 nm, then the energy is then transferred to Pr^{3+} to its underlying $^1S_0$ state through 4f-5d transition. Subsequently, a blue photon is emitted at 408 nm ($^1S_0 \rightarrow {}^1I_6$ transition). Another red photon is also emitted at 620 nm ($^3P_0 \rightarrow {}^3H_6$ transition). They reported an external quantum efficiency of 140 ±15%.
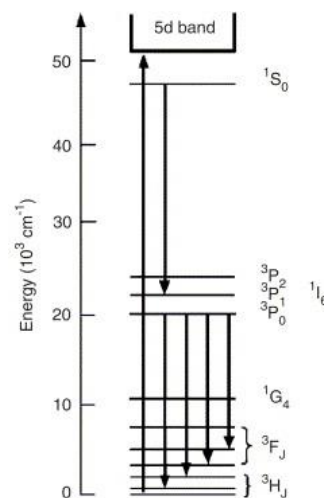
Figure 5.2.2. QC in YF$_3$:Pr^{3+}. Up-on absorption of UV photon at 185 nm by the YF$_3$ host, Pr^{3+} generates two photons at 408 nm ($^1S_0 \rightarrow {}^1I_6$ transition) and 620 nm ($^3P_0 \rightarrow {}^3H_6$ transition) through its energy levels states[179].

c) Down conversion using rare-earth ion pairs

This process occurs in ion pairs systems, in which the RE ions are physically interacting by energy transfer. In this system, IR and UV losses encountered using single ion can be avoided by choosing appropriate pairs. The possibility of generating two-photon emission through energy transfer was predicted in the 1950s by Dexter [309]. Basic DC mechanisms are depicted in figure 5.2.3.
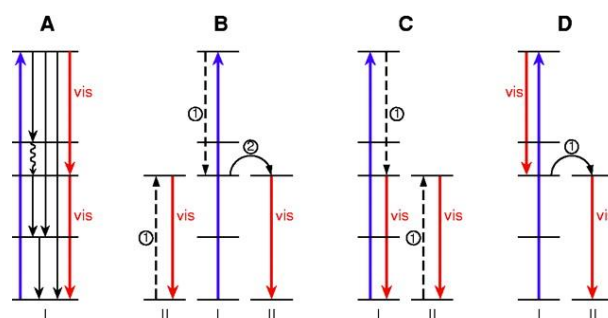
Figure 5.2.3. Hypothetical quantum cutting mechanisms for two RE ions system: (A) two photons emission from one single ion. Down conversion with ion pair by (B) cross relaxation ① and   energy transfer ②from ion I to ion II. (C) and (D) describe the cross relaxation followed by emission[179, 310, 311].

The DC process in case (B) occurs in two steps: ① by cross relaxation from ion I to ion II, followed by energy transfer from ion I to ion II. The emission then is performed by ion B. in cases (c) and (d) the photon emission is ensured by the two ions.

Some examples on RE ions pairs for potential down conversion are presented in figures 5.2.4 and 5.2.5
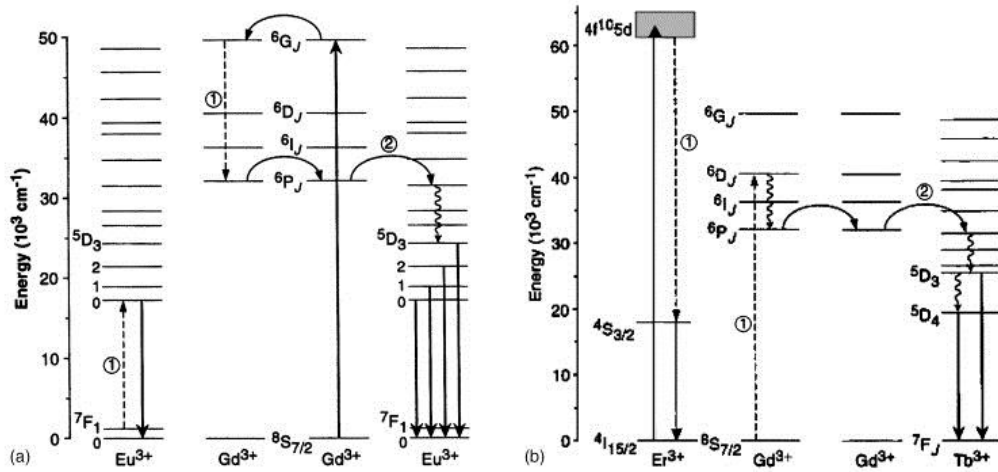
Figure 5.2.5 Energy level diagrams of two down-conversion mechanisms with a potential quantum efficiency of greater than unity. The two-step energy transfer from Gd^{3+} to Eu^{3+} in the $LiGdF_4:Eu^{3+}$ phosphor system are shown in (a) and the steps are indicated by ⊖ (cross-relaxation) and ⊖ (transfer of remaining energy on Gd^{3+} to Eu^{3+}). Down-conversion is also possible by (b) energy transfer upon excitation in the $4f^{10}$–5d state of the $Er3^+$ ion of $LiGdF_4:Er^{3+},Tb^{3+}$ (adapted from Wegh et al.[310]) and **reprinted** from ref [179]
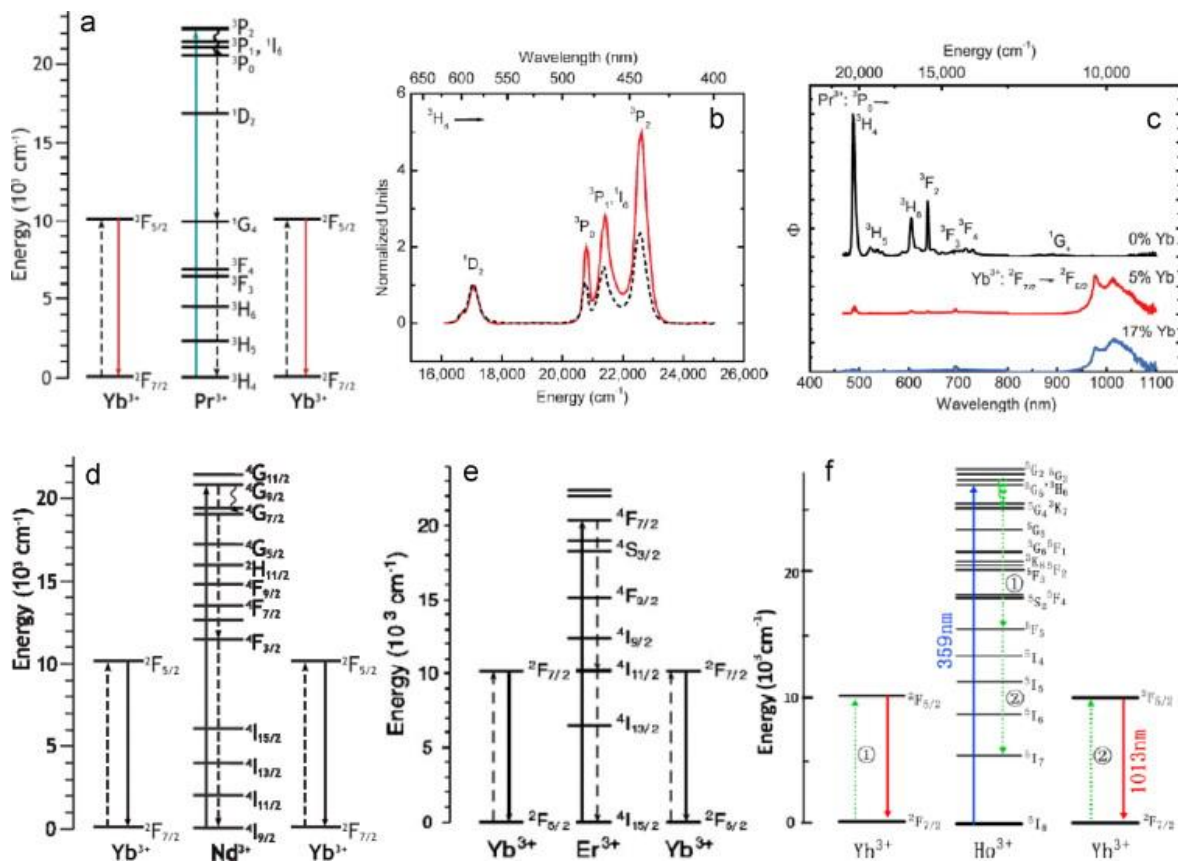
Figure 5.2.4 DC mechanism for (a) Pr^{3+}–Yb^{3+}, (d) Nd^{3+}–Yb^{3+}, (e) Er^{3+}–Yb^{3+} and (f) Ho^{3+}–Yb^{3+} couples. A A two-step energy transfer occurs upon excitation into ^3P_J (J=0, 1, 2) and $^1I_6$ states of Pr^{3+}, $^4G_{9/2}$ state of Nd^{3+}, $^4F_{7/2}$ state of Er^{3+} and $^5G_5$, $^3H_6$ states of Ho^{3+}. A single UV–vis photon absorbed by these ions is thereby converted into two ~1000 nm photons of Yb^{3+}. Solid, dotted and curved arrows represent optical transitions, non-radiative energy transfers and non-radiative relaxation, respectively. (b) Diffuse reflectance (dashed black curve) and excitation spectra (solid red line) of the Pr^{3+}/Yb^{3+}: SrF_2 sample, demonstrating the occurrence of DC luminescence. Each spectrum is normalized to the $^1D_2$ peak. The excitation spectrum, obtained by monitoring Yb^{3+} emission at 980 nm, is corrected for wavelength-dependent instrument response. (c) Room temperature emission spectra of Pr^{3+} (0.1 mol%)/Yb^{3+} (x mol%): SrF_2 (x=0, 5, 17), recorded under the identical conditions and were corrected for the wavelength dependent response of the detector system. **reprinted** from ref [176].

5.3 Quantum Yield measurements

The quantum yield (QY) as reported in chapter 2 corresponds to the ratio between the number of emitted photons and absorbed ones. The number of absorbed photons is calculated by means of integrating sphere. The QY experiments were carried out at IJL-Nancy under the supervision of Pr H. Rinnert. The results are very preliminary given the difficulty in the measurements but we decided to present them in this sub-section.

The experimental procedure was the following: We first measured the diffusion of the excitation peak on the sample, and then on the blank. The difference between the two signals corresponds to photons being absorbed by the films. The number of photons emitted from the sample can be extracted directly from the emission spectra by subtracting the blank fluorescence in the sphere.

To summarize, we record four spectra

LA: Diffusion of blank in the sphere

EA: Fluorescence of blank in the sphere

LC: Diffusion of the sample in the sphere

EC: Fluorescence of the sample in the sphere

The Quantum Yield is therefore calculated using the equation (1):

QY= (Ec-Ea)/ (La-Lc)   (1)

The issue in measuring an accurate QY for our system is that the emission of the RE is too low as compared to the diffusion of the Blanc. In order to avoid the saturation, the excitation energy was divided by 10 using a filter.

The QY measurements were carried out on Nd-doped SnOx (0,6% Nd), Yb-doped SnOx (1,3% Yb) and (Yb,Nd)-doped SnOx (2.7 at.% Nd + 1.54 at.% Yb) films.

a) QY of Nd-doped SnO$_x$ thin films

The absorption of the SnO$_x$ host matrix was measured from 290 to 315 nm, and it is shown in figure 5.3.1. The red curve corresponds to the diffusion from the Blanc while the black curve corresponds to the diffusion from the substrate. The difference between them indicate the part of photons absorbed by the film (the matrix in this wavelengths range); in the right side we collect the fluorescence spectra. The color cod means the same. When calculating the QY, we have found (Ec-Ea)/ (La-Lc) = 0.125. By introducing the first corrections due the setup, we have found QY=0.125/6000 = 0,0000209.

This first test on the Nd-doped SnOx exhibit extremely low QY values which can be partially due to the low efficiency of this system but a part of the result is likely due to a non optimal calibration of the set-up system at the time of measurements.
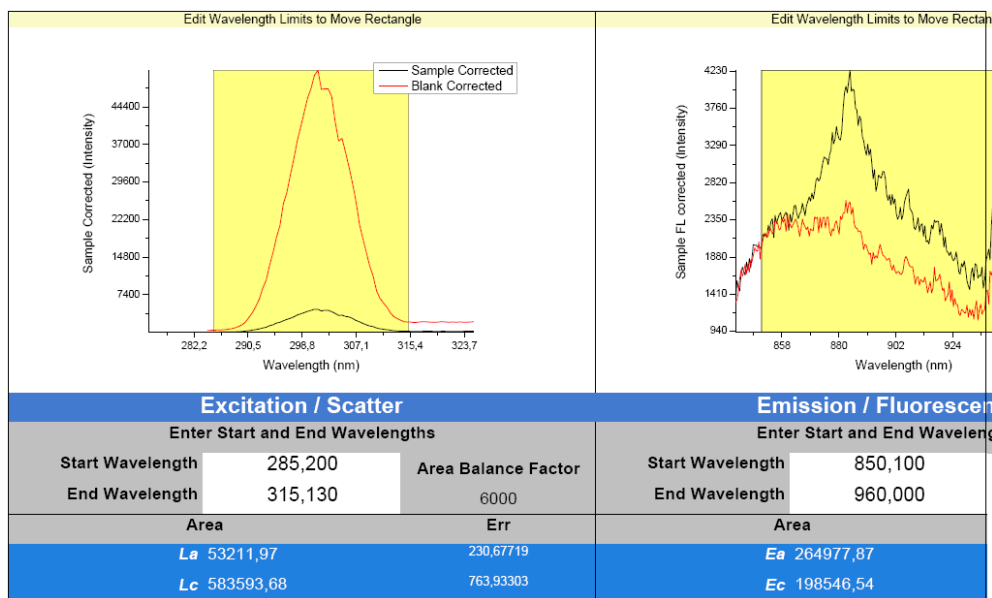

Figure 5.3.1. QY measurement for selected Nd-doped SnO$_x$ thin film

b) QY of Yb-doped SnO$_x$ thin films

We have carried out the measurements of QY on a Yb-doped SnO$_x$ film deposited at …and having 1.3% Yb in the matrix. The data are shown in figure 5.3.2
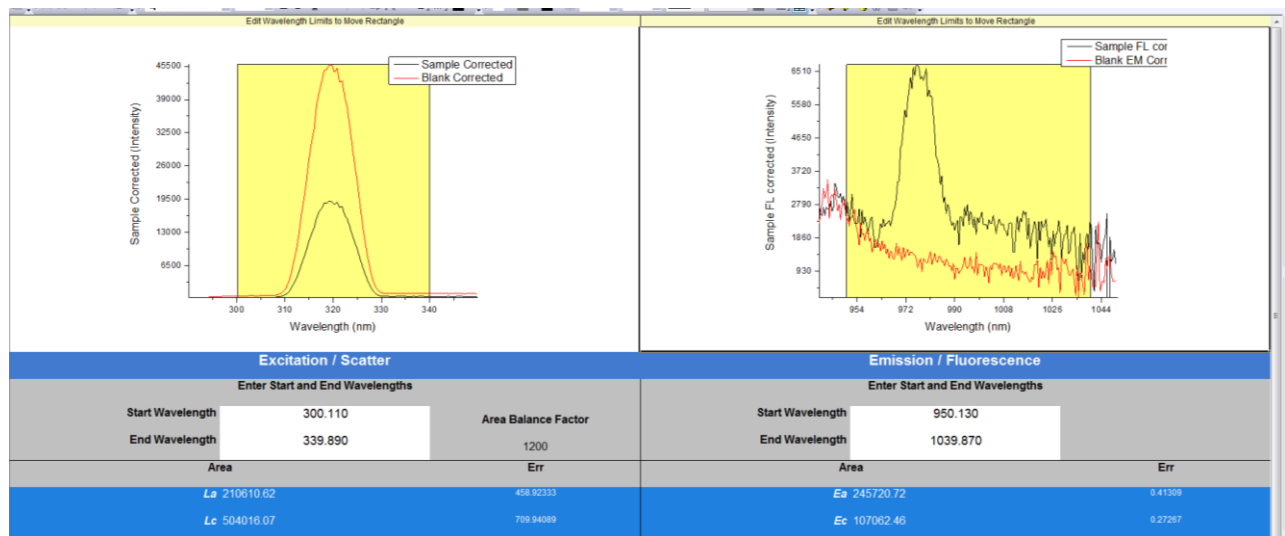
Figure 5.3.2. QY measurement for selected Yb-doped SnO$_x$ thin film

A quantum yield of about 0.04% is obtained with the Yb-doped samples, meaning that 0.0004 IR photons are emitted by Yb from one UV absorbed photons by the matrix in the investigated ranges. We do think that this result is primary and higher values can be reached. In this measurement we have selected a UV wavelength range from 310 to 330nm. We have to notice that the intensity of the spectral radiation within this range is extremely small. For more accurate estimation of the effective QY, we do think that the absorption should be monitored from 300 to 400 nm in order to calculate the real efficiency of the system and energy transfer. This wavelength range corresponds to where the gain in EQE/IQE measurements of solar cells is expected.

c) QY of (Nd, Yb) co-doped SnO$_X$ powders

The QY results on (Yb,Nd)-doped SnOx films are shown in figure 5.3.3, for the case 2.7 at.% Nd + 1.54 at.% Yb. In chapters 3 and 4 we have demonstrated an energy transfer between the host matrix and the rare earth element as well as an energy transfer between Nd and Yb. However, we were unable to quantify the energy transfer from the host to the RE for a setu-up reason; in contrast the QY of the energy transfer occurring between Nd and Yb is measured to be about 1.90% upon excitation in the range 572-594nm. This (Yb,Nd)-doped SnOx system has shown rich emission spectra in the infrared. It will therefore be interesting to complete the studies by measuring QYs for different samples with

different rare earths concentrations. This will require adapting the absorption and emission ranges for the measurements. We believe that much higher QY values can be obtained.
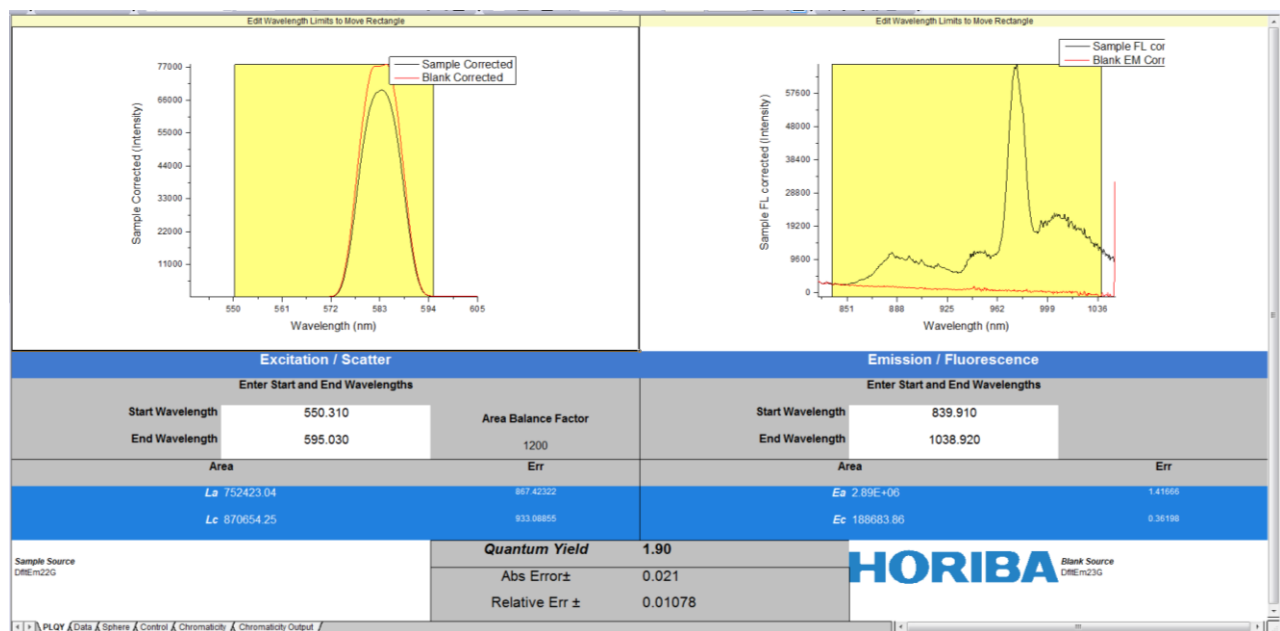
Figure 5.3.3. QY measurement for selected (Nd,Yb) co-doped SnO_x powders, the efficiency of the energy transfer measured here is between Nd^{3+} and Yb^{3+} ions.

5.4. Electrical properties of the RE-doped SnO_x thin films

This section deals with the electrical properties of the synthesized SnO_x thin films during this work, namely undoped, Nd, Yb and (Nd,Yb) co-doped samples. SnO_2 is an n-type semiconductor and its conductivity is mainly arising from structural defects such as oxygen vacancies. SnO is rather a p-type material. We have shown that is possible to produce materials from SnO2 to Sno thanks to the deposition parameters such as oxygen flow. We will demonstrate below a correlation between luminescence properties and electrical properties. Finally, we will show that the high optical transparency of the RE:SnO_x thin films associated with their good electrical properties are making them potentially applicable as Functionalized Transparent Conducting Oxides for silicon and CIGS solar cells

5.4.1 Undoped SnO_x

Hall measurements were carried out on undoped SnOx films produced by sputtering under different flow of oxygen while maintaining the Ar flow at 12 sscm. The measured carrier concentration, resistivity and mobility of the deposited films are presented in table 5.4.1. The oxygen poorest film

deposited with O_2 gas flow of 3 sccm exhibits a p type character, with a high density of carrier concentration of about $3.85x \ 10^{20}$. This is consistent with the structural and optical results which have shown a SnO structure for the film A. Because of its amorphous character, this film is found to be very resistive as its resistivity value and carriers mobility are about 0.315 Ω.cm and 0.06 cm^2/V.s, respectively.

Increasing the oxygen flow during deposition to 4 sccm leads to the formation of an n-type SnO_2 material with a carrier concentration of $-7.58.10^{+19}$. The presence of little more oxygen atoms in the structure switches the conductivity from p to n and enhances both the resistivity and the mobility since values of 0.0059 Ω.cm and 14 cm^2/V.s, respectively are measured. When increasing further the oxygen flow, the films kept their n-type character but their electrical properties of the film degrade in general. Thus, for sample C (O_2=5 sccm), the resistivity increases and the mobility decreases, which can be explained by the presence of some defects such as oxygen atoms in interstitial sites. As for the film deposited with O_2=6 sccm, the resistivity slightly enhances, the mobility drops to very low values but surprisingly the carriers concentration stays very high and approaches that of sample A (O_2=3 sccm). It can be recall that both samples A and D have as a common point the structure which is amorphous as witnessed by the wide diffraction band in their diffraction patterns. It is proposed that the additional free carriers present in these layers are originating from the disorder in the crystalline structure (point defects).The disorder in the structure is also responsible of the low mobility values recorded for these samples. A similar conclusion was reported by Davesnee [312] for the case of Eu doped ZnO films. Increasing further the oxygen flow to 7 sccm results in lower resistivity and enhanced mobility as the film possess a crystalline structure.

Table.5.4.1. Carrier concentration, resistivity and carrier mobility of undoped SnO_x films as a function of the O_2 gas flow (sccm). The deposition was carried out at 50°C. The Ar flow was to set to 12 sccm.

Sample label	O_2 (sccm)	Carrier concentration (cm^{-3})	Resistivity (Ω.cm)	Mobility (cm^2/V.s)
A	3	$4.74 \ 10^{+20}$	0.32	0.04
B	4	$-7.58 \ 10^{+19}$	0.005	14.0
C	5	$-4.10 \ 10^{+19}$	0.066	2.3
D	6	$-4.24 \ 10^{+20}$	0.054	0.27
E	7	$-4.47 \ 10^{+19}$	0.026	4.28

Overall, the electrical properties of the undoped films seem to be strongly correlated to the structural characteristics and elemental composition of the films: SnO versus SnO_2, amorphous versus

crystalline. Besides, the measured electrical parameters of some of these undoped SnO_x films are encouraging for applications as TCOs.

Table 5.4.2 displays the electrical properties of SnO_x thin films elaborated at different deposition temperatures but under a fixed flow of Ar and O_2 : 8 and 2 sccm, respectively. We have shown previously that the growth temperature strongly affect the electrical properties of the films. The carrier's concentration is found to gradually increase as a function of the deposition temperature and the resistivity is clearly improved particularly at 400 and 500°C. The carriers mobilities recorded here remain quite low but reasonable for such carrier concentration values. This study serves as reference for further comparison with doped SnO_x films.

Table.5.4.2. Carrier concentration, resistivity and carrier mobility of undoped SnO_x films as a function of the deposition temperature (T_d). The Ar and oxygen gas flows were fixed at 8 and 4 sccm, respectively.

T_d (°C)	Carrier Concentration (cm^{-3})	Resistivity (Ω.cm)	Mobility (cm^2/V.s)
15	- 1.918 10^{+20}	0.017	1.81
100	- 3.125 10^{+18}	2.683	0.74
200	- 1.354 10^{+19}	0.050	9.16
300	- 3.365 10^{+19}	0.045	4.11
400	- 3.812 10^{+20}	0.021	5.76
500	- 2.04 10^{+20}	0.023	1.33

5.4.2 Nd-doped SnO_x

Table 5.4.3 gives the transport parameters within the Nd-doped SnO_2 films as a function of the gas ratio R. As for the case of undoped films, the data shows that the increase of oxygen concentration (through the decrease of R) leads to different electrical properties as the structure changes from SnO to SnO_2. Low oxygen content in the SnO_x:Nd film (R=4, sample Nd-A) results in p-type material with a high hole mobility (about 54 cm^2/V.s) and a low resistivity (0.06 Ω.cm). Such result is expected from a SnO material as reported recently [313]. At the opposite side, the most oxygen rich film (Nd-D, R=2) has n-type conductivity with an electron mobility exceeding 120 cm^2/V.s and a resistivity as low as 0.001 Ω.cm. It is remarkable that a slight change in R from 2 to 3 results in a lower quality SnO_2 material as the electron mobility drops down to 21 cm^2/V.s and the increases up to 0.005 Ω.cm, yet with n-type character. The measured electrical parameters of sample Nd-B (R=3.5) confirm that this material is a mix of SnO and SnO_2 as the measured carrier concentrations were varying from positive to negative over several measurements.

Table 5.4.3. Electrical properties of the Nd-doped SnO$_x$ films as a function of the gas flow ratio R (Ar/O$_2$)

Sample label	O2	Carrier concentration (cm^{-3})	Resistivity (Ω.cm)	Mobility (cm^2/V.s)
Nd-A	4	$+1.7.10^{+18}$	0.066	54.4
Nd-B	3.5	$4.18\ 10^{+20}/ - 2.40\ 10^{+20}$	0.014	2.3/2.0
Nd-C	3	$-5.32\ 10^{+19}$	0.005	21.6
Nd-D	2	$-3.22\ 10^{+19}$	0.0018	129

The first message from this study is that the electrical results are very consistent with the structural and optical results of the doped films as they confirm the modification of the electrical properties when the structure changes from SnO to SnO$_2$. This was also the case for the undoped samples.

The second message is that the very good insertion of Nd atoms into the SnO$_2$ matrix is favourable, and probably responsible of the very efficient conduction of the carriers in these Nd-SnO$_x$ materials. The Nd atoms are reacting like conventional dopants in a semiconductor.

We have also looked to the effect of of the growth temperature on the transport properties of Nd-doped SnO$_2$ films. For this study, the Ar and O$_2$ gas flows were fixed to 8 and 4sccm, respectively. The results are summarized in Table 5.4.4. Regardless of the deposition temperature, all films exhibit n-type conductivity as expected for SnO$_2$ material[50]. The highest electrons mobility value of 597.6 cm^2/V.s was measured for the fine-grained structure obtained at 15°C and for which no Nd emission was collected. By increasing the deposition temperature up to 300°C, the mobility dramatically decreases and the carriers concentration increases by two order of magnitude. At 400°C the film becomes suddenly more resistive with less carrier concentration. It is important to underline that the highest carrier concentration is measured for the sample exhibiting the strongest Nd related PL, meaning that the optical activity of the Nd^{3+} ions is partially and indirectly controlling the electrical properties.

In fact, many factors such as the microstructure, strain and the Nd insertion can affect the electrical transport in the deposited films. Thangaraju [97] reported that the ionized impurity scattering is a dominant mechanism that limits the carriers mobility. This is consistent with our results since the enhancement of the optical activity of Nd within the SnO$_2$ matrix when increasing temperature up to 300°C could mean better electrical activity and therefore lower carriers mobility in the film. The lower conductivity of the sample at 400°C can be attributed to the increase of the band gap as well as to the decrease of the Nd related PL (300°C). These results confirm the strong effect of the optical activity of the Nd.

Table 5.4.4. Electrical properties of the Nd-doped SnO$_x$ films as a function of the deposition temperature, the Ar and O$_2$ gas flows were fixed to 8 and 4sccm, respectively.

Deposition temperature (°C)	Carrier Concentration (cm^{-3})	Resistivity (mΩ.cm)	Mobility (cm^2/V.s)
15	-2.15 10^{+18}	0.004	597.6
100	-4.71 10^{+18}	0.004	276.2
200	-6.40 10^{+18}	0.012	75.5
30.120	-6.02 10^{+19}	0.008	11.5
400	-1.38 10^{+18}	0.034	132.3

Finally, we have investigated the effect of Nd content on the transport properties of the Nd-doped SnO$_x$ films. The electrical properties of the Nd-doped SnO$_x$ films as a function of the Nd concentration are summarized in Table 5.4.5. In this study the deposition temperature was set at 100°C and the gas flow at 8 sccm of Ar and 4 sccm of O$_2$.

Table 5.4.5. Electrical properties of the Nd-doped SnO$_x$ films as a function of the Nd concentration (at.%)

Nd at.%	Carrier concentration (cm^{-3})	Resistivity (Ω.cm)	Mobility (cm^2/V.s)
0	-4.343 10^{+18}	2.682	0.578
0.6	-4.71 10^{+18}	0.004	276.2
1.1	-4.17 10^{+20}	0.027	0.55
1.4	-1.33 10^{+20}	0.012	3.8

The increase of the Nd content in the films leads to the increase of the carrier's concentration. This is quite consistent with what was reported in chapter 1 about the electrical properties of SnO$_2$. In fact, the insertion of Nd into the structure, particularly in substitutional sites (Nd^{3+} substitutes Sn^{4+}) generates free electrons in the electronic structure of SnO$_x$. Moreover, we have shown that the incorporation of REs creates more oxygen vacancies in the structure which are also responsible of the increase of the carrier's concentration. Resistivity as low as 0.001 Ω.cm and mobility as high as 136.3 cm^2/V.s were recorded for the sample for which a maximum of Nd PL was observed. Correlation to the structural and optical properties of the films confirms that the electrical properties are related to the presence of rare earth in the structure and strongly dependent on its optical activity.

5.4.3 Yb-doped SnO$_x$

Table 5.4.6 summarize the electrical properties of the Yb-doped SnO$_x$ thin films as a function of the O$_2$ gas flow during deposition. It appears that all the films exhibit an n-type conductivity whatever is the O$_2$ gas flow. The film grown with the lowest oxygen flow showed the highest carrier concentration value (10^{20} cm^{-3}) with a low carrier mobility of about 0.62 cm^2/V.s. this is consistent with the structural and optical results, since we expect that this structure is rich with oxygen vacancies, usually known as the source of n-type carriers. Despite the likenesses between the 2 sccm and 3 sccm discussed in the sections above, the film deposited with 3 sccm showed decreasing carrier concentration values by two order of magnitude but much enhanced conductivity. This behaviour is completely coherent with the structure evolution since we found that more oxygen atoms are incorporated into the structure. The conductivity is found to increase further for the film deposited with 4 sccm in addition to a reasonable carrier concentration of -3.5x10^{19} cm^{-3}. However, this deposition condition is not favourable to the Yb emission as demonstrated above. Increasing further the oxygen content (5 and 6 sccm in the chamber) leads to a remarkable decrease in conductivity and mobility as well a dramatic decrease in carrier concentration by 3 orders of magnitude. This result can be explained by the presence of more defects in the structure. In fact the measured net carrier concentration consists of the difference between the total carrier concentration and the density of electron traps. It is difficult to determine the effective carrier concentration since we do not have a quantitative number of the density nor the type of defects present within the structure. The decrease of the conductivity at high oxygen content is rather a consequence of the decrease of the carrier concentration as $\rho = q. \mu. n$

Table.5.4.6. Carrier concentration, resistivity and carrier mobility of Yb-doped SnO$_x$ films as a function of the O$_2$ gas flow (sccm). The deposition was carried out at at 50°C. The Ar flow was to set to 12 sccm.

Oxygen (sccm)	Carrier concentration (cm^{-3})	Resistivity (Ω.cm)	Mobility (cm^2/V.s)
2	- 6.234 x 10^{+19}	0.006	15.4
3	- 4.166 x 10^{+18}	0.053	28.17
4	- 3.583 x 10^{+19}	0.003	52.62
5	- 8.693 x 10^{+16}	14.2	4.62
6	- 5.794 x 10^{+16}	16.39	8.3

We present in table 5.4.7 some electrical properties of the Yb-dopesd SnO$_x$ thin films as a function of the deposition temperatures, and for different Ar and O$_2$ values.

*Table 5.4.7. Transport properties of the Yb-doped SnO$_x$ films as a function of the deposition temperature, the Ar and O$_2$ gas flows were fixed to **8** and **5**sccm, respectively*

Ar :O$_2$ (**8:5**)	Carrier concentration (cm^{-3})	Resistivity (Ω.cm)	Mobility (cm^2/V.s)
100°C	- 8.539 10^{+16}	14.09	5.89
300°C	- 2.950 10^{+20}	0.030	0.73
400°C	- 6.584 10^{+19}	0.040	2.43
500°C	- 1.663 10^{+17}	16.3	2.43

Ar :O$_2$ (**8:3**)	Carrier concentration (cm^{-3})	Resistivity (Ω.cm)	Mobility (cm^2/V.s)
100°C	- 4.166 10^{+18}	0.053	28.17
300°C	- 1.939 10^{+19}	0.0064	50.16
500°C	- 2.279 10^{+20}	0.0018	14.60

Ar :O$_2$ (**8:2**)	Carrier concentration (cm^{-3})	Resistivity (Ω.cm)	Mobility (cm^2/V.s)
15°C	- 5.344 10^{+19}	0.0065	18.22
100°C	- 6.234 10^{+19}	0.006	15.4
200°C	- 2.568 10^{+20}	0.0095	4.55
300°C	- 2.896 10^{+19}	0.015	15.19

Overall, Yb-doped SnO$_x$ films exhibit good electrical values. Resistivities as low as 0.006 (Ω.cm) and moibilities as high as 50 cm^2/V.s with electrons concentration of 2 10^{19} were measured. This result is particularly recorded for high emission of Yb in the NIR region. Such compromise between electrical and optical properties shows the potential of Yb-doped SnO$_x$ films for TCO applications.

Overall, Yb-doped SnO$_x$ films exhibit good electrical values. Resistivities as low as 0.006 (Ω.cm) and moibilities as high as 50 cm^2/V.s with electrons concentration of 2 10^{19} were measured. This result is particularly recorded for high emission of Yb in the NIR region. Such compromise between electrical and optical properties shows the potential of Yb-doped SnO$_x$ films for TCO applications.

To get a larger picture, Figure 5.4.1 compares the carrier mobility measured in undoped, Nd-doped SnO$_x$ and Yb-doped SnO$_x$ films as a function of the oxygen flow during deposition. The figure clearly shows different trends. For the undoped films, the mobility decreases until 4 sccm and then increases. Such behaviour was already observed in the case of polycrystalline silicon with different grained

materials and the trend was linked to the density of charges trapped in the grain boundaries. For the Yb-SnO$_2$ the mobility curve is rather depending on the defects density and types. Besides, it is evident from the graph that the carrier mobility is enhanced when doping with Yb. It is also the case for the Nd-doped SnO$_x$, mobility considering the same range of oxygen flow.
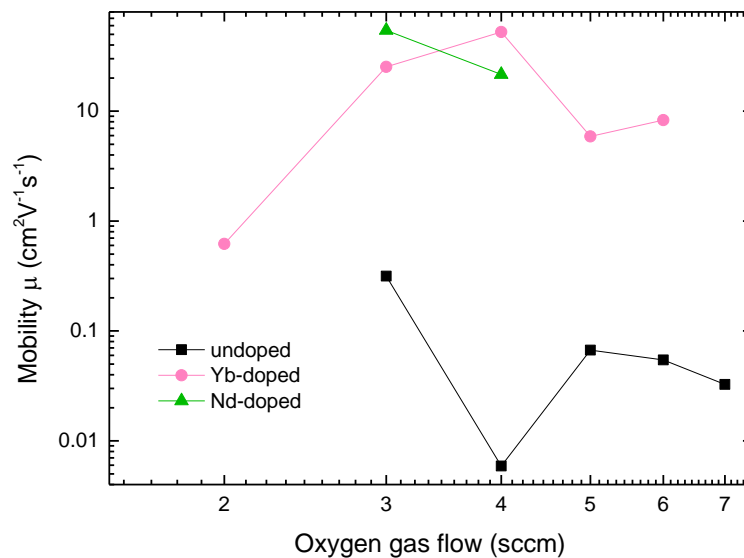

Figure 5.4.1. Mobility of the undoped, Nd-doped and Yb-doped SnO$_x$ thin films as a function of the oxygen gas flow during samples elaboration.

5.4.4 (Nd,Yb) co-doped SnO$_x$

Electrical properties of the co-doped films are reported in table 5.4.8as a function of the O$_2$ gas flow . As noticed with the undoped and Nd-doped samples, amorphous structure for (Nd,Yb) co-doped samples obtained with the lowest oxygen flow also shows p-type conductivity with high carriers concentration value. The increase of the oxygen content to 4 sccm during deposition of the films does not affect seriously the films resistivity. Interestingly, both n and p conductivities have been recorded for the 5 and 6 sccm samples; this is quite coherent with their compositions that have shown a content of p-type SnO of at least 40%. On the other hand, we have shown in chapter 4 that NIR emissions of Nd and Yb are very weak for samples elaborated under 5, 6, 7 and 8 sccm of oxygen. Once more we demonstrate a relationship of the electrical properties with the optical activation of the rare earths elements. The strongest emission lines were in fact recorded for the 3 sccm sample, which here exhibit resistivity of 0.03 Ωcm and carrier mobility of 22 cm^2/V.s.

Table.5.4.8. Carrier concentration, resistivity and carrier mobility of (Nd, Yb) co-doped SnO$_x$ films as a function of the O$_2$ gas flow (sccm). The deposition was carried out at 100°C. The Ar flow was to set to 8sccm.

O$_2$ (sccm)	Carrier concentration (cm^{-3})	Resistivity (Ω.cm)	Mobility (cm^2/V.s)
2	+3.299 x 10^{+19}	0.016	11.79
3	- 8.793 x 10^{+18}	0.034	21.93
4	- 6.276 x 10^{+19}	0.017	5.72
5	+1.898 x 10^{+15}/- 2.546 x 10^{+15}	39.25/36.11	73.76/81.18
6	+ 1.373 x 10^{+15}/- 3.154 x 10^{+15}	60.89/59.22	81.88/51.73
7	+ 4.152 x 10^{+15}	96.493	15.60
8	+ 1.781 x 10^{+16}	150.725	2.50

To confirm even further this last statement, we have investigated the electrical properties of co-doped samples elaborated under 8:3 sccm at different temperatures. The extracted parameters are reported in table 5.3.9. The Data clearly show the dependence of transport properties on the optical activity of the rare earths. In this set of samples, the best Nd and Yb PL have been recorded for the 400°C sample (see section 4.4.2.2). This condition corresponds to that exhibiting the best electrical results.

Table.5.4.9. Carrier concentration, resistivity and carrier mobility of (Nd, Yb) co-doped SnO$_x$ films as a function of the O$_2$ gas flow (sccm). The deposition was carried out at 100°C. The Ar flow was to set to 8sccm.

Td (°C)	Carrier concentration (cm^{-3})	Resistivity (Ω.cm)	Mobility (cm^2/V.s)
100	- 8.793 x 10^{+18}	0.034	21.93
200	- 1.093 x 10^{+19}	0.024	25.08
300	- 6.500 x 10^{+18}	0.156	6.15
400	- 2.882 x 10^{+19}	0.007	29.60
500	- 3.974 x 10^{+17}	1.436	10.95

5.5. Application of RE-doped SnO$_x$ films to solar cells

5.5.1. Silicon solar cells

In chapter 3 and 4, we have described the photon conversion process combining transparent SnO$_x$ films and RE elements (Nd and Yb). In this system, an energy transfer process has been experimentally demonstrated, in which the host matrix SnO$_x$ absorbs UV light and simultaneously sensitizes the RE which gives rise to photon emission in the NIR region. The transparency of the films in the visible-IR range is good enough and the electrical properties are reasonable to envisage the use of these layers as transparent conductive oxides on solar cells.

The silicon solar cells were fabricated at ICUBE following a simple procedure: the emitter was formed by phosphorus diffusion from a spin on source at 850°C for 15min. The back surface field was produced by alloying an aluminium layer evaporated at the rear surface of the silicon and annealed at 850°C for 30min. After cleaning, a Ti/Pd/Ag grid contact was evaporated on the front surface while a plane aluminium layer was evaporated at the back.

We have then sputtered undoped or Nd-doped SnOx films (~100 nm) at 400°C with the condition 8:4 for Ar:O$_2$. The concentration of Nd was about 1.3 at.%. The deposition temperature of 400°C was chosen because of it provide the best Nd optical activity. The external quantum efficiency (EQE) of the coated cells are presented in figure 5.5.1.

The low EQE values for the non-coated cell are due to the high reflectance (35%) of silicon. On the other hand, the cell coated with the undoped SnO$_x$ film exhibits an enhanced EQE, which clearly evidences the role of SnO$_x$ films as an antireflection coating. In addition, a small but significant increase of EQE is observed in the UV region for this cell, particularly from 300 to 400 nm with an optimum at 320 nm.
A relative gain in quantum efficiency of about 10% was recorded against the reference cell. This means that SnO$_x$ matrix alone is already able to enhance the solar cell response in the UV, thanks to the photon conversion of UV photons. We have shown that strong emission in SnO$_x$ is arising from structural defects in its electronic structure.
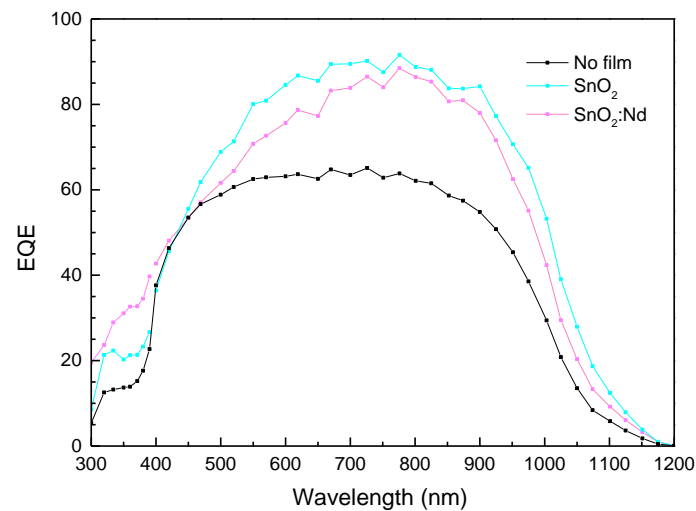
Figure 5.5.1 EQE for c-Si solar cell without coating, with undoped and Nd-doped SnO_x films.

More interestingly, the use of Nd doped SnO_x film on top of the Si cells increases significantly the cell response in the UV range. Higher EQE values are obtained compared to the undoped case. The optimum response is at around 360 nm with an EQE of 32.6 % against 13.8 % for the reference cell. Such result is very encouraging and proves the impact of photons conversion through energy transfer from the SnO_x host to Nd^{3+} ions that efficiently emit in the infrared. The EQE response does take into account the reflectance of the layer in this region. For a complete understanding, IQE has to be calculated by dividing EQE over (1-R) to extract the real efficiency of conversion in this region, which should increase after calculations. In contrast to the gain, a small decrease of the cell response in the visible region is observed. This is most likely due to the slight absorption of the rare earth in this region.

5.5.2. CIGS solar cells

We have deposited Nd-doped SnO_x layers with 0.6 Nd at.% on CIGS solar cells. The latest were provided by Yeungnam University in the frame of collaborative program named REACT-PV.   The cell is composed of a CdS emitter deposited on a CIGS absorbing material grown on a Mo/glass substrate. The CIGS p-type absorber was prepared in 2 steps: sputtering following by a selenization process while the CdS n-type buffer layer was made by the standard chemical bath deposition method. It is worth noticing that the quality of the absorbing CIGS layer was not optimized for this study. The structure of the cell is as follows: SLG/Mo/CIGS/CdS/Nd-SnO$_2$/AZO. The converting Nd-SnO$_2$ layer was deposited at different temperatures and a Cu/Ni grid contact was finally evaporated. We have managed the deposition time to result in 100 nm of Nd-doped SnO_2 regardless of the deposition temperature. The Nd-SnO$_2$ layers will be serving as TCO and photon converters. Mo and AZO layers

represent the back and top contacts, respectively. The structure of the cell is shown in figure 5.5.2.a. SEM images of undoped and Nd-doped SnO_x films on the top of the cells are also reported in figure 5.5.2.b.
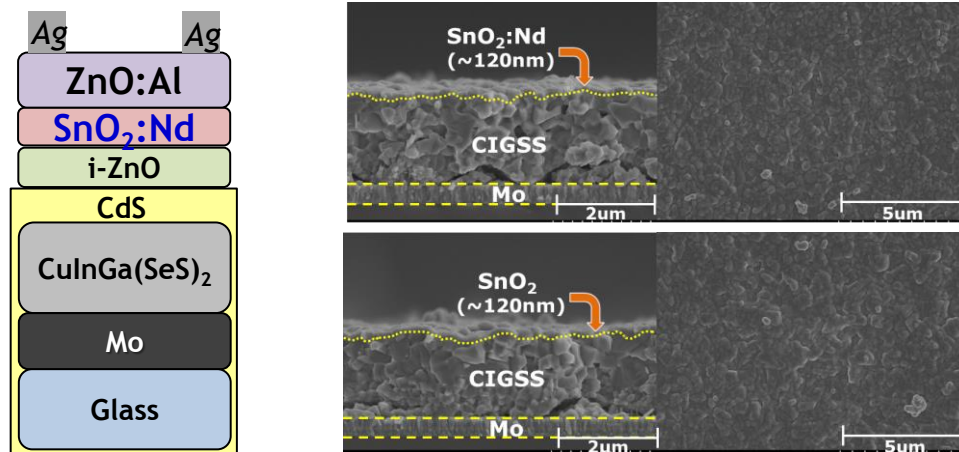

Figure 5.5.2 a) Solar cell structure, **b)** cross section and plane SEM images of the cell with SnO_x layers.

Table 5.5.1 gives the average values (measured on four cells) of open circuit voltage Voc, short circuit current density Jsc, fill factor FF, and cell efficiency η as a function of the growth temperature of Nd-SnO_2 layers at 100, 300, and 400°C.

Table.5.5.1. Voc, Jsc, FF, and efficiency η of the CIGS solar cells with SnO_2:Nd films deposited at different T

Deposition temperature	Voc (mV)	Jsc(mA/cm^2)	FF (%)	Efficiency η (%)
100°C	615 ±5	30.9 ±1	45.7 ±1	8.7
300°C	575 ±5	32.3 ±1	56.1 ±1	10.4
400°C	510 ±5	25.9 ±1	26.1 ±1	3.4

The open circuit voltage of the cells is observed to decrease substantially and continuously as the deposition temperature increases. This can be due to the degradation of the CdS emitter and/or CIGS absorbing layer upon thermal annealing during deposition. In contrast, the fill factor is found to be optimal for the cell with Nd-SnO_2 layer deposited at 300°C. This is consistent with the electrical properties reported in Table II of these films where the conduction properties are found to be very good for the 300°C case. For higher temperatures, FF is reduced as the layer resistivity is high. More importantly, the short circuit current density is the highest for the most luminescent sample (300°C) as stated with the PL and PLE experiments. Such result is an indirect proof of the effect of an efficient down-shifting process via the Nd-SnO_2 film thanks to the energy transfer from the SnO_2 matrix to Nd

ions. As a result, the combination of good TCO properties and photon conversion ability provided the largest power conversion efficiency to the cell with Nd-SnO$_2$ deposited at 300°C. This work opens routes for photon management properties through the use of rare earth elements doped TCO films for photovoltaic solar cells.

We have also performed a study to compare between undoped and Nd-doped ZnO and SnOx on CIGSS cells and found that Nd doped films have led to better results (figure 5.5.4)
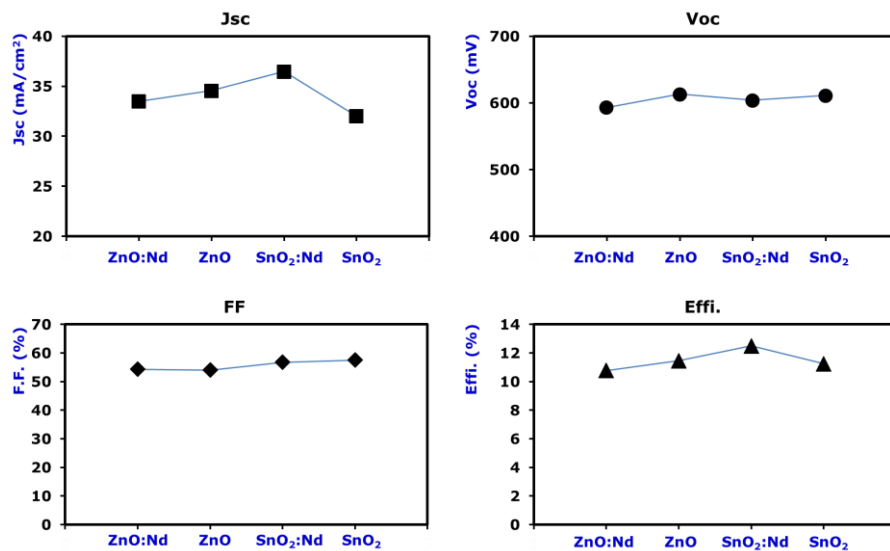

Figure 5.5.4 evolution of Jsc, Voc, FF and efficiency of the cells with undoped and Nd-doped ZnO and SnO$_x$ conversion layers.

5.5. Conclusion

Electrical properties of the undoped and RE-doped SnO$_x$ are reported (RE=Nd, Yb and (Nd,Yb)). N-type conductivity with good electrical values has been measured for the SnO$_2$ samples where p-type conductivity was recorded for SnO samples. The effect of the oxygen gas flow and deposition temperature during samples elaboration have been investigated for undoped and doped SnO$_x$ films. We have found that best electrical results are correlataed to the RE optical activity of the RE elements. For the doped films, resistivity as low as $1.85 \ 10^{-3}$ with mobility as high as 136.3 cm^2/V.s were recorded. The application of these layers to c-Si based solar cells has shown the increase of the EQE of the cells in the UV region for undoped and Nd-doped films, confirming the efficiency of the photon conversion process. Converter Nd doped films were also applied to Cds/CIGS based solar cells. The sample exhibiting the best electrical data and Nd-PL response has demonstrated the highest cell performances. The efficiency was increased by 2% as comparing with the 100°C elaborated sample. Such results demonstrate the potential interest of RE-doped SnO$_x$ thin films as functional TCO for solar cells.

5.6. References

[296] W. Shockley, H.J. Queisser, Detailed balance limit of efficiency of p‑n junction solar cells, Journal of applied physics, 32 (1961) 510-519.

[297] M.A. Green, Third generation photovoltaics: solar cells for 2020 and beyond, Physica E: Low-dimensional Systems and Nanostructures, 14 (2002) 65-70.

[298] M.A. Green, Third generation photovoltaics: Ultra‑high conversion efficiency at low cost, Progress in Photovoltaics: Research and Applications, 9 (2001) 123-135.

[299] T. Trupke, M.A. Green, P. Würfel, Improving solar cell efficiencies by down-conversion of high-energy photons, Journal of Applied Physics, 92 (2002) 1668-1674.

[300] T. Trupke, M.A. Green, P. Würfel, Improving solar cell efficiencies by up-conversion of sub-band-gap light, Journal of Applied Physics, 92 (2002) 4117-4122.

[301] T. Trupke, A. Shalav, B.S. Richards, P. Würfel, M.A. Green, Efficiency enhancement of solar cells by luminescent up-conversion of sunlight, Solar Energy Materials and Solar Cells, 90 (2006) 3327-3338.

[302] R.A. Ze'ev, A. Niv, X. Zhang, Solar energy enhancement using down-converting particles: A rigorous approach, Journal of Applied Physics, 109 (2011) 114905.

[303] C. Strümpel, M. McCann, G. Beaucarne, V. Arkhipov, A. Slaoui, V. Švrček, C. Del Cañizo, I. Tobias, Modifying the solar spectrum to enhance silicon solar cell efficiency—An overview of available materials, Solar Energy Materials and Solar Cells, 91 (2007) 238-249.

[304] B.M. Van Der Ende, L. Aarts, A. Meijerink, Lanthanide ions as spectral converters for solar cells, Physical Chemistry Chemical Physics, 11 (2009) 11081-11095.

[305] Q. Zhang, X. Huang, Recent progress in quantum cutting phosphors, Progress in Materials Science, 55 (2010) 353-427.

[306] H.Q. Wang, M. Batentschuk, A. Osvet, L. Pinna, C.J. Brabec, Rare‑Earth Ion Doped Up‑Conversion Materials for Photovoltaic Applications, Advanced Materials, 23 (2011) 2675-2680.

[307] W.W. Piper, J.A. DeLuca, F.S. Ham, Cascade fluorescent decay in Pr3+-doped fluorides: Achievement of a quantum yield greater than unity for emission of visible light, Journal of Luminescence, 8 (1974) 344-348.

[308] J.L. Sommerdijk, A. Bril, A.W. de Jager, Two photon luminescence with ultraviolet excitation of trivalent praseodymium, Journal of Luminescence, 8 (1974) 341-343.

[309] D. Dexter, Possibility of luminescent quantum yields greater than unity, Physical Review, 108 (1957) 630.

[310] R.T. Wegh, H. Donker, E.V.D. van Loef, K.D. Oskam, A. Meijerink, Quantum cutting through downconversion in rare-earth compounds, Journal of Luminescence, 87–89 (2000) 1017-1019.

[311] R.T. Wegh, H. Donker, K.D. Oskam, A. Meijerink, Visible Quantum Cutting in LiGdF4:Eu3+ Through Downconversion, Science, 283 (1999) 663-666.

[312] C. Davesnne, Elaboration et caractérisation de films de ZnO dopé pour des applications optoélectroniques, in, Université de Caen Basse Normandie, 2014.

[313] W. Guo, L. Fu, Y. Zhang, K. Zhang, L. Liang, Z. Liu, H. Cao, X. Pan, Microstructure, optical, and electrical properties of p-type SnO thin films, Applied Physics Letters, 96 (2010) 2113.

Conclusions and perspectives

This thesis work concerned the investigations of structural, optical and electrical properties of rare earth doped tin oxide materials. The main objective being to produce a layer that efficiently converts UV-visible photons into near-infrared photons, better absorbed by conventional solar cells. The understanding of the transfer mechanism is highlighted.

We have investigated the properties of undoped, Nd-doped, Yb-doped and (Nd, Yb) co-doped SnO_2 nanoparticles and thin films. Most of these materials are reported for the first time. Thanks to the strong collaboration with other research groups at IPCMS, IJL and ILV institutes, several characterization techniques were employed to characterize the synthesized materials. The structural and chemical properties were analysed by XRD, Raman, XPS, RBS, SEM, TEM, SAED and EDS. The optical properties were characterized by UV-Vis-IR, PL, PLE as well as QY techniques. The electrical and solar cells properties were evaluated by Hall Effect, EQE and I-V measurements.

The study of RE-doped SnO_2 nanoparticles (NPs) by co-precipitation and sol-gel has provided valuable information on the insertion processes of REs in SnO_2 matrix. The latter allowed incorporation of Nd up to 3.43 at. % and Yb up to 3.5 at.% in the case of individual doping of the NPs. For co-doping case, up to 6.03 at.% of Nd and 1.65 at.% of Yb have been successfully inserted into the structure. We have shown that above a certain RE content in interstitial and substitutional sites, insertion is performed at the grains boundaries. Thanks to optical characterizations, we have gained insight on the conversion mechanisms of such systems. Efficient infrared emissions of Nd^{3+} and Yb^{3+} ions were recorded through efficient energy transfer from the host matrix. In the case of co-doped NPs, a rich emission spectrum including PL of both rare earths under host matrix excitation was reported. Moreover, we have experimentally demonstrated efficient energy transfer from Nd^{3+} to Yb^{3+} ions; this system is also interesting for shifting visible photons to red ones.

The study of Nd or Yb doped thin films have revealed how the elaboration parameters affect the incorporation of the RE elements in the matrix and their subsequent optical activity. We have studied thoroughly the effect of the oxygen gas flow during deposition, the substrate temperature and post annealing treatment for each rare earth element separately as well as jointly. The oxygen in all films was found to be a key parameter for the rare earth activation. We have shown for Nd-doped films that the excess of oxygen is needed for its optical activity. Thanks to the study on the optical activity of Nd in SnO and SnO_2 host matrices, we demonstrated that the sensitization from the SnO_2 host is necessary for efficient UV photons conversion into infrared.

In the case of Yb and co-doped films, XPS results have revealed, unexpectly, that all films were composed of a mixture of SnO and SnO_2 oxides with at least 40% of SnO. We have reported that the Yt pumps the oxygen bound to Sn (IV) and reduces SnO_2 to SnO, which led to an oxidation state of 3+, favourable for an optical activation. Efficient energy transfer from the host to the rare earths was also reported. However, up to a certain concentration of optically active REs, non-radiative transitions were favoured and less PL was recorded. We have also revealed the presence the presence of Yb^{2+} ions in some films that sensitizes the Yb^{3+} ions. On the other hand, we have found that the deposition temperature does not affect that much the oxides proportions, nor the density of RE^{3+}, but enhances the crystalline quality of the films. This has been translated as a reduction of the interatomic distance between ions and transfer centres because of the decrease in the lattice parameter. Consequently, the efficiency of energy transfer was enhanced.

In co-doped Nd,Yb-SnO_x thin films, we have also identified two photons conversions processes: (i) UV photons can be converted into infrared through an energy transfer from the host to both Yb^{3+} and Nd^{3+} ions; (ii) The visible photons can be converted into infrared through an energy transfer from Nd^{3+} to Yb^{3+} ions.

Application of undoped and Nd-doped thin films (about 100 nm) to silicon based solar cells have shown a relative gain of 18.8 % in the 300-400 nm range of EQE against the reference cell. Yet, undoped SnO_2 thin films have also shown a gain of 10% because of the UV photons conversion through its own defects states within its band gap. The application to CIGS solar cells has shown an increase of the solar cell efficiency of 2 % relative to cells with Nd-films without Nd PL.

Overall, this work has shown that functionalizing a transparent conductive oxide such as tin oxide with rare earth elements is an interesting alternative to overcome the thermalization losses in some solar cells such as silicon, chalcogenides and organic solar cells.

Future work and perspectives

Several investigations are still required to get a clear picture of the down conversion/photon shifting process in such transparent conducting oxide materials. In particular, it will be interesting to determine the positions of Yb and Nd within Yb and co-doped films in order to understand the origin of the PL quenching. It also could be of interest to quantify the Yb^{2+} and Yb^{3+} contents in the films and understand deeply the transfer mechanisms occurring between them. More importantly, it is important to quantify accurately of the quantum yield of the different energy transfer routes for the different structures. Application to solar cells with a low EQE in the UV region should be prioritized.

Résumé en français

Les matériaux oxydes, au-delà de leur rôle traditionnel en tant que diélectriques, sont devenus des matériaux fonctionnels pour la haute technologie. En effet, de par la diversité de leur composition, ils couvrent presque toutes les facettes des sciences des matériaux pour des applications dans le domaine des semi-conducteurs, de la supraconductivité ou de la ferroélectricité. Les propriétés des oxydes sont en général très sensibles au moindre défaut dans la structure comme les joins de grains, les lacunes d'oxygène ou les impuretés.

En particulier, les oxydes semi-conducteurs présentent la classe de matériaux la plus prometteuse pour la nouvelle génération de l'électronique transparente et particulièrement la technologie des écrans plats. Les composants clés pour cette application sont les semi-conducteurs à large bande interdite, pour lesquels le dopage permet d'avoir des matériaux aux excellentes performances électroniques. De tels matériaux combinant une bonne transparence dans le visible et une bonne conductivité, connus sous l'appellation : oxydes transparents conducteurs (TCO), ont fait des progrès impressionnants dans un temps relativement court. Les TCOs sont appliqués un peu partout ; on les trouve dans les écrans plats, les cellules solaires, les diodes électroluminescentes inorganiques (LEDs) et organiques (OLEDs), et d'autres dispositifs optoélectroniques. Ils peuvent également être utilisés dans les capteurs de gaz, comme des revêtements réfléchissants sur les collecteurs solaires, des éléments chauffants dans les microscopes, ou des revêtements pour vitrage automobile afin de réduire la transparence de la lumière UV et IR.

Au-delà de la transparence et la conductivité, le dopage des matériaux aux éléments de terres rares permet des nouvelles fonctionnalités et des propriétés optiques fascinantes, ouvrant ainsi la porte à d'autres types d'applications orientées vers l'optique comme les lasers, les fibres optiques, ainsi que dans l'optoélectronique comme les OLED et les cellules solaires.

Pour la dernière application, les semi-conducteurs à large band-gap comme le ZnO, ITO, In_2O_3 et SnO_2 peuvent être dopés aux terres rares (TR) afin de modifier en amont une partie du spectre solaire incident et mieux l'adapter à l'absorption de la cellule solaire. En choisissant la bonne combinaison d'éléments TR et de l'oxyde semi-conducteur, le spectre solaire peut être converti via différents procédés : conversion de photons rouges en photons visible (up-conversion), de photons ultraviolet en photons visibles (down-shifting ou down conversion). Dans le dernier cas, la conversion permet de réduire la thermalisation des

photons très énergétiques et en conséquence d'augmenter le rendement de conversion quantique.

L'un des principaux axes de cette thèse est la conversion de photons afin d'améliorer le rendement des cellules solaires photovoltaïques. Ces pertes peuvent être réduites grâce à une couche de conversion de photons, rajoutée à la cellule. La conversion proposée est de type « down » c'est-à-dire que l'on souhaite convertir un photon UV en si possible deux photons IR ou visible qui pourront être utilisés dans la cellule.

Dans ce travail de thèse, nous nous intéressons à des oxydes transparents dont le rôle est d'absorber principalement des photons UV et de les convertir essentiellement en photons rouges bien plus utiles à des cellules solaires en silicium ou en CIGS.

Cela a été réalisé grâce à une combinaison simple de semi-conducteur à large bande interdite avec des terres rares qui émettent dans le visible et l'infrarouge (Nd, Yb, Pr, Tb). Beaucoup d'études ont été publiées sur ce type de couplage dont l'efficacité est prometteuse. En tenant compte du nombre d'études qui ont été déjà faites dans la littérature, le choix de la matrice est crucial. Nous avons donc choisi la matrice du SnO_2 caractérisée par un large gap (3,6 eV-4.1 eV), par une haute transparence dans le visible, de bonnes propriétés électriques et surtout par la structure tétragonale qui permet l'insertion de la terre rare et favorise celles avec une valence égale à 3. Toutes ces propriétés montrent l'intérêt de l'application des couches SnO_2 dopées aux terres rares en conversion photonique et comme TCO.

Nous avons étudié la possibilité d'insertion des terres rares (Nd, Yb, Pr et Tb…) dans une matrice de SnO_2 en utilisant des méthodes de synthèses chimiques (sol-gel, co-précipitation) et physiques (pulvérisation cathodique). Les investigations ont concerné des analyses physico-chimiques, optiques et électriques des matériaux SnO_2 dopés. Le point de mire est la démonstration de l'activité optique et la luminescence de la terre rare ainsi que la démonstration de la conversion de photons. Le rôle de la composition de la matrice hôte de la terre rare dans le mécanisme de conversion a été démontré. L'application des couches de conversion aux cellules solaires à base de CIGS et silicium cristallin a été réalisée.

Nous avons commencé par une étude de la synthèse de poudre/nanoparticules de SnO_2 dopées aux différentes terres rares, notamment Pr, Yb, Tb et Nd. L'étude de la poudre nous a permis dans un premier temps de vérifier si la matrice SnO_2 permet d'incorporer les différents

éléments de terre rare. Nous avons vérifié la présence des terres rares dans la matrice par des spectroscopies d'absorption (UV-Vis) et d'émission (PL), et microscopie électronique à balayage (MEB) ainsi que des analyses de composition chimique (EDX). Des analyses complémentaires par diffraction des rayons X et Raman nous ont montré que chaque terre rare à un impact différent sur la structure, selon le site d'insertion, l'élément TR peut créer plus de défauts comme elle peut provoquer une dilatation de la maille élémentaire.

Comme le montre la figure 1 donnant le spectre de photoluminescence, le dopage de la matrice SnO_2 avec les différentes terres rares a été réalisé avec succès. La photoluminescence de l'Ytterbium et le Néodyme dans l'infrarouge et le Tb dans le visible prouve bien l'activité optique de ces éléments au sein de la matrice SnO_2. La réponse sous une excitation dans l'UV (zone d'absorption de la matrice) suggère un transfert d'énergie de la matrice vers les terres rares.
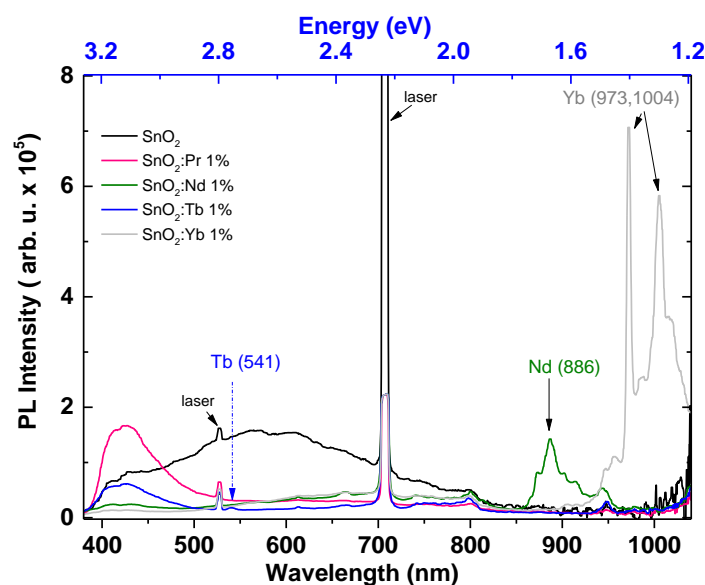
Figure 1. Spectres de photoluminescence des poudres SnO_2 dopées aux terres rares sous une excitation UV (325 nm)

Dans la suite nous avons choisi de développer une étude plus approfondi avec l'élément dopant Nd. Le choix s'est porté sur la zone d'émission de la terre rare utile à la cellule solaire. Nous avons synthétisé des poudres de SnO_2 dopées Nd avec différentes concentrations et par le biais de deux voies chimiques : la co-précipitation et la voie sol-gel. L'effet de la concentration sur les propriétés structurale et optique a été profondément étudié. On a trouvé que l'effet du dopage est différent avec les deux techniques. Les poudres synthétisées par co-

précipitation ont montré une évolution de structure différente car l'élément Nd à tendance à s'insérer aléatoirement dans des sites substitutionnel ou interstitiels. La conséquence est visible sur la valeur de l'énergie de gap du matériau SnO_2 dopé Nd qui varie d'une façon aléatoire également. Des mesures de photoluminescence ont montré que malgré les différents sites d'insertion, les ions Nd^{3+} sont très bien insérés dans la matrice et donne lieu à une photoluminescence dans l'IR sous une excitation dans l'UV. L'intensité de cette émission augmente avec la concentration en Nd. Les poudres synthétisées par voie sol-gel ont montré une tendance d'évolution de propriétés structurale et optique lorsqu'on augmente la concentration en Nd. L'augmentation de la maille élémentaire en fonction de la teneur en N suggère que les impuretés Nd substituent les atomes d'étain dans la matrice. Les analyses par XRD (grande échelle) et microscopie électronique à transmission (TEM) (petite échelle) ont montré une diminution de la taille des cristallites (figure 2.a et 2.d), ce qui veut dire que le dopage par Nd crée des contraintes dans la structure qui brise les grains. De plus, la figure 2 montre les plans atomiques des nanoparticules ce qui appuis la cristallinité à l'échelle nanométriques.
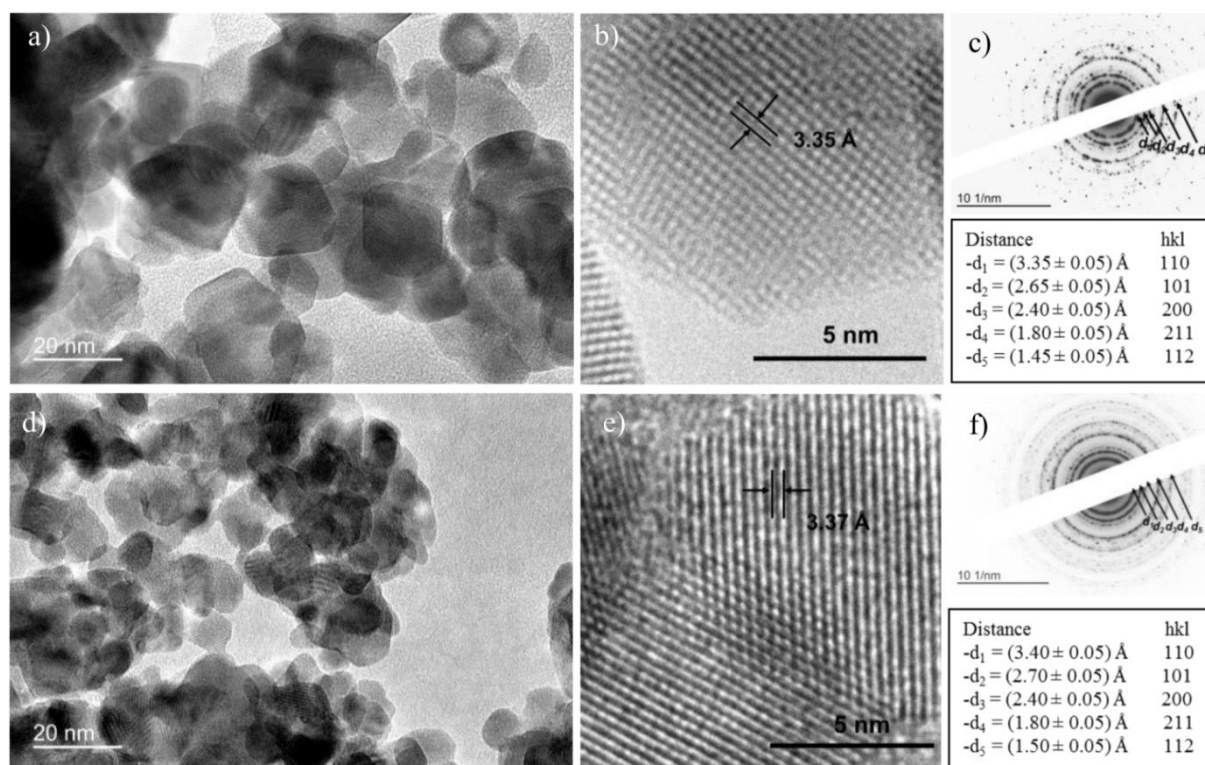

Figure 2.images de MET, METHR et SAED des poudres non-dopées (a, b et c) et le dope à 3 % de Nd (d, e et f) respectivement.

Des analyses d'absorption par l'UV-Vis on révélé les pics d'absorption du Nd dans le visible et le NIR dont l'intensité augmente lorsqu'on augmente la concentration de la terre rare Nd.
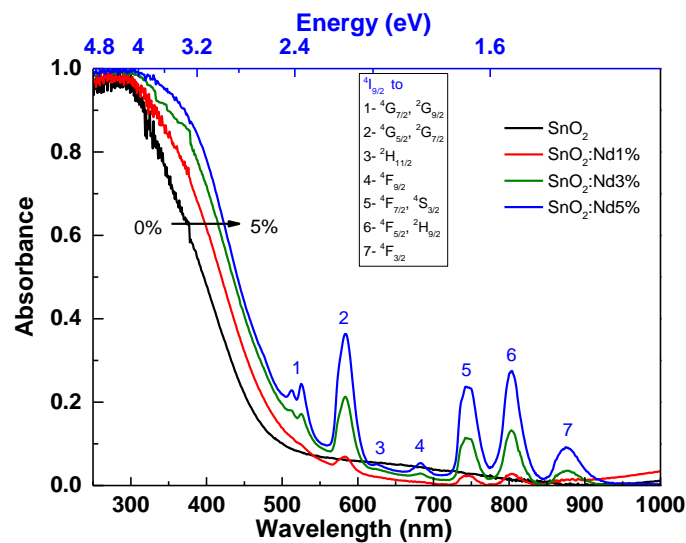

Figure 3. Spectres d'absorption des poudres SnO_2 dopées aux Nd en fonction de la concentration de Nd.

La figure 3. Montre aussi une évolution intéressante de la largeur de la bande interdite (gap) de la matrice en fonction du dopage. Plus on introduit du Nd, plus le gap diminue. Les pics d'absorption correspondent à des transitions des électrons dans les niveaux d'énergie du Nd.

Grace à la photoluminescence et à la photoluminescence d'excitation, des signaux d'émission dans le proche infrarouge ont été collectés.
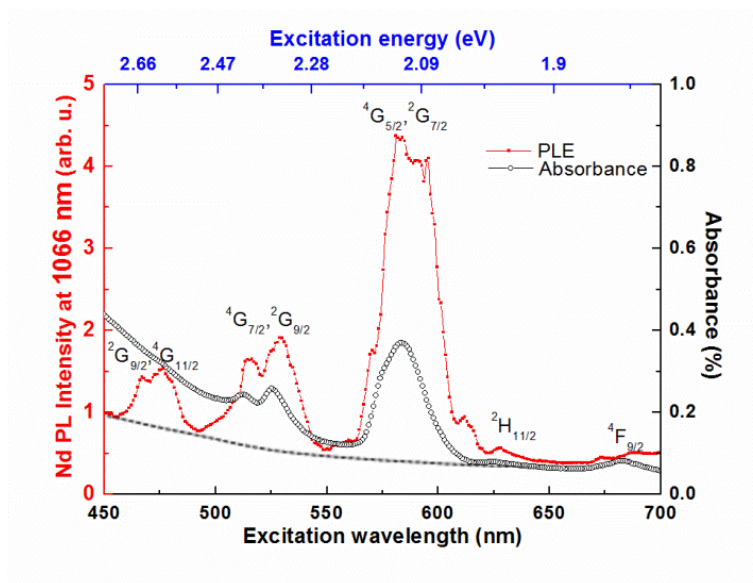
Figure 4. Spectres de photoluminescence d'excitation du SnO₂ dopé 3% Nd. La détection est focalisée sur 1066 nm (pic d'émission du Nd)

Le spectre de PLE dans la figure 4 montre quelques niveaux d'énergie du Nd, ce qui nous a permis de construire une partie de sa structure électronique. Nous avons également démontré que ses ions de terre rare sont bien optiquement actifs. Enfin un transfert d'énergie se passant entre la matrice et la terre rare a été démontré.

Ensuite, nous avons étudié le dopage des nanoparticules de SnO₂ avec Yb de la même manière que le Nd. Le résultat est assez prometteur. Nous avons identifié un transfert d'énergie assez efficace de la matrice qui absorbe la lumière UV vers la terre rare qui a son tour émet des photons NIR (proche infrarouge).La même étude a été menée pour un système plus complexe. C-à-d, nous avons co-dopé ces nanoparticules de SnO₂ avec les deux terres rares (Nd et Yb). Et grâce à un transfert d'énergie de la matrice vers les deux terres rares, nous avons pu enregistrer des spectres de photoluminescence très riche dans la région NIR. Nous avons également suivi l'excitation de l'Yb par le Nd. Nous avons montré que lorsque le Nd est directement excité, l'Yb émet simultanément de la lumière NIR.

Dans la deuxième partie du manuscrit, nous avons développé les propriétés de films SnO₂ dopé au Nd obtenus cette fois ci par une voie physique, à savoir la pulvérisation cathodique. Pour commencer, nous présentons les résultats des films réalisés sous différents rapports de gaz (Argon et oxygène lors du dépôt). Cette expérience permet la possibilité d'élaborer des

matrices d'oxyde avec différentes teneurs en oxygène, couvrant SnO, SnO$_2$ et un mélange des deux phases.

Les diffractogrammes des rayons X dans la figure 5 montre l'évolution de la structure et le changement du matériau d'un SnO à un SnO$_2$. Ce resultat a été confirmé par des analyses structurales complémentaires par XPS (X-ray photoélectron), et NEXAFS (Near edges X-analysis fine structure) ce qui nous a permis, en plus, de déterminer l'environnement chimiques constituant l'oxyde à base d'étain, oxygen et Néodyme.

Aussi nous avons pu accéder aux spectres de bandes de valence et déterminer l'interaction entre les différents éléments. Par ailleurs, des analyses complémentaires optiques et électriques ont montré des comportements très différents entre les structures SnO et SnO$_2$. L'enjeu de l'étude est de voir comment les atomes Nd s'insèrent dans les différentes matrices.
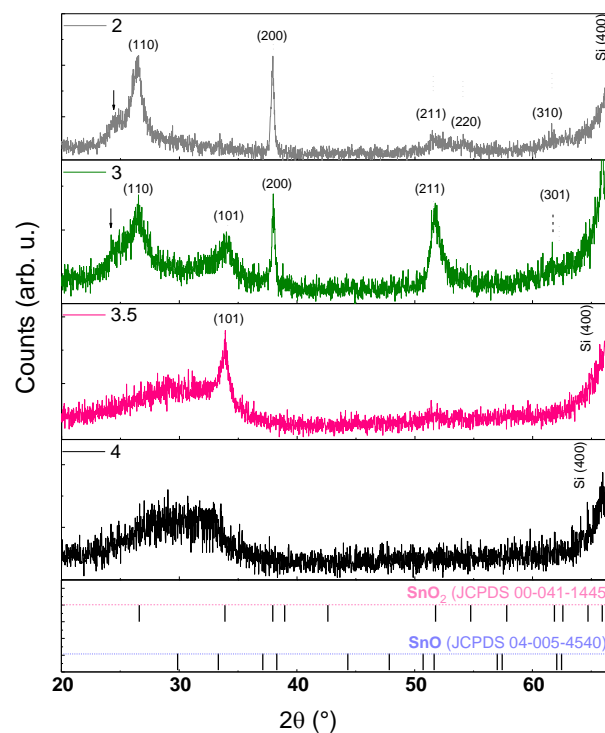

Figure 5. Diffractogrammes XRD des couches minces SnO$_2$ dopées Nd déposées sous différents flux de gaz (Ar et O$_2$)

Le résultat remarquable qu'on a trouvé est que les éléments Nd sont bien insérés dans les différentes matrices synthétisées, mais ne peuvent être optiquement actifs que si la structure

est bien définie (SnO et SnO$_2$), comme dans le cas de la poudre, nous avons pu identifier plusieurs niveaux d'énergie de la terre rare.
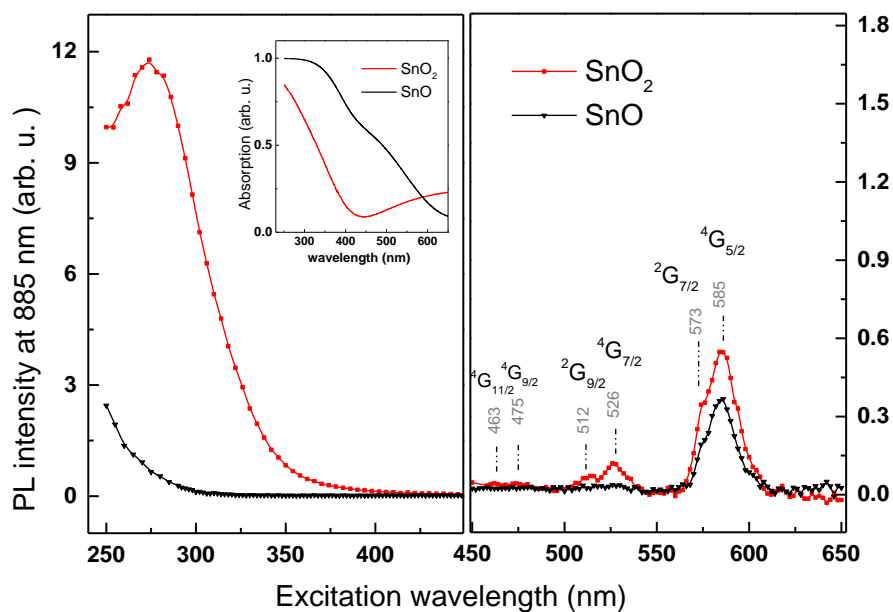

Figure 6. Spectres de PLE des films SnO et SnO$_2$ dopés au Nd. La détection est focalisée à 885 nm.

Nous avons conclu que l'origine de la photoluminescence du Nd provient d'un transfert très efficace de la matrice SnO$_2$. Par contre, nous avons découvert un résultat intéressant, c'est que malgré le petit gap du SnO les photons UV très énergétique (hv > 4,13 eV) sont transférés au Nd pour une émission dans l'IR (Figure 6). On n'a pas pu déterminer l'origine de ce processus, mais des hypothèses de transfert ont été rapportées. Nous avons trouvé aussi que l'émission de la terre rare est 20 fois plus efficace si elle est indirectement excitée via la matrice que par excitation directe.

Par ailleurs nous avons étudié l'effet de la température du dépôt sur les propriétés structurales et optiques des couches. Nous montrons que le matériau a tendance de s'améliorer en augmentant la température de dépôt. Nous avons trouvé que SnO$_2$ se cristallise selon des orientations préférentielles en fonction de la température. Les analyses par XPS nous ont montré que la stochiométrie (composition chimique) est stable quelque soit la température de dépôt ; par contre une diminution de l'énergie de gap a été observée. Les Analyses par PL et PLE, ont déterminé 100°C comme un point de transition pour laquelle un transfert de la matrice SnO$_2$ vers SnO serait possible.

L'effet de la concentration du Nd sur la structure et la photoluminescence des films a été également étudié. Nous avons trouvé que dans le cas des couches minces pulvérisées, la matrice SnO_2 permet l'incorporation de la terre rare jusqu'à 1.3 at%. L'incorporation du Nd dans la structure induit des défauts et donc retarde la formation du SnO_2 cristallin, la clé pour son activité optique. Plus on rajoute le Nd, plus on a besoin de remonter en température de dépôt pour avoir un meilleur signal de PL. Finalement, un transfert d'énergie de la matrice à la terre rare a été prouvé grâce à la spectroscopie de photoluminescence d'excitation. Nous montrons que les photons UV de très haute énergie peuvent être convertis avec succès en photons IR. De plus, les propriétés électriques des couches montrent l'intérêt potentiel des couches SnO_2 dopé Nd comme des oxydes transparents conducteurs.

Dans une dernière phase, nous avons exploré le dopage de SnO_2 par la terre rare Ytterbium Yb. Cette dernière a un rayon ionique plus important que celui du Nd, donc l'insertion de cette terre rare dans la matrice du SnO_2 a été plus difficile. Nous avons commencé l'étude par l'élaboration de la poudre par voie sol-gel. Différentes concentrations d'Yb ont été testées. Des caractérisations structurales par XRD, Raman, MEB et TEM ont été réalisées. Nous avons trouvé que l'Yb, à l'instar de Nd, peut s'insérer facilement dans la matrice sans modifier la phase cristalline et induit une augmentation de la maille élémentaire. Les bandes d'absorption de la terre rare ont été mis en évidence par spectroscopie d'absorption. Grace à la spectroscopie de PL, nous avons montré que la terre rare est optiquement active et engendre une photoluminescence dans l'IR autour de 978 nm. Comparant à l'Yb dans la matrice ZnO, la matrice du SnO_2 est responsable de la dégénérescence du niveau d'énergie d'Yb et donne lieu à une bande supplémentaire centrée à 1010 nm.

Après validation de l'activité optique de la terre rare par le signal de photoluminescence dans l'IR, nous nous sommes orientés vers l'étude de SnO_2 dopé à l'Yb réalisé en couche mince. Nous avons commencé par varier la concentration d'oxygène dans les films afin d'avoir différents rapports de gaz. Contrairement au Nd, les films dopés à l'Yb avaient une structure SnO_2 quel que soit la teneur en oxygène. L'analyse XPS des bandes de valence ont confirmé une structure SnO_2. Ensuite, grâce à une analyse plus fine des niveaux $3d_{5/2}$ et 1s de l'étain et oxygène, respectivement, nous avons montré que les couches sont composé d'un mélange SnO et SnO_2 avec minimum 40 % de SnO. La déconvolution est présentée dans la figure 7.
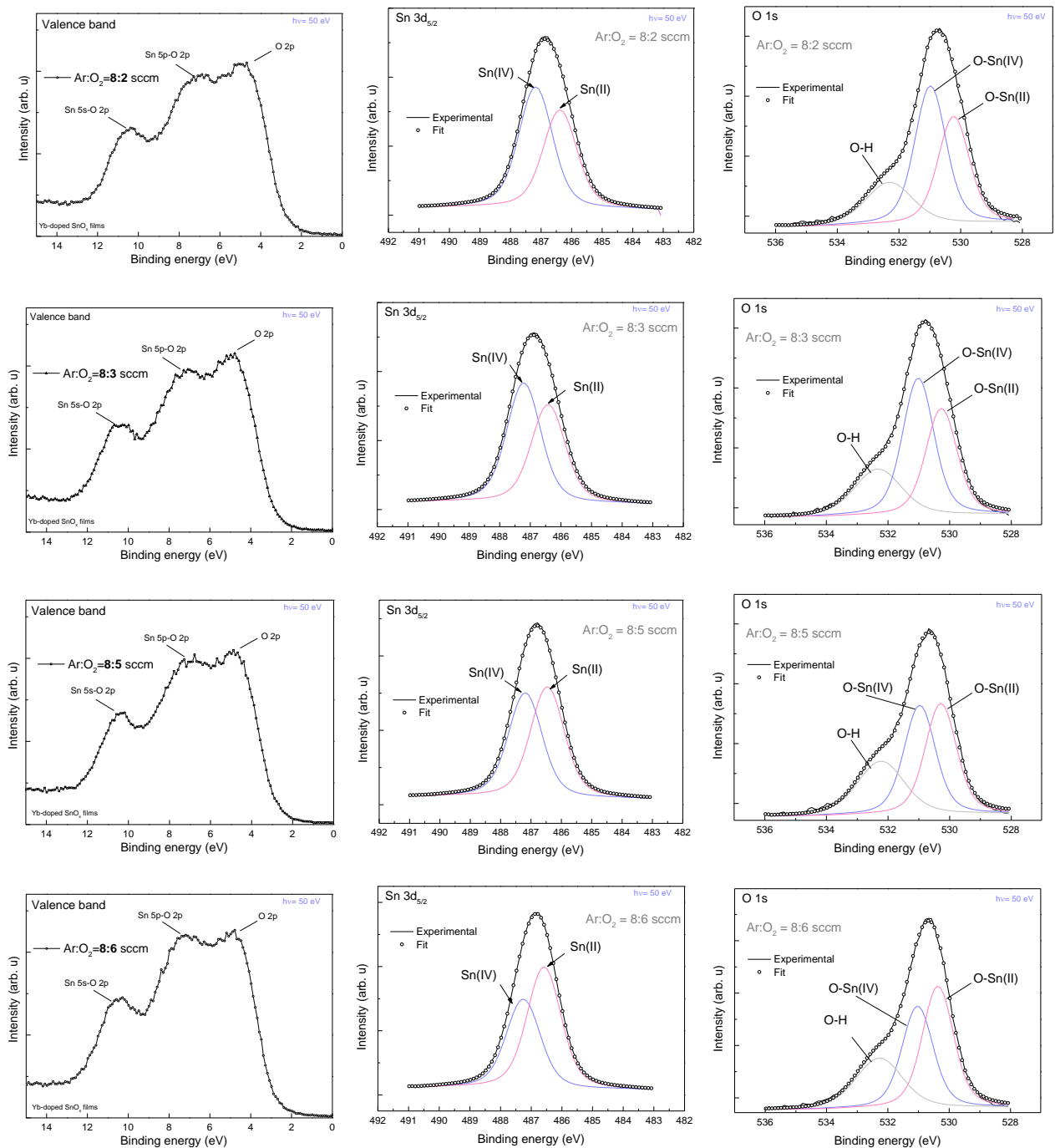
Figure 7. (a) bande de valences, (b) Spectres des niveaux de Coeur Sn $3d_{5/2}$ and (c) O 1s des couches minces dopées Yb, élaborées avec différentes concentrations en oxygène

Nous avons pu également détecter l'élément de l'Yb malgré sa faible concentration dans la structure. L'augmentation de la teneur en oxygène lors du dépôt et qui a conduit à une

augmentation de la phase SnO dans la structure a également induit des changements au niveau de l'environnement chimique de l'Yb. Nous avons trouvé que plus la phase SnO_2 diminue plus le pic de l'Yb augmente, cela est montré dans la figure 8. Nous proposons que la réduction de cette phase d'oxyde provienne de l'élément Yb qui lui est gourmand à l'oxygène.
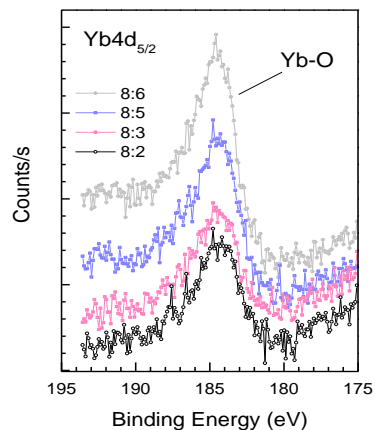

Figure 8. Niveau de cœur $4d_{5/2}$ de l'Yb dans les films SnO_x, élaborés sous différents flux d'oxygène.

Les propriétés d'émission et de conversion ont été testées par la spectroscopie de photoluminescence (PL) et de photoluminescence d'excitation (PLE). Le résultat est présenté dans la figure 9.
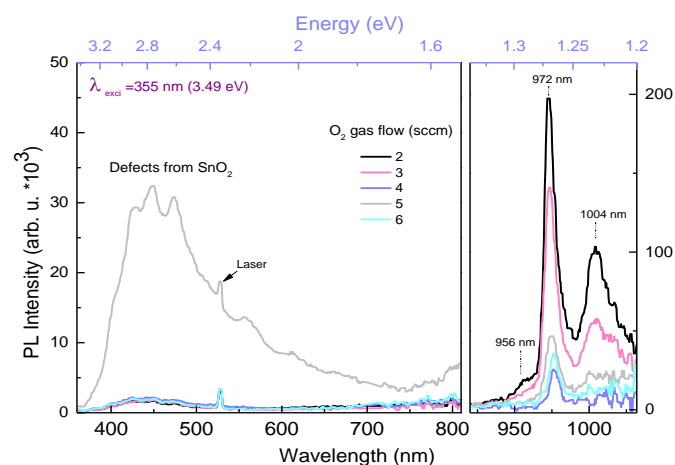

Figure 9. Spectres de photoluminescence des couches minces SnO_x dopées à l'Yb, sous une excitation à 355 nm.

Sous une excitation laser dans l'UV, à une longueur d'onde de 355 nm les films SnO_x dopés à l'Yb présentent une photoluminescence faible dans le visible, et intense dans l'infrarouge. La dernière correspond à la photoluminescence de l'Yb. Ce qui prouve la fonctionnalité de conversion de photons UV en photons IR. Des mesures de PLE ont montré un transfert de la matrice vers la terre rare qui ce fait de 250 à 400 nm.

Nous avons ensuite étudié de l'effet du recuit post-déposition sur la photoluminescence de la terre rare. Des recuits à 500, 700 et 900°C ont été réalisé sur des films élaborés sous 8:2 d'Ar et O_2. Comme elle le montre la figure 10, sous une excitation de 300 nm (UV), les films présente des spectres d'émission assez différents. Nous avons constaté que l'augmentation de la température de recuits entraine une dégénérescence des pics d'émission de l'Yb dans l'infrarouge. La température optimale est conclue à 700°C. Les analyses structurales par XRD, XPS et MEB ont montré qu'à 900°C, la structure des films est complètement déformée.
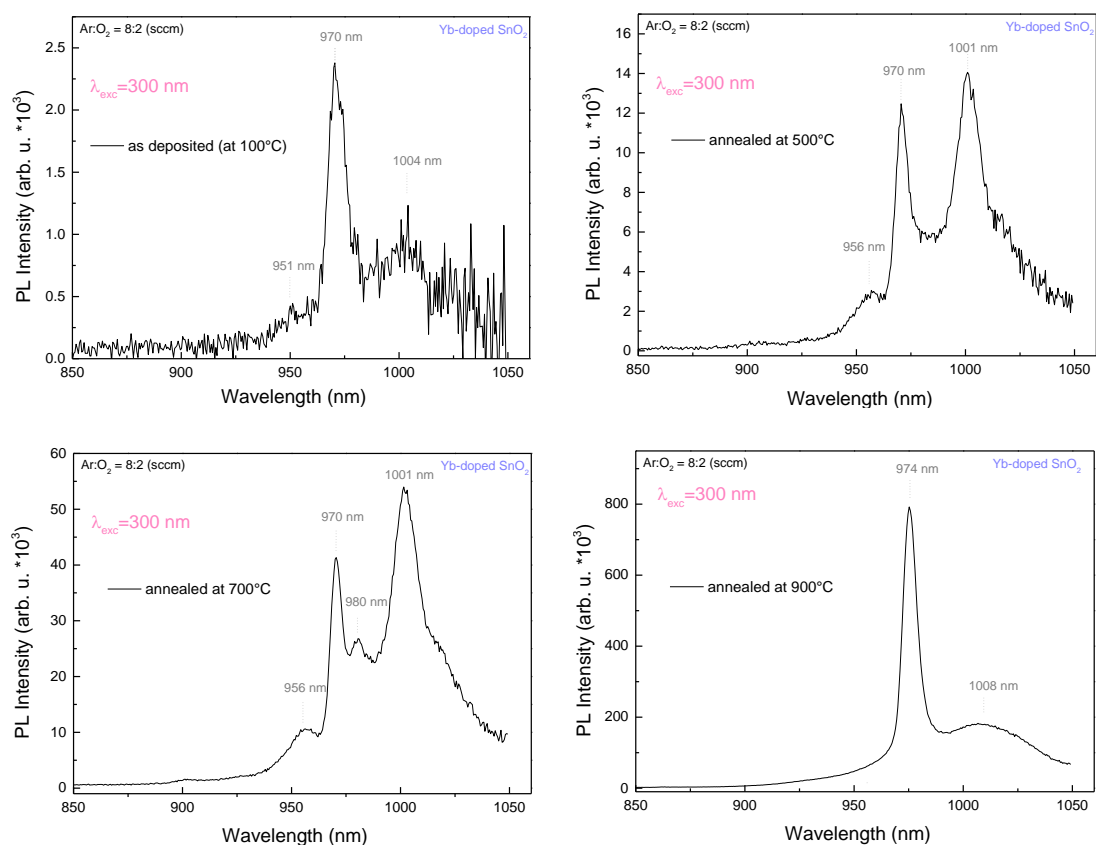

Figure 10. Spectres de PL des films SnO_x dopés Yb élaborés à 8 :2 sccm à 100°C, et recuits à 500°C, 700°C et 900°C. L'excitation a été réalisée par une lampe Xénon.

Nous nous sommes intéressés à la déconvolution du pic de photoluminescence de l'Yb afin de déterminer son diagramme des niveaux d'énergie ainsi que les transitions correspondantes. Le résultat est présenté dans la figure 11. Plus de 7 composantes ont été nécessaire pour la déconvolution de la photoluminescence. A partir de la position de ces pics nous avons pu construire le diagramme présenté à droite. Nous avons trouvé que le dégénérescence des deux niveaux d'énergie de l'Yb est complète.
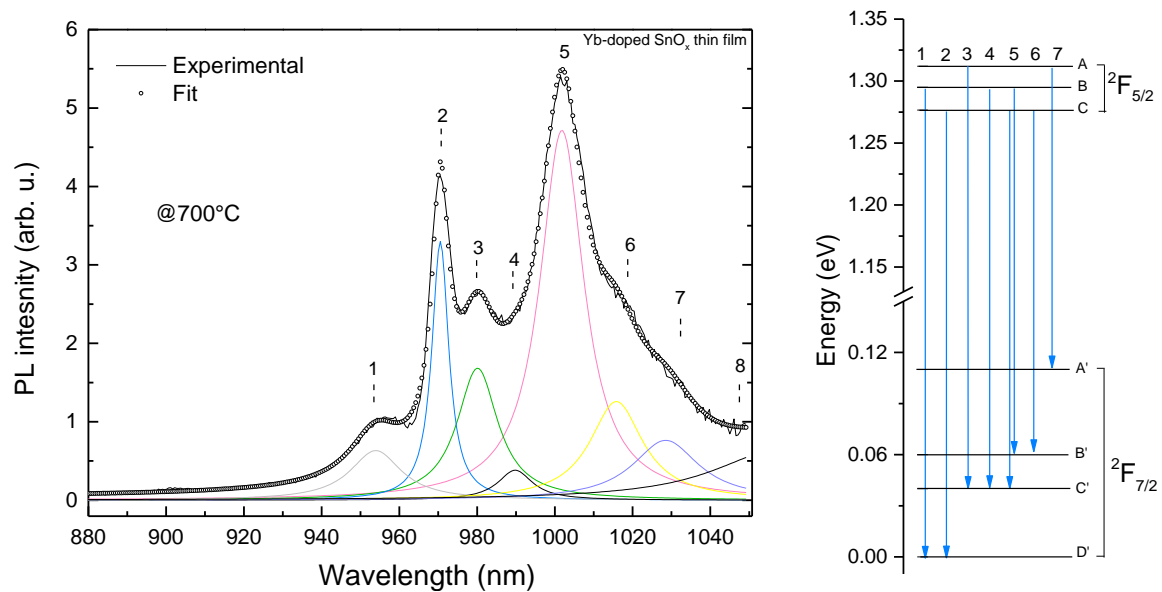

Figure 11.a) déconvolution de la photoluminescence de l'Yb dans le NIR, b) diagramme des niveaux d'énergie de l'Yb ainsi que les transitions correspondantes aux pics identifiés dans la figure à gauche.

Pour conclure cette partie nous montrons dans la figure 12 les spectres de photoluminescence d'excitation de l'Yb. La détection est fixée à 971 nm. La température de recuit joue un rôle très important sur l'efficacité du transfert de la matrice à la terre rare.
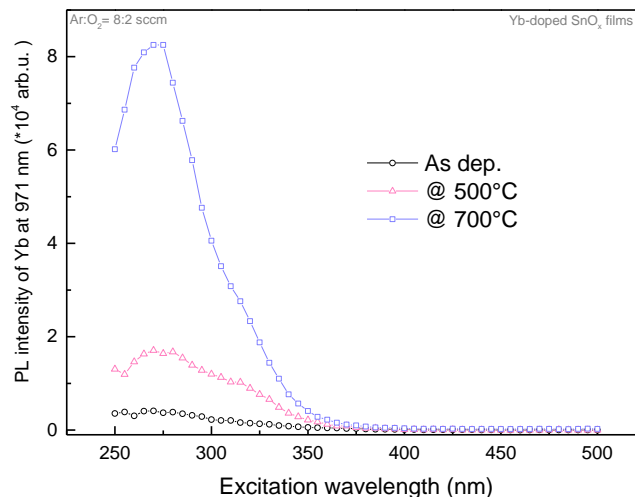
Figure 12. Spectres de PLE des couches SnO$_x$ dopés à l'Yb, recuits à différentes températures. La détection est fixée à 971 nm.

Nous avons par la suite étudié le mécanisme d'insertion des deux terres rares, Nd et Yb avec de faibles concentrations. Plusieurs tests ont été réalisés afin de déterminer le meilleur environnement atomique favorable à l'émission des deux terres rares. La figure 13 montre les spectres de photoluminescence des couches SnO$_2$ co-dopées avec Nd et Yb en faibles teneures (0.6 et 1.3 at.%, respectivement). Ces spectres montrent à quel point la PL du Nd et Yb est sensible à la variation du flux d'oxygène pendant le dépôt. Des analyses complémentaires par XPS ont permis de comprendre certain phénomènes ou conditions nécessaires pour la conversion de photons. Grâce à la spectroscopie de photoluminescence d'excitation, nous avons pu identifier deux types de conversion de photons. Grace à un transfert d'énergie de la matrice SnO$_x$ vers les deux terres rares, la lumière UV est convertie en lumière proche infrarouge, et grâce à une forte interaction entre les deux terres rares, la lumière visible peut être aussi convertie en lumière proche infrarouge. Cela provient d'un transfert d'énergie du Nd vers l'Yb.

Nous montrons finalement dans la figure 14 un schéma les deux types de transfert discutés ci-dessus.
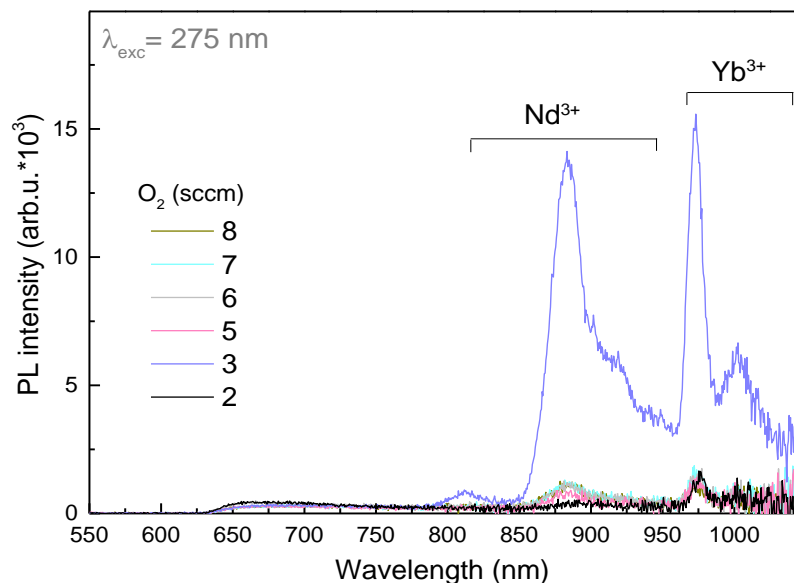
Figure 13. Spectres de photoluminescence des couches minces SnO_2 co-dopées aux Nd et Yb.
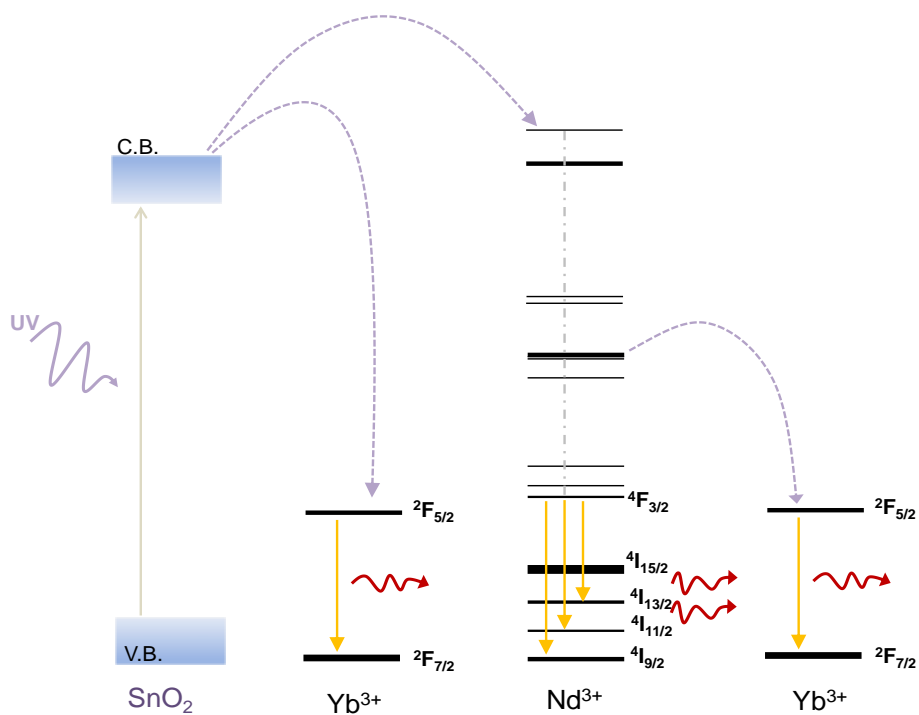

Figure 14. Schéma de transferts d'énergie possible dans le système SnO_x co-dopés Nd et Yb.

Dans une dernière phase, nous avons appliqué certaines structures développées précédemment aux cellules solaires. Après un bref rappel de l'intérêt, nous présenterons le cas des couches

SnO_2 dopé Nd aux cellules solaires de type CIGS/CdS ainsi que des cellules à base de silicium cristallin. Nous avons montré une amélioration des propriétés photovoltaïques des cellules CIGS lorsqu'on a une bonne activité optique de la terre rare. Pour finir, nous comparerons l'effet du TCO, notamment ZnO, ZnO dopé Nd, SnO_2 et SnO_2 dopé Nd sur le fonctionnement de la cellule.

Nous montrons également que l'application de ces couches sur autres types de cellules solaires est tout à fait possible. Un gain dans la réponse spectrale de la cellule dans la partie UV a été noté. Les cellules avec des couches de conversion au-dessus montrent des valeurs de 32.6 % d'EQE contre 13.8% des cellules standards. La réponse spectrale de la cellule dans la partie visible du spectre a été également améliorée, et cela est dû à un effet de passivation des couches SnO_x dopées Nd comme le montre la figure 15.
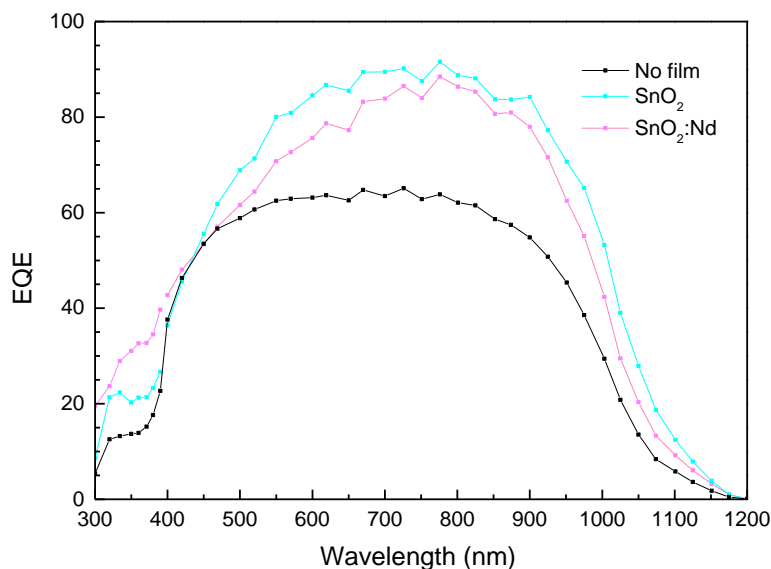

Figure 15. Réponse sepctrale (EQE) des cellules solaires à base de silicium cristallin sans et avec couches de SnO_x dopées Nd

En résumé, lors de ce travail de thèse nous avons montré que la matrice de SnO_2 permet l'incorporation de différentes terres rares notamment l'Yb, Tb, Pr, et Nd. Nous avons pu identifier quelques niveaux d'énergie pour les deux terres rares, Nd et Yb aussi bien que l'effet de leur insertion sur la structure et la photoluminescence. Dans le cas des couches minces, nous avons mis en évidence l'importance de la matrice pour l'activation optique de la

terre rare. Lors du dopage par l'élément Nd, seule la structure SnO_2 donne lieu à une photoluminescence importante, alors que dans le cas du dopant Yb, la photoluminescence est obtenue avec les deux matrice SnO et SnO_2. Nous avons prouvé la présence d'un transfert d'énergie de la matrice SnO_2 vers Nd ou Yb, ou bien depuis SnO vers Yb. Dans le co-dopage des couches minces aux Nd et Yb, nous avons pu identifier deux types de transfert d'énergie ou deux types de conversion de photons, de l'UV vers le proche infrarouge grâce au transfert de la matrice vers les deux terres rares, du visible vers le proche infrarouge grace au transfert du Nd vers l'Yb. Enfin, nous avons appliqué avec succès les films $Nd:SnO_2$ comme convertisseur de photons UV en photons visible et leur efficacité pour augmenter le rendement de conversion.

Publications :

"Optical and structural properties of Nd doped SnO_2 powder fabricated by the sol–gel method". Bouras. K. et al. (2014). J. Mater. Chem. C **2**, 8235-8243

"Structural, Optical and Electrical properties of Nd-doped SnO_2 thin films fabricated by reactive magnetron sputtering for solar cell devices" Bouras. K. et al. (2016) Solar Energy Materials & Solar Cells (SOLMAT), **145**, 134-141

"Deposition Time Effect on the Physical Properties of Cu_2ZnSnS_4 (CZTS) Thin Films Obtained by Electrodeposition Route onto Mo-coated Glass Substrates" (2015) Energy Procedia **84**, 127-133

Karima BOURAS

RE-Doped SnO$_2$ Oxides for Efficient UV-Vis to Infrared Photon Conversion: Application to Solar Cells

Résumé

Ce travail a porté sur la synthèse et caractérisations structurales, optiques et électriques des films d'oxyde d'étain (SnO$_x$) dopés avec des éléments de terres rares (RE: Néodyme, Praséodyme ou Ytterbium). L'objectif est de démontrer la conversion de photons UV, voire Visible, en photons rouges via ces films RE :SnO$_x$, tout en conservant leurs propriétés come oxydes transparents conducteurs. Les films ont été produits par des méthodes chimiques (sol-gel, précipitation) ou physiques (pulvérisation cathodique). Grâce à de nombreuses analyses fines (Raman, XPS, XRD…), nous avons pu corréler les propriétés structurales et de composition des couches RE :SnO$_x$ avec leurs propriétés d'émission de photons. Nous avons pu établir les conditions optimales de conversion photonique dans des systèmes à une seule ou double terre rare. Les mécanismes régissant le transfert dans ces films ont été identifiés. Enfin, nous avons appliqué ces couches minces RE :SnO$_x$ optimisés sur des cellules solaires en silicium et en CIGS et nous avons montré un net gain dans la réponse spectrale de la cellule dans l'UV. Comme conséquence, nous avons démontré une amélioration des paramètres photovoltaïques des cellues comprenant les couches de conversion.

Mots-clés : Oxydes, TCO, terres rares, SnO$_2$, conversion de photons, cellules solaires, Si, CIGS

Résumé en anglais

Photon conversion using lanthanide doped materials with high performances is a great challenging topic and of particular interest for photovoltaics. This work aims at functionalizing transparent conductive oxide (TCO) materials with rare earth (RE) elements for photons conversion purpose without harm to transparency, nor carriers transport properties of the TCO. The spectral conversion targeted in this thesis is of type "shifting", in other words, converting high energy UV photons into low energy visible and/or NIR photons useful to solar cells. Here we investigated the doping process of SnO$_2$ as a host material in which rare earths such as Nd, Tb, Pr, and Yb were inserted. The first part of this work concerns the study of structural and optical properties of RE-doped SnO$_2$ nanoparticles (powders). The latest were synthesised by two chemical methods: co-precipitation and sol-gel. The results have shown an efficient insertion of the RE into the SnO$_2$ structure with excellent photon emission properties. The second part of this thesis reports on the properties of RE-doped SnO$_x$ thin films produced by magnetron sputtering technique. Indeed, the use of films is more appropriate when visioning applications of these structures as TCOs for solar cell. Several deposition parameters and post deposition treatments have been carried out in order to find the best chemical environment favourable to the RE emission. We have identified the region of the UV light converted into NIR photons and proposed several energy transfer mechanisms occurring between the host SnO$_x$ and the REs. In case of co-doping with Nd and Yb elements, a complementary spectral conversion process has been identified: visible photons are efficiently converted into NIR photons through energy transfer from Nd^{3+} to Yb^{3+} ions. In the final chapter, we have demonstrated an efficient application of the RE-doped SnO$_2$ conversion layers to CIGS and Si based solar cells. We have identified an increase of the spectral response of the cell in the UV region, thanks to the conversion of the UV photons into NIR photons. Overall, we have shown an improvement of the photovoltaic properties of the cells through an enhancement of the short circuit current, and consequently, the conversion efficiency. In addition, we have highlighted the good electrical properties of the RE-doped SnOx layers. This work shows that the RE-SnO$_x$ converting layers are capable of offering improved solar cells performances without additional technical steps.

Keywords: Oxides, TCO, Rare earths, SnO$_2$, Photons conversion, solar cells, Si, CIGS, Sputtering